Understanding Modelled Sea-Air CO_2 Flux Biases in the Southern Ocean through the Seasonal Cycle

Ndunisani Precious Mongwe

August 2018

A dissertation presented for Doctor of Philosophy

Faculty of Science

Department of Oceanography, University of Cape Town

Supervisors : Dr. Pedro M.S. Monteiro (Council for Scientific and Industrial Research)

Associate Professor Marcello Vichi (University of Cape Town)

Acknowledgements

First, I want to thank my supervisors Dr Pedro Monteiro and Associate Prof Marcello Vichi, for their support and guidance throughout this process. Their mentorship in both the doing and thinking about science was excellent; I learnt a lot from them. I want to also acknowledge their financial support for attending local and international scientific conferences and workshops which was undoubtedly fruitful for my learning and development. A special thanks to Prof John Field who kindly offered to read my dissertation prior to submit; his feedback was instrumental in clarifying the text. I want to thank Dr Olivier Amount and Dr Marina Lévy for hosting me at LOCEAN, France on a SOCCLI research exchange at the beginning of my PhD. I also want to thank Dr Nicolette Chang, who set up the NEMO PISCES model used in chapter 3 and was a co-author of my first paper. I also want to thank fellow office mates, friends, and colleagues whom also played a crucial role during my PhD; Bernardino Nhantumo, Dr Luke Gregor, Dr Sarah Nicholson, Dr Steward Bernard, Dr Sebastiaan Swart , Christo Whittle, Marcel du Plessis, Dr Alice Lebehot, Renaud Person, Pholoso Montsho and Dr Racheal James. This work was undertaken with financial support from the Department of Science and Technology (DST), National Research Foundation (NRF) and Applied Centre for Climate and Earth Systems Science (ACCESS). I also want to thank the CMIP5 model community, Peter Landschützer, Taro Takahashi and Luke Gregor for making their products available. I want to acknowledge the Council of Scientific and Industrial Research (CSIR) and the Centre for High-Performance Computing (CHPC) for providing the computational resources used for this dissertation. Finally, a special thanks to my mother and family for giving me the courage to finish what I start.

Abstract

The Southern Ocean forms a vital component of the earth system as a sink of CO_2 and heat, taking over 40% of the annual oceanic CO_2 uptake (75% of global heat uptake), slowing down the accumulation of CO_2 in the atmosphere and thus the rate of climate change. However, recent studies based on the Coupled Model Intercomparison Project version 5 (CMIP5) Earth System Models (ESMs) show that CMIP5 ESMs disagree on the phasing of the seasonal cycle of the CO_2 flux (FCO_2) and compare poorly with available observation estimates in the Southern Ocean. Notwithstanding these differences, the seasonal cycle is a dominant mode of CO_2 variability in the Southern Ocean, and hence this is an important bias. Previous studies suggest that these biases of FCO_2 in ESMs might be a significant limitation to the long-term simulation of CO_2 characteristics in the Southern Ocean. Consequently, this study has three primary objectives: first, to develop a process-based diagnostic method to analyze and isolate key biases and their underlaying mechanisms in the model-observations seasonal cycle of FCO_2 differences for forced ocean models and ESMs. Second, to use this framework to examine sources of biases responsible for the limited skill of CMIP5 models in simulating the seasonal cycle of FCO_2 with respect to observed estimates. Thirdly, to investigate how these present-day biases in the seasonality and drivers of CO_2 in CMIP5 ESMs affect modelled long-term changes in the mechanisms of CO_2 uptake in the Southern Ocean. In the first part of the dissertation, an objective diagnostic framework was established to analyze model-observation biases in the seasonal scale of FCO_2 using the NEMO PISCES ORCA2LP model output, and Takahashi et al. (2009) observed estimates. The diagnostic framework focuses on examining the relative contributions of the competing drivers (SST and DIC) and related processes (solubility, biological and mixing) to instantaneous monthly changes in surface pCO_2 (and FCO_2) at the seasonal scale. In the second part of the dissertation, this approach is applied to 10 CMIP5 models in the Southern Ocean, to investigate the mechanistic basis for the seasonal cycle of FCO_2 biases. It was found that FCO_2 biases in CMIP5 models can be grouped into two main categories, i.e. group-SST and group-DIC. Group-SST models are characterized by an exaggeration of the seasonal rates of change of Sea Surface Temperature (SST) in autumn and spring during the cooling and warming peaks, respectively. These faster-than-observed rates of change of SST tip the control of the seasonal cycle of pCO_2 and FCO_2 towards SST and result in divergence between the observed and modelled seasonal cycles, particularly in the Sub-Antarctic Zone. While almost all analyzed models show these SST-driven biases, 3 out of 10 (namely NorESM1-ME, HadGEM2-ES and MPI-ESM, collectively the group-DIC models) compensate the solubility bias because of their exaggerated primary production, such that biologically-driven DIC changes become the regulators of the seasonal cycle of FCO_2. It was also found that despite significant differences in the spatial characteristics of the mean annual fluxes, CMIP5 models show a zonal homogeneity in the seasonal cycle of FCO_2 at the basin-scale in contrast

to observed estimates. In the final third of the dissertation, using five CMIP5 ESMs from the RCP8.5 scenario, it was found that CMIP5 models present climate biases in the seasonality and drivers of FCO_2 are fundamental to how models simulate long-term changes in the mechanisms of CO_2 uptake in the Southern Ocean. Although all five analyzed models show an increased annual mean CO_2 uptake by the end of the century, they show significant differences in the mechanisms. The present-day temperature biased models (group-SST) generally maintain the dominance of the temperature driver in the seasonal variability of FCO_2 to end of the century. But show enhanced CO_2 uptake due to increased anthropogenic atmospheric CO_2 and decreased surface CO_2 buffering capacity but they display a weak to null role of biological activity in the increased CO_2 sink. On the other hand, the increased CO_2 uptake at the end of the century in group-DIC models is explained increased biological driven CO_2 uptake in spring, linked to increased Revelle factor and solubility driven CO_2 uptake in winter. Increased Revelle factor at the end of the century enhance pCO_2 changes for even smaller DIC changes.

Declaration

I declare that the project proposal for this dissertation was co-develop by myself and my PhD supervisors, where I played a major role in designing the focus of the project. The execution, analyses, interpretation and writing of the dissertation represent my own work under the guidance of my supervisors. The thesis was composed by myself, and the work contained here is my own except where explicitly stated in the text and has not been submitted for any other degree or professional qualification.

Date: 28 August 2018

Signed by candidate

Signature:

Acronyms

ACC Antarctic Circumpolar Current

AABW Antarctic Bottom Water

AAIW Antarctic Intermediate waters

AZ Antarctic Zone

Chl Chlorophyll-a

CDW Circumpolar Deep Water

CMIP5 Coupled Model Intercomparison Project Version 5

CO_2 Carbon dioxide

CSIR Council for Scientific and Industrial Research

DIC Dissolved Inorganic Carbon

ENSO El Niño – Southern Oscillation

ESM Earth System Model

FCO_2 Sea-Air CO_2 Flux

GLODAP Global Ocean Data Analysis Project

L14 Landschützer et al., 2014 data product

MIZ Marginal Ice Zone

MLD Mixed Later Depth

NEMO Nucleus for European Modelling of the Ocean

NPP Net Primary Production

pCO_2 Partial pressure of carbon dioxide

PISCES Pelagic Interaction Scheme for Carbon and Ecosystem Studies

PF Polar Front

RCP 8.5 Representative Concentration Pathway 8.5 scenario

SAM Southern Annular Mode

SAMW Sub-Antarctic Mode Water

SAZ Sub-Antarctic Zone

SOCAT Surface Ocean Carbon Atlas

SST Sea Surface Temperature

STF Sub-Tropical Front

TAlk Total Alkalinity

T09 Takahashi et al., 2009 dataset

WAO03 Word Ocean Atlas 2003 data

Table of Contents

Chapter 1

Introduction

1.1 Defining the problem

Since the industrial revolution (1750s) atmospheric CO_2 has increased from 277 ppm (Joos and Spahni, 2008) to over 400 ppm in the contemporary climate (Dlugokencky and Tans, 2015), mostly linked to fossil fuel emissions and cement production (Le Quéré et al., 2018). The land and ocean play a key role as sinks and reservoirs of CO_2, slowing down the accumulation of CO_2 in the atmosphere and thus the rate of climate change (Fung et al., 2005; Gruber et al., 2009; Majkut et al., 2014), Fig. 1.1.

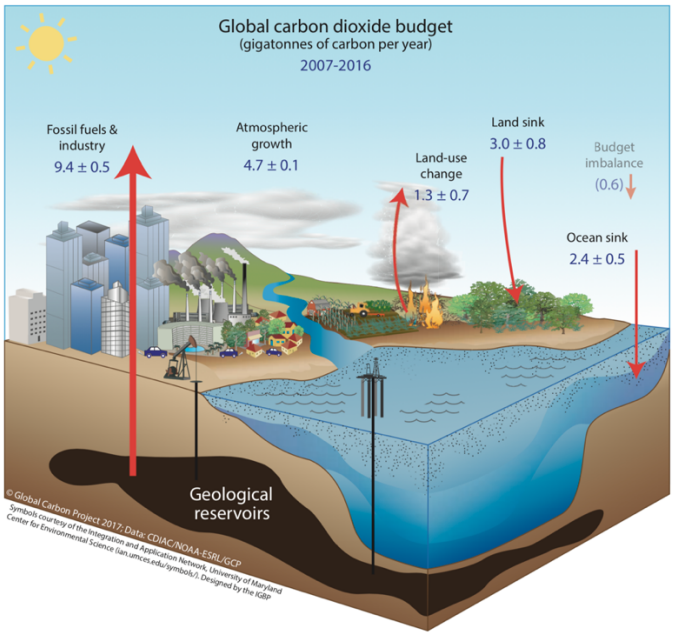

Figure. 1.1. Schematic of the global carbon cycle caused by anthropogenic activities, averaged globally for the decade 2007–2016. The values represent emission from fossil fuels and industry, emissions from deforestation and other land-use change, the growth rate in atmospheric CO_2 concentration , and the uptake of carbon by the sinks in the ocean and land reservoirs, and the budget imbalance. All fluxes are in units of GtC yr^{-1}, with uncertainties reported as ±1σ (68 % confidence that the real value lies within the given interval), (figure from Le Quéré et al., 2018).

The Southern Ocean accounts for over 40% of the annual oceanic CO_2 uptake, storing about 43% of anthropogenic CO_2 and 75% of global heat uptake and thus it is an important sink and reservoir of CO_2 and heat, (Frölicher et al., 2015, Khatiwala et al., 2009; Sabine et al., 2004; Mikaloff Fletcher et al., 2006; Gruber et al., 2009; Takahashi et al., 2012), Fig. 1.2.

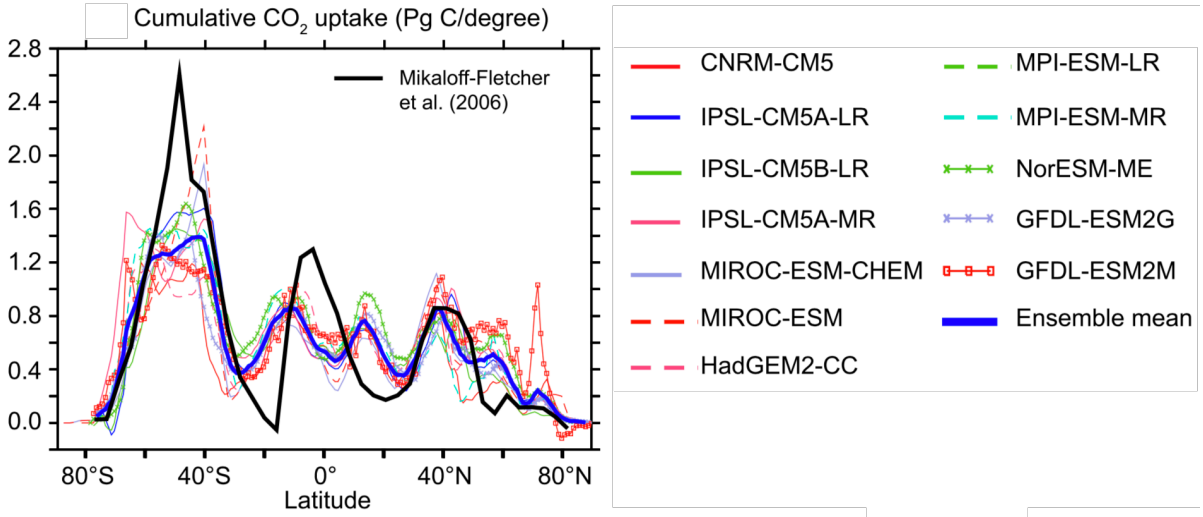

Figure 1.2. Zonal integrated estimation of the oceanic anthropogenic carbon storage from 90ºS to 90ºN for 12 CMIP5 models. The observation-based estimate of oceanic anthropogenic carbon transport is the divergence of the anthropogenic carbon flux estimates of Mikaloff Fletcher et al. (2006), (Figure from Frölicher et al., 2015).

The Southern Ocean capacity for CO_2 uptake has however been projected to change due to global change (Fung et al., 2005; Le Quéré et al., 2007, 2010; Sarmiento and Gruber, 2006; Wang et al., 2016; Zickfeld et al., 2008). Several studies suggest that the CO_2 sink in the Southern Ocean will weaken in response to the intensification of the positive anomaly of the Southern Annular Mode (SAM), which was initially driven by ozone depletion and is projected to continue weakening in the future (Lovenduski and Gruber, 2005; Lenton and Matear, 2007; Le Quéré et al., 2007; Son and Gerber, 2010; Thompson et al., 2011; Takahashi et al., 2012). However, changes in the carbonate chemistry of the Southern Ocean, in particular a decrease in the CO_2 buffering capacity at high latitudes, are also expected to become an increasingly important factor as oceans take more anthropogenic CO_2. The weakening of the buffering capacity enhances the ocean sensitivity to increasing to CO_2 and hence smaller changes in DIC will result larger pCO_2 variability. Consequently projected increased Revelle factor will enhance the amplitude of seasonal pCO_2 changes and strengthen the biological CO_2 uptake by end of the century (Hauck and Völker, 2015; Kwiatkowski and Orr, 2018; McNeil and Sasse, 2016). Consequently, some studies propose a long-term strengthening of the CO_2 sink in the Southern Ocean (Hauck and Völker, 2015; Landschützer et al., 2014; Wanninkhof et al., 2013; Zickfeld et al., 2008), thus the predicted evolution of the CO_2 sink in the Southern Ocean is still under scientific debate and presents a particular challenge to modelling the century-scale evolution of global CO_2. Long-term changes in the climate-carbon feedbacks related to

ocean warming, wind-stress and ocean circulation changes are likely also to play a role to the evolution of the Southern Ocean CO_2 sink (Falkowski et al., 1998; Friedlingstein et al., 2003)

Whilst the Southern Ocean is an important region of sea-air CO_2 ventilation, because of its extreme weather conditions, especially during winter, it still remains under-sampled with respect to CO_2 (Monteiro et al., 2010). Consequently, Earth System Models (ESMs) and Ocean Biogeochemical models (OBGMs) are important tools for studying physical and biogeochemical processes related to the CO_2 sink, in addition to in-situ measurements. It is also known that Earth System Models (ESMs) from the latest Coupled Model Intercomparison Project (CMIP), version 5 have limited skill in simulating the seasonal cycle of sea-air CO_2 Fluxes (FCO_2) with respect to available observation estimates in the Southern Ocean (Anav et al., 2013; Kessler and Tjiputra, 2016; Lenton et al., 2013). The seasonal cycle is a dominant mode of variability for biogeochemistry (Thomalla et al., 2011) and CO_2 in the Southern Ocean (Lenton et al., 2012). As a result, it provides a rigorous test of how well ESM's simulate CO_2 variability in relation to the observed ocean.

Consequently, the limited comparison of the seasonal cycle of FCO_2 between CMIP5 ESMs FCO_2 and observed estimates presents a significant challenge for the simulated century-scale changes in the Southern Ocean CO_2 sink (Lenton et al., 2013). It is not clear how these contemporary FCO_2 seasonal cycle biases affect the simulated long-term CO_2 characteristics in the Southern Ocean.

Whilst the seasonally averaged drivers of FCO_2 variability have been extensively explored in previous studies in the Southern Ocean and are well-known (e.g. Metzl, 2009; Takahashi et al., 2002, 2009; Lenton et al., 2013; Metzl et al., 2006; Takahashi et al., 2012; Munro et al., 2015), ESMs and ocean forced models generally do not well resolve the seasonal cycle FCO_2 with respect to observed estimates. Several statistics-based approaches have previously been used to cope with individual model biases, the most common being taking an ensemble mean (e.g. Anav et al., 2013; Frölicher et al., 2015; Kessler and Tjiputra, 2016). Othe studies use observations to optimize model selection for an ensemble (Wang et al., 2016; Wang and Overland, 2012), others weighted model ensemble (Gohar et al., 2017) and in recent years, emergent constraints (Boé et al., 2009; Collins, 2009; Cox et al., 2018). While all four methods have been shown to be useful in some respect, a process-based diagnostic approach that allows examination of key drivers responsible for these mode-observations biases for the seasonal cycle of FCO_2 has not been developed.

1.2 Literature review

1.2.1 The role of ocean in the earth system CO_2 budget

The link between atmospheric CO_2 and the planetary energy budget was made by Joseph Fourier in 1827, who was first to suggest that the atmosphere is absorbing and re-emitting heat that warms the surface of the planet, what would later be called the greenhouse effect (Ekholm, 1901). In the following decades, John Tyndall demonstrated experimentally that CO_2, in particular, was responsible for re-emitting infrared energy and acting like the earth's insulator (Tyndall, 1861). In the absence of greenhouse gases, average earth surface temperatures would have been about -21ºC as opposed to 14ºC which allows habitability of the planet (Anderson et al., 2016). Svante Arrhenius (1896) later formally demonstrated mathematically how greenhouse gases influence the planetary energy budget. In subsequent years, Stewart Callendar (1938) provided one of the first simulations of anthropogenically-linked temperature changes based on improvement of Arrhenius's equations. Callendar calculated that about half of the warming between 1880 – 1935 could be attributed to changes in atmospheric CO_2. By the 1950s, with the boom of the industrial revolution, anthropogenic CO_2 emissions increased and the problems of anthropogenic climate change were increasingly recognised (Anderson et al., 2016). Among these, the most recognized is the heroic work of Roger Revelle and Charles Keeling who played a central role in the early stages of understanding the role of the ocean as a sink and its buffering of atmospheric CO_2 (Keeling et al., 1976; Revelle and Suess, 1957). Their work led to the inception of the iconic Mauna Loa observatory in Hawaii which continues to provide valuable atmospheric CO_2 measurements to date (Keeling et al., 1976; Dlugokencky and Tans, 2015).

Since then atmospheric CO_2 has continued to rise, linked to fossil emissions, cement production and land use change, posing a threat to ocean ecosystems. Average temperatures are predicted up to 3ºC rise by the end of the century related to climate change (IPCC, 2014; Le Quéré et al., 2016, 2018; Sarmiento et al., 1998; Szulejko et al., 2017; Williams et al., 2017b), Fig. 1.1. About 40% of the emitted CO_2 has remained in the atmosphere ($\approx 880 \pm 35$ $GtCO_2$), the rest is removed into sinks and reservoirs (land and ocean), and is circulated through the natural carbon cycle (IPCC, 2014). The ocean forms the largest reservoir of the three, it has taken up about 41 % of the anthropogenic CO_2 and storing about 93% of CO_2 (40 000$GtCO_2$), (Feely et al., 2004; IPCC, 2014; Khatiwala et al., 2009). Since the mid-1800s the oceanic CO_2 storage has been shown to have increased and hence plays an important role in slowing down the accumulation of CO_2 in the atmosphere. The global ocean absorbs about 2.3±0.6 Pg C yr^{-1} anthropogenic CO_2 annually, about 40% of this is taken up by the Southern Ocean, making it one of the primary pathways for oceanic CO_2 uptake (Khatiwala et al., 2009; Le Quéré et al., 2018; Sabine et al., 2004), Fig. 1.2. While the oceanic CO_2 sink is expected to increase, modelled ocean CO_2 sink still show large uncertainties (up to 30%), mostly attributed to model internal variability and as well emission scenarios (Khatiwala et al., 2013; Lovenduski et al.,

2016; McKinley et al., 2016a; Randerson et al., 2015). A recent study based on the MPI-ESM shows that the largest internal variability are in the Southern Ocean and North Atlantic (Li and Ilyina, 2018).

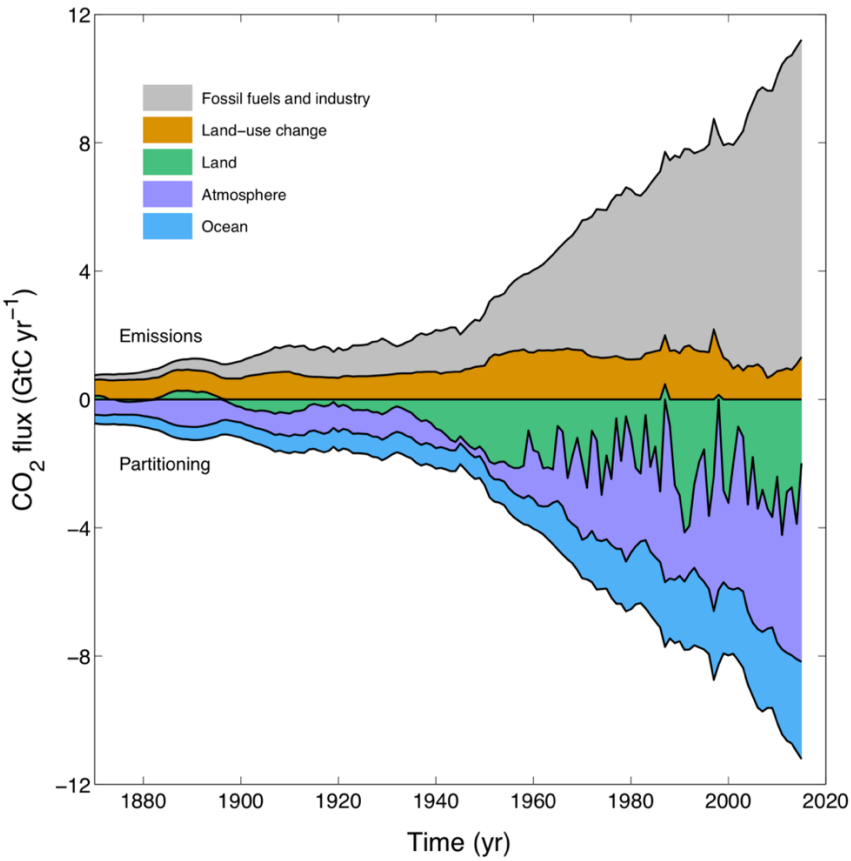

Figure. 1.3 Combined components of the global carbon budget illustrated in Fig. 1.1 as a function of time, emissions from fossil fuels and industry (grey) and emissions from land-use change (brown), as well as their partitioning among the atmosphere (purple), land (green), and oceans (dark blue). All series are given in GtC yr^{-1} (Figure from Le Quéré et al., 2016)

The following section explores the physical and biogeochemical characteristics of the Southern Ocean related to CO_2 uptake.

1.2.2 Southern Ocean: physical and biogeochemical characteristics

The Southern Ocean covers about 30% of the world oceans but constitutes over 40% of the oceanic CO_2 sink and 75% of global heat uptake (Frölicher et al., 2015; Gruber et al., 2009; Sara E. Mikaloff Fletcher et al., 2006; Takahashi et al., 2012), Fig. 1.4. It is characterized by three main basins (i.e. Pacific, Atlantic and the Indian Ocean) connected by the Antarctic Circumpolar Current (ACC),

(Graham and De Boer, 2013). The ACC forms the world's largest ocean current and flows eastward around the Southern Ocean driven by westerly winds (Rintoul and Trull, 2001). It is comprised of water masses of various properties with respect to density and chemical composition divided by density fronts. The major fronts in the Southern Ocean from the south are as follows: Polar Front (PF), that separates the most polar newly upwelled bottom cold dense and salty waters, rich in CO_2 and nutrients (Antarctic zone) from the subduction zone of these newly upwelled directly northwards. The Sub-Antarctic Front (SAF) divides these waters from mid-latitude mode waters which are less buoyant and more ventilated mode waters (Sub-Antarctic zone). Lastly, the Subtropical Front (STF) separates Sub-Antarctic zone waters from the warm sub-tropical waters (Graham and De Boer, 2013). These fronts are illustrated in Fig.1.4.

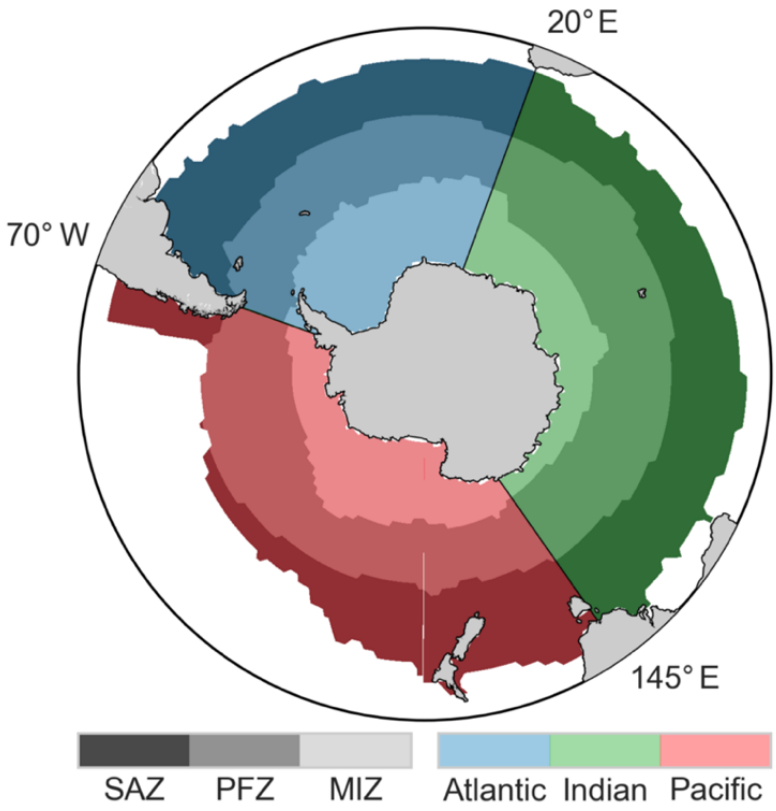

Figure. 1.4 The zonal structure of Southern ocean surface waters (fronts defined using the Orsi et al., 1995 criteria), from the north: the Sub-Subtropical zone (SAZ), demarcated by the Subtropical Front form the north and Sub-Antarctic front in south, immediately south is the Marginal Ice Zone (MIZ) and south of the polar front is the Antarctic zone (AZ). (Figure from Gregor et al., 2018).

Because of these characteristics, the Southern Ocean water masses form a key area of sea-air ventilation (Abernathey and Ferreira, 2015; Roy et al., 2011; Sallée et al., 2013; Sarmiento and

Gruber, 2006). The mechanism of ventilation in the Southern Ocean is primarily driven the deflection of surface waters by strong winds (westerly winds) exposing bottom waters through a process known as Ekman transport (Sallée et al., 2010). Ekman transport occurs when winds transfer momentum to the surface ocean, which is deflected to the left of the direction of the wind to account for the rotation of the earth (Coriolis force) in the Southern Hemisphere (Mignone et al., 2006; Sarmiento and Gruber, 2006). The resulting local divergence of surface waters exposes the dense and salty Circumpolar Deep Waters (CDW) which are rich in carbon (compared to the atmosphere) and nutrients. Eventually this leads to outgassing of natural CO_2 at high latitudes (Gruber et al., 2009; Sarmiento and Gruber, 2006; Talley et al., 2011). The easterly wind stress in the high latitudes cause the downwelling of part of the newly upwelled CDW immediately northwards (Marshall and Speer, 2012; Talley et al., 2011). Thus, given that the CDW is denser and saltier than the surrounding waters, some of it is subducted into the deep ocean south of the PF, taking with it atmospheric CO_2, forming the Antarctic Bottom Water (AABW), (Anderson et al., 2009), Fig. 1.5. This wind-driven northward transport is balanced/opposed by baroclinic instabilities of the thermal wind at depth which transport water masses and heat poleward though standing or transient mesoscale eddies along the ACC (Dufour et al., 2015; Marshall and Speer, 2012). The other portion migrates northwards into the mid-latitudes forming the Antarctic Intermediate Water (AAIW) and Sub-Antarctic Mode Water (SAMW), (Marinov et al., 2006; Sallée et al., 2010, 2013). The meeting of the cool, nutrients (including iron) and carbon-rich SAMW with the warm subtropical waters in the Sub-Antarctic zone induce primary production which draws down atmospheric CO_2. The subsequent net surface cooling also induces uptake through increased CO_2 solubility. Consequently this region (40 – 50^{o}S) forms the largest Southern Ocean CO_2 sink zone (Sabine et al., 2004; Takahashi et al., 2012). The northward supply of nutrients by the CDW from the Southern Ocean is hypothesized to be a dominant mechanism of global ocean nutrient supply for primary production (Sarmiento et al., 2004).

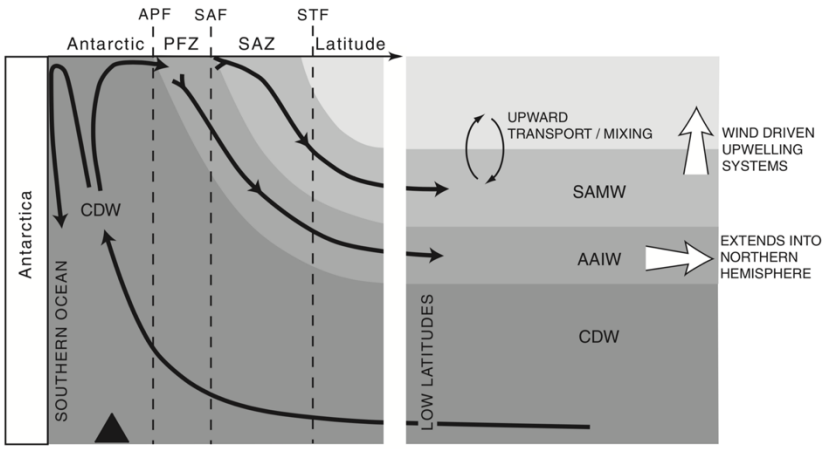

Figure. 1.5 The Southern Ocean water masses. The wind-driven upwelling brings CDW to the surface within the zone south of the Antarctic Polar Front. A portion of the upwelled water moves southward eventually

forming AABW. Part of the Antarctic surface water mixes with subtropical surface water to form SAMW, the densest form the AAIW. The Polar Front Zone (PFZ) and Sub-Antarctic Zone (SAZ) are the regions between the APF and Sub-Antarctic Front (SAF), and between the SAF and Subtropical Front (STF), respectively (Figure from Anderson et al., 2009).

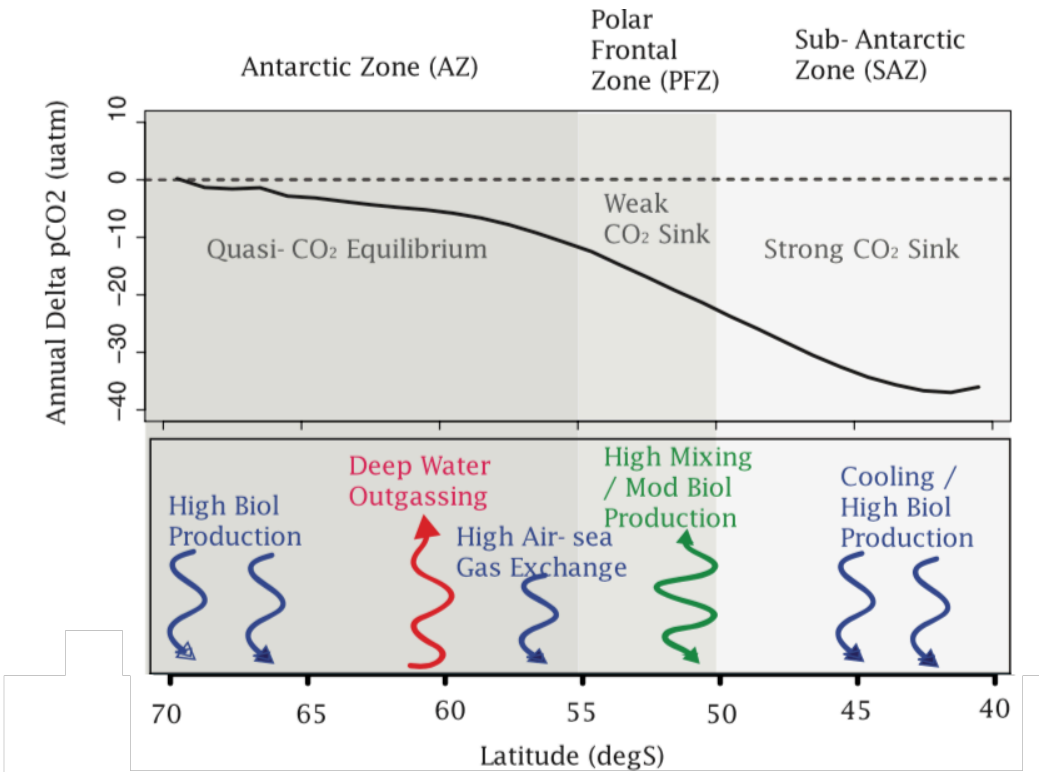

Figure 1.6 The zonally averaged annual delta pCO_2 distribution (sea-air) in the Southern Ocean and the mechanism of sea-air CO_2 exchange, the blue lines show regions of CO_2 uptake, red shows outgassing zones and green represents region of high mixing (and the resulting biological CO_2 uptake and/or outgassing) (modified from McNeil et al., 2007)

The chemical composition and density properties of the Southern Ocean water masses have seasonal variations driven by changes in the Mixed Layer Depth (MLD) and heat fluxes (Bracegirdle et al., 2013; Iudicone et al., 2008). During the winter season, surface waters cool, weakening the buoyancy flux and enhancing vertical mixing which leads to SAMW formation and enhanced ventilation (Dong et al., 2008). Enhanced vertical mixing generally weakens CO_2 uptake from the atmosphere and leads to natural CO_2 outgassing in some instances (Metzl et al., 2006; Metzl, 2009). The MLD shallows when the surface ocean warms during spring-summer seasons, the subsequent surface stratification and availability of nutrients induce primary production at the presence of light which converts surface CO_2 into organic matter through photosynthesis (Sokolov, 2008; Swart et al., 2014). The reduction of surface CO_2 through primary production increases the sea-air CO_2 gradient which eventually leads to

increased oceanic uptake of atmospheric CO_2 (Metzl et al., 2006; Takahashi et al., 2009). In addition to induced primary production during summer, surface ocean warming also weakens CO_2 solubility which counteracts the CO_2 uptake by production; however, in most cases observations show a net CO_2 sink during the spring-summer seasons in the Southern Ocean (Takahashi et al., 2012).

Sea-air CO_2 fluxes and water masses characteristics in the Southern Ocean are also modulated by larger climate variability such as the Southern Annular Mode (SAM), (Lovenduski et al., 2007; Lovenduski and Gruber, 2005; Takahashi et al., 2012). The SAM is commonly referred to as the Antarctic Oscillation, it is the leading mode of atmospheric variability in the Southern Hemisphere and is characterized by an asymmetric oscillation of the pressure gradient between higher and mid-latitudes (Latif et al., 2017; Marshall, 2003; Thompson and Wallace, 2000; Visbeck, 2009). The positive phase of the SAM is associated with a poleward shift and enhancement of the westerly winds (Thompson and Wallace, 2000). Thus, the resulting enhanced westerly winds strengthen the Ekman transport and hence upwelling of natural CO_2 and nutrient south of the PF (outgassing of CO_2), (Lovenduski and Gruber, 2005). The bottom water in the Southern Ocean is major source of micronutrients including iron which are essential for biological processes (Sarmiento et al., 2004; Tagliabue et al., 2012). As a consequence, the upwelled iron induce primary production at high latitudes (Antarctic zone) but the concurrent enhanced natural CO_2 outgassing generally results in the net weakened CO_2 sink (Lovenduski et al., 2007; Lovenduski and Gruber, 2005). Some previous studies suggest that the intensification of the westerly winds as result of the SAM positive index is likely to weaken the Southern Ocean CO_2 sink in the long-term (Lenton and Matear, 2007; Le Quéré et al., 2007; Son and Gerber, 2010; Thompson et al., 2011). Dufour et al. (2013) suggest that about a third of the Ekman driven natural CO_2 upwelling is likely to be compensated by standing or transient eddies in the Southern Ocean. This variety of arguments indicates that the long-term characteristics of the SAM and the role it plays on the Southern Ocean CO_2 sink are still not well understood and a subject of ongoing research (Ito et al., 2010; Lovenduski and Gruber, 2005).

1.2.3 Carbonate chemistry

When atmospheric $CO_{2(gas)}$ dissolves in the surface ocean it forms carbonic acid ($H_2CO_3^*$), which is unstable and immediately dissociates into bicarbonate ions (HCO_3^-), bicarbonate ions further dissociate into carbonate ions (CO_3^{2-}) by losing hydrogen protons, (Eq. 1.1) (Sarmiento and Gruber, 2006). Because of this process pathway, only 1 out of 20 atmospheric CO_2 molecules increases the surface oceanic $CO_{2(aq)}$ concentration, the rest react with carbonic ions to from two bicarbonate ions (Eq. 1.2).

$$CO_{2(gas)} + H_2O \underset{\leftrightarrow}{\overset{K_0}{}} H_2CO_3^* \underset{\leftrightarrow}{\overset{K_1}{}} HCO_3^- + H^+ \underset{\leftrightarrow}{\overset{K_2}{}} CO_3^{2-} + H^+ \qquad (1.1)$$

$$H_2CO_3^* + CO_3^{2-} \leftrightarrow 2HCO_3^- \quad (1.2)$$

Where K_0, K_1 and K_2 are dissociation constants, which are functions of temperature and salinity (Sarmiento and Gruber, 2006). The K_0 is the solubility coefficient and is insensitive to salinity (only temperature changes), and thus salinity changes in pCO_2 are governed by K_1/K_2. But given that salinity changes are almost insignificant with respect to temperature variability at the seasonal scale in the Southern Ocean, the dissolution of the atmospheric CO_2 is mostly governed by the thermodynamic solubility changes through K_0 (Sarmiento and Gruber, 2006).The sum of H_2CO_3, HCO_3^- and CO_3^{2-} is referred to as the total dissolved inorganic (DIC), (Bopp and Le Quéré, 2009; Sarmiento and Gruber, 2006). In the surface ocean the proportions of DIC components as; about 1% as CO_{2aq}, 95% [HCO_3^-] and 4% [CO_3^{2-}], (Takahashi et al., 201

Another essential parameter in the carbonate chemistry is the Total Alkalinity (TAlk, Eq. 1.3) is defined as the excess of proton acceptors over donors with respect to the chosen zero level of the protons (Dickson and Millero, 1987; Wolf-Gladrow et al., 2007). In a closed system changes in DIC and TAlk are conservative with respect to temperature in the ocean and thus are used as state variables in the ocean carbon cycle models (Sarmiento and Gruber, 2006; Wolf-Gladrow et al., 2007).

$$TAlk = [HCO_3^-] + 2[CO_3^{2-}] + B(OH)^- + [OH^-] - [H^+] + minor\ anions\ of\ weak\ acids \quad (1.3)$$

The sea-air gradient of the of CO_2 gradient partial pressure ($dpCO_2$) provides the thermodynamic forcing for CO_2 transfer across the ocean-atmosphere interface and thus determines the direction of the flux (Takahashi et al., 2009; Wanninkhof et al., 2009). Wind plays a role in determining the magnitude and rate of CO_2 transfer (Wanninkhof et al., 2013, 2009). But since atmospheric CO_2 is relatively uniform over the Southern Ocean (Fujita et al., 2003), changes in sea-air CO_2 flux (FCO_2) at the seasonal scale are mainly modulated by surface pCO_2. Seasonal surface pCO_2 changes are mainly modulated by variations in temperature through solubility (K_0), biological processes (primary production and respiration) and transport.

The sensitivity of pCO_2 to temperature changes under constant DIC and TAlk was linearized by Takahashi et al.,(1993) shown in Eq. 1.4 for the temperature range 2-28ºC and salinity 34 – 36 psu.

$$\frac{1}{pCO_2}\frac{\partial pCO_2}{\partial SST} = \frac{\partial lnpCO_2}{\partial SST} \approx 0.0423^oC \quad (1.4)$$

Consequently, the enhancement of CO_2 solubility by cooling and weakening by warming can be scaled using Eq.1.4. Biological activity influences FCO_2 through two main processes: a) photosynthetic CO_2 uptake through the formation of organic matter and the reverse process whereby organic matter returns to DIC through respiration and remineralization, and b) through the formation

of $CaCO_3$ (calcium carbonate) shells by oceanic organisms through calcification (Sarmiento and Gruber, 2006).

During photosynthesis marine organisms (phytoplankton) use surface CO_2 in the presence of sunlight and nutrients (nitrate, phosphate, silicate and micronutrients including iron) to form organic matter (Eq. 1.5) (Le Quéré and Saltzman, 2013).

The sum of H_2CO_3, HCO_3^- and CO_3^{2-} is referred to as the total dissolved inorganic (DIC), (Sarmiento and Gruber, 2006). In the surface ocean the proportions of DIC components as; about 1% as CO_{2aq}, 95% [HCO_3^-] and 4% [CO_3^{2-}] (Takahashi et al., 2012). Another useful capacity parameter in the carbonate chemistry is the Total Alkalinity (TAlk, Eq. 1.3) is defined as the excess of proton acceptors over donors with respect to the chosen zero level of the protons (Dickson and Millero, 1987; Wolf-Gladrow et al., 2007). In a closed system changes in DIC and TAlk are conservative with respect to temperature in the ocean and thus are used as state variables in the ocean carbon models (Sarmiento and Gruber, 2006; Wolf-Gladrow et al., 2007).

$$106\,CO_2 + 16\,HNO_3 + H_3PO_4 + 78\,H_2O \Leftrightarrow C_{106}H_{175}O_{42}N_{16}P + 150\,O_2 \qquad (1.5)$$

In the Southern Ocean, productivity is generally limited by the availability of sunlight and nutrients (Gruber and Sarmiento, 2006; Thomalla et al., 2011). About half of the newly formed organic matter is converted back to CO_2 through respiration by auto- and heterotrophs (reverse of photosynthesis) and the remainder constitutes the net ecosystem production , this happens in the ocean surface layer (Bopp and Le Quéré, 2009). A fraction of net ecosystem production is exported to the deeper ocean in the form of particulate organic carbon (POC), which includes dead and living organisms. Photosynthesis also produces dissolved organic carbon (DOC) which is also transported to the deep ocean by physical processes. A portion of the DOC is also remineralised to DIC by bacterial respiration and then transported back to the mixed layer via physical processes (Bopp and Le Quèrè., 2009). This mechanism is commonly referred to as the soft-tissue pump or biological pump (Volk and Hoffert, 1985).

Calcification is the second major biological process with respect FCO_2 in the ocean. It entails the formation and dissolution of calcite or aragonite ($CaCO_3$ shells) by marine organisms (e.g. coccolithophorids, pteropods and foraminifers)

$$Ca^{2+} + CO_3^{2-} \Leftrightarrow CaCO_3 \qquad (1.6)$$

The formation/dissolution of a single molecule of calcium carbonate changes TAlk twice as much as DIC. One mole of CO_3^{2-} is equivalent to two moles of TAlk, but one mole to DIC. Marine organisms

produce these calcite shells in the surface layer of the ocean and at their die their shells sink to the deep ocean, drawing down CO_3^{2-} with them. This process constitutes the carbonate pump (Bopp and Le Quèrè, 2009).

The Revelle Factor or gamma (γ_{DIC}) defines the sensitivity of pCO_2 to changes in DIC. Formally, it is defined as the ratio of the change in pCO_2 ($dpCO_2/pCO_2$) for a change in DIC (dDIC/DIC) (Eq. 1.8) and quantifies the sensitivity of the ocean to an increase in atmospheric CO_2 (Broecker et al., 1979; Egleston et al., 2010; Sarmiento and Gruber, 2006). This buffering of atmospheric CO_2 uptake in the surface ocean was first pointed out by Roger Revelle and is central to how the ocean regulates air-sea CO_2 fluxes.

$$\gamma_{DIC} = \left(\frac{\Delta pCO_2}{pCO_2}\right) / \frac{\Delta DIC}{DIC} \qquad (1.8)$$

In the global oceans, the Revelle factor is generally larger in polar regions and lower in the tropical areas (Sarmiento and Gruber, 2006), consequently pCO_2 changes are more sensitive to increasing DIC changes in polar systems with respect to tropical areas. Modelling studies predict that the Revelle factor will increase as the ocean takes up more atmospheric CO_2 under the business as usual emission scenario (RCP 8.5), (Hauck, 2018; J. Hauck and Völker, 2015b; McNeil and Sasse, 2016a). Under a decreased buffering capacity, surface DIC changes will result in a relatively larger pCO_2 change, hence comparable biological driven DIC changes are projected to induces a more substantial CO_2 uptake. Because of this feature, increased Revelle factor is projected to reinforces CO_2 uptake even if biological processes may not change significantly by the end of the century (Hauck and Völker, 2015). The increasing of Revelle factor is thus projected to amplify the seasonal pCO_2 amplitude (winter-summer), (Hauck, 2018). A recent observation-based study by Landschützer et al. (2018) demonstrates that these changes (increased Revelle factor and amplified seasonal pCO_2 amplitude) are already apparent from historical observational datasets (1982 – 2015) in the Southern Ocean.

The final mechanism of surface pCO_2 changes that I consider here is physical transport, most due to mixing. In the surface ocean, MLD changes occur through storms, mesoscale dynamics and seasonal buoyancy variations driven by seasonal changes in temperature (Dong et al., 2008; Swart et al., 2014). Changes in the MLD induce mixing which entrains subsurface waters (usually richer in DIC and nutrients) to the surface; this increases the net surface CO_2 and nutrient concentration. During the autumn-winter seasons, increased surface CO_2 concentrations generally weaken CO_2 uptake; however in the summer-spring season this mechanism can induce and/or sustain primary production which conversely strengthens CO_2 uptake (Iudicone et al., 2011; Monteiro et al., 2015; Nicholson et al., 2016; Swart et al., 2014).

Aims of the study

This study has three main objectives;

i) To develop a process based methodological framework that can be used to diagnose model-observation biases in seasonal cycle characteristics of FCO_2 ESMs.

ii) To analyse the main biases responsible for the limited skill of CMIP5 models in simulating the seasonal cycle of FCO_2 with respect to observed estimates in the Southern Ocean.

iii) To investigate how the present-day biases in the seasonality and drivers in CMIP5 ESMs affect modelled long-term (century-scale) changes in the mechanisms that drive CO_2 uptake in the Southern Ocean.

The results for the first two items have been published in peer reviewed journals, Ocean modelling (Mongwe et al., 2016) and Biogeosciences respectively (Mongwe et al., 2018) respectively.

The dissertation is partitioned as follows; the methodology (chapter 2) describes the datasets used (observation estimates, data products and modelling datasets) and it provides a technical description of the main approach used to analyse model-observation biases. Chapter 3 provides an elaborate description of the process-based diagnostic framework developed to analyse model-observations biases using a numerical ocean biogeochemistry model and observation estimates (Mongwe et al., 2006). In chapter 4, the diagnostic framework (chapter 3) is applied to 10 CMIP5 ESM models to investigate sources of their seasonal cycle of FCO_2 biases with respect to observed estimates in the Southern Ocean . Chapter 5 uses five projected simulation scenarios from the CMIP5 ESM models to investigate how the present-day biases in the seasonal cycle of FCO_2 in CMIP5 models affect long-term simulate the mechanisms of CO_2 uptake in the Southern Ocean at the end of the century. Chapter 6 concludes with a synthesis of the main findings and their implications.

Chapter 2

Methodology

This chapter is divided into three subsections; the first section describes the datasets used for the study (i.e. in-situ observations, observation-based data products and model output datasets), second section defines the study region and describes how geographic boundaries used were defined. The third section provides a technical description of the main methodology used to evaluate model-observations biases in the seasonal cycle of FCO_2 and the calculation for DIC entrainment fluxes.

2.1. Datasets

2.1.1 in-situ observations and observations-based data products

The following datasets have been used in this work:

a) Partial pressure of CO_2 (pCO_2), Sea-Air CO_2 fluxes (FCO_2), Sea Surface Temperature (SST) and surface salinity, Takahashi et al., (2009), http://www.ldeo.columbia.edu/res/pi/CO2/carbondioxide/pages/air_sea_flux_2000.html, l (last access: January 2015),

b) FCO_2 and pCO_2 data product, Landschützer, et al, 2014, http://cdiac.ornl.gov/ftp/oceans/spco2_1982_2011_ETH_SOM-FFN, FCO2, (accessed March 2017)

c) pCO_2 data product, https://figshare.com/articles/_/5369038, Groger et al., 2018

d) Mixed layer Depth (MLD) dataset, defined using the $\sigma_0 = 0.03$ density criteria, 2008 updated version, de Boyer Montégut, (2004), http://www.ifremer.fr/cerweb/deboyer/mld/home.php, (last access: November 2017),

e) Satellite chlorophyll dataset, Johnson et al., 2013, https://imos.aodn.org.au/imos123/, (last access: February 2016),

f) Dissolved Inorganic Carbon (DIC) dataset, GLobal Ocean Data Analysis Project (GLODAP), Key et al., (2004), (last access: January 2015),

g) DIC dataset, GLobal Ocean Data Analysis Project version 2 (GLODAP2), Lauvset et al., (2016), (last access: November 2017)
h) SST and surface salinity dataset, Word Atlas data version version (WOA3), Locarnini et al., (2013), (accessed January 2015).

The Takahashi et al. (2009) dataset is comprised of a compilation of about 3 million global surface measurements (4° latitude x 5° longitude) of pCO_2, FCO_2, SST, salinity and other ocean variables (not used for this study). The dataset comprised of measurements obtained from 1970 – 2007, and corrected for the reference year 2000. A full description of this dataset is presented in Takahashi et al. (2009). For this study Takahashi et al., (2009) is mainly referred to as T09. No further corrections/calculations were made to the T09 dataset for this analysis. The FCO_2 is computed using Eq. 2.1 in T09.

$$FCO_2 = k \times K_0 \times \Delta pCO_2 \quad (2.1)$$

Where;

$$k = 0.251 \times \left(\frac{Sc}{660}\right) < U_{10m}^2 > \quad (2.2)$$

$$\Delta pCO_2 = pCO_{2sea} - pCO_{2atmosphere} \quad (2.3)$$

Where k is the CO_2 gas transfer velocity coefficient, which represents the wind-driven air-sea kinetic gas transfer; it is a function of the second moment (variance) of wind speed at 10 m above sea level $<U^2_{10m}>$ and the Schmidt number (Sc/660). The Schmidt number accounts for the turbulence at the sea-ocean interface (Jähne et al., 1987). K_0 is the CO_2 solubility coefficient for an aqueous phase; it is a function of surface temperature and salinity (Weiss, 1974). And ΔpCO_2 is the air-sea CO_2 partial pressure gradient. For this study net FCO_2 into the ocean is expressed as a negative value by convention consistent with Wanninkhof et al. (2013).

Using monthly means SST and salinity from Takahashi et al (2009) we reconstructed Total Alkalinity (TAlk) using the Lee et al. (2006) formulation. To compute the uncertainty of the calculated (TAlk), we made a comparison of a calculated total alkalinity ($Talk_{calc}$) based on ship measurements of SST and surface salinity dataset with the actual observed $TAlk_{obs}$ of the same measurements. Based on a winter (August) dataset collected in the Southern Ocean. The two datasets were found to be significantly correlated ($r^2 = 0.79$, with a regression of $y = 0.92x + 182$), Fig. 2.1. The computed monthly TAlk and pCO_2 from T09 were used to calculate the total dissolved inorganic carbon (DIC) using CO2SYS (Pierrot et al., 2006), using K1, K2 from Mehrbach et al., 1973 refitted by Dickson and Millero, 1987. This same calculation was applied in Chapter 4, however, using SST and surface salinity from the W0A13 dataset and a data product based pCO_2 from Landschützer et al (2014).

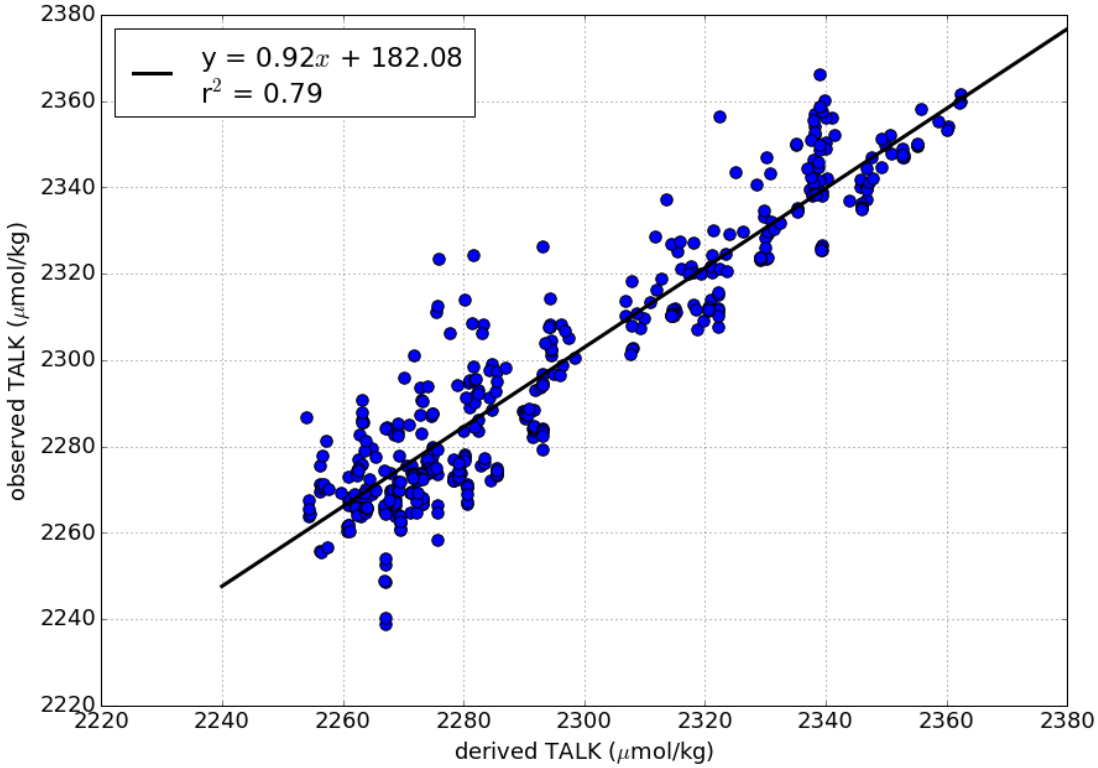

Figure 2.1. Regression plot comparing the derived (following Lee et al., 2006) and observed TAlk dataset for about 500 surface TAlk samples collected in the Indian sector of the Southern Ocean.

The Global Ocean Data Analysis Project (GLODAP) is an interpolated dataset consisting of 9618 hydro-graphic stationed based on 95 cruises between 1999 and 2393 additional historical hydro-stations between 1972 and 1990 (Key et al., 2004). The GLODAP DIC dataset was regridded into 180x149 grid similar to the 2x2 degree grid mode used in Chapter 3. In Chapter 4 the latest version of 1^{o}x1^{o} grid (version 2) was used which comprises of data updated to the year 2013 (Lauvset et al., 2016).

The Landschützer et al. (2014) observations data product (FCO_2 and pCO_2) was used as the main suite of observations-based estimates against which compare the models. The Landschützer et al. (2014) dataset is synthesized from Surface Ocean CO_2 Atlas version 2 (SOCAT2) observations and high-resolution winds using a self organizing map through a feed forward neural network approach (Landschützer et al., 2013). While Landschützer et al (2014) dataset is based on more in situ observations (SOCAT2, 15 million source measurements Bakker et al., 2014) in comparison to Takahashi et al., 2009 (3 million surface measurements), used in chapter 3. One is nevertheless mindful that due to the general paucity of observations in Southern Ocean, this data product is still subject to uncertainties (e.g. Ritter et al., 2018). To evaluate the uncertainty between data products the

Landschützer et al (2014) data was compared with another recent observations-based data products from Gregor et al (2018) as well as against Takahashi et al (2009) for pCO_2 in the Southern Ocean. Gregor et al (2018) is based on two independent empirical models: support vector regression and random forest regression. The comparison between these three datasets was based on pCO_2 instead of FCO_2 for two reasons. This was because Gregor et al., (2018) only provided fugacity and pCO_2. Hence computing FCO_2 would increase the level of uncertainty considering the choice of wind product and transfer velocity constant (Swart et al., 2014a). Secondly because while the focus of the analysis is on the examination biases in the FCO_2, the major part of the diagnostic analysis is based on surface pCO_2, which primarily determines the direction and part of the magnitude of the fluxes (Roobaert et al., 2018). It was found that the three data products agree on the seasonal phasing of pCO_2 in the Sub-Antarctic zone, but they show differences in the magnitudes (Fig. 2.2). In the Antarctic zone, all three datasets agree in both phasing and amplitude (Fig. 2.2).

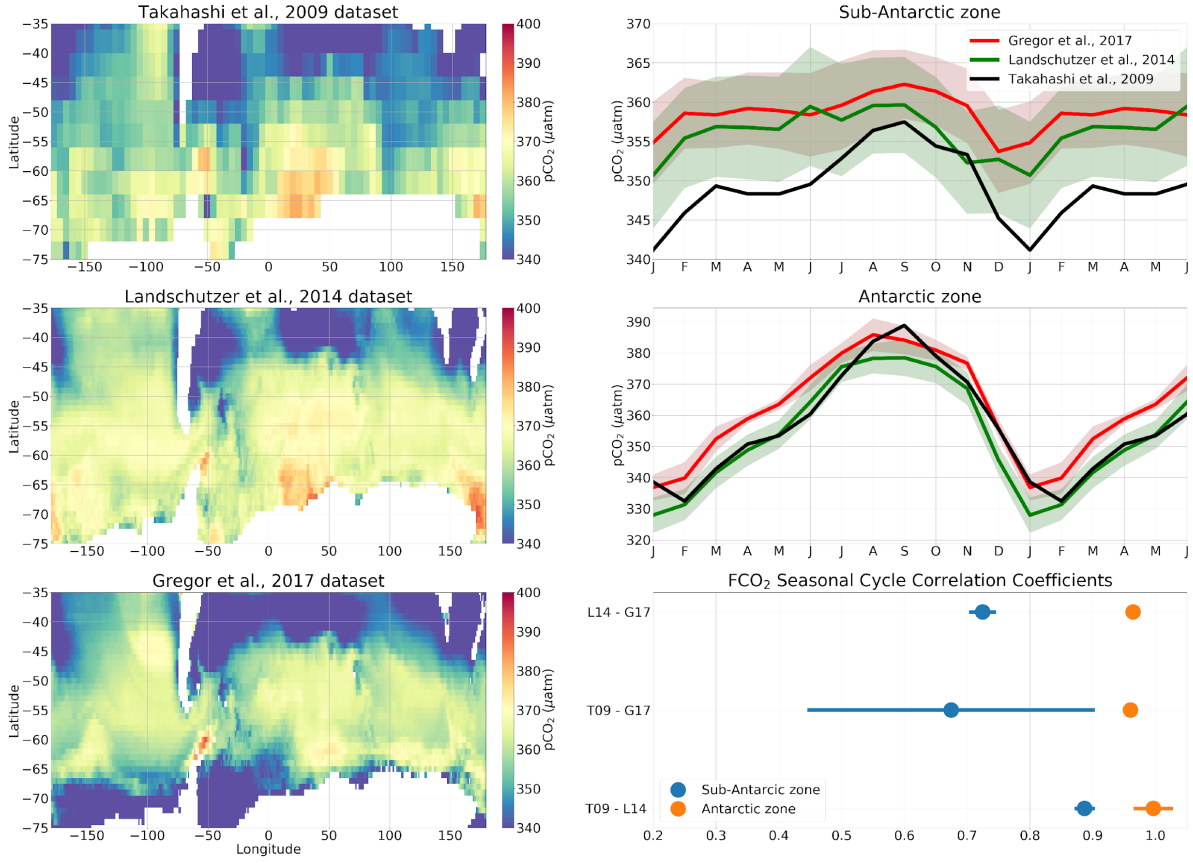

Figure. 2.2 pCO_2 (µatm) spatial (climatology) and seasonal cycle differences in Landschützer et al (2014), Gregor et al (2017), Takahashi et al (2009) data products in the Southern Ocean. The seasonal cycle climatology of pCO_2 in the Sub-Antarctic and Antarctic zone is based on the period 1998 – 2011. The shaded areas show the standard deviation of the interannual variability of the seasonal cycle for this period. The bottom left figure shows the correlation coefficient (r^2) mean monthly seasonal cycle of FCO_2 between Landschützer et

al (2014) (L14), Gregor et al (2017) (G17), Takahashi et al (2009) (T09) in the Sub-Antarctic and Antarctic zone.

For chlorophyll, a 9 km resolution satellite dataset was used (Johnson et al., 2013), taking the climatological mean over 2007 – 2011 and applying regridding to a 360x180 regular mesh. To minimize uncertainties during the winter season, winter dataset were excluded for the analysis. The Mixed Layer Depth (MLD) data was taken from de Boyer Montégut et al. (2004), on a 1^{o} x 1^{o} grid, the data is provided as monthly means climatology and was used as provided.

2.1.2 Model output

Three sets of model output datasets were used; an Ocean Biogeochemical Model (OBGM) NEMO PISCES in Chapter 3, 10 Earth System Models (ESMs) from the Coupled Model Intercomparison Project version 5 (CMIP5) historical scenario in Chapter 4. And 5 CMIP5 ESMs from the business as usual Representative Concentration Pathway (RCP) 8.5 scenario in chapter 5.

2.1.2.1 Ocean biogeochemical model

The Nucleus for European Modelling of the Ocean (NEMO) Pelagic Interaction Scheme for Carbon and Ecosystem Studies (PISCES, Aumont and Bopp, 2006) in a ORCA2 configuration (Madec, 2015) mode was used. The choice of the NEMO-PISCES model for this study is linked to it being the model of choice in the Southern Ocean Carbon - Climate Observatory (SOCCO) programme as well as that it is the ocean-engine for some of the CMIP5 models. The simulation used consists of interacting models of ocean (OPA Oćean PArralleliśe), ice (LIM2 Louvain-la-Neuve Ice Model) and biogeochemistry (PISCES), thus designated ORCA2-LIM-PISCES (ORCA2LP). It consists of an ORCA2 global tripolar grid by (Madec and Imbard, 1996) with a horizontal model grid resolution of 2^{o}x 2^{o} cos (latitude), ranging from ~200 km at the equator to about ~100 km around the latitude of the Polar Front. In the vertical, the grid consists of 31 levels with partial bottom steps, with highest vertical resolution in the upper ocean (15 vertical levels in the upper 200 m) and decreasing resolution with depth. For vertical mixing the turbulent kinetic energy closure scheme was used. Due to the coarse resolution, the Gent and McWilliams (1990) eddy parameterization was used to account for enhanced buoyancy forcing and mixing by mesoscale eddies.

Initial conditions for the model were derived from a World Ocean Atlas 2001 (WOA01) (Conkright et al., 2002) climatology and integrating the model for 10 years with CORE IIb (normal year forcing), climatology derived from NCEP reanalysis and satellite data (Large and Yeager, 2004). The

experiment was run in several steps: a pre-industrial period with constant forcing from 1768 to 1827 using the constant carbon value for 1828 and then from 1828 to 2007 using increasing anthropogenic CO_2 concentrations. This dataset spans from 1948 to 2007, so to drive the dynamics of the full 240-year experiment this 60-year dataset was re-initialized repeatedly. Seawater temperature at the surface is calculated using bulk formulae, but salinity was restored to WOA01 monthly climatology to constrain freshwater fluxes. For the purposes of this study, the final model years of 1996-2006 are analysed. The model output presented here represents a low-resolution, interannually varying ocean with carbon content equilibrated to the atmosphere and subject to annual-mean observed global atmospheric CO_2 concentrations. The model output was then extracted as daily means and converted into five-day means for the seasonal cycle plots and monthly means for phase diagrams (Chapter 3). Annual CO_2 fluxes in the model output were computed from the mean decadal annual flux for the period 1996 – 2006 with an uncertainty defined here as the standard deviation within the 10 years of study.

2.1.2.2 CMIP5 historical scenario dataset

Ten models from the Coupled Model Intercomparison Project version 5 (CMIP5) Earth System Models (ESM) was used in chapter 4, shown in Table 2.1. The selection criterion for the models was based on the availability of essential variables for the analysis in the CMIP5 data portal (http://pcmdi9.llnl.gov) at the time of writing: i.e. monthly FCO_2, pCO_2, chlorophyll, net primary production (NPP), surface oxygen, surface Dissolved Inorganic Carbon (DIC), MLD, Sea Surface Temperature (SST), vertical temperature fields and annual DIC for the historical scenario. The analysis is primarily based on the climatology over 1995 – 2005, which was selected to match a period closest to the available observational data product (Landschützer et al., 2014; 1998 – 2011). However, as a test, the consistency of the seasonality of FCO_2 over periods longer than 10 years was examined by comparing the seasonal cycle of FCO_2 and temporal standard deviation of 30 years (1975 – 2005) vs 10 years (1995 – 2005) for HadGEM2-ES and CanESM2. It was found that the seasonal cycle of FCO_2 remains consistent ($R = 0.99$) in both HadGEM2-ES and CanESM2 over 30 years (Fig. 2.3). All CMIP5 model outputs were regridded into a common $1^{o}x1^{o}$ regular grid throughout the analysis, except for annual CO_2 mean fluxes, which were computed on the original grid for each model.

Table 2.1: A description of the 10 CMIP5 ESMs that were used in this analysis. It shows the ocean resolution, atmospheric resolution, and available nutrients for the biogeochemical component, sea-ice model, vertical levels and the marine biogeochemical component for each ESM.

Full name and Source	Model Name	Ocean Resolution	Atmospheric Resolution	Nutrients	Sea ice model	Veridical Coordinate & Levels	Ocean Biology	Reference
Canadian Centre for Climate Modelling and Analysis, Cananda	CanESM2	CanOM4 0.9° x1.4°	2.8125° x 2.8125°	N (accounts for Fe limitation)	CanSIM1	z 40 levels	NPZD	Zahariev et al., 2008
Centro Euro-Mediterraneo Sui Cambiamenti Climatici, Italy	CMCC-CESM = CMCC	OPA8.2 0.5-2°x2°	3.8° x 3.7°	P, N, Fe, Si	CICE4	z 21 levels	PELAGOS	Vichi et al., 2007
Centre National de Recherches Météorologiques-Centre Européen de Recherche et de Formation Avancée en Calcul Scientifique, France	CNRM-CM5 = CNRM	NEMOv3.3 1°	1.4°	P, N, Fe, Si	GELATO5	z 42 levels	PISCES	Séférian et al., 2013
Institut Pierre-Simon Laplace, France	IPSL-CM5A-MR = IPSL	NEMO2.3 0.5-2° x 2°	2.58° x 1.25°	P, N, Fe, Si	LIM2	z 31 levels	PISCES	Séférian et al., 2013
Max Plank Institute for Meteorology, Germany	MPI-ESM-MR = MPI	MPIOM 1.41°×0.89°	1.875° x 1.875°	P, N, Fe, Si	MPIOM	z 40 levels	HAMOCC5 .2	Ilyina et al., 2013
Community Earth System Model, USA	CESM1-BGC = CESM1	0.3° x1°	0.9° x 1.25°	(P), N, Fe, Si		z 60 levels	BEC	Moore et al., 2004
Norwegian Earth System Model, Norway	NorESM1-ME = NorESM1	MICOM 0.5° x 0.9°	2.5° x 1.9°,	P, N, Fe, Si	CICE4.1	ρ 53 levels	HAMOCC	Tjiputra et al., 2013
Geophysical Fluid Dynamics Laboratory Earth System Model, USA	GFDL-ESM2M = GFDL	0.3° x 1°	2.5° x 2.0°	N, P, SiO4, Fe	SISp2	z 50 levels	TOPAZ2	Dunne et al., 2013
Meteorological Research Institute-Earth System Model Version 1, Japan	MRI-ESM = MRI	0.5° x 1°		P, N	MRI.COM 3	σ-z 51 levels	NPZD	Adachi et al., 2013
Hadley Global Environment Model 2 – Earth System, UK	HadGEM2-ES = HadGEM2	0.3° x 1°	2.5° x 2.0°	N,Fe,S		40 levels	Diat-HadOCC	Palmer and Totterdell, 2001

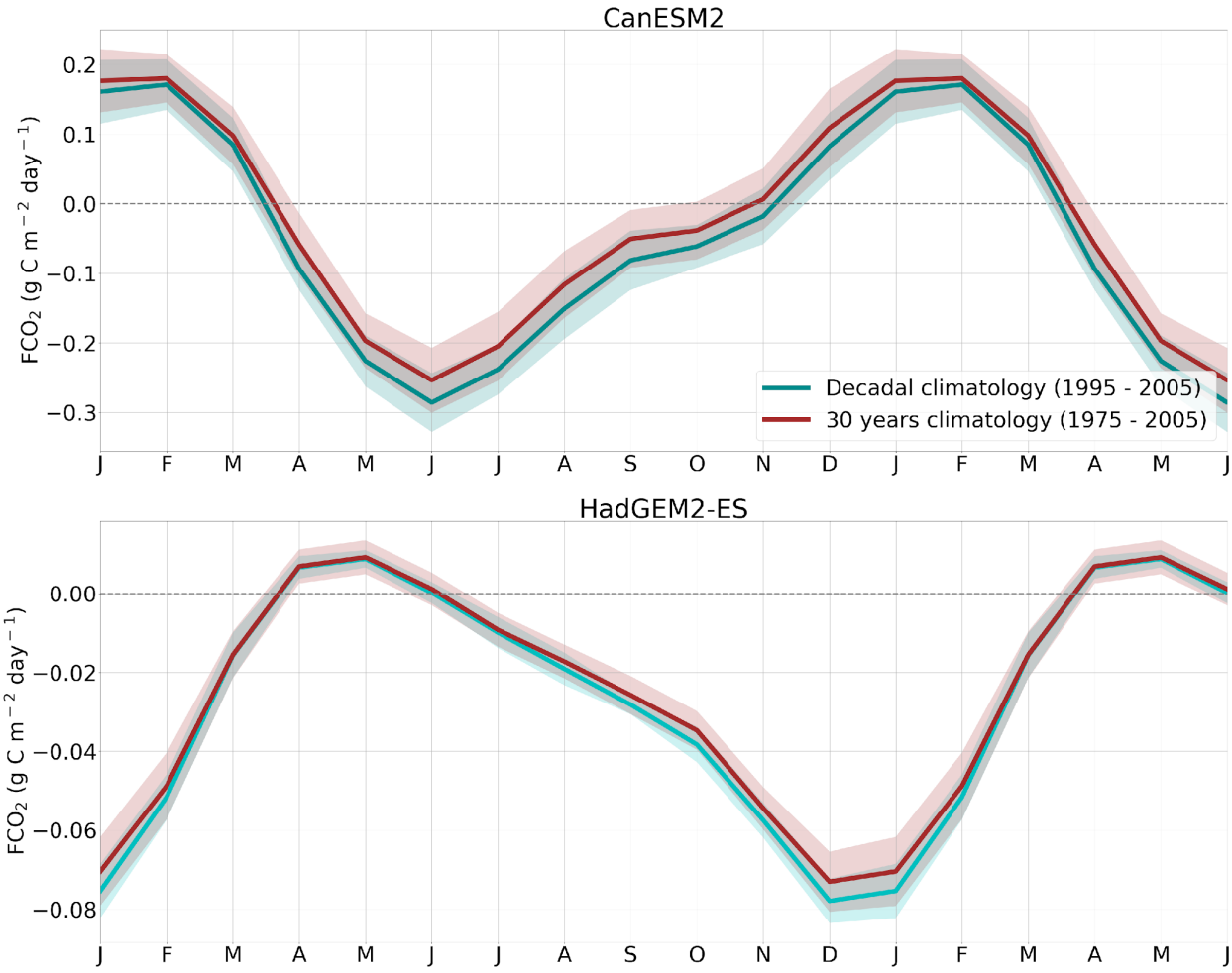

Figure. 2.3. Compares the seasonal cycle of Sea-Air CO_2 fluxes over 30 year (1975 – 2005 and 10 years (1995 – 2015) in the Sub-Antarctic zone. The shaded area shows the standard deviation.

2.1.2.2 CMIP5 RCP8.5 scenario dataset

Five models from the Coupled Model Intercomparison Project version 5 (CMIP5) Earth System Models (ESM) was used, focusing on the Representative Concentration Pathway (RCP) 8.5 scenario shown in Table 2.2. The selection criterion for the models was based on the availability of essential variables for the analysis on the public servers (https://esgf-data.dkrz.de/search/cmip5-dkrz/) at the time of writing: i.e. monthly FCO_2, partial pressure of CO_2 (pCO_2), surface dissolved inorganic carbon (DIC), vertical annual DIC, ocean temperature and vertical temperature fields. With respect to the models used in chapter 4, MRI-ESM and CNRM-CM5 were neglected in chapter 5 due to temperature ranges that are out of the other models' range, the updated CNRM-CM5.2 was not used here since it does not have the RCP8.5 scenario dataset (Séférian et al., 2016). NorESM1-ME was also neglected because it shows a decreasing DIC concentration with depth in the upper 100 m in the contemporary climate, which is contrary to available observations and other CMIP5 models. The

analysis consist of a comparison of the climatology of the current climate, which is here approximated by the first 10 years of RCP8.5 scenario (2006 – 2015) vs. the end of the century (2090-2100). All CMIP5 model outputs were re-gridded into a common 1°x1° regular grid throughout the analysis; except for annual CO_2 mean fluxes calculation.

Table 2.2: A description of the 10 CMIP5 ESMs that were used in this analysis. It shows the ocean resolution, atmospheric resolution, and available nutrients for the biogeochemical component, sea-ice model, vertical levels and the marine biogeochemical component for each ESM.

Full name and Source	Model Name	Ocean Resolution	Atmospheric Resolution	Nutrients	Sea ice model	Veridical Levels	Ocean Biology	Reference
Canadian Centre for Climate Modelling and Analysis, Cananda	CanESM2	CanOM4 0.9° x1.4°	2.8125° x 2.8125°	N (accounts for Fe limitation)	CanSIM1	40 levels	NPZD	Zahariev et al., 2008
Centro Euro-Mediterraneo Sui Cambiamenti Climatici, Italy	CMCC-CESM	OPA8.2 0.5-2°x2°	3.8° x 3.7°	P, N, Fe, Si	CICE4	21 levels	PELAGOS	Vichi et al., 2007
Institut Pierre-Simon Laplace, France	IPSL-CM5A-MR	NEMO2.3 0.5-2° x 2°	2.58° x 1.25°	P, N, Fe, Si	LIM2	31 levels	PISCES	Séférian et al., 2013
Max Plank Institute for Meteorology, Germany	MPI-ESM-MR	MPIOM 1.41°×0.89°	1.875° x 1.875°	P, N, Fe, Si	MPIOM	40 levels	HAMOCC5.2	Ilyina et al., 2013
Hadley Global Environment Model 2 – Earth System, UK	HadGEM2-ES	0.3° x 1°	2.5◦ x 2.0◦	N,Fe,S		40 levels	Diat-HadOCC	Palmer and Totterdell, 2001

2.2 Study region

The study of air-sea fluxes in the Southern Ocean has historically used geographically defined boundaries, where Southern Ocean is defined as south of 44°S for example (e.g. Mikaloff Fletcher et al., 2006; Gruber et al., 2009; Takahashi et al., 2009; Lenton et al., 2013; Majkut et al., 2014). However, some studies have recently highlighted the bias emerging from the use of geographical boundaries given their inability to depict distinct regions of FCO_2 variability (Séférian et al., 2012a). This includes the inability of geographical boundaries to reflect meridional shifts of dynamic frontal boundaries across basins as well as their seasonal variability (Sokolov and Rintoul, 2009; Séférian et al., 2012). This is important because of the distinct characteristics of FCO_2 within the Sub-Antarctic zone and Antarctic zone relative to adjacent water masses (Sabine et al., 2004; McNeil et al.,

2007;Boutin et al., 2008). In a recent study by Lenton et al., (2013), for example, the Southern Ocean was defined as south of 44°S which excluded significant parts of the Sub-Antarctic zone, a major CO_2 uptake region; when the northern boundary was extended to 40°S, the calculated CO_2 annual uptake almost doubles. In this study we investigate FCO_2 seasonal cycle characteristics within latitudinally varying boundaries, where the Sub-Antarctic zone and Antarctic zone are defined using climatological frontal positions.

The Southern Ocean is here defined as the ocean south of the Sub-Tropical Front (STF, defined according to Orsi et al., (1995), 11.3°C isotherm at 100 m), Fig. 2.4. It is divided into two main domains, the Sub-Antarctic Zone between the STF and the Polar Front (PF: 2°C isotherm at 200 m) and the Antarctic Zone, south of the PF. In Chapter 4 the Sub-Antarctic Zone and Antarctic Zone were further partitioned into the three main basins of the Southern Ocean i.e. Pacific, Atlantic and the Indian zone for basin scale analysis as shown in Fig. 2.4.

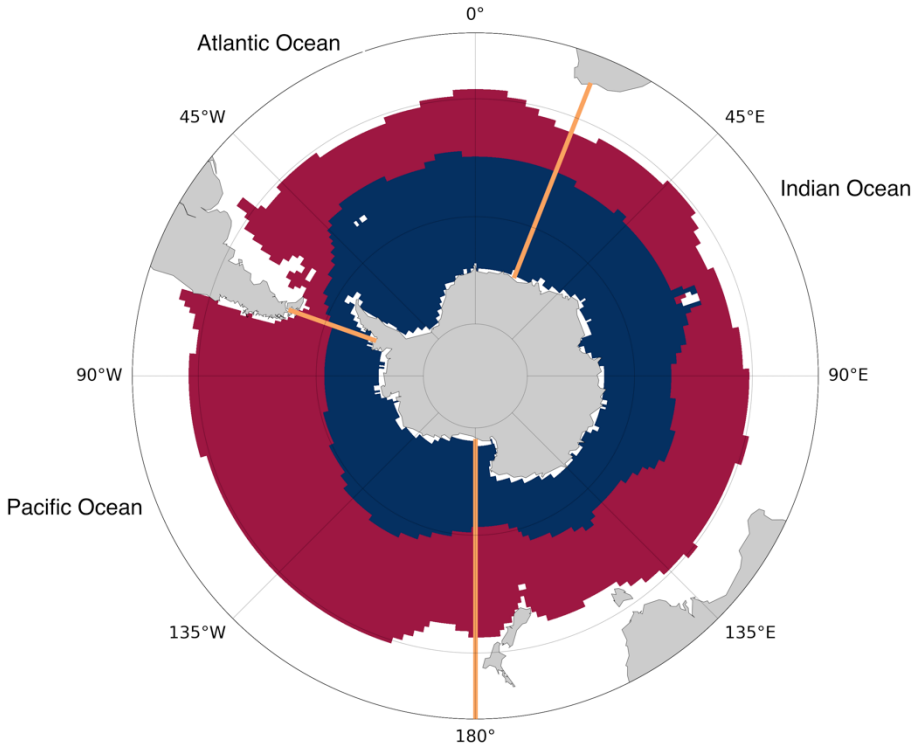

Figure. 2.4 The Sub-Antarctic zone (light Maroon) and Antarctic zone (dark blue) for observations defined according to Orsi et al., (1995) based on W0A13 dataset. The light sandy brown lines show how basin boundaries were defined.

2.3 Analytical approach

This section describes the main methodology used to examine model-observations biases in the seasonal cycle of FCO_2 in this study and calculation for the estimations of entrainment fluxes.

2.3.1 Sea-Air CO_2 flux drivers: The Seasonal Cycle Diagnostic Framework

The seasonal cycle of the ocean-atmosphere pCO_2 gradient (ΔpCO_2) is the main driver of the variability of FCO_2 over comparable periods (Sarmiento and Gruber, 2006; Wanninkhof et al., 2009; Mongwe et al., 2016). Wind speed plays a dual role as a driver of FCO_2: it drives the seasonal evolution of buoyancy-mixing dynamics, which influences the biogeochemistry and upper water column physics (but these processes are incorporated into the variability of the DIC), as well as the rate of gas exchange across the air-sea interface (Wanninkof et al., 2013). However, because winds in the Southern Ocean do not have large seasonal variation (Young, 1999), for this analysis, the wind is considered a secondary driver in terms of the seasonal cycle of FCO_2. Consequently, the seasonal cycle of FCO_2 is directly linked to surface pCO_2 variability, influenced by changes in temperature, salinity, TAlk and DIC and nutrients (Sarmiento and Gruber, 2006; Wanninkhof et al., 2009).

The seasonal cycle diagnostic framework was developed as a way of scaling the relative contributions from the rates of change of SST- and the total DIC-driven changes to the seasonal cycle of pCO_2 on to a common DIC scale. The framework is used to explore how understanding differences emerging from the temperature- and DIC-driven CO_2 variability could be helpful as a diagnostic of the apparent observations–model seasonal cycle biases in the Southern Ocean.

The total derivative of change of DIC in the surface layer consists of the contribution of air-sea exchanges, biological, vertical and horizontal transport-driven changes (Eq. 2.4).

$$\left(\frac{dDIC}{dt}\right)_{Tot} = \left(\frac{\partial DIC}{\partial t}\right)_{air-sea} + \left(\frac{\partial DIC}{\partial t}\right)_{Bio} + \left(\frac{\partial DIC}{\partial t}\right)_{Vert} + \left(\frac{\partial DIC}{\partial t}\right)_{Hor} \quad (2.4)$$

Because zonal means from low and medium resolution models were used, horizontal terms are assumed to be negligible, though the author is aware that there could be a seasonal cycle in the divergence of the horizontal transport due to a latitudinal gradient in DIC perturbed by Ekman flow in some regions of the Sub-Antarctic Zone (Rosso et al., 2017). This leaves sea-air exchange, vertical

fluxes (advection and diffusion) and biological processes as the dominant drivers of DIC.

Since temperature does not affect DIC changes directly, but only pCO_2 through solubility, it was necessary to scale the influence of temperature into equivalent DIC. Thus, in order to constrain the contribution of temperature on the seasonal variability of pCO_2 and FCO_2 a new synthetic temperature-linked term "DIC equivalent" (DIC_T) is defined as: the magnitude of DIC change that would correspond to a change in pCO_2 driven by a particular temperature change. In this way the ΔpCO_2 driven solely by modelled or observed temperature change, is converted into equivalent DIC units, which allows its contribution to be scaled against the observed or modelled total surface DIC change (Eq. 2.4). Shifts between temperature and DIC control of pCO_2 are reflect major shifts in the mechanisms that drive pCO_2 variability. This as the basis to investigate the possible mechanisms behind model biases in the seasonal cycle of pCO_2.

This calculation of DIC_T is done in two steps: firstly, the temperature impact on pCO_2 is calculated using the Takahashi et al. (1993) empirical expression that linearizes the temperature dependence of the equilibrium constants as follows;

$$\left(\frac{dpCO_2}{dt}\right)_{SST} = 0.0423 \times pCO_2 \times \left(\frac{\partial SST}{\partial t}\right) \qquad (2.5)$$

Though this relationship between dSST/dt and $dpCO_2/dt$ is based on a linear assumption (Takahashi et al., 1993), this formulation has been shown to hold in varies cases (e.g. Bakker et al., 2014; Feely et al., 2004; Marinov and Gnanadesikan, 2011; Takahashi et al., 2002; Wanninkhof et al., 2009; Landschützer et al., 2018). It was found that the extension of this expression into polar temperature ranges (SST < 2°C) only introduces a minor additional uncertainty of 4 -5% (Fig. 2.5).

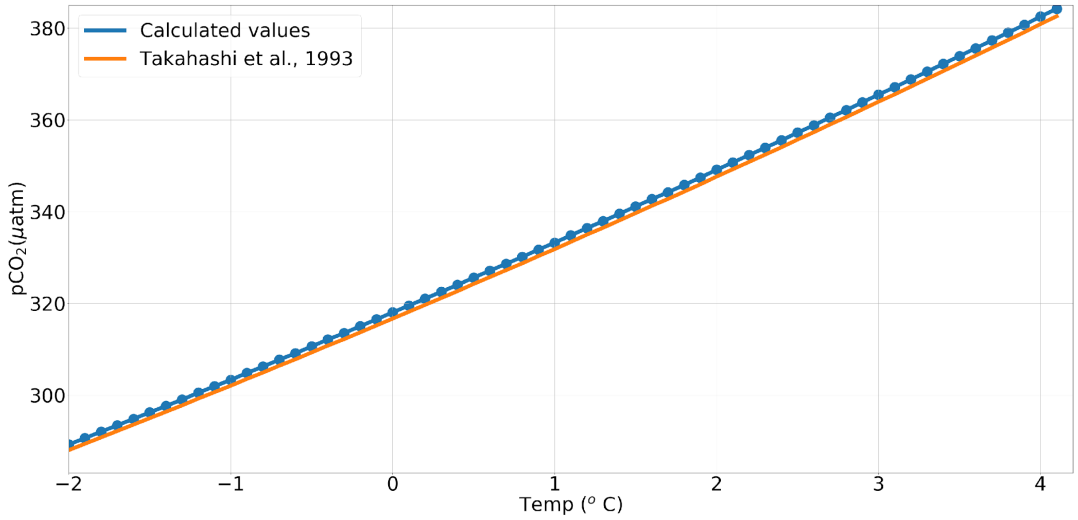

Figure. 2.5 Comparison between of dependence of pCO_2 to temperature changes according to the Takahashi et

al., (1993) empirical the constant ($0.0423^{o}C^{-1}$) and the computed ratio of temperature dependence, from the carbonate system equations (CO2SYS, Pierrot, et al., 2006) using mean climatological data from GLODAP2 (Salinity, TAlk, DIC, silicate & phosphate) and pCO_2 from Landschützer et al (2014) for the Antarctic zone and a temperature range of -2.0ºC to 4ºC (0.1ºC intervals).

Secondly, the temperature-driven change in pCO_2 is converted to an equivalent DIC_T using the Revelle factor.

$$\left(\frac{\partial DIC_T}{\partial t}\right)_{SST} = \frac{DIC}{\gamma_{DIC} \times pCO_2}\left(\frac{\partial pCO_2}{\partial t}\right)_{SST} \quad (2.6)$$

Here a fixed value for the Revelle Factor was used (γ_{DIC}=14), typical of polar waters in the Southern Ocean (Sarmiento and Gruber, 2006). In order to assess the error linked to this assumption, we recomputed the Revelle factor in the Sub-Antarctic and Antarctic Zones using annual mean climatologies of TAlk, salinity and sea surface temperature. Firstly, examinining DIC changes for the nominal range of pCO_2 change (340 – 399 µatm:1 µatm intervals) and then used this dataset to derive the Revelle factor. The range of calculated Revelle factors in the Southern Ocean was between γ_{DIC} ~ 12 – 15.5 with an average of γ_{DIC} = 13.9±1.3. This justifies our use of γ_{DIC} = 14 for the conversion of the solubility-driven pCO_2 change to an equivalent DIC (DICT) throughout the analysis.

The rate of change of DIC was discretized using monthly mean as follows:

$$\left(\frac{\partial DIC_T}{\partial t}\right)_{SST} \approx \left(\frac{\Delta DIC}{\Delta t}\right)_{n,l} = \frac{DIC_{n+1,l} - DIC_{n,l}}{1\ month} \quad (2.7)$$

Where n is time in month, l is vertical level (in this case the surface, l =1), taking the forward derivative such that November rate is the difference between 15 November and 15 December, thus being centered at the interval between the months.

Finally, to characterize periods of temperature or DIC dominance as main drivers of the instantaneous (monthly) pCO_2 change we subtract Eq. 2.4 from Eq. 2.6, which yields a residual indicator $M_{T\text{-}DIC}$ (Eq. 2.8.) $M_{T\text{-}DIC}$ is then used as indicator of the dominant driver of instantaneous pCO_2 changes at the monthly scale.

$$M_{T-DIC} = \left|\left(\frac{\partial DIC_T}{\partial t}\right)_{SST}\right| - \left|\left(\frac{\partial DIC}{\partial t}\right)_{Tot}\right| \quad (2.8)$$

$M_{T\text{-}DIC} > 0$ indicates that the pCO_2 variability is dominated by the temperature-driven solubility and when $M_{T\text{-}DIC} < 0$, it indicates that pCO_2 changes are mainly modulated by DIC processes (i.e. biological CO_2 changes and vertical scale physical DIC mechanisms). The following DIC processes are also examined; 1) biological DIC changes using chlorophyll, NPP, export carbon, surface oxygen, and 2). Physical DIC mechanisms using estimated entrainment rates at the base of the mixed layer. Details of this calculation are in section 2.3.2.

In the Southern Ocean, salinity and TAlk are considered lower-order drivers of the seasonal cycle of pCO_2 (Takahashi et al., 1993). This is demonstrated in Fig. 2.6 bellow, which shows that salinity and TAlk do not play a major role as drivers of the local seasonal cycle of pCO_2. This is done by computing the equivalent rate of change of DIC resulting from seasonal variability of salinity and TAlk as done for temperature (Eq. 2.5), i.e. still assuming empirical linear relationships from Takahashi et al. (1993): $\left(\frac{\ln(pCO_2)}{\ln(TAlk)} \approx -9.4\right)$ and $\left(\frac{\ln(pCO2)}{\ln(Sal)} = 0.94\right)$. By applying these relationships to the model data, we confirmed that indeed salinity and TAlk are secondary drivers of pCO_2 changes i.e. $\left[\left(\frac{\partial DIC}{\partial t}\right)_{Sal}\right]_{average} \approx 0.6$ µmol kg^{-1} month^{-1} and $\left[\left(\frac{\partial DIC}{\partial t}\right)_{TAlk}\right]_{maximum} \approx 0.4$ µmol kg^{-1} month^{-1}, while $\left[\left(\frac{\partial DIC}{\partial t}\right)_{Tot}\right]_{average} \approx 5$ µmol kg^{-1} month^{-1}.

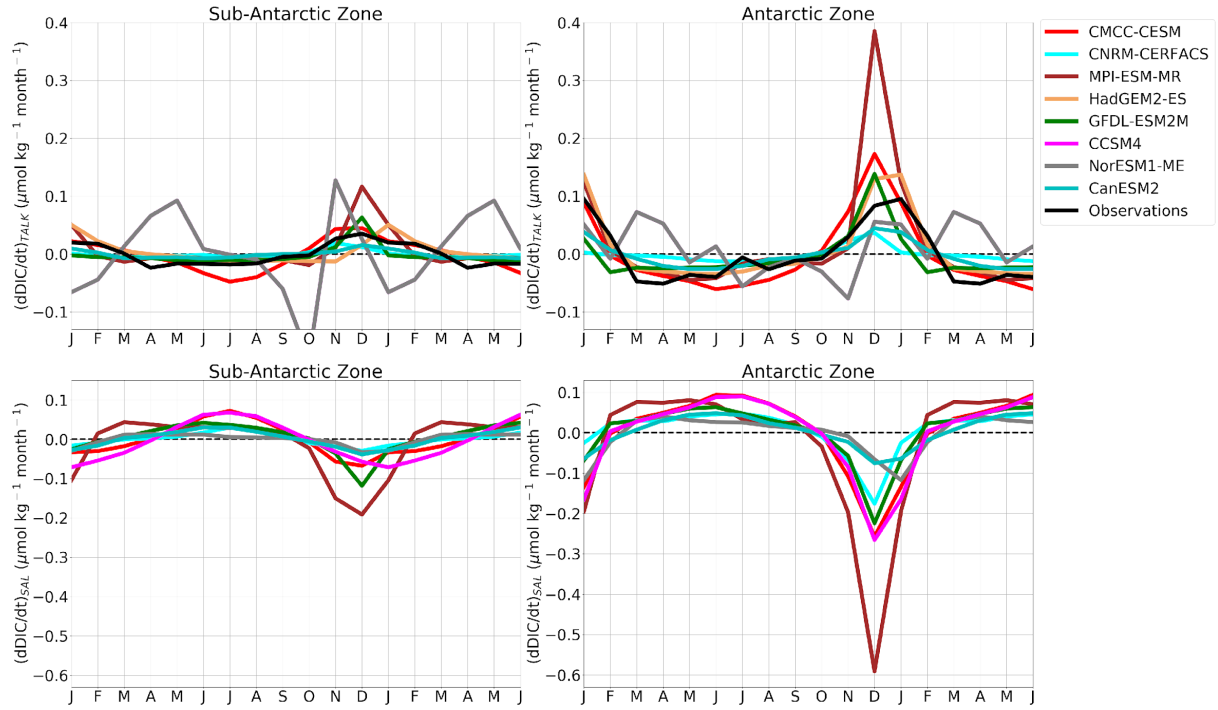

Figure. 2.6 The seasonal cycle of the rate equivalent DIC changes in Salinity and total alkalinity computed using Takahashi et al., 1993 formulations.

2.3.2 Estimation of mixing due to entrainment

CO_2 uptake by the Southern Ocean has been shown to weaken during winter linked to the entrainment of sub-surface DIC as the MLD deepens (e.g. Lenton et al., 2013; Metzl et al., 2006; Takahashi et al., 2009). Here the rate of entrainment (RE) is estimate this using Eq. 2.9, which computes the advection of preformed DIC at the base of the mixed layer (thee estimated RE was only used in chapter 4):

$$RE = U_e \left(\frac{\partial DIC}{\partial z}\right)_{MLD} \quad (2.9)$$

$$RE_n = \left(\frac{\Delta MLD_n}{\Delta t}\right)\left(\frac{\Delta DIC}{\Delta z}\right)_{n,MLD} \quad (2.10)$$

$$\left(\frac{\Delta DIC}{\Delta z}\right)_{n,MLD} = \frac{DIC_{n,MLD_{n+1}} - DIC_{n,MLD_n}}{\Delta z} \quad (2.11)$$

In which U_e is an equivalent entrainment velocity based on the rate of change of the MLD, n is the time in months, MLD_n is the MLD at time n, DIC_n is the annual mean DIC concentration at depth MLD_n, Δt is a monthly timestep and Δz is the depth between MLD_{n+1} - MLD_n in meters. This approximation of vertical entrainment is necessary as it is not possible to compute this term from the CMIP5 data because the vertical DIC distribution is only available as an annual mean. The computed entrainment rates were used to estimate the influence of subsurface/bottom DIC changes on surface DIC changes and subsequently pCO_2 and FCO_2. These estimates were mainly used between autumn-winter, where the MLD ≥ 60 m in the Sub-Antarctic Zone and ≥ 40 m in the Antarctic Zone, at this depth levels seasonal variations in DIC are anticipated to be minimal. However, it is noted as a caveat that this rate of entrainment is only a coarse estimate because annual means are used here.

Chapter 3

The Seasonal Cycle as a Mode to diagnose modelled CO_2 Flux in the Southern Ocean

3.1 Introduction

The seasonal cycle is the dominant mode of variability for chlorophyll (Thomalla et al., 2011) and CO_2 (Lenton et al., 2012) in the Southern Ocean. Thus, it provides a rigorous test of how well modelled CO_2 describes the observed ocean properties. The examination of the seasonal cycle of FCO_2 in OBGM and CMIP5 ESMs against available observed estimates by Anav et al. (2013) and Lenton et al. (2013) were among to the first to highlight the limited skill of modelled seasonal cycle of FCO_2 in the Southern Ocean. Consequently, this raised concerns about the sensitivity of models to capture modes of variability that are key to the links between physical and biogeochemical processes needed to make robust projections of the evolution of the coupled carbon-climate system (a. Lenton et al., 2013; Majkut et al., 2014). Hence the need to understand sources of biases that constrain the ability of OBGMs and ESMs to resolve the seasonal characteristics of FCO_2 in the Southern Ocean with respect to observed estimates.

Historically OBGM vs observation comparison studies of CO_2 have been undertaken using annual means and Taylor diagrams (e.g. Mikaloff Fletcher et al. 2007; Gruber et al. 2009; Anav et al. 2013; Lenton et al. 2013; Majkut et al. 2014). This type of framework remains essential as a statistical basis to investigate mean state differences and coherence between dynamic modes such as the seasonal cycle in data and models. However, they do not reveal the source of the observed anomalies, and hence their interpretation is hard to link to process dynamics. The approach taken here focuses on examining the representation of the seasonal variability of the main drivers of FCO_2 in OBGMs with respect to observed values. This is done by quantifying the phase and the magnitude of the relative contribution of physical properties (temperature dependent-solubility) and biogeochemistry (DIC, TAlk) to the thermodynamic potential of $dpCO_2$ ($pCO_{2ocean} - pCO_{2atm}$) in models and observed

estimates. The objective of this chapter is to provide a methodological framework that can be used to diagnose seasonal cycle characteristics of FCO_2 in coupled ocean models and ESMs. To develop this approach, I use the NEMO-PISCES OBGM as the primary model, and Takahashi et al. (2009) observed estimates.

3.2 Methods

3.2.1 Datasets

The datasets used for this study include surface CO_2 observations from Takahashi et al. 2009 (T09), (http://www.ldeo.columbia.edu/res/pi/CO2/carbondioxide/pages/air_sea_flux_2000.html), Mixed layer Depth (MLD) data from de Boyer Montégut, (2004), 2008 updated version (http://www.ifremer.fr/cerweb/deboyer/mld/home.php), and model output from the Nucleus for European Modelling of the Ocean (NEMO) and the Pelagic Interaction Scheme for Carbon and Ecosystem studies (PISCES) biogeochemistry model, ORCA2 LIM PISCES (2^o x 2^o) configuration (Aumont and Bopp, 2006; Madec, 2008). An expanded description of these datasets is given in chapter 2; they are briefly described below.

3.2.1.1 Observations

The T09 dataset is comprised of a compilation of about 3 million surface measurements of oceanic partial pressure of CO_2 (pCO_2) globally, obtained from 1970 – 2000 and corrected for reference year 2000. The net FCO_2 into the ocean is here expressed as a negative value by convention as consistence with Wanninkhof et al., 2013 and Lenton et al., 2013. TAlk is calculated in accordance to Lee et al. (2006) using TAlk and SST from T09. The total dissolved inorganic carbon (DIC) is calculated using CO2SYS (Pierrot and Wallace 2006, http://cdiac.ornl.gov/ftp/co2sys/CO2SYS_calc_XLS_v2.1) based on calculated TAlk and pCO_2, SST, salinity from T09 and nominal nutrients values of the Southern Ocean (Sarmiento and Gruber, 2005). The seasonal cycle of FCO_2 was then constructed from monthly mean observations and annual CO_2 fluxes as summations of the monthly fluxes in the selected Sub-Antarctic and Antarctic zones. The MLD dataset was extracted in the form of a 2^ox2^o climatological monthly mean over 1941 – 2008, the methodological construction of the dataset is presented in de Boyer Montégut (2004).

3.2.1.2 NEMO PISCES

The NEMO v3.4 modelling platform was used (Madec, 2008). This consists of interacting models of ocean (OPA Oćean PAralleliśe), ice (LIM2 Louvain-la-Neuve Ice Model) and biogeochemistry (PISCES). The model configuration used for this study was designated ORCA2-LIM-PISCES (ORCA2LP) and consists of an ORCA2 global tripolar grid by (Madec and Imbard, 1996) with a horizontal model grid resolution of 2ºx 2º cos(latitude), ranging from ~200km at the equator to about ~100km at 60ºS around the latitude of the Polar Front. In the vertical, the grid consists of 31 vertical levels with partial bottom steps with highest vertical resolution at the surface (15 vertical levels in the upper 200m) and increases with depth. For vertical mixing, the Turbulent Kinetic Energy closure scheme was used. Due to the coarse resolution the Gent and Mcwilliams. (1990), eddy parameterization was used to account for mixing by subgrid-scale mesoscale eddies.

3.3 Results and Discussion

This section is partitioned into four subsections. Section 3.3.1 contrasts the mean summer and winter spatial variability of FCO_2 between the model (ORCA2LP) and T09 observations. Section 3.3.2 provides a more detailed characterization of the mean zonal and decadal seasonal cycle of FCO_2, and the role of physical and biogeochemical drivers (i.e. pCO_2, SST, transfer velocity (k), K_0 , MLD and chlorophyll). Section 3.3.3 uses phase diagrams to examine the changing seasonal contributions of physical (temperature-dependent solubility) and biogeochemical drivers to the thermodynamic potential of pCO_2 in the Sub-Antarctic and Antarctic zones for ORCA2LP and T09. Section 3.3.4 quantifies and examines the relative contributions to the instantaneous roles of temperature and DIC on the seasonal cycle of pCO_2 and FCO_2.

3.3.1 Mean Seasonal CO_2 fluxes

The broad characteristics of the observation-based mean summer and winter seasonal contrasts of the sea-air CO_2 fluxes for the Southern Ocean are depicted in Fig. 3.1(a, b), these are comparable to Takahashi et al. (2012) and Lenton et al. (2012). T09 observations and ORCA2LP show contrasting spatial biases in FCO_2 in the Southern Hemisphere that are particularly evident in the Southern Ocean (Fig. 1.1). For T09 the mid-latitudes are significant CO_2 sink zones throughout the year consistent

with (Sabine et al., 2004), but more pronounced in the austral summer ($FCO_2 \sim -5$ mmol C m^{-2} day^{-1}). FCO_2 in the Sub-Antarctic zone is modulated seasonally by the summer intensification of the biological pump and the seasonal variability of SST (Takahashi et al., 2009; Thomalla et al., 2011; Lenton et al., 2012; Majkut et al., 2014; Rodgers et al., 2014). The region south of 60ºS (Antarctic zone) CO_2 outgassing features are mainly associated with CDW upwelling of natural CO_2 (Gruber et al., 2009b; J L Sarmiento and Gruber, 2006). This process weakens in summer and reverses during the seasonal poleward progression of summer productivity linked to the retreat of the marginal ice zone (MIZ) (Fig. 1.1a,b). The model seasonal climatology shows some spatial biases relative to observations; it shows a spatially uniform strong CO_2 in-gassing (most < −5 mmol C m^{-2} day^{-1}) throughout the Southern Ocean in winter. In summer it shows weaker CO_2 in-gassing fluxes with sub-regional outgassing areas(Fig. 1.1c,d). These seasonal contrasts in the spatial distribution and magnitudes of FCO_2 between observations and the ORCA2LP model outputs are consistent with earlier findings of differences in the characteristics of the seasonal cycle of FCO_2 for a wider range of models (Lenton et al., 2013). Consequently, this points to differences in the characteristics of the seasonal cycle of FCO_2 between observations and models that warrant further investigation.

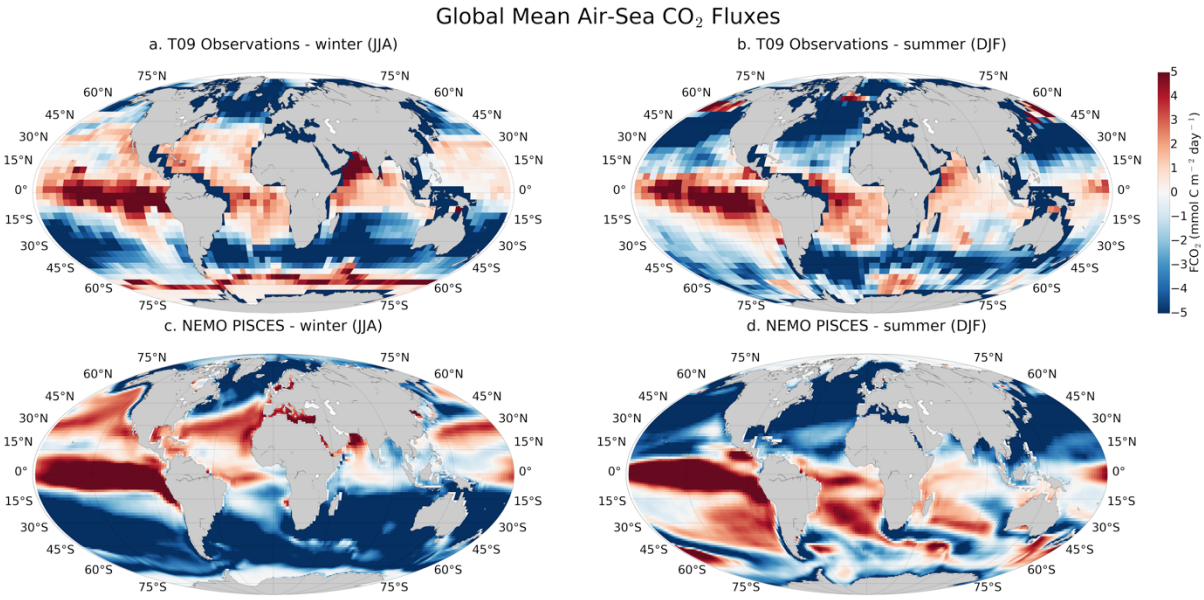

Figure. 3.1 Climatologies contrasting mean seasonal (summer and winter) CO_2 air-sea flux for T09 observations (a,c), and NEMO PISCES climatology over 1993 – 2006 (b,d), given in mmol C m^{-2} day^{-1}. Negative reflects fluxes into the Ocean. The black line shows the mean position of the Sub-tropical front (STF) and Polar Front (PF) from Orsi et al (1995). T09 observations show as expected, general CO_2 outgassing zone south of the PF and a stronger in-gassing zone in the Sub-Antarctic zone across the central Atlantic, Indian Ocean and western Pacific Ocean. ORCA2LP shows a contrasting spatial seasonal mean of air-sea fluxes from observations reflecting weaker outgassing south of the PF and weaker in gassing in the Sub-Antarctic Zone.

The differences between the mean seasonal FCO_2 in the ORCA2LP model output and the T09 dataset are reflected in the magnitudes of the mean annual fluxes; in ORCA2LP the total annual uptake of CO_2 for the Southern Ocean is -0.97±0.04 $PgCyr^{-1}$, which is about 25% higher than T09 observations (-0.72 $PgCyr^{-1}$), (Table 3.1). This seems linked to the underestimation of the outgassing CO_2 fluxes south of the Polar Front (PF) in ORCA2LP particularly during the autumn-winter period when CDW outcrop and mixed layer entrainment is strongest (Séférian et al. 2012). A comparison of the zonal mean fluxes in the Sub-Antarctic and Antarctic zone (Table 3.1) show that model and data are in close agreement in the Sub-Antarctic where the ORCA2LP annual CO_2 flux (-0.64 $PgCyr^{-1}$) is comparable to observations (-0.58 $PgCyr^{-1}$). In this zone, seasonal and annual CO_2 fluxes dynamics are mainly driven by a combination of primary productivity, the meridional cooling of sub-tropical waters and winter convective entrainment of deep water with elevated DIC (Metzl et al., 2006b; Metzl, 2009). The main differences however, arise in the Antarctic zone where ORCA2LP has a stronger in-gassing flux of CO_2 (-0.39 PgC y^{-1}) than T09 (-0.08 PgC y^{-1}) probably because of the weaker modelled outgassing flux from upwelling of CDW (Fig 3.1a). Here, the seasonal and annual dynamics are driven mainly by the physics, upwelling of CDW and winter convective entrainment of CDW (Sarmiento and Gruber, 2006; Gruber et al. 2009). In both regions a combination of physical and biological dynamics could explain the differences between the model and the observation estimates. The next section explores the characteristics of the seasonal cycle for zonally averaged flux of CO_2 towards a process-based examination of the apparent differences between the magnitude and annual phasing of CO_2 fluxes in the Sub-Antarctic and Antarctic zone for ORCA2LP and T09.

Table 1.1 The decadal scale mean annual air-sea CO_2 fluxes derived from NEMO PISCES over 1993 – 2006 and decadal mean observations for the year 2000 (Takahashi et al., 2009). Negative sign reflects the flux into the Ocean. The annual fluxes are given in $PgCy^{-1}$.

Region	T09 observations	ORCA2LP
Southern Ocean (south of STF)	-0.72	-0.97±0.04
Sub-Antarctic zone	-0.64	-0.58±0.02
Antarctic zone	-0.08	-0.39±0.04

3.3.2 Characterization of FCO_2 seasonal cycle

The seasonal cycles of FCO_2 and its drivers for T09 observations and ORCA2LP model outputs are shown in Fig. 3.2 for the Sub-Antarctic zone and Fig. 3.3 for the Antarctic zone. The driving mechanisms are the air-sea pCO_2 gradient ($dpCO_2$) (b), MLD (c), SST (d), gas transfer velocity (k) (e) and chlorophyll (f). While the $dpCO_2$ determines the magnitude and direction of FCO_2, SST and k influence the seasonal variability of the magnitude (Wanninkhof, 1992; Wanninkhof et al. 2013). Low

SST strengthen surface CO_2 solubility which favours CO_2 uptake, and vice versa for high SST (Sarmiento and Gruber, 2006). Given that the variability of atmospheric pCO_2 is relatively low in the Southern Ocean (Fujita et al., 2003), seasonal variability of $dpCO_2$ is almost completely driven by changes in surface pCO_2. In this section, I use these variables (Figs. 3.2 and 3.3 b - f) to investigate how these seasonal processes may be driving surface pCO_2 changes and hence FCO_2 in the observed and modelled data.

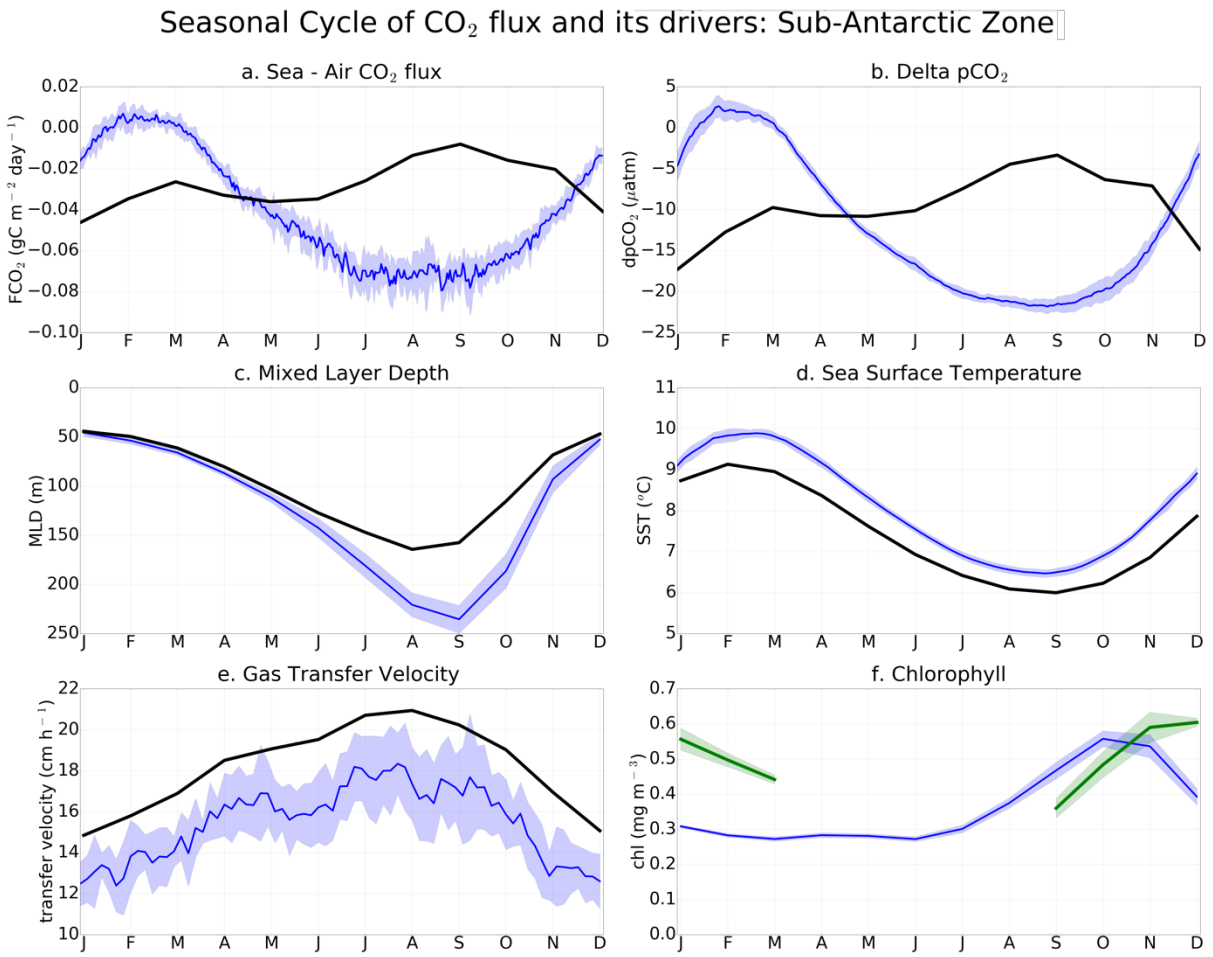

Figure. 3.2 Shows the contrasting seasonal cycles of air-sea CO_2 flux and ancillary variables for NEMO PISCES (blue), the shaded area shows the standard deviation over 1993 – 2006, and T09 observations (black line) normalized to the year 2000 at the Sub-Antarctic Zone. (a) CO_2 flux ($gCm^{-2}yr^{-1}$) negative indicates flux into the ocean (b) Delta pCO_2 (µatm), (c) Mixed layer depth (MLD m), (d) Sea Surface Temperature (SST ºC), (e) Gas transfer velocity (ms^{-1}) , (f) CO_2 solubility Coefficient ($mmolL^{-1}atm^{-1}$). NEMO PISCES air-sea CO_2 flux show similar phasing with T09 observations between Jan – Mar but remain out of phase for the rest of the year.

The seasonal cycles of FCO_2 and $dpCO_2$ in the Sub-Antarctic zone (Fig. 3.2a) highlight significant differences between T09 and ORCA2LP, whereas there is close agreement in the mean annual CO_2 fluxes in Table 3.1. The seasonal cycles of FCO_2 and $dpCO_2$ in ORCA2LP are out of phase with T09

(Fig. 3.2a, b) with an exception a brief period in late summer (Jan - Feb). ORCA2LP switches from a weak CO_2 outgassing flux in late summer to a strong in-gassing in winter (Jun - Aug) which is out of phase with T09 observations. These plots show that although the mean annual flux may be similar (Table 3.1), ORCA2LP and T09 differ in both amplitude and phasing of the seasonal cycles of FCO_2 and $dpCO_2$ consistent with the findings of Lenton et al. (2013).

The phasing differences in FCO_2 between T09 and ORCA2LP appear to be mainly linked to differences in $dpCO_2$, the seasonal cycle of which is coherent with the FCO_2 (Fig. 3.2a, b). The remaining drivers of FCO_2 and $dpCO_2$ (MLD, SST, gas transfer velocity) show remarkable coherence in the phasing between T09 and ORCA2LP even if there are differences in their magnitudes except for of chlorophyll (Fig. 3.2). However, note that ORCA2LP also shows a comparable phasing coherence between SST and $dpCO_2$, but T09 does not (Fig. 3.2b, d). This agreement of the phasing of SST and $dpCO_2$ in ORCA2LP (Fig. 3.2b, d) may suggest that the influence of the seasonal cycle of SST on $dpCO_2$ may be more significant than expected.

In the Antarctic zone, the differences in the phasing and magnitude of the seasonal cycles of FCO_2 between T09 and ORCA2LP are sharper than in the Sub-Antarctic zone (Figs 3.3 a, c, f and 3.2 a, c,f). The T09 seasonal cycle of FCO_2 is closer to the conventional variability in the Antarctic zone, showing a productivity-linked minimum in summer and a CDW upwelling-linked outgassing in the ice-free areas during winter (Fig. 3.3 a), (Lenton et al. 2013; Majkut et al. 2014). As in the Sub-Antarctic, $dpCO_2$ is the best predictor for the phasing of the seasonal cycle of FCO_2 for both T09 and ORCA2LP (Fig. 3.3 a, b). Once more the seasonal cycles of FCO_2 and $dpCO_2$ in the Antarctic zone are out of phase with T09 observations (Fig. 3.3 b). Here the winter MLD deepening occurs a month earlier (February) and at a faster rate with respect T09, however, this does not strengthen the CO_2 outgassing flux in ORCALP2. Though the model shows a slight weakening of the CO_2 in-gassing flux from April - November, these magnitudes are small with respect to T09 observations (Fig. 3.3 a, c). The model data suggest that the seasonal phasing of the surface temperatures (stronger solubility-driven CO_2 uptake during winter) may be key to the explanation. ORCA2LP shows correct phasing of chlorophyll with respect to observations, as both peak in December - January, but underestimates magnitudes during spring - early summer (Sept - Dec). It should be noted that the de Boyer et al. (2004) dataset has limited observations during the period of maximum ice cover (May - Oct) in the Antarctic zone, thus observed MLDs are likely underestimated during this period.

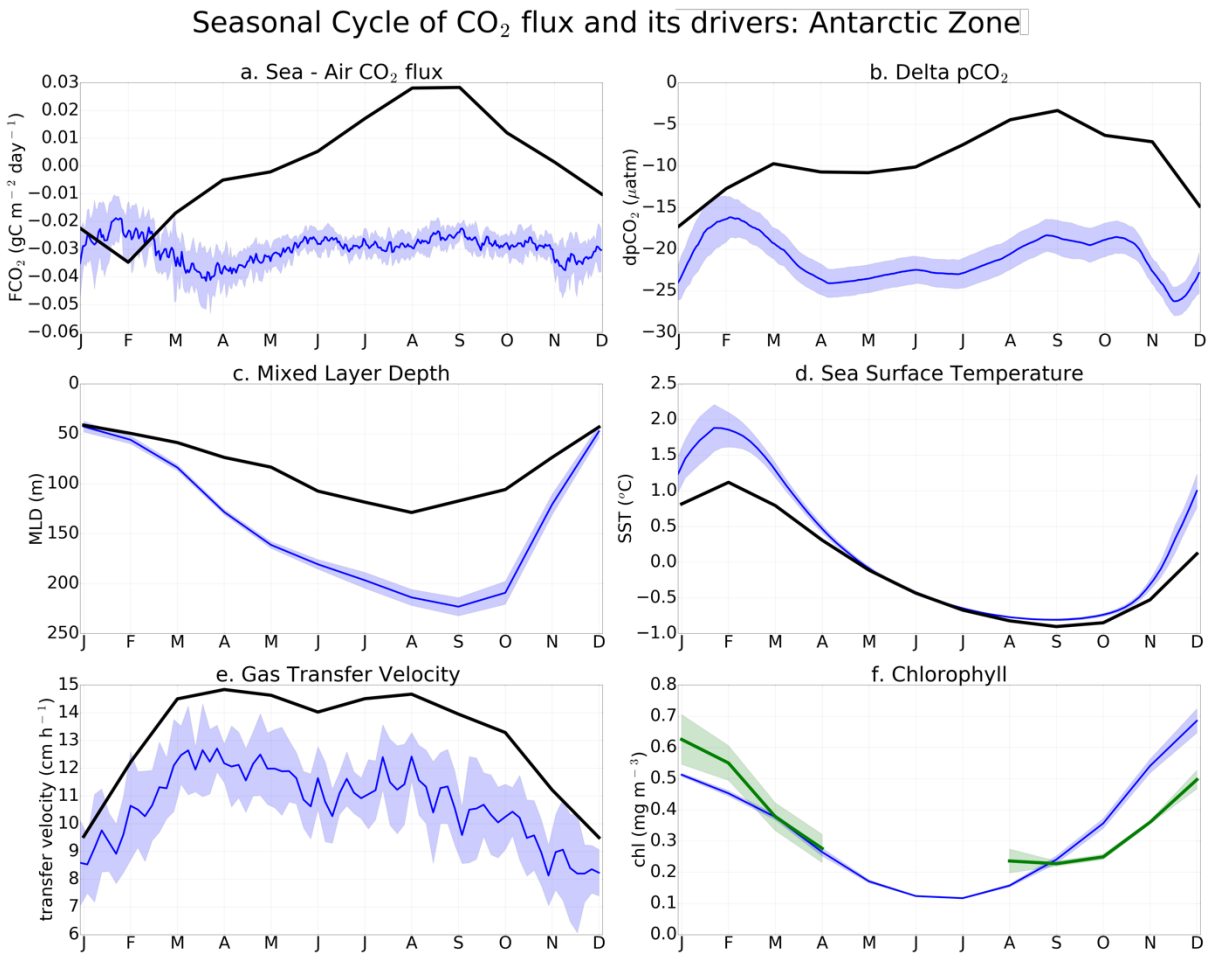

Figure. 3.3 Shows the contrasting seasonal cycles of air-sea CO_2 flux and ancillary variables for NEMO PISCES (blue), the shaded area show the standard deviation over 1993 – 2006 and T09 observations (black line) normalized to year 2000 at the Antarctic zone (a) CO_2 flux ($gCm^{-2}yr^{-1}$) negative indicates flux into the ocean (b) Delta pCO_2 (µatm) , (c) Mixed layer depth (MLD m) , (d) Sea Surface Temperature (SST ºC), (e) Gas transfer velocity (ms^{-1}) , (f) CO_2 solubility Coefficient ($mmolL^{-1}atm^{-1}$). ORCA2LP air-sea CO_2 flux seasonal cycle is completely out of phase with T09 observations.

Overall, these results suggest that the phasing differences of FCO_2 (and $dpCO_2$) between T09 and ORCA2LP may be linked to unexpectedly strong temperature driven control in the model. Weaker than expected influence of primary productivity in summer and deep entrainment of DIC in winter may an important constraints in ORCA2LP.

In the next section, I use phase diagrams to examine how differences in the physical and biogeochemical processes (i.e. sea-air gas exchange, convective mixing, solubility and biological productivity) help explain the differences in seasonal characteristics between T09 and ORCA2LP FCO_2.

3.3.3. Seasonal cycle phase diagrams

The variability of surface ocean pCO_2 has two fundamental drivers: biogeochemical - physical (DIC/TAlk) and thermal (SST) (Metzl et al., 2006; Sarmiento and Gruber, 2006; Wanninkhof et al., 2009). Both DIC and TAlk are influenced by summer primary production and winter mixing. At a constant temperature and salinity, an increase in DIC increases pCO_2, while TAlk has the opposite effect. Here I use the mean monthly DIC and TAlk as indicators of the expected seasonal cycle of pCO_2, DIC and TAlk are high in winter and lowest in summer. The magnitude and phasing of zonally averaged mean monthly pCO_2 with its main biogeochemical and physical drivers (DIC, TALK and SST) for T09 dataset and ORCA2LP model outputs are shown in Figs. 3.4 and 3.5 for the Sub-Antarctic and the Antarctic zone respectively. Here I aim to show how these plots not only re-emphasize the sharp contrasts shown earlier between the seasonal cycles of T09 and model FCO_2 (Figs. 3.2 and 3.3), but also point to a useful diagnostic tool for those differences and an indication of how model improvements may be approached.

As anticipated ORCA2LP and T09 show significant differences in the seasonal amplitude of DIC and TAlk (winter-summer maxima) in Fig. 3.4 a, e. The seasonal amplitudes are about two orders of magnitude lager in T09 with respect to ORCA2LP (e.g. DIC ≈ 40 μmol kg^{-1} in T09 vs. ≈ 20 μmol kg^{-1} for ORCA2LP, Fig. 3.4 a, e). Whereas the seasonal phasing of pCO_2 is coherent with seasonal cycle of DIC and TAlk for the observations (high in winter and low in summer), ORCA2LP shows an inverse relationship in the Sub-Antarctic zone. However, in the Antarctic zone, the seasonal cycle of DIC shows coherence for both seasonal amplitude and magnitude of DIC between ORCA2LP and T09 (≈ 40 μmol kg^{-1}) with respect to the Sub-Antarctic (Fig. 3.5). When differences in this expected pCO_2 vs. DIC relationship emerge, as in the case of ORCA2LP, which shows a controversial out of phase seasonal relationship between pCO_2 and DIC, this probably suggests that an alternative physical driver (probably SST) is playing a stronger role in the seasonal variability of pCO_2. Assuming that, despite its coarse resolution, the observations dataset at least reflects the correct phasing in T09, this highlights an area of the biogeochemical ocean model where the process and/or scale sensitivities are not adequately resolved.

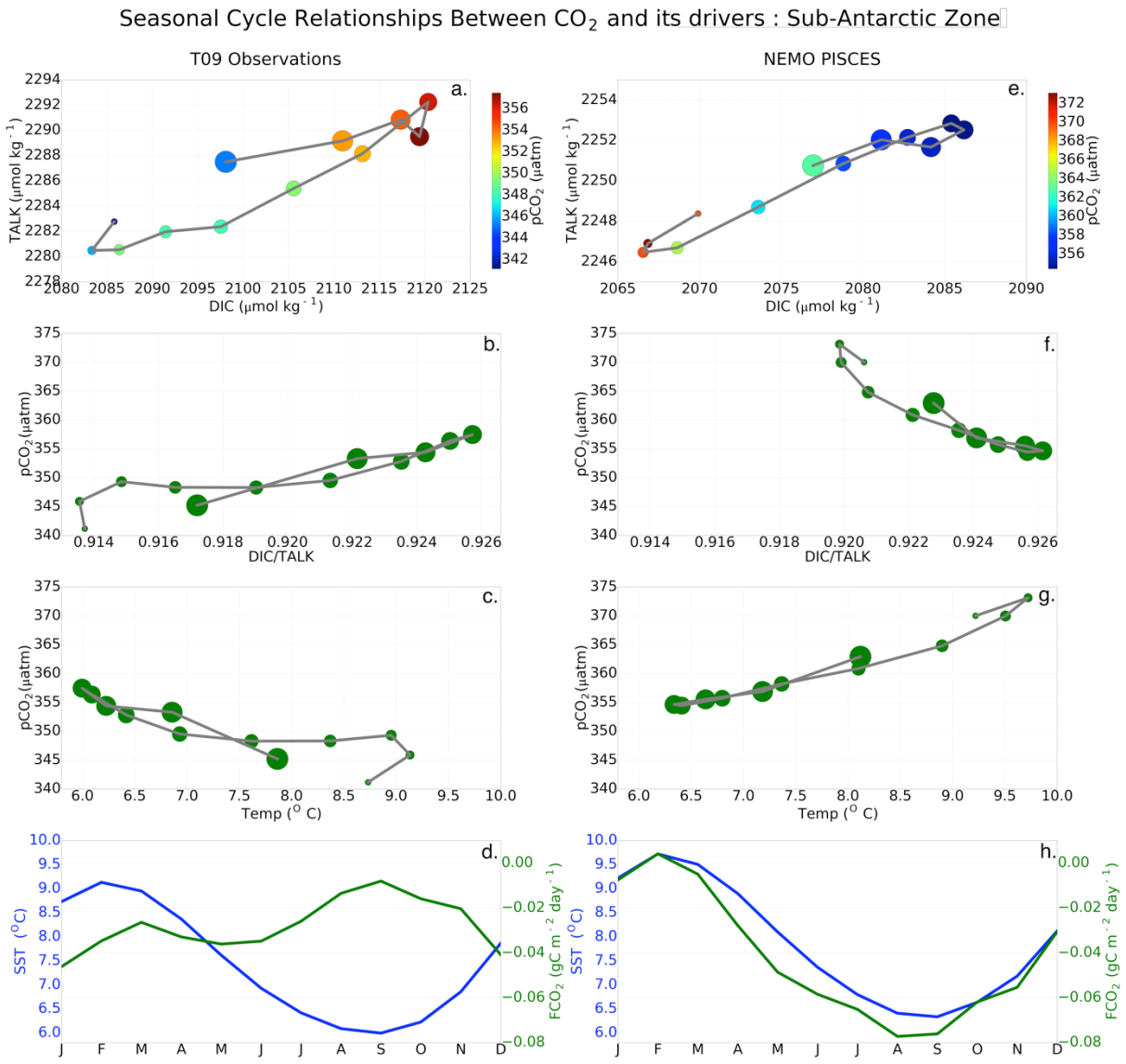

Figure. 3.4 Sub-Antarctic zone: relationships in the phasing and magnitude in the seasonal cycles of oceanic surface pCO_2 with Dissolved Inorganic Carbon (DIC), Total Alkalinity (TA) and Sea Surface Temperature (SST) for observations (a-d) and NEMO PISCES (e-h). The individual pairs of plots are DIC vs TA with pCO_2(µatm) in the z axis (a,e), DIC/Talk ratio vs pCO_2 (b,f), pCO_2 vs Temp (c,g), seasonal cycles of air-sea CO_2 fluxes (green) and SST (blue; d,h). The size of the dots in a) and e) represent time in months, ranging from January (smallest) to December (largest). Note that Figs 3.a and 3e are not the same scale.

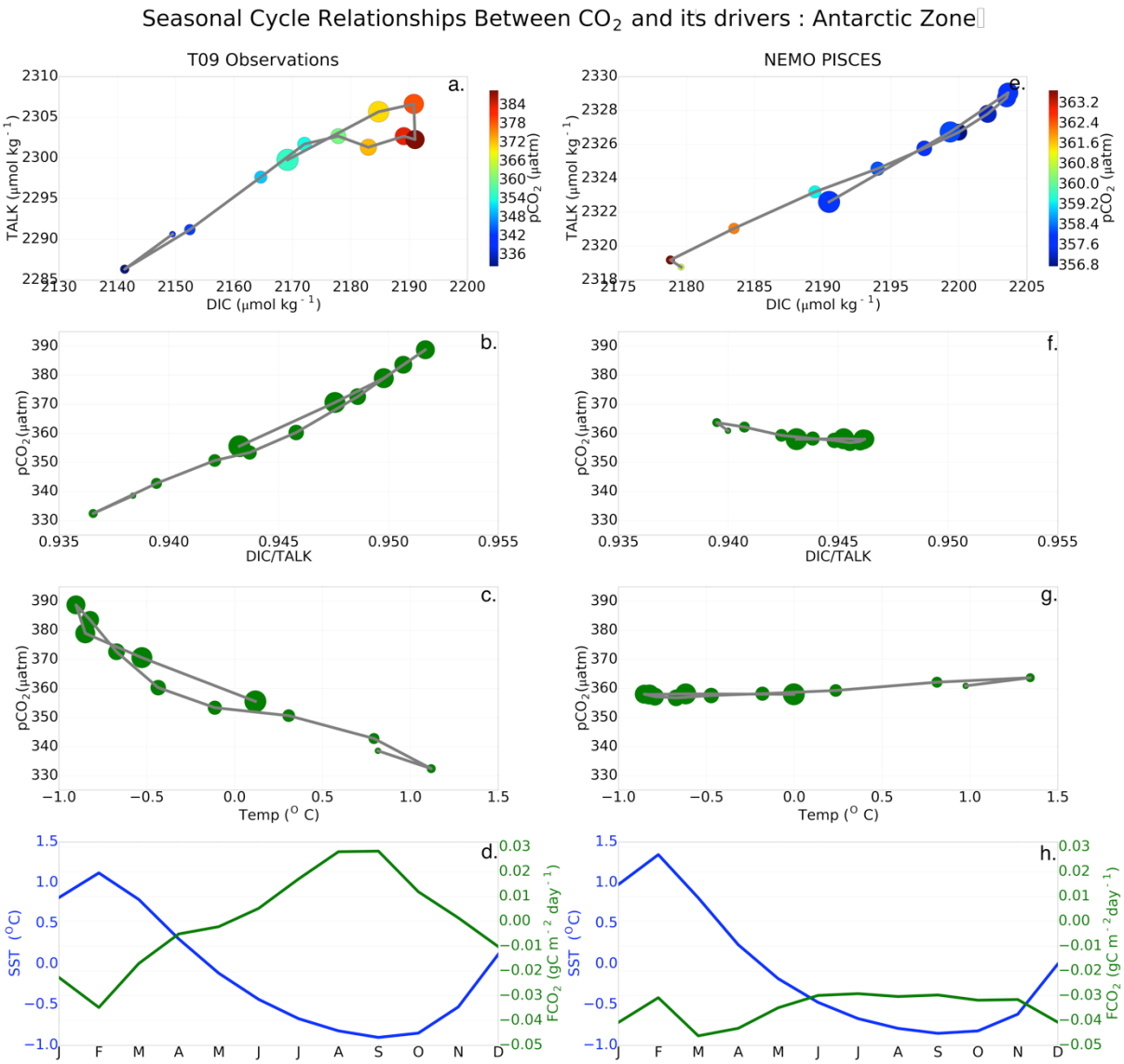

Figure. 3.5 Antarctic zone: relationships in the phasing and magnitude in the seasonal cycle of oceanic surface pCO_2 with Dissolved Inorganic Carbon (DIC), Total Alkalinity (TA) and Sea Surface Temperature (SST) for observations (a-d) and NEMO PISCES(e-h). The individual pairs of plots are DIC vs TA with pCO_2(uatm) in the z axis (e,f) , DIC/Talk ratio vs pCO_2 (b,f), pCO_2 vs Temp (c,g), seasonal cycles of air-sea CO_2 fluxes (green) and SST(blue), (d,h). The size of the dots in a) and e) represent time in months, ranging from January (smallest) to December (largest). Note that figure 5.a and 5e are not the same scale.

The sensitivity of pCO_2 to DIC and TALK forcing is captured in Eq. (3.1), which shows that at constant temperature and salinity, pCO_2 changes can be related to changes in the DIC/TAlk ratio, which determine the buffering capacity (Sarmiento and Gruber, 2006).

$$\ln \Delta pCO_2 \approx \gamma_{DIC} \ln \Delta DIC - \gamma_{TA} \ln TA \qquad (3.1)$$

Where $\gamma_{DIC} = \frac{\partial \ln pCO_2}{\partial \ln DIC}$ and $\gamma TA = \frac{\partial \ln pCO_2}{\partial \ln TA}$ are dimensionless sensitivities of pCO_2 to DIC and TAlk changes (Takahashi et al. 1981; Sarmiento and Gruber, 2006). This expression (Eq. 3.1) is the basis for exploring the ratio of DIC/TAlk as a primary test of the seasonal evolution of pCO_2 in observations and model outputs (Figs. 3.4 and 3.5). The DIC/TAlk ratio is here used to examine how instantaneous changes in pCO_2 could be explained by the seasonal evolution of DIC and TAlk in in the Sub-Antarctic and Antarctic zone (Figs. 3.4 c, d and 3.5 c,d).

In the Sub-Antarctic zone, T09 shows a positive DIC/TAlk slope between winter-summer (Jul - Dec) and a flatter slope (close to zero) for summer-winter (Jan - Jun) (Fig. 3.4 b). However, in the Antarctic zone there is a consistent positive slope throughout the year (Fig. 3.5 b). The increase in Talk/DIC during winter is known be associated with convective mixing and entrainment of sub-pycnocline waters which bring these DIC rich subsurface waters into the mixed layer, resulting in a net increase of the DIC concentration (Metzl et l. 2006;2009). During the spring - summer (Sept - Dec) period, photosynthesis causes the net reduction of DIC and a small increase in TAlk, most likely through nitrate reduction, thus driving a net decrease in the Talk/DIC ratio (Figs. 3.4b and 3.5b), (Philibert et al. 2015). This process (spring production) occurs in both Sub-Antarctic and Antarctic zones, though the effect is strongest in the Sub-Antarctic zone (Figs. 3.4 b and 3.5 b).

There are two alternative mechanisms that could influence the reduced sensitivity of pCO_2 to Talk/DIC from late summer to autumn in T09 data. The first option is that decreased DIC and TAlk change the pCO_2 sensitivities through changes in buffer factors γ_{DIC} and γ_{TA}. However, the impact of these seasonal ranges of DIC and TAlk on γ_{DIC} and γ_{TA} are too small to account for the strong changes in the sensitivity of pCO_2 to DIC and TAlk. The more likely explanation probably lies with the concomitant role of temperature through surface CO_2 solubility changes. It more probable that temperature exerts a stronger influence on instantaneous pCO_2 changes such that pCO_2 variability is mainly driven by surface CO_2 solubility changes, rather than changes in DIC and TAlk (Figs 3.4 b, d and 3.5 b, d).

In T09, the phasing of pCO_2 is coherent with SST for the first four months of the year (Jan - Apr) in the Sub-Antarctic zone (Fig. 3.4 c, d). This probably suggests that the rate of SST changes (warming (Jan - Feb) summer and cooling (from March) is greater than the impact of the seasonal convective entrainment on the rate of change of DIC/TAlk for the first four months. However, note that between mid-autumn and the beginning of winter (Apr - Jun) there is a transition period when the influence of temperature (cooling) and Talk/DIC (entrainment mixing) on pCO_2 balances such that $d(DIC/TAlk)/dpCO_2) \approx d(SST)/dpCO_2)$ and hence $dpCO_2/dt \approx 0$ (Fig. 3.4 b, c). During this period, the rate of increase in DIC flux from entrainment is probably balanced by a comparable rate of cooling in

the Sub-Antarctic zone (Fig. 3.4 c). From June to the end of the year the influence of the rate of cooling decreases and entrainment flux increases, driving pCO_2 increase; later (spring to mid-summer (Dec)) surface DIC reduces through primary production. Thus, the DIC/TAlk ratio takes over again as the main regulator of the seasonal instantaneous pCO_2 between Jun - Dec (Fig. 3.4 b, d). In contrast, the Antarctic zone shows a consistent negative slope for the relationship between pCO_2 and temperature, confirming that seasonal pCO_2 variability is largely regulated by changes in Talk/DIC changes (entrainment mixing and biological driven DIC changes).

For the ORCA2LP model output, the anomalous seasonal sensitivity of pCO_2 to Talk/DIC with respect to T09 is clearly evident for both the Sub-Antarctic (Fig. 3.4 f, g) and the Antarctic zone (Fig. 3.5 f, g). In the Sub-Antarctic zone, the ORCA2LP shows an inverse relationship between Talk/ DIC and pCO_2 throughout the year, showing that TAlk DIC changes (entrainment and biological DIC changes) do not play dominate roles in surface pCO_2 changes. For the Antarctic zone, similar behaviour is shown in summer and flat for the remainder of the year, showing that either temperature or Talk/DIC strongly dominates surface pCO_2 changes. These relationships confirm that the ORCA2LP does reflect biases in the dynamics of the expected seasonal cycle of pCO_2. The negative or near-zero seasonal slopes in the Sub-Antarctic and Antarctic zones indicate that the expected biogeochemical control of pCO_2 reflected in observed estimates does not emerge from the modelled seasonal dynamics. This points to the model seasonal cycle of pCO_2 being controlled mainly by seasonal dynamics of physical properties (temperature-dependent solubility), rather than the biogeochemistry. Note that this does not mean that there is no underlying biogeochemical influence, model outputs do show seasonal varying primary productivity. Rather, it shows that the net effect of the concurrent physics (temperature change) is the principal driver over biogeochemistry (DIC change) dynamics. This is clearly evident in plots of the seasonal cycle of pCO_2 - temperature (Figs. 3.4 g and 3.5 g), where the seasonal phasing of SST is coherent with FCO_2 in ORCA2LP, but the opposite is observed for T09 observations estimates. If temperature is the dominant driver then the expected seasonal relationship of pCO_2 with temperature is positive, reflecting the seasonal dynamics of CO_2 solubility.

The plots for T09 show that in instances when pCO_2 is regulated mainly by biogeochemical forcing, the slope with temperature is between nil and negative (Figs 3.4 c and 3.5 c). In contrast, the model outputs for both the Sub-Antarctic and the Antarctic zones show positive seasonal relationships between pCO_2 and temperature throughout the year (Figs 3.4 g and 3.5 g), consistent with temperature control of solubility. In the next section I scale up relative contributions of temperature and DIC changes (entrainment and biogeochemistry) to the seasonal cycle of pCO_2 and FCO_2 since in reality both play roles in the seasonality of pCO_2.

3.3.4. Scaling the roles of temperature and DIC to the seasonal cycle of pCO_2

The two major processes that drive surface pCO_2 variability are surface ocean CO_2 solubility (thermal component -SST) and physical- biogeochemical variability of DIC. In this section, I investigate the sensitivity of pCO_2 to the relative rates of change of SST and DIC. The role each plays in surface pCO_2 and $dpCO_2$ variability is described by Eq. 3.2 - 3.4, (Takahashi et al., 1993; Sarmiento and Gruber, 2006).

$$\frac{1}{pCO_2}\frac{\partial pCO_2}{\partial SST} = \frac{\partial lnpCO_2}{\partial T} \approx 0.0423^oC \quad (3.2)$$

$$\left(\frac{\partial pCO_2}{\partial t}\right)_{SST} = 0.0423 \times pCO_2 \times \frac{\partial SST}{\partial t} \quad (3.3)$$

$$\left(\frac{\partial DIC_T}{\partial t}\right)_{SST} = \frac{DIC}{pCO_2 \times \gamma_{DIC}}\left(\frac{\partial pCO_2}{\partial t}\right)_{SST} \quad (3.4)$$

The first two expressions (Eq. 3.1-3.2) quantify the change in surface pCO_2 driven by temperature changes alone (dSST/dt), the thermal component of pCO_2 changes. The seasonal cycle of SST rates of change (dSST/dt) are shown in Fig. 3.6 a, b. for T09 and ORCA2LP in the Sub-Antarctic and Antarctic zones. T09 and ORCA2LP show close agreement in the phasing as well as the magnitude of the rate of change of SST. This agreement suggests that differences between the modelled and observed seasonality of FCO_2 for this case probably do not rest on warming and/or cooling differences. This reflects how surface temperatures for both observations and model outputs are driven and made coherent by the seasonal cycle of solar heat fluxes. Although there are small biases in the summer season, where the onset of modelled surface cooling is delayed by a month (Jan) with respect to observations (Dec) in the Sub-Antarctic zone, I will show that these are not significant differences between T09 and ORCA2LP. The seasonal amplitude for cooling - warming rates are as expected, larger for the Sub-Antarctic zone (≈ -1 °C month^{-1}) in comparison to the Antarctic zone (-0.5°C month^{-1}), given the seasonal presence of sea-ice in the Antarctic zone (Fig. 3.6 a, b).

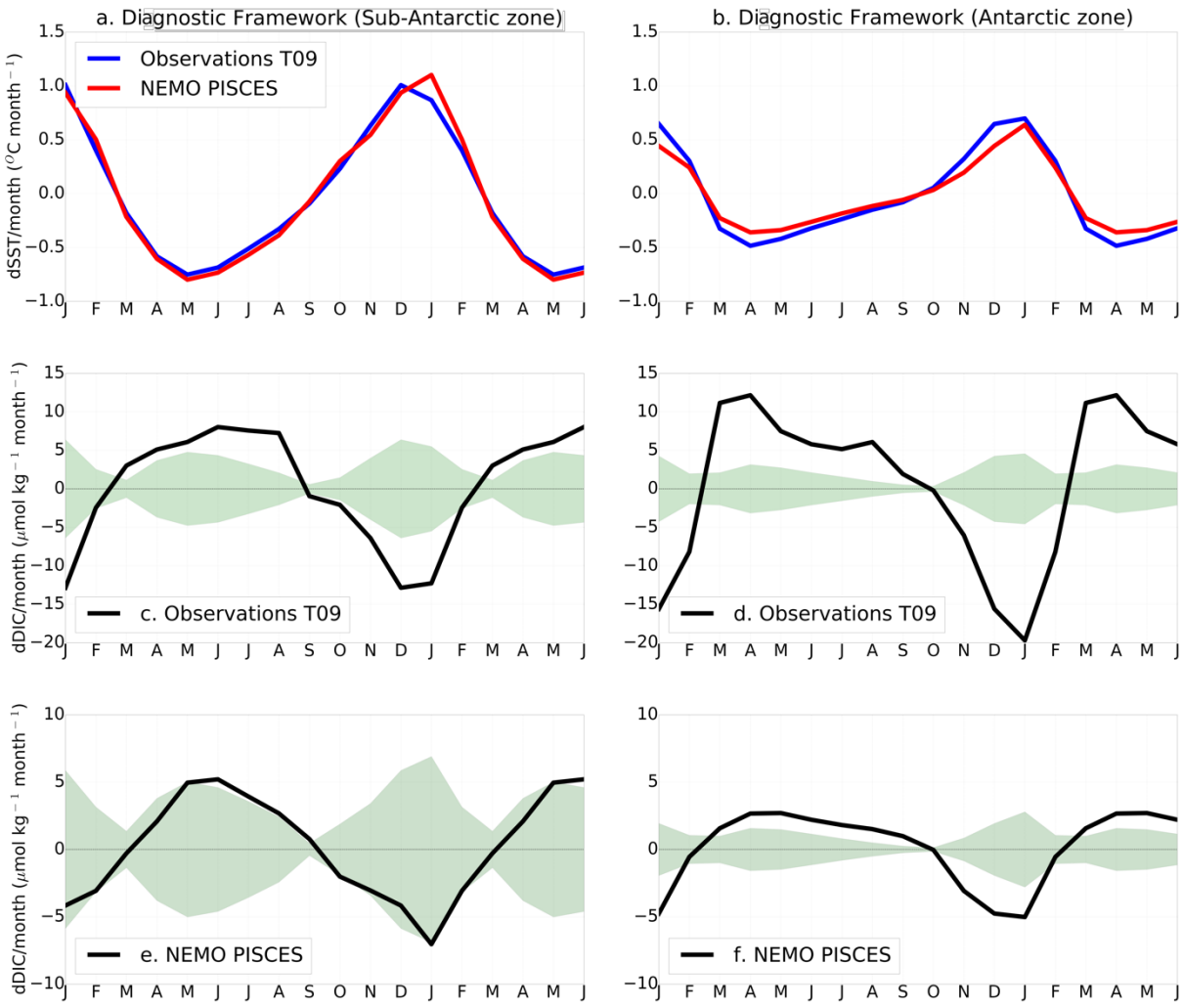

Figure. 3.6 Depicts the rate of change of temperature (dSST/dt) (a–b) in the observations and NEMO-PISCES (b), and DIC (dDIC/dt) (c–f) in the Sub-Antarctic Zone and Antarctic Zone. The shaded area (green) shows the thresholds of a region of dDIC/dt where temperature primarily drives the pCO_2 variability. Outside the threshold indicates that biogeochemical – physical advection processes drive the observed pCO_2 variability.

The calculated thermally driven pCO_2 change in Eq. 3.3 is then used to derive the equivalent change in DIC $(dDIC_T/dt)_{SST}$ using Eq. 3.4. The seasonal cycle of the absolute value of the $(dDIC_T/dt)_{SST}$ (shaded area) and the total rate of change of DIC are shown in Fig. 3.6 c - f. The surface rate of change of DIC (dDIC/dt, black line) represent the total contribution of the DIC terms i.e. air-sea exchange, biological driven DIC changes (primary production and respiration), vertical and horizontal advection term (Eq. 3.3)

$$\left(\frac{dDIC}{dt}\right)_{Tot} = \left(\frac{\partial DIC}{\partial t}\right)_{air-sea} + \left(\frac{\partial DIC}{\partial t}\right)_{Bio} + \left(\frac{\partial DIC}{\partial t}\right)_{Vert} + \left(\frac{\partial DIC}{\partial t}\right)_{Hor} \qquad 3.5$$

The $((dDIC_T/dt)_{SST}$ term is a DIC equivalent term (proxy), it does not contribute to the sum of DIC terms in Eq. 3.5, it quantifies the solubility driven pCO_2 changes in DIC units. This is done by using the Revelle factor (Eq. 3. 6) to convert solubility pCO_2 changes into equivalent DIC magnitudes. The Revelle factor is an experimentally derived factor that scales equivalent DIC changes for a change in pCO_2 (Egleston et al., 2010; Zeebe and Wolf-Gladrow, 2001). It varies meridionally, here I use 14 as described in the methodology section, nominal for the Southern Ocean (Sarmiento and Gruber, 2006).

$$\gamma_{DIC} = \left(\frac{\partial pCO_2}{pCO_2}\right) / \left(\frac{\partial DIC}{DIC}\right) \qquad 3.6$$

Thus the seasonal cycle of $|(dDIC_T/dt)_{SST}|$ (shaded area) and dDIC/dt in Fig. 3.6, compares the relative contribution of the SST driven pCO_2 changes and DIC changes to total surface pCO_2 variability. I use the absolute value for solubility equivalent $|(dDIC_T/dt)_{SST}|$ but not for the total DIC changes; the solubility component is only driven by temperature changes, thus the magnitude gives sufficient information. However, DIC changes can either be caused by entrainment mixing or biological processes which have a contrasting net impact on surface CO_2 concentration, hence information of the direction of change is useful for the analysis. Entrainment mixing increases surface CO_2 when it starts and pCO_2 falls as it matures; primary production reduces surface DIC by forming inorganic matter when it starts and in some instances the subsequent surface respiration increases surface CO_2 concentration.

Consequently, when the total surface rate of change of DIC (dDIC/dt, black line) is below the shaded area, it signifies that temperature change is a dominant driver of the instantaneous pCO_2 changes through solubility. When the modelled or observed magnitudes of rates of change of DIC are outside the $|(dDIC_T/dt)_{SST}|$ boundaries, then pCO_2 variability is primarily driven by DIC changes. I now use this framework to diagnose the differences in the drivers of pCO_2 variability for T09 and ORCA2LP outputs (Fig. 3.6c–f).

In the Sub-Antarctic zone, this framework shows that for T09 observations, the seasonal cycle of dDIC/dt is almost always completely outside the critical $|(dDIC_T/dt)_{SST}|$ thresholds (Fig. 3.6 c), while the opposite can be seen in the model output (Fig. 3.6 e). Model-derived dDIC/dt is mostly inside the $|(dDIC_T/dt)_{SST}|$ thresholds throughout the seasonal cycle (Fig. 6 e). This confirms that the annual cycle of modelled pCO_2 is primarily explained by the seasonal cycle of SST and that the influence of DIC is secondary. This explains the coherence of the seasonal cycle of SST and FCO_2 in Figs 3.2 b, d and 3.4 g). It suggests that the amplitude of the annual cycle of DIC in the model is too small and hence solubility changes mainly control the seasonal cycle of pCO_2 and FCO_2 in ORCA2LP.

In contrast, in the Antarctic zone both T09 and ORCA2LP show that DIC is the primary driver of the seasonal cycle of pCO_2 throughout the year, dDIC/dt variability is outside the thresholds of $|(dDIC_T/dt)_{SST}|$. Here solubility has a secondary influence. Although the model shows a weaker DIC control (average $|(dDIC_T/dt)_{SST}| - |dDIC/dt| \approx 2$ μmol kg^{-1} $month^{-1}$) with respect to T09 (average $|(dDIC_T/dt)_{SST}| - |dDIC/dt| \approx 6$ μmol kg^{-1} $month^{-1}$), overall the physical- biogeochemical dynamics of DIC variability are the primary drivers of the seasonal cycle of FCO_2 in both modelled and observed FCO_2.

3.4. Discussion

This chapter is framed by two challenges. Firstly, statistical correlation-based methods used to compare model outputs with data cannot diagnose the causes of the differences between them (Taylor, 2001). Secondly, while models show comparable mean annual CO_2 flux with observed estimates, the same is not observed for the seasonal cycles of CO_2 fluxes (Lenton et al. 2013). Here I have shown that the net sensitivity of pCO_2 to changes in the forcing of DIC and SST depends critically on how well the models reflect both the phasing and the magnitude of their seasonal cycles. In this case, I showed that the main cause of the model - data difference was that the seasonal dynamics in the ORCA2LP model did not adequately reflect the influence of summer productivity and winter entrainment on the seasonal amplitude of both DIC and TAlk. The smaller seasonal amplitude of DIC in the model resulted in it being below the threshold necessary to override the influence of temperature on the seasonal flux of CO_2. As a result, the modelled seasonal cycle of pCO_2 shifted from being driven predominantly by seasonal DIC to being controlled mainly by SST. This probably explains the differences in the phasing of the seasonal variability of FCO_2 between the model and T09 data. I now discuss how the model's limitations in processes linked to summer primary production and winter convective entrainment may have influenced the seasonal cycle bias of $dpCO_2$ and FCO_2 .

3.4.1. Summer phase of the seasonal cycle: primary production

The seasonal cycle of chlorophyll highlights important contrasts between the model and observations, which may have a bearing in explaining the pCO_2 seasonal cycle anomalies during the spring-summer-autumn period (Figs 3.2 f and 3.3 f). It was found that while the magnitudes of the chlorophyll spring-summer bloom are comparable in the model and data in Sub-Antarctic (Figs. 2f and 3f), chlorophyll peaks a month early (Oct) in ORCA2LP. The implication of the early bloom peak in the model is that it coincides with the early winter - spring transition, when the rate of temperature

change is increasing (Figs 3.2 f and 3.6 a). Once again this is a rate of change rather than a mean concentration problem. The plot in Fig. 3.6 e shows that as the model dDIC/dt emerges out of winter and primary productivity increases after bloom initiation, it moves the trend almost out of the thermal threshold space, but the rate of warming (dSST/dt) then increases further and maintains the thermal control of pCO_2 (Fig. 3.6 e). But as dSST/dt increases to a peak in January, the modelled productivity declines rapidly, weakening dDIC/dt, which then sustains thermal control (Fig. 3.6 e).

To explore how ORCA2LP represent biological processes, I compare modelled chlorophyll model output with satellite chlorophyll from Johnson et al. (2013). It is crucial to note that although this dataset provided one of the most improved satellite products for the Southern Ocean, satellite chlorophyll is still prone to uncertainties mostly associated with cloud covering and spatial covering due the rotation of the earth and the sun (Brandt and Spiegel, 2014). For example, I here neglected winter datasets for this analysis because satellite cannot see south of 45°S in winter due to the sun angle. seasonal cycle of chlorophyll in Fig. 3.2 f shows three features that are different with respect to the model: the bloom initiation is delayed by at least a month, the spring-summer bloom peaks 1 - 2 months later, and there is a post-bloom period of sustained elevated biomass that declines more gradually than the modelled seasonal cycle. The net effect of these three features is that for observations in the summer, the threshold dDIC/dt is mostly > $|(dDIC_T/dt)_{SST}|$ (Fig. 3.6c). In the Antarctic zone, there is greater coherence in the seasonal phasing of chlorophyll in the summer to autumn period (Fig. 3.3f). The major difference between the Antarctic and the Sub-Antarctic zone in the model outputs is that in the former the post-summer bloom peak declines slower and at a comparable rate to the seasonal cycle of observed chlorophyll (Figs 3.2 f and 3.3 f). Because of this sustained summer bloom, both modelled and observed dDIC/dt are outside thermal control, confirming that in the Antarctic zone, the spring - autumn part of the seasonal cycle of pCO_2 is largely regulated by the seasonal cycle of DIC.

This analysis highlights that the phasing of the spring-summer-autumn bloom and the lack of sustained post-bloom period in the Sub-Antarctic zone is a challenge for the model. Different dynamics may explain the early, middle and late phases of the seasonal cycle of primary production. The timing and the mechanisms that explain observation-based bloom initiation and late summer persistence in the Southern Ocean have been explored in a number of recent studies (Thomalla et al. 2011, 2015; Swart et al. 2014). The interaction of storms with mesoscale and sub-mesoscale features emerged as key aspects in explaining the onset and evolution of spring - summer blooms and their sustainability, through their regulation of light limitation and dissolved iron (dFe) supply (Thomalla et al. 2011, 2015; Swart et al. 2014; Tagliabue et al. 2014, 2016).

However, these fine-scale dynamics are absent in the 2°x2° model configurations such as the ORCA2LP, where the phasing could be controlled either by the physics (MLD and its control of light limitation and dFe supply) or by the functionality (iron, nutrient, light limitation functions) of the phytoplankton model in PISCES that regulate the sensitivity of growth limitation. Recent work has examined these kinds of bloom phasing problems through reparameterization of the phytoplankton model (Li et al., 2010; Rodgers et al., 2014) and the physics, adapting an ad hoc enhanced wind-stirring parameterization to match the phasing of summer MLDs (Rodgers et al. 2014). The latter study found that the enhanced wind-stirring parameterization reduces the MLD shoaling rate, which delays the start of the bloom by a month.

Our work supports Rodgers et al. (2014) in that, to address the phasing problem with the initiation and phasing of the summer bloom in the Southern Ocean, attention should focus on improving the parameterization of the PISCES 3.4 phytoplankton model. Our findings suggest that, though the model reproduces summer MLDs in the Sub-Antarctic zone (phasing MLD comparable to Rodgers et al. (2014)), it still does not resolve the FCO_2 seasonal cycle as in Rodgers et al. (2014). This analysis suggests that adapting the Li et al. (2010) growth rate equation in PISCES, as in Rodgers et al. (2014), might play an important role in the improvement of FCO_2. However, our analysis also suggests that a significant part of the problem lies in the inability of the model to sustain the blooms through the summer in the Sub-Antarctic zone part of the Southern Ocean (Fig. 3.2 f). This is the single biggest difference between the model- and observation-based pCO_2 and FCO_2 (Figs 3.2 and 3.3a, b).

3.4.2. Winter phase of the seasonal cycle: deep entrainment of DIC

The winter end of the seasonal cycle of surface ocean DIC and TAlk is largely regulated by the depth of convective mixing that entrains DIC-rich waters, the magnitude of which depends on the DIC profile in the upper 500m. Deep winter MLDs are known to induce entrainment of high-DIC waters from below the thermocline. This typically increases surface concentrations of CO_2, which then weakens or reverses the CO_2 in-gassing flux (Bakker et al., 2008; Metzl et al., 2006a). Our analysis shows that for the model outputs in the Sub-Antarctic zone, the rate of change of DIC (dDIC/dt) over the winter phase (Jun - Sept) of the seasonal cycle is marginally at the boundary of thermal control (dDICT/dt) (Fig. 3.6 e). This suggests that the rate of entrainment linked to the winter deepening of the MLD is not sufficient to enable DIC to control this phase of the seasonal cycle of pCO_2. In sharp contrast, for the observations the seasonal cycle of dDIC/dt is well outside the thermal control threshold (Fig. 3.6 c).

Note that the difference probably does not lie with the depth of the winter MLD because the model MLD winter is actually deeper than in observations (Fig. 3.2 b). Rather, the explanation may lie in the

DIC profile of the ocean interior in the Southern Ocean (Fig. 3.7). The DIC profiles depicted in Fig. 3.7 highlight differences between modelled DIC profile (blue) and observed DIC profile (black) in the Sub-Antarctic zone (≈ 100 µmol kg^{-1} ,Fig. 3.7). The GLODAP DIC vertical profile in the Sub-Antarctic zone shows an increase of DIC with depth from 20 m to 400 m, ranging from 2060 $\mu molkg^{-1}$ to 2130 µmol kg^{-1}, consistent with previous studies (Hauck et al., 2015; J L Sarmiento and Gruber, 2006). In contrast, the weak modelled vertical winter DIC profile in the Sub-Antarctic zone explain the smaller dDIC/dt magnitudes. In the case of the Antarctic zone, the mean modelled DIC profile is much higher, probably reflecting the stronger impact of upwelling of DIC-rich CDW (Fig. 3.7). This is consistent with our analysis showing that in the Antarctic zone, the winter phase of the seasonal cycle of dDIC/dt is outside the thermal control threshold. Thus the seasonal cycle of FCO_2 phasing is comparable with observation estimates for most of the year (Mar- Sept), though the dDIC/dt rates are lower in ORCA2LP (Fig. 3.6 d,f).

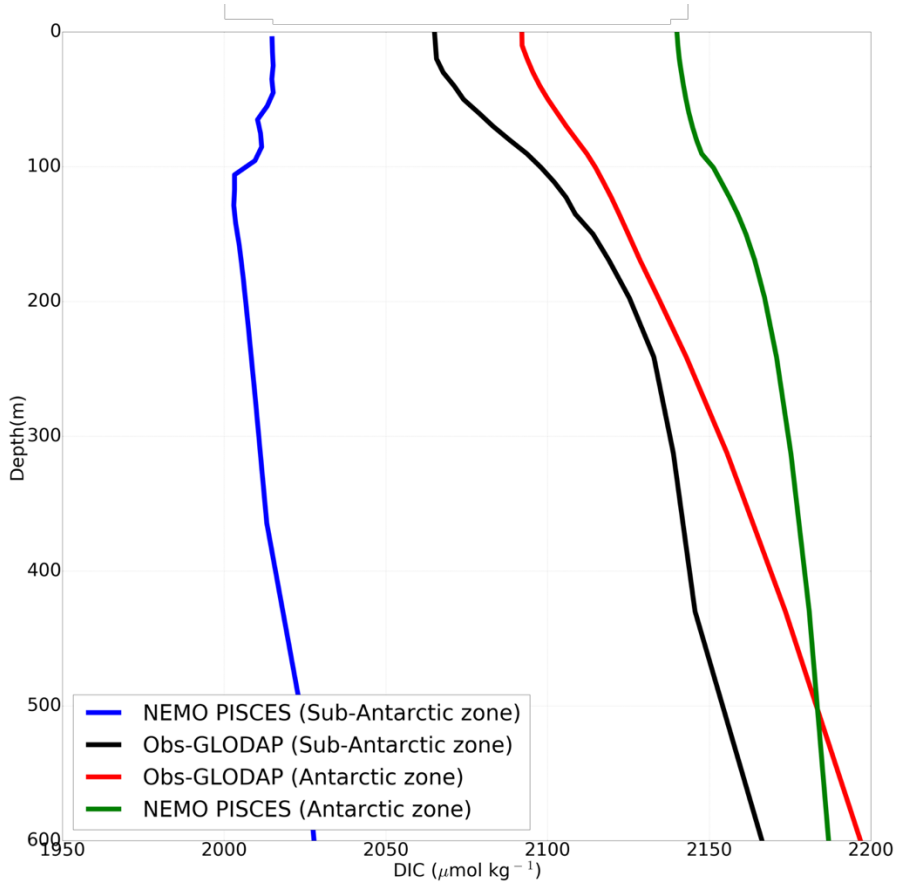

Figure. 3.7 DIC vertical profiles (µmol kg^{-1}) from observations (Global Ocean Data Analysis Project, GLODAP) and the NEMO-PISCES model in the Sub-Antarctic Zone and in the Antarctic Zone . These reveal that, particularly in the SAZ, the DIC concentrations are significantly lower in the model than observations, which then reduces the magnitude of the winter entrainment fluxes.

This analysis helps to explain why the winter phase of the seasonal cycle of FCO_2 is driven by thermal (SST cooling and warming) control, rather than by the large changes in the surface DIC reservoir linked to winter convective entrainment (Fig. 3.2 a, b).

3.4.3. Limitations

In undertaking this analysis, I am mindful of the potential limitations of making these comparisons with a global dataset (Takahashi et al., 2009) that is compiled on the basis of a number of well-established assumptions to attempt to overcome its spatial and temporal limitations, particularly in the Southern Ocean (Takahashi et al. 2009, 2012; Majkut et al. 2014). It is worth mentioning that among other uncertainties, datasets used in T09 are biased towards summer due to limited in situ measurements in the winter Southern Ocean (Fay et al., 2018; Gregor et al., 2018). This is a significant limitation in the dataset; T09 suggests that it may add up to 25% uncertainty overall. Thus, it is possible that winter estimated fluxes may not capture observed dynamics adequately in the Southern Ocean. For example, a recent study based on SOCCOM biogeochemical floats measurements by Gray et al. (2018) found a controversial significantly larger winter CO_2 outgassing flux than suggested by these datasets, however, even these have an unknown uncertainty in the calculation of pCO_2 from pH and derived Total Alkalinity.
Nevertheless, it is worth highlighting that the T09 data estimates are comparable with the data products based on the most recent available measurements (i.e. Landschützer et al. 2014 and Gregor et a., 2017). Although the comparison of multiple data products such as T09 with Landschützer et al. (2014) and Gregor et a., (2017) does not validate them, their correlation in the seasonal and annual magnitudes of CO_2 shows convergence . It is also possible that they all have the same bias from the lack of winter data. Overall, it is widely recognized that uncertainties linked to data sparsity in the Southern Ocean are significant and unconstrained in these data products, and other biases may be introduced due to spatial smoothing algorithms used to cope with the lack of data (e.g. Fay et al., 2018; Gregor et al., 2018). Uncertainties linked to the sparsity and data aliasing of observations in the Southern Ocean also apply to the GLODAP data product, hence vertical DIC profiles used are also subject to the same caution on their uncertainties (Lauvset et al., 2016).

Moreover, I am cautious about the impact that the choice of mean dynamic boundaries could have on the framework in the Southern Ocean. I selected mean dynamic boundaries (Orsi et al., 1995), but alternative water mass outcrop-based definitions could have been used (Iudicone et al., 2011; Séférian et al., 2012b).

3.5. Conclusion

In this study set out to develop a diagnostic framework to diagnose apparent biases between models and observations of the seasonal cycle of FCO_2 in the Southern Ocean.

This analyses exploited clear differences in the phasing and magnitude of the zonally averaged Sub-Antarctic and Antarctic zone seasonal cycle of the FCO_2 between observations (T09) and model (ORCA2LP) outputs. The results showed what aspects of the model dynamics affect the magnitude of the seasonal cycle of DIC, and how these influence the magnitude and phasing of the seasonal cycle of FCO_2 in the Southern Ocean. This approach has proven useful isolating key differences in processes driving FCO_2 seasonal cycle between modelled and observed values.

In this case of ORCA2LP, I demonstrated that the key difference in the seasonal cycle of FCO_2 between the model and the T09 observations in the Sub-Antarctic lie in the underestimation of the seasonal cycle amplitude of DIC. This is particularly linked to underestimated primary production in summer and convective entrainment in winter. This work supports earlier studies suggesting that changes in the parameterization of the phytoplankton model may be essential to correct the differences in the onset and phasing of the spring- summer bloom (Rodgers et al. 2014). However, this analysis also highlights a part of the seasonal cycle of primary production where differences between observations and models may be even larger than the phasing of the spring bloom, post-bloom differences. It was found that the sustained summer production in observations is crucial to resolve observed biologically driven CO_2 changes (uptake) during the spring-summer seasons and thus the sharp decay of the bloom in ORCA2LP is problematic (Thomalla et al. 2011; Swart et al. 2014). This is less likely to be only a phytoplankton parameterization problem than a gap in mixed layer physics arising from the low resolution of the model. I propose that the approach used here could be complementary to already widely used statistical comparison methodologies (e.g. Taylor diagrams). Thus, I infer that this approach provides a diagnostic framework to examine model – observations biases in terms of the seasonality of FCO_2. In the next chapter, I use this diagnostic framework to diagnose sources of the seasonal cycle of FCO_2 biases in 10 CMIP5 models to isolate key constraints in EMS's ability to simulate the seasonal cycle of FCO_2 with respect to observed estimates

Chapter 4

The Seasonal Cycle of pCO_2 and CO_2 fluxes in the Southern Ocean: Diagnosing Anomalies in CMIP5 Earth System Models

4.1. Introduction

The Coupled Model Intercomparison Project (CMIP) is a globally concerted platform that harnesses global efforts in Earth system modelling for comparison and synthesis under agreed standards facilitated by the World Climate Research Program (WRCP), (Taylor et al., 2012). It provides results of earth system models and projection under different forcing scenarios for the Intergovernmental Panel on Climate Change (IPCC). As explained in the previous chapter, ESMs from the Intercomparison project version 5 (CMIP5) were found to show a limited skill in simulating the seasonal cycle of FCO_2 with respect to available observations estimates in the Southern Ocean (Anav et al., 2013b; Kessler and Tjiputra, 2016; a. Lenton et al., 2013; Majkut et al., 2014). Given that the seasonal cycle is the dominant model of variability for CO_2 in the Southern Ocean (Lenton et al., 2012), this is a significant bias. Some studies suggest that this might be a key limitation to CMIP5 ESMs ability to appropriately simulate long-term changes in the Southern Ocean sink of CO_2 and related climate sensitivities (e.g. Lenton et al., 2013). Thus, the need to understand the sources of these biases.

Efforts to improve simulations of CO_2 properties with respect to observations in the Southern Ocean is have been made using forced ocean models (e.g. Pasquer et al. 2015; Rodgers et al. 2014; Visinelli et al. 2016; Rosso et al. 2017). However, reconciling models with observations remains a challenge for fully coupled simulations. In the previous chapter, a diagnostic framework was developed to evaluate the seasonal characteristics of the drivers of modelled FCO_2 was developed (Mongwe et al. 2016). This chapter explores this approach further with 10 CMIP5 models and the data product estimates based on the lasted available data in the Southern Ocean. This chapter investigates processes leading to main biases responsible for the CMIP5 model's limited skill in resolving observed seasonal properties of FCO_2 in the Southern Ocean. This work has been published in the

Biogeosciences journal and also as part of the 10th International Carbon Dioxide Conference (ICDC10) special issue (Mongwe et al., 2018).

4.2. Methods

The Southern Ocean is here defined as south of the Sub-Tropical Front (STF) and boundaries are defined as described in the methodology chapter (Fig. 2.4). Below is a brief description of the datasets, expanded in chapter 2.

4.2.1 Observations datasets

The Landschützer et al. (2014) data product (FCO_2 and partial pressure of CO_2 (pCO_2) was used as the main suite of observations-based estimates against which to compare the models throughout the analysis. The Landschützer et al. (2014) dataset is synthesized from Surface Ocean CO_2 Atlas version 2 (SOCAT2) observations and high-resolution winds using a Self-Organizing Map (SOM) through a Feed Forward Neural Network (FNN) approach (Landschützer et al. 2013). The Takahashi et al. (2009) dataset was also used as a complementary source for comparison of spatial FCO_2 properties in the Southern Ocean. Using monthly mean Sea Surface Temperature (SST) and salinity from the World Ocean Atlas 2013 (WOA13) dataset (Locarnini et al. 2013), I reconstructed total alkalinity (TAlk) using the Lee et al. (2006) formulation. As done in the previous chapter, the computed monthly TAlk and pCO_2 from Landschützer et al. (2014) were used to compute Dissolved Inorganic Carbon (DIC) using CO2SYS (Pierrot et al. 2006, http://cdiac.ornl.gov/ftp/co2sys/CO2SYS_calc_XLS_v2.1), using K1, K2 from Mehrbach et al. (1973) refitted by Dickson and Millero (1987). For interior ocean DIC, I used the Global Ocean Data Analysis Project version 2 (GLODAP2) annual means dataset (Lauvset et al., 2016). The Mixed Layer Depth (MLD) data was taken from de Boyer Montégut et al. (2004), on a 1^o x 1^o grid consisted with the previous chapter, the data is provided as monthly means climatology and was used as provided. I also use the satellite chlorophyll dataset from Johnson et al. (2013).

4.3. Results

4.3.1 Climatological sea-air CO_2 fluxes: spatial characteristics

The annual mean climatological distribution of FCO_2 in the Southern Ocean obtained from observational products is spatially variable, but mainly characterized by two key features: (i) CO_2 in-gassing north of 50°-55°S (Polar Frontal Zone, PFZ) within and north of the Sub-Antarctic Zone, and (ii), CO_2 out-gassing between the PF (~ 58°S) and the Marginal Ice Zone (MIZ, ~ 60° - 68°S) (Fig. 1 a-b). Most CMIP5 models broadly capture these features, however, they also show significant differences in space and magnitude between the basins of the Southern Ocean (Fig. 4.1). With the exception of CMCC, which shows a northerly-extended CO_2 out-gassing band between about 40°S and 50°S, CMIP5 models generally show the CO_2 out-gassing zone between 50°S- 70°S in agreement with observational estimates (Fig. 4.1).

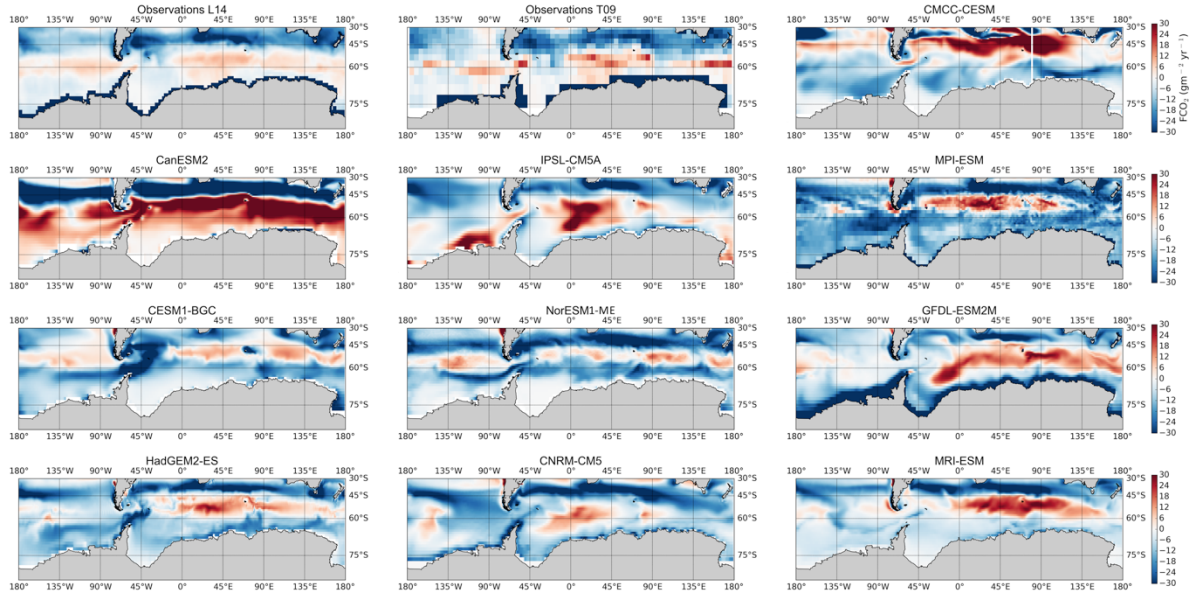

Figure. 4.1: The annual mean climatological distribution Sea-Air CO_2 Flux (FCO_2, in gC m^{-2} yr^{-1}) for observations (L14: Landschützer et al., 2014 and T09: Takahashi et al., 2009) and 10 CMIP5 models from 1995 - 2005. CMIP5 models broadly capture the spatial distribution of FCO2 with respect to L14 and T09; however, they also show significant differences in space and magnitude between the basins of the Southern Ocean with a few exceptions.

The analyzed 10 CMIP5 models show a large spatial dispersion in the spatial representation of the magnitudes of FCO_2 with respect to observational estimates (Fig. 4.1, Table 4.2). They generally overestimate the upwelling-driven CO_2 out-gassing (55°S -70°S) in some basins relative to observations. IPSL, CanESM2, MPI, GFDL and MRI for example, show CO_2 out-gassing fluxes reaching up to 25 g m^{-2} yr^{-1}, while observations only show a maximum of 8 g m^{-2} yr^{-1} (Fig. 4.1). Between 40°S- 56°S (Sub-Antarctic Zone), observations and CMIP5 models largely agree, showing a CO_2 in-gassing feature, which is mainly attributable to biological processes (McNeil et al. 2007; Takahashi et al. 2012). South of 65°S, in the MIZ, models generally show an excessive CO_2 in-gassing with respect to observations (with the exception of CanESM2, IPSL and CNRM). Note that as much as this bias south of the MIZ might be a true divergence of CMIP5 models from the observed ocean, it is also possibly due to the paucity of observations in this region, especially during the winter season (Bakker et al. 2014; Monteiro, 2010).

Table 4.2: Sea-Air CO_2 fluxes (Pg C yr^{-1}) annual mean uptake for the climatology over 1995 – 2005 for models and 1998 – 2011 for observations. The uncertainty is here defined as the standard deviation of the temporal variability over these periods. The Southern Ocean here defined as south of the Sub-tropical front, Sub-Antarctic zone (second column) and Antarctic zone (third column). The third and fourth column shows the Pattern Correlation Coefficient (PCC) and Root Mean Square Error (RMSE) for the whole Southern Ocean for each model. Observations here refer to Landschützer et al., 2014 (L14).

MODEL	SOUTHERN OCEAN	SUB-ANTARCTIC ZONE	ANTARCTIC ZONE	PCC	RMSE
CNRM-CM5	-0.823±0.003	-0.682±-0.002	-0.122±0.001	0.44	17.9
GFDL-ESM2M	-0.161±0.005	-0.074±0.004	-0.077±0.002	0.43	8.47
IPSL-CM5A-MR	-0.496±0.003	-0.582±0.006	0.101±0.003	0.53	10.5
CESM1-BGC	-0.532±0.006	-0.132±0.003	-0.385±0.004	0.47	9.15
CANESM2	-0.058±0.008	-0.720±0.006	0.661±0.004	0.54	19.5
CMCC-CESM	0.121±0.006	0.367±0.004	-0.225±0.003	-0.09	17.9
MRI-ESM	-0.048±0.002	0.022±0.003	-0.070±0.001	0.36	15.6
HADGEM2-ES	-0.489±0.005	-0.284±0.003	-0.197±0.001	0.55	10.9
MPI-ESM-MR	-0.870±0.006	-0.530±0.002	-0.326±0.002	0.37	9.87
NORESM1-ME	-0.669±0.004	-0.412±0.003	-0.270±0.002	0.60	8.96
OBSERVATIONS (L14)	-0.253±0.3	-0.296±0.3	0.053±0.3		

The Pattern Correlation Coefficient (PCC) and the Root Mean Square Error (RMSE) for the analyzed models are given in Table 4.2, which are here used to quantify the models' spatial and magnitude performances against the Landschützer et al. (2014) data product. Out of the 10 models, six show a

moderate spatial correlation with Landschützer et al. (2014), (PCC = 0.40 – 0.60), i.e. CNRM, GFDL, HadGEM2, IPSL, CESM1, NorESM1 and CanESM2. While MPI (PCC = 0.37), MRI (PCC = 0.36) and CMCC (PCC = -0.09) show a weak to null spatial correlation with observations, the latter is mainly due to the overestimated out-gassing region. Spatially, GFDL and NorESM1 are the most comparable to Landschützer et al. (2014), (RMSE < 9), while CCMC CanESM2, MRI and CNRM show the most differences (RMSE > 15). The rest of the models show a modest comparison (RMSE 9 - 11).

NorESM1 and CESM1 are the only two of the 10 models showing a consistent spatial (REMSE < 9) and magnitude (PCC ≈ 0.50) performance. From Table 4.2, it is evident that an appropriate representation of the spatial properties of FCO_2 with respect to observations does not always correspond to comparable magnitudes. CanESM2 for example, shows a good spatial comparison (PCC = 0.54), yet a poor estimation of the magnitudes (RMSE = 19.5). In this case this is caused by overestimation of CO_2 uptake north of 55ºS (≈ - 28 g m^{-2} yr^{-1}) and CO_2 out-gassing (> 25 g m^{-2} yr^{-1}) in the Antarctic zone, resulting in a weak net total annual sink (-0.05 Pg C m^{-2} yr^{-1}) for the Southern Ocean.

4.3.2 The variability and biases of the seasonal cycle of sea-air CO_2 fluxes

The seasonal cycle of FCO_2 is shown in Fig. 4.2. The seasonality of FCO_2 in the 10 CMIP5 models shows a large dispersion in both phasing and amplitude, but mostly disagrees with observations in the phase of the seasonal cycle while also diverging from one another. This discrepancy is consistent with the findings of Anav et al. (2013), who, however used fixed latitude criteria. Based on the phasing, the seasonality of FCO_2 in CMIP5 models can be a priori divided in two main groups based on their seasonal cycle phasing: group-DIC models, comprising of MPI, HadGEM2 and NorESM1, and group-SST models, the remainder, GFDL, CMCC, CNRM, IPSL, CESM1 MRI and CanESM2 (Fig. 4.3). The naming convention is suggestive of the mechanism driving the seasonal cycle, as will be clarified below. A similar grouping was also identified by Kessler and Tjiputra (2016) using a different criterion. The seasonal cycle of FCO_2 of an equally-weighted ensemble of the two groups of models compared to observations is shown in Fig. 4.3; the shaded area represents the decadal standard deviation of the models and the standard deviation of the Landschützer et al. (2014) data product for 1998-2014, in the various regions.

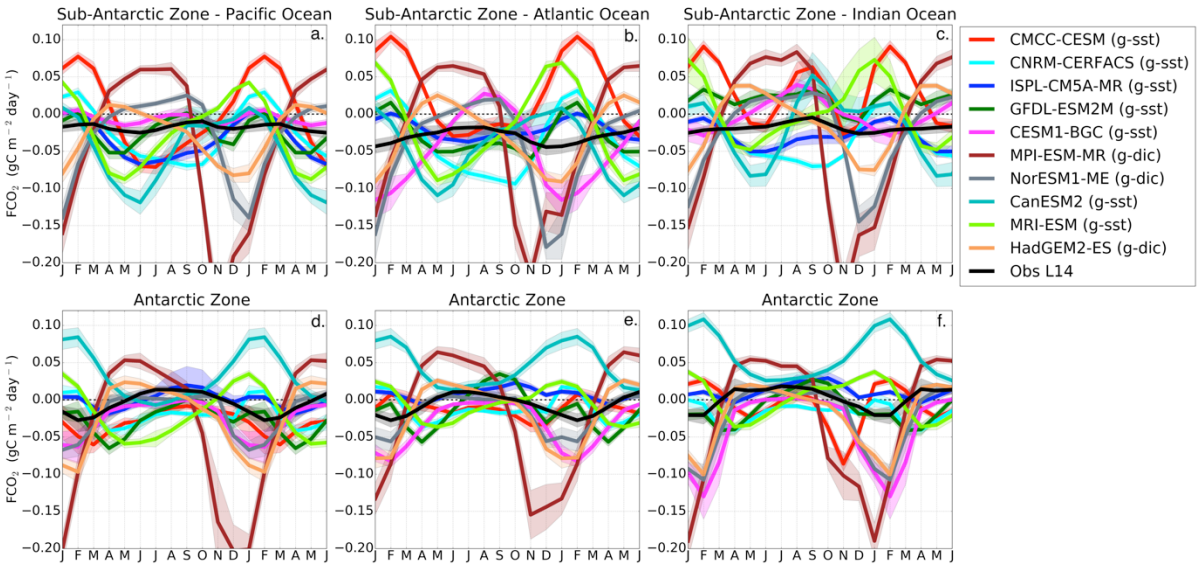

Figure. 4.2: Seasonal cycle of Sea-Air CO_2 Flux (FCO_2, in gC m^{-2} yr^{-1}) in observations and 10 CMIP5 models in the Sub-Antarctic and Antarctic zones of the Pacific Ocean (first column), Atlantic Ocean (second column) and Indian Ocean (third column). The shaded area shows the temporal standard deviation over the considered period (1995 – 2005), g-sst and g-dic shows the clustering of CMIP5 models into group-SST and group-DIC as shown in Fig. 3 (section 3.2).

In the Sub-Antarctic Zone, the Landschützer et al. (2014) product shows a weakening of CO_2 uptake during winter (less negative values in June-August) with values close to zero at the onset of spring (September) in all three basins. Similarly, during the spring season, all three basins are seen to maintain a steady increase of CO_2 uptake until mid-summer (December), while they differ during autumn (March-May). The Pacific basin shows an increase in CO_2 uptake during autumn that is not observed in the other basins (only marginally in the Indian zone). More quantitatively, CMIP5 models show weak to negative correlations with the Landschützer et al. (2014) data product in the Sub-Antarctic Zone and have slightly higher correlations in the Antarctic Zone (Fig. 4.4). In the Antarctic zone, the observed FCO_2 seasonal cycle is mostly similar in all three basins (Fig. 4.4 d-f). While this seasonal cycle consistency may suggest spatial uniformity of the mechanisms of FCO_2 at the Antarctic, it is also possible that this may be due to a result of the paucity of observations in this area. In the Antarctic Zone, all three basins show a weakening of uptake or increasing of out-gassing from the onset of autumn (March) until mid-winter (June–July). The winter CO_2 out-gassing is followed by a strengthening of the CO_2 uptake throughout spring to summer, when it reaches a CO_2 in-gassing peak.

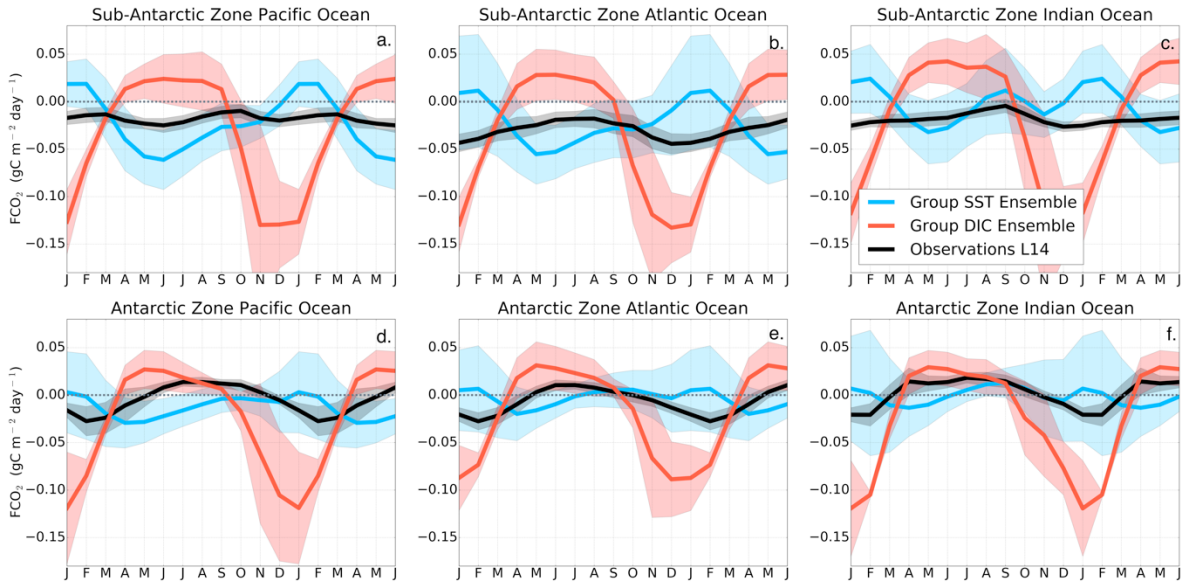

Figure. 4.3. Seasonal cycle of the equally-weighted ensemble means of FCO_2 (gC m^{-2} yr^{-1}) from Fig. 2 for group DIC models (MPI-ESM, HadGEM-ES and NorESM) and group SST models (GFDL-ESM2M, CMCC-CESM, CNRM-CERFACS, IPSL-CM5A-MR, CESM1-BGC, NorESM2, MRI-ESM and CanESM2). The shaded areas show the ensemble standard deviation. The black line is the Landschützer et al. (2014) observations.

The differences in the seasonal cycle of FCO_2 across the three basins of the Sub-Antarctic Zone found in the observational product (Fig. 4.2) are probably a consequence of spatial differences seen in Fig. 4.1. To verify this, the correlation between the seasonal cycles from the Landschützer et al. (2014) observational product was calculated in the three basins (Fig. 4.5). The FCO_2 seasonal cycle in the Sub-Antarctic Atlantic and Indian basins are similar (R = 0.8), while the other basins are quite different from one another (R = -0.1 for Pacific – Atlantic and R ~ 0.4 for Pacific – Indian). Contrary to the observational product, CMIP5 models show the same seasonal cycle phasing across all three basins in the Sub-Antarctic Zone (basin – basin correlation coefficients are always larger than 0.50 in Fig. 4.4 despite the spatial differences in Fig. 4.2, with the exception of three models (i.e. CMCC, CESM1 and GFDL). Thus, contrary to Landschützer et al. (2014), CMIP5 models shows zonal homogeneity in the seasonal cycle of FCO_2, which may suggest that the drivers of CO_2 are less regional. In the Antarctic Zone, CMIP5 models agree with observations in the spatial uniformity of the seasonal cycle of FCO_2 across the three basins.

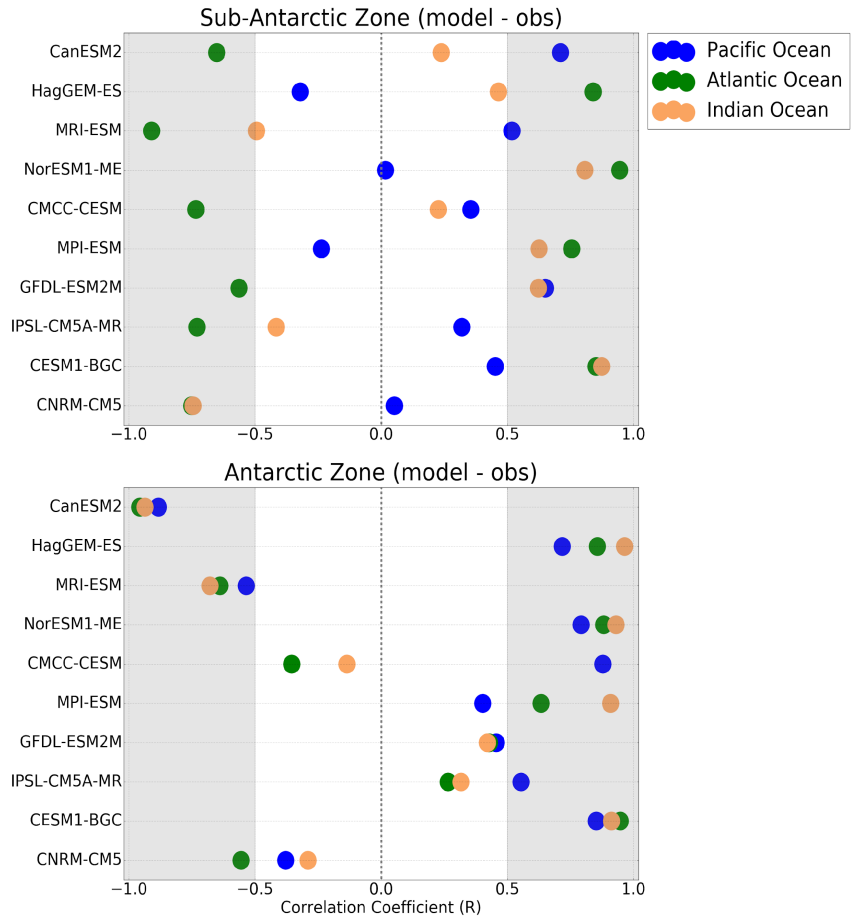

Figure. 4.4: The correlation coefficients (R) of the seasonal cycle of FCO_2 for observations (Landschützer et al., 2014) and CMIP5 models at the three basins of the Southern Ocean (i.e. Pacific, Atlantic and Indian) in the Sub-Antarctic (SAZ) and Antarctic Zone (AZ).

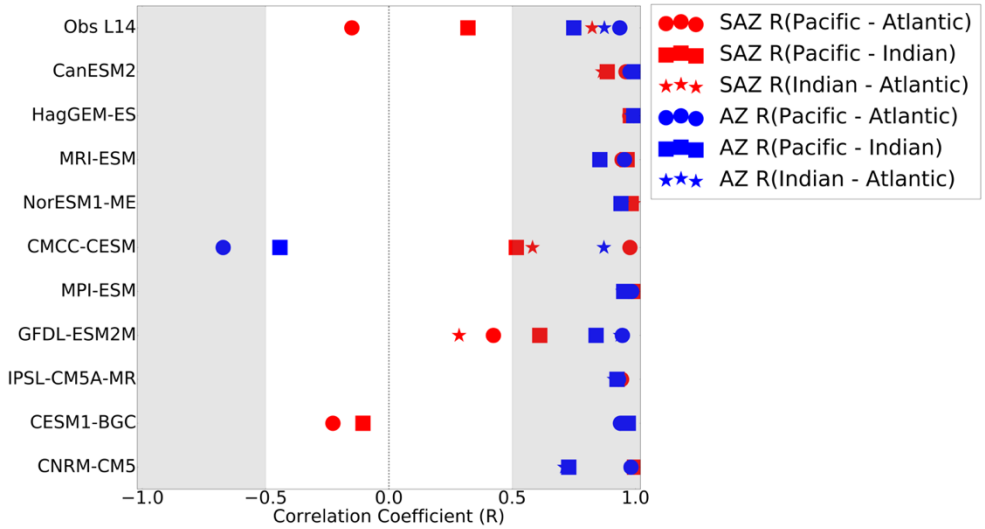

Figure. 4.5: The correlation coefficients (R) of basin – basin seasonal cycles of FCO_2 for observations (Landschützer et al., 2014) and 10 CMIP5 models in the three basins of the Southern Ocean i.e. Pacific, Atlantic and Indian basin.

Group-DIC models are characterized by an exaggerated CO_2 uptake during spring-summer (Fig. 4.3) with respect to observation estimates and CO_2 out-gassing during winter. These models generally agree with observations in the phasing of CO_2 uptake during spring but overestimate the magnitudes. It is worth noting that the seasonal characteristics of group-DIC models are mostly in agreement with the observations in the Atlantic and Indian basin in Sub-Antarctic Zone ($R > 0.5$ in Fig. 4.5). The large standard deviation (~ 0.01 g C m^{-2} day^{-1}) during the winter and spring-summer seasons in the Atlantic basin shows that, although group-DIC models agree in the phase, magnitudes vary considerably (Fig. 4.2 & 4.4b). For example, MPI reaches up to 0.06 g C m^{-2} day^{-1} out-gassing during winter, while HadESM2 and NorESM1 peak only at ~ 0.03 g C m^{-2} day^{-1}. Group-SST models on the other hand are characterized by a CO_2 out-gassing peak in summer (Dec-Feb) and a CO_2 in-gassing peak at the end of autumn (May), and their phase is opposite to the observational estimates in the Atlantic and Indian basins (Fig. 4.4 b, c). Group-SST models only show a strengthening of CO_2 uptake during spring in the Indian basin. Interestingly, group-SST models compare relatively well with the observed FCO_2 seasonal cycle in the Pacific basin, whereas group-DIC models disagree the most with the observed estimates (Fig. 4.4 a). This phasing difference within models and against observed estimates probably suggests that the disagreement in FCO_2 of CMIP5 models with observations is not a matter of a relative error/constant magnitude offset, but probably points to differences in the seasonal drivers of FCO_2.

In the Antarctic Zone (Fig. 4.4 d-f), both group-DIC and group-SST models perform better than in the Sub-Antarctic, in respect of phasing and amplitude, as shown by the correlation analysis in Fig. 4.3. Like in the Sub-Antarctic Zone, models reflect comparable pCO_2 seasonality in the different basins of the Antarctic zone to the observational products (Fig. 4.5, with the exception of MRI and CanESM2 where $R < 0$ for all three basins). Here FCO_2 magnitudes oscillate around zero with the largest disagreements occurring during mid-summer, where observation estimates show a weak CO_2 sink (≈ -0.03 gC m^{-2} day^{-1}), and group-SST show a zero net CO_2 flux and a strong uptake in group DIC (e.g. ≈ -0.12 gC m^{-2} day^{-1} in the Pacific basin). The large standard deviation (≈ 0.01 gC m^{-2} day^{-1}) here indicates considerable differences among models (Fig. 4.4 d-f).

4.3.3 Seasonal Scale Drivers of Sea-Air CO_2 Flux

How changes in temperature and DIC regulate surface pCO_2 and FCO_2 variability will next be examined at the seasonal scale following the method described in Section 2.3.1. Fig. 4.6 shows the monthly rates of change of SST (dSST/dt) for the 10 models compared with WOA13 SST. CMIP5 models generally show agreement in the timing of the switch from surface cooling ($dSST/dt < 0$) to

warming (dSST/dt > 0) and vice versa; i.e. March (summer to autumn), and September (winter to spring) respectively. In both the Sub-Antarctic and Antarctic Zone CMIP5 models agree with observations in this timing (Fig. 4.6). However, while they agree in phasing, the amplitude of these warming and cooling rates are overestimated with respect to the WOA13 dataset with the exception of NorESM1. Subsequently these differences in the magnitude of dSST/dt have important implications for the solubility of CO_2 in seawater; larger magnitudes of |dSST/dt| are likely to enhance the response of the pCO_2 to temperature through CO_2 solubility changes. For example, because the observations in the Indian basin show a warming rate of about 0.5ºC month^{-1} lower compared to the other two basins, a relatively weaker role of surface temperature in this basin is expected.

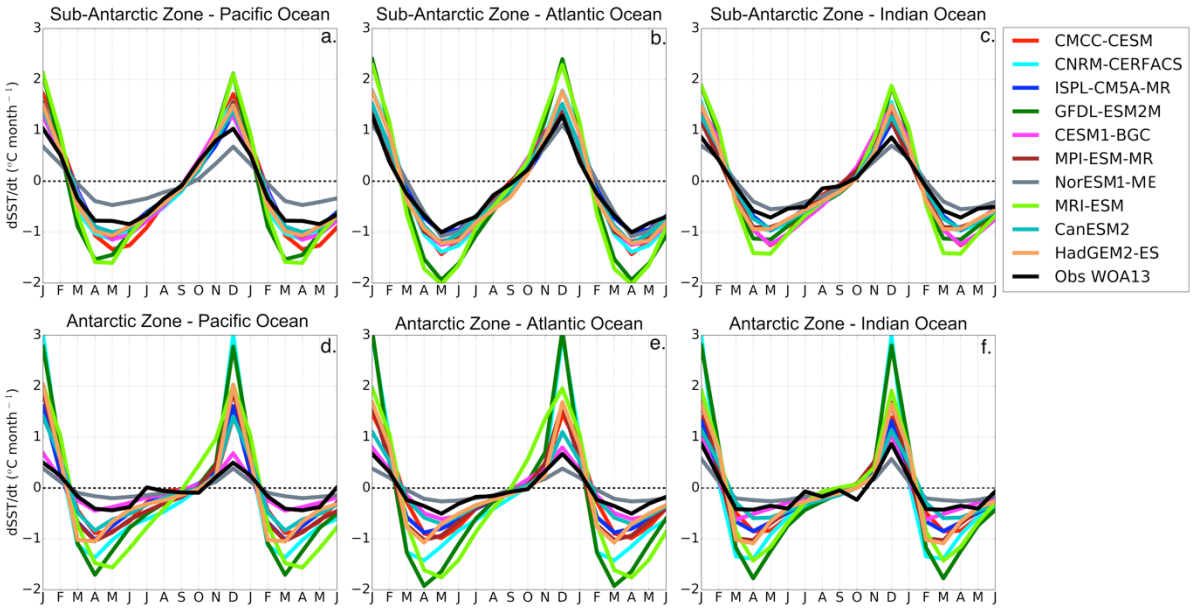

Figure. 4.6: Mean seasonal cycle of the estimated rate of change of sea-surface temperature (dSST/dt, ºC month^{-1}) for the Sub-Antarctic and Antarctic zones of the Pacific Ocean (first column), Atlantic Ocean (second column) and Indian Ocean (third column).

As described in Chapters 2 and 3, the computed dSST/dt magnitudes were used to estimate the equivalent change in DIC units by using the Revelle factor (Eq. 2.2). Hence the computed $dDIC_T/dt)_{SST}$ scale up surface CO_2 solubility changes into DIC units. Consequently, to examine the relative contribution of SST (solubility) and DIC changes (entrainment mixing and/or biological DIC changes) on surface pCO_2 (and FCO_2) instantaneous changes is done by comparing $|(dDIC_T/dt)_{SST}|$ vs. $(dDIC/dt)_{Tot}$. The seasonal cycle of $|(dDIC_T/dt)_{SST}|$ vs. $(dDIC/dt)_{Tot}$ for the 10 CMIP5 models analyzed and observations is shown in Fig. 4.7 for the Sub-Antarctic (Fig. 4.7 a) and Antarctic zone (4.7 b). The characteristics of $|(dDIC_T/dt)_{SST}|$ vs. $(dDIC/dt)_{Tot}$ in Fig. 4.7 shows two general outcomes. First, CMIP5 ESMs shows two main clusters with the two groups identified based on phasing in section 4.3.2 group-DIC and group-SST models). Group-DIC models show that $|(dDIC_T/dt)_{SST} < (dDIC/dt)_{Tot}$

for most of the year, while group-SST models show $|(dDIC_T/dt)_{SST}|$ and $(dDIC/dt)_{Tot}$ magnitudes. Thus, the DIC driver (entrainment and/or biological DIC changes) plays a dominate role in the seasonal variability of surface pCO_2 for the most part in group-DIC models, yet the same is not true for group-SST models especially in the Sub-Antarctic zone (Fig. 4.7 a). Second, group-SST models generally show $|(dDIC_T/dt)_{SST}| > (dDIC/dt)_{Tot}$ for the first three-five months of the year (Fig 4.7 b), implying a consistent solubility dominance in surface pCO_2 changes between mid-summer and mid-late autumn (Jan – Apr/May), (Fig. 4.7a). To investigate these in detail, the computed $M_{T\text{-}DIC}$ $\left(\left|\left(\frac{\partial DIC_T}{\partial t}\right)_{SST}\right| - \left|\left(\frac{\partial DIC}{\partial t}\right)_{Tot}\right|\right)$ is constrained to seasonal means for visual purposes (Fig. 4.8). These are shown in Fig. 4.8, in this figure increase in the positive direction (increasing red color intensity) signifies the strengthening solubility driver and the negative direction (increasing blue color intensity), the DIC driver.

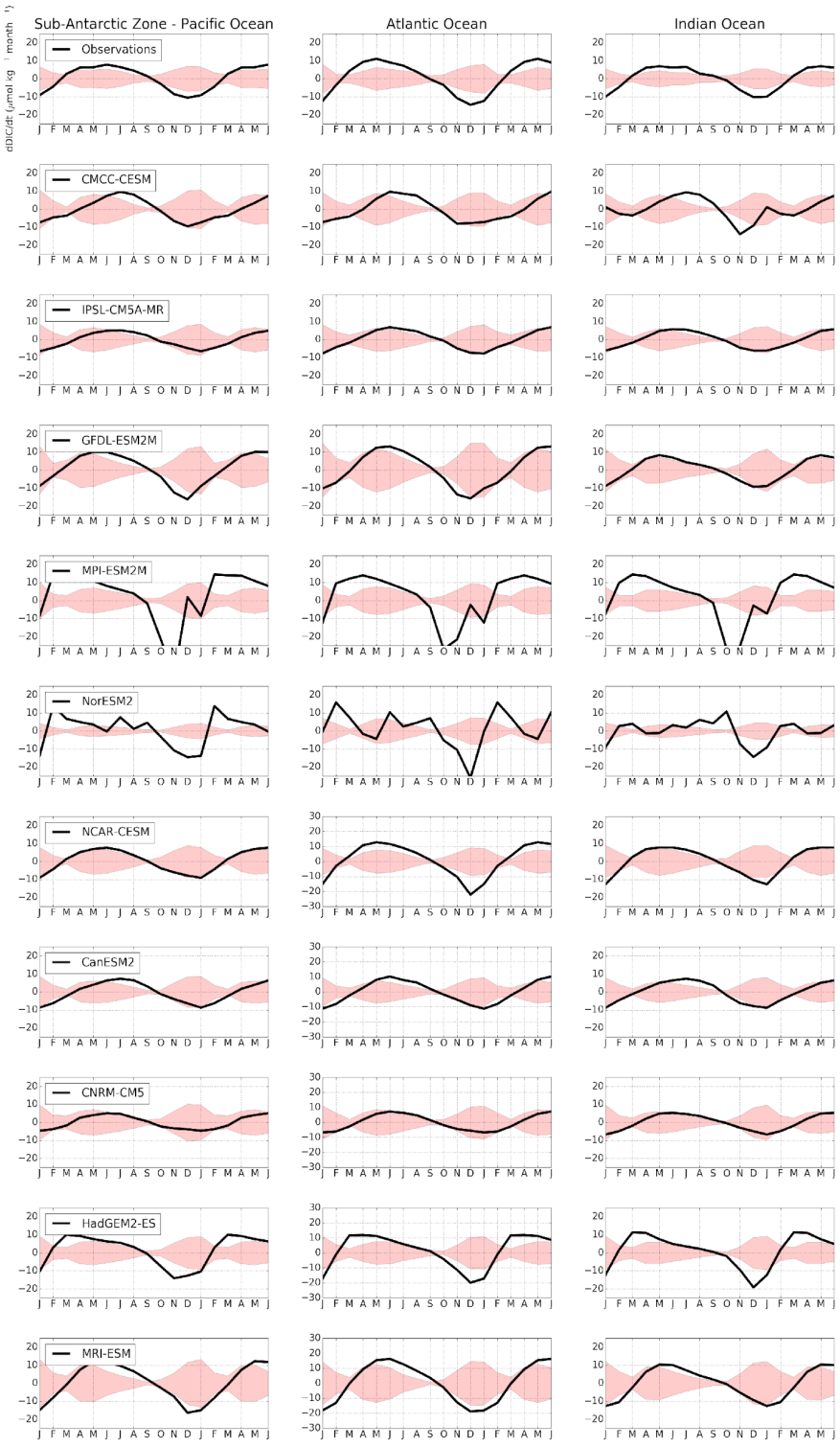

Figure. 4.7a. Seasonal cycle of the rate of change of DIC $\left(\frac{\partial DIC}{\partial t}\right)_{Tot}$, black line and the estimated maximum DIC variability equivalent driven by temperature $\left(\frac{\partial DIC}{\partial t}\right)_{SST}$ *shaded area*, for monthly data given in µmol kg^{-1} month^{-1} at the Sub-Antarctic zone i.e. Pacific Ocean (first column), Atlantic Ocean (second column) and Indian Ocean (third column). The estimated equivalent temperature driven solubility DIC changes (shade area) is compared to the total surface rate of change (black line) such that when $\left|\left(\frac{\partial DIC}{\partial t}\right)_{SST}\right| > \left(\frac{\partial DIC}{\partial t}\right)_{Tot}$, the role of temperature

dominates instantaneous pCO_2 variability and conversely when $\left|\left(\frac{\partial DIC}{\partial t}\right)_{SST}\right| < \left(\frac{\partial DIC}{\partial t}\right)_{Tot}$, DIC process are is the dominant mode of instantaneous pCO_2 changes.

Fig. 4.7b: Same as Fig. 2a for the Antarctic zone

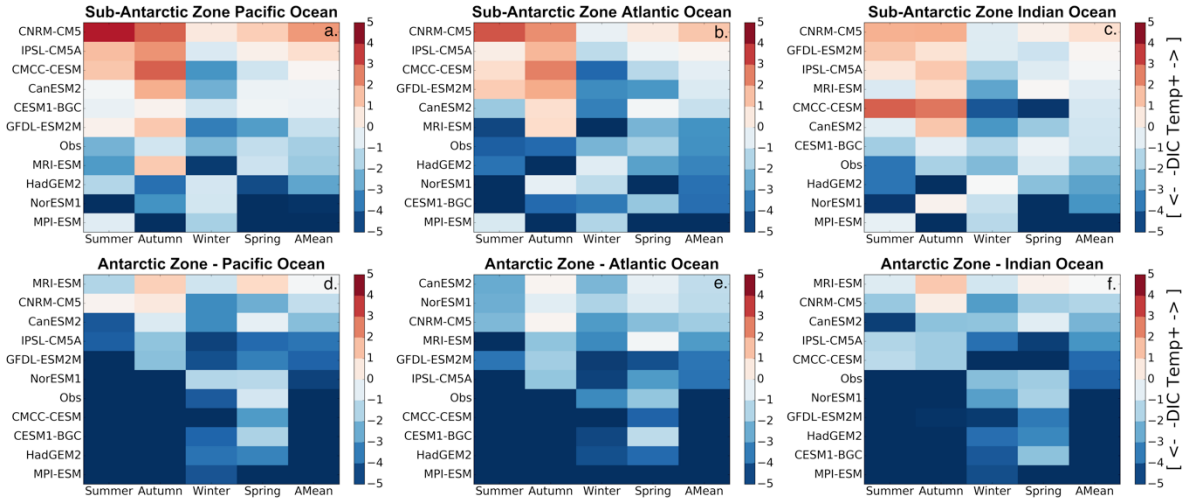

Figure. 4.8: Mean seasonal and annual values of the DIC–temperature control index ($M_{T\text{-}DIC}$). The increase in the red color intensity indicates increase in the strength of the temperature driver and the blue intensity shows the strength of the DIC driver. The models are sorted according to the annual mean value of the indicator presented in the last column (Amean).

According to the $M_{T\text{-}DIC}$ magnitudes in Fig. 4.8, the seasonal cycle of pCO_2 in the observational estimates is predominantly DIC-driven most of the year in both the Sub-Antarctic and Antarctic Zone. However, note importantly that during periods of high |dSST/dt|, i.e. autumn and spring, observations show a moderate to weak DIC control ($M_{T\text{-}DIC} \approx 0$). The Antarctic Zone is mostly characterized by a stronger DIC control (mean Annual $M_{T\text{-}DIC} > 3$) except for during the spring season (Fig. 4.6). Consistent with the similarity analysis presented in Fig. 4.5, the Antarctic Zone shows coherence in the sign of the temperature –DIC indicator ($M_{T\text{-}DIC} > 0$) within the three basins.

4.3.4 Source terms in the DIC surface budget

To further constrain the surface DIC budget (CH2, Eq. 2.4), the role of the biological source term is examined using chlorophyll and Net Primary Production (NPP) as proxies. The seasonal cycles of chlorophyll, NPP and the rate of surface DIC changes (dDIC/dt) are shown in Fig. 4.9. The observed seasonal cycle of chlorophyll (Johnson et al., 2013) shows a similar seasonal cycle within the three basins during the spring-summer seasons (autumn-winter data are removed due to the satellite limitation) in both the Sub-Antarctic and Antarctic Zones. Magnitudes are however different in the Sub-Antarctic Zone; the Atlantic basin shows larger chlorophyll magnitudes (chlorophyll reach up to 1.0 mg m^{-3}) compared to the Pacific and Indian Basins (Chl < 1 mg m^{-3}).

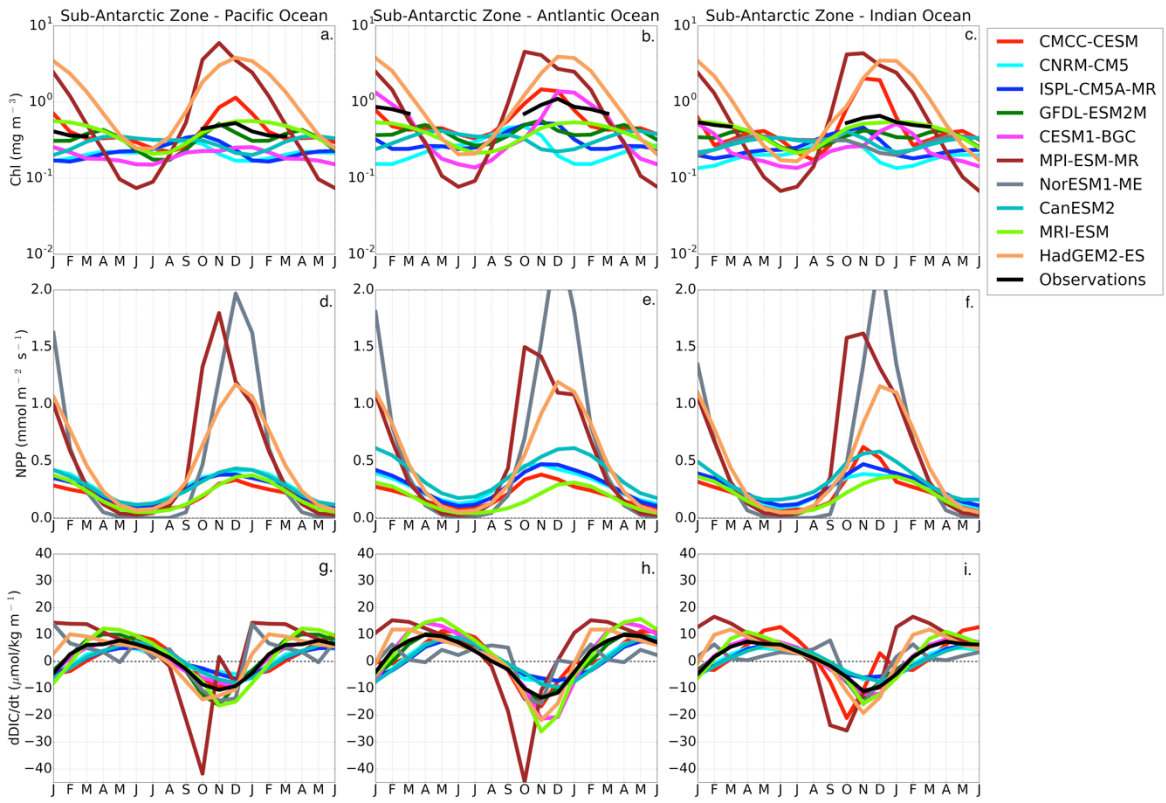

Figure. 4.9a: The seasonal cycle of chlorophyll (mg m^{-3}), Net Primary Production (mmol m^{-2} s^{-1}) and the surface rate of change of DIC (μmol kg^{-1} $month^{-1}$) in the Sub-Antarctic zone of the Pacific Ocean (first column), Atlantic Ocean (second column) and Indian Ocean (third column).

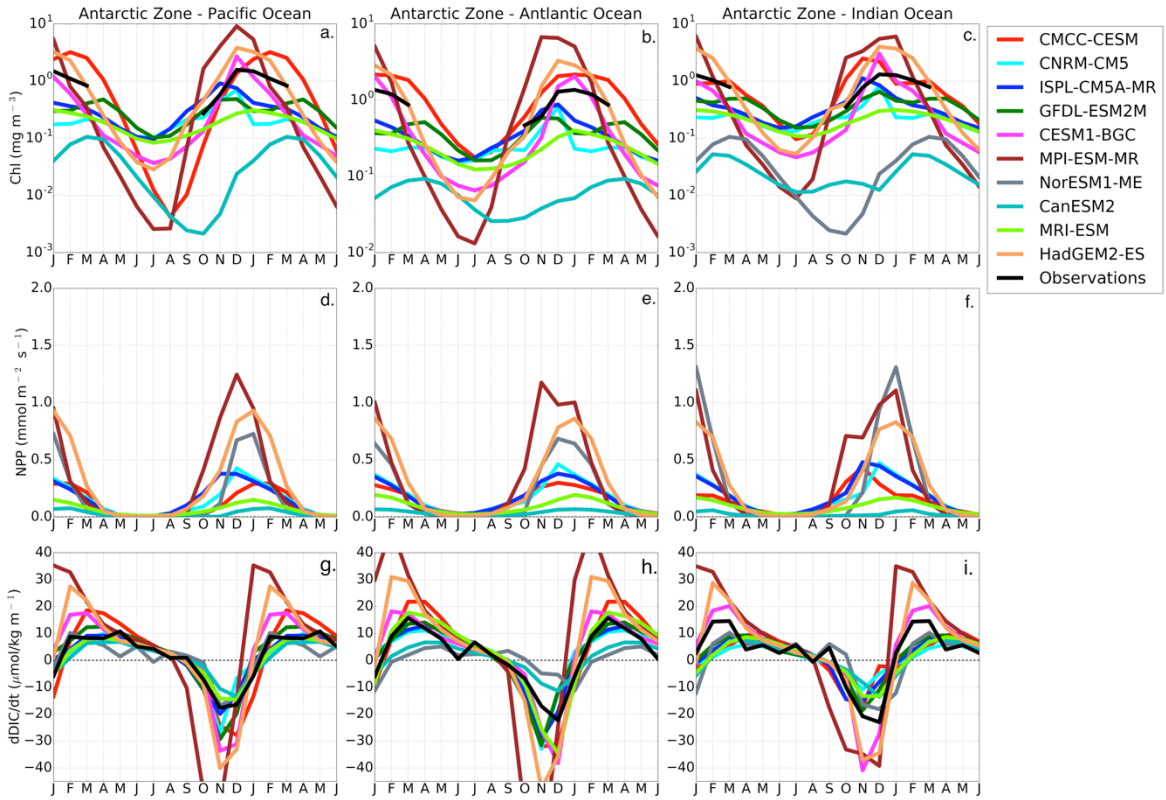

Figure. 4.9b Same as Fig. 9a for the Antarctic zone.

CMIP5 models here show a clear partition between group-DIC and group-SST models. While they mostly maintain the same phase, group-DIC shows larger amplitudes of chlorophyll relative to group-SST and observed estimates in the Sub-Antarctic Zone. This difference is even clearer in NPP magnitudes, where group-DIC models show a maximum of NPP > 1 mmol m^{-2} s^{-1} in summer, while group-SST magnitudes show about half of that. Except for CESM1 and CMCC (and NorESM1 for NPP), each CMIP5 model generally maintains a similar chlorophyll seasonal cycle (phase and magnitude) in all three basins of the Southern Ocean. This is contrary to the observations, which show signgicant differences in the magnitude (Fig. 4.9). Consistent with the observational product, CESM1 simulates larger amplitude in the Atlantic basin. While CMCC also has this feature, it also shows an overestimated chlorophyll peak in the Indian basin (Fig. 4.9a, b). In the Antarctic Zone both observations and CMIP5 models generally agree in both phase and magnitude (except for CanESM2) of the seasonal cycle of chlorophyll in all three basins.

The influence of the vertical DIC rate is now examined, using estimated entrainment rates (RE, Eq. 2.9) based on MLD and vertical DIC gradients (see Section 2.3.2). Fig. 4.10 shows the seasonal changes of MLD compared with the rate from the observational product. CMIP5 models largely agree on the timing of the onset of MLD deepening (February in the Pacific basin, and March for the Atlantic and Indian Basins) and shoaling (September) in the Sub-Antarctic Zone (with the exception of NorESM1-ME and IPSL-CM5A in the Pacific Basin). The Indian Basin generally shows deeper winter MLD in both observations and CMIP5 models in the Sub-Antarctic Zone. Note that while CMIP5 models generally show the observed deeper MLDs in the Indian Basin, they also show a large variation; for example, the winter maximum depth ranges from 100 m (CMCC, pacific basin) to 350 m (CanESM2, Indian Basin) in the Sub-Antarctic Zone. In the Antarctic Zone CMIP5 models are largely in agreement on the timing of the onset of MLD deepening (February) with the exception of NorESM1, but also variable in their winter maximum depth. For example, CanESM2 maximum winter depth is 350 m while CMCC only shows 210 m in the Sub-Antarctic zone (Fig. 4.10 c). It is worth noting that the observed MLD seasonal cycle might be biased due to limited in situ observations particularly in the Antarctic Zone (de Boyer Montégut et al., 2004).

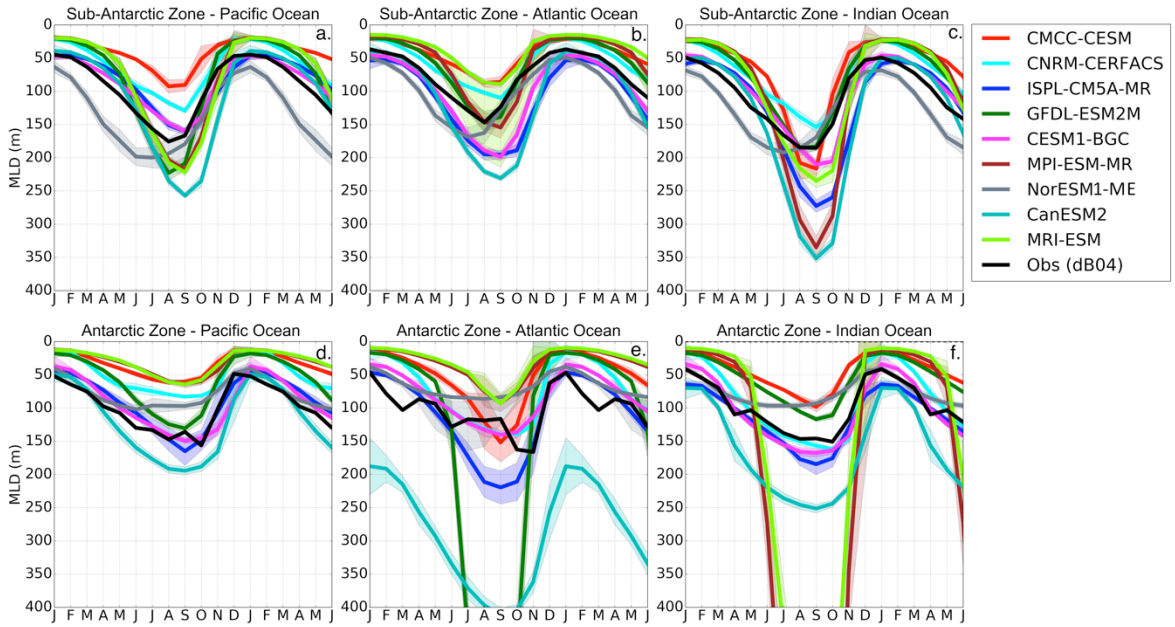

Figure. 4.10: Seasonal cycle of the Mixed Layer Depth (MLD) in the Sub-Antarctic and Antarctic zones of the Pacific Ocean (first column), Atlantic Ocean (second column) and Indian Ocean (third column).

The estimated entrainment mixing values in Fig. 4.10 show that almost all CMIP5 (with the exception of NorESM1-ME) entrain subsurface DIC into the mixed layer during autumn-winter in agreement with the observational estimates. In the Sub-Antarctic Zone, the estimates using the observational products show the strongest entrainment in the Atlantic Basin in May (RE reaches up to 10 µmol kg^{-1} $month^{-1}$), while it is lower in the other basins. In the Antarctic Zone, observed RE conversely shows stronger entrainment rates in the Pacific and Indian Basins (RE > 15 µmol kg^{-1} $month^{-1}$) in comparison to the Atlantic Basin (RE = 11 µmol kg^{-1} $month^{-1}$). CMIP5 model's entrainment rates are variable but not showing any particular deficiency when compared with the observational estimates. Also, the group-DIC and group-SST models show no clear distinction, the major striking features being the relatively stronger entrainment in MPI and CanESM2 across the three basins in the Sub-Antarctic Zone in mid to late winter (RE = 15 µmol kg^{-1} $month^{-1}$), and the large winter entrainment in IPSL in the Antarctic Pacific Basin. The supply of DIC to the surface due to vertical entrainment is therefore generally comparable between model simulations and the available estimate.

However, the RE values are estimated at the base of the mixed layer, which is not necessarily a complete measure of the vertical flux of DIC at the surface. The annual mean vertical DIC gradients are therefore investigated in Fig. 4.11 as an indicator of where the surface uptake processes occur. The simulated CMIP5 profiles are similar to GLODAP2, but some differences arise. In the Sub-Antarctic Zone, GLODAP2 shows a shallower surface maximum in the Atlantic basin consistent with higher biomass in this basin (Fig. 4.9a, b and 4. 10 b) ($(dDIC/dz)_{smax}$ = 0.55 µmol kg^{-1} m^{-1}, at 50 m) compared to the Pacific ($(dDIC/dz)_{smax}$ = 0.60 µmol kg^{-1} m^{-1}, at 80 m) and Indian Basin ($(dDIC/dz)_{smax}$

= 0.40 µmol kg^{-1} m^{-1}, at 80 m). CMIP5 models generally do not show this feature in the Sub-Antarctic Zone, except for CESM1-BGC1 ($(dDIC/dz)_{smax}$ = 0.50 µmol kg^{-1} m^{-1}, at 50 m). Instead, they show the surface maxima at the same depth in all three basins. In the Antarctic Zone both CMIP5 models and observations show larger $(dDIC/dz)_{smax}$ magnitudes and nearer surface maxima (with the exception of CanESM2 and CESM1). This difference in the position and magnitude of the DIC maxima between the Sub-Antarctic and Antarctic Zones has important implications for surface DIC changes and subsequently pCO_2 seasonal variability. Because of the nearer surface DIC maxima in the Antarctic Zone, surface DIC changes are more influenced by these strong near-surface vertical gradients than rather MLD changes. This implies that even if the entrainment rates at the base of the MLD are comparable between the Sub-Antarctic and the Antarctic, the surface supply of DIC may be larger in the Antarctic Zone.

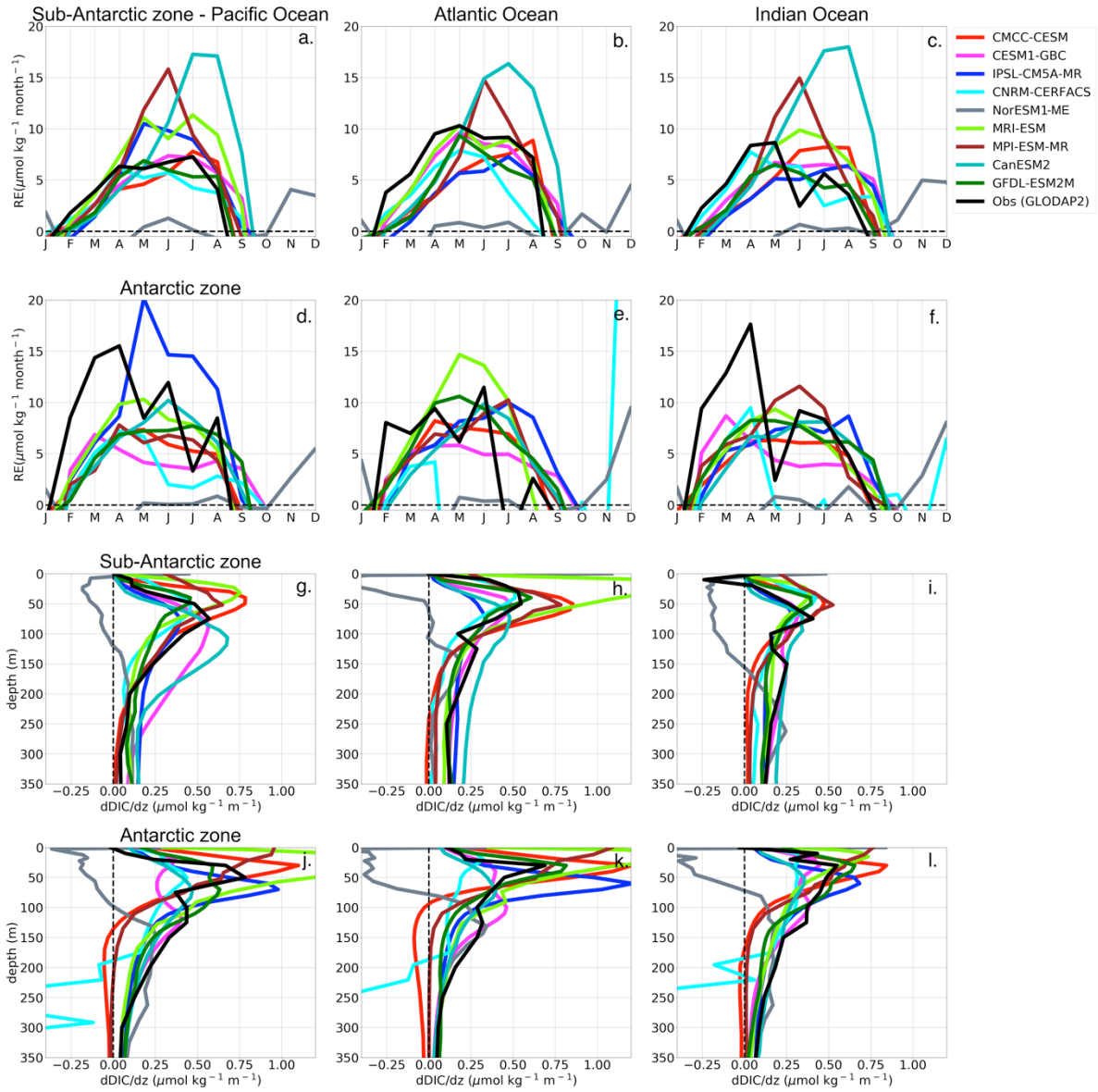

Figure. 4.11: (a-f) Estimated DIC entrainment fluxes (mol kg month^{-1}) at the base of the mixed layer and (g-i) vertical DIC gradients (μmol kg^{-1} m^{-1}) in the Sub-Antarctic and Antarctic zone of the Pacific Ocean (first column), Atlantic Ocean (second column) and Indian Ocean (third column).

4.4 Discussion

Recent studies have demonstrated that important differences exist between the seasonal cycle of FCO_2 in models and observations in the Southern Ocean (Lenton et al., 2013; Anav et al., 2015). Paradoxically, although the models may be in relative agreement for the mean annual flux, they diverge in the phasing and magnitude of the seasonal cycle (Lenton et al., 2013). These differences in the seasonal cycle raise questions about the climate sensitivity of the carbon cycle in these models because they may reflect differences in the process sensitivities to drivers that are themselves climate sensitive.

Once more this chapter expands on the framework proposed in Mongwe et al. (2016) and presented in Chapter 3, which examined the competing roles of temperature and DIC as drivers of pCO_2 variability and the seasonal cycle of pCO_2 and FCO_2 in the Southern Ocean. Here this approach is used to explain the mechanistic basis of seasonal biases in pCO_2 and FCO_2 between the Landschützer et al. (2014) data product and CMIP5 models. This analysis has shown that although the models have different seasonal cycles (Fig. 4.2), they could be grouped into two categories, here named group-SST and group-DIC according to their mean seasonal bias of temperature or DIC control for surface pCO_2 variability (Figs 4.3 & 4.7-8).

A few general insights emerge from this analysis. Firstly, despite important differences in the spatial characteristics of the mean annual fluxes (Fig. 4.1), models show unexpectedly greater inter-basin coherence in the phasing seasonal cycle of FCO_2 and SST-DIC control than observational products (Figs 4.3 & 4.6). However, clear inter-basin differences have been highlighted based on recent data products (Landschützer et al., 2015; Gregor et al., 2017) for climatology and interannual variability studies that examined pCO_2 and CO_2 fluxes as well as phytoplankton chlorophyll (Thomalla et al., 2011; Carranza et al., 2016). Briefly, the Atlantic Basin shows the highest mean primary production in contrast to the Pacific Basin, which has the lowest (Thomalla et al., 2011). Similarly, strong inter-basin differences for pCO_2 and FCO_2 have been highlighted and ascribed to SST control (Landschützer et al., 2016) and wind stress - mixed layer depth (Gregor et al., 2017). The combined effect of these regional differences in forcing of pCO_2 and FCO_2 would be expected to be reflected in the CMIP5 models as well. However, notwithstanding these, a quantitative analysis of the correlation

of the phasing of the seasonal cycle of FCO_2 between basins for different models shows that all the models except three (CMCC, GFDL and CESM1) are characterized by strong inter-basin correlation in both the Sub-Antarctic and the Antarctic Zones (Fig. 4.4-5). This most likely implies that CMIP5 models are not sensitive to regional FCO_2 variability at the basin scale and hence FCO_2 seasonal biases are zonally uniform.

Secondly, an important part of this analysis is based on the assumption that the observational products that are used to constrain the spatial and temporal variability of pCO_2 and FCO_2 reflect the correct seasonal cycles of the Southern Ocean. This assumption requires significant caution not only due to the limitations in the sparseness of the in-situ observations but also due to limitations of the empirical techniques in overcoming these data gaps (Gregor et al., 2017a, 2017b; Landschützer et al., 2014; Ritter et al., 2017; Rödenbeck et al., 2015). The uncertainty analysis of these studies suggests that, while the seasonal bias in observations may be less in the Sub-Antarctic Zone and Polar Frontal Zone, it is the highest in the Antarctic Zone where access is limited mostly to summer, and winter ice-cover results in uncertainties that may limit the significance of the data-model comparisons. It is important to note that though the observational product used here (Landschützer et al., (2014) is based more on surface measurements (about 10 million, SOCAT v3) than previous datasets (e.g. Takahashi et al., 2009, 3 million), the data are still sparse in time and space in the Southern Ocean (Gregor et al., 2017a). Thus, in using this data product as the main observational estimates for this analysis one needs to be mindful of the limitations in the discussion below.

Thirdly, the seasonal cycle of ΔpCO_2 is the dominant driver of the seasonal of variability in FCO_2 (Wanninkhof et al., 2009; Mongwe et al., 2016). Although winds provide the kinetic forcing for sea-air fluxes of CO_2 and indirectly affect FCO_2 through mixed layer dynamics and associated biogeochemical responses (Mahadevan et al., 2012; du Plessis et al., 2017), ΔpCO_2 sets the seasonally varying direction of the flux. Surface pCO_2 changes are mainly driven by DIC and SST (Takahashi et al., 1993; Hauck et al., 2015). Therefore, the correct sensitivity of CMIP5 models to how DIC and SST regulate the seasonal cycle of FCO_2 is fundamental to the model's ability to resolve the observed FCO_2 seasonal cycle. Thus, the influence of DIC and SST on FCO_2 is examined at the seasonal scale for 10 CMIP5 models with respect to observed estimates. Because temperature does not directly affect DIC changes, the impact of SST changes on pCO_2 was first scaled up through surface CO_2 solubility to equivalent DIC units using a mean Revelle factor as in the previous the Chapter. In this way, one can quantitatively distinguish the influence of SST and DIC changes (i.e. biological and physical) on pCO_2 and hence on FCO_2 in comparable units (DIC: $\mu mol\ kg^{-1}$).

Fourthly, using this diagnostic framework (Section 2.3.1, summarized in Figs 4.7-4.8) it is seen that the FCO_2 biases of CMIP5 models cluster into two groups, namely group-DIC ($M_{T\text{-}DIC} < 0$) and group-

SST ($M_{T\text{-}DIC} > 0$). Group-DIC models are characterized by an overestimation of the influence of DIC on pCO_2 with respect to observational estimates, which indicate that estimated physical and biogeochemical driven changes in the DIC mainly regulate the seasonal cycle of FCO_2 (in short, DIC control). Group-SST models show a dominate temperature influence on pCO_2; here temperature related surface CO_2 solubility biases are mainly responsible for the departure of modelled FCO_2 from the observational products. While CMIP5 models generally show a singular dominant influence of these extremes, observations show a modest influence of both, with a dominance of DIC changes as the main driver of seasonal FCO_2 variability. Below the seasonal cycle characteristics is discussed along with possible mechanisms for these two groups of CMIP5 models in the Sub-Antarctic and Antarctic Zones of the Southern Ocean.

4.4.1 Sub-Antarctic Zone

This diagnostic analysis indicates that the seasonal cycle of pCO_2 in the observational product (Landschützer et al., 2014) is mostly DIC controlled across all three basins of the Sub-Antarctic Zone ($M_{T\text{-}DIC} < 0$ in Fig. 4.6). The Atlantic Basin shows a stronger DIC control (Annual mean $M_{T\text{-}DIC} \geq 2$) compared to the Pacific and Indian Basins (Annual mean $M_{T\text{-}DIC} \approx 1$). This stronger influence of DIC on pCO_2 in the Atlantic Basin is consistent with higher primary production in this basin during summer (Graham et al., 2015; Thomalla et al., 2011), here shown by the larger mean seasonal chlorophyll from remote sensing in the Atlantic Basin with respect to the Pacific and Indian Basins (Fig. 4.10). This significant basin difference is most likely linked to the fact that the Atlantic Basin has longer periods of shallow MLD compared to the Pacific and Indian Basins (Fig. 4.9 a-c, Nov - Mar & Nov - Feb respectively) and has been shown to have larger supplies of continental shelves and land-based iron (Boyd and Ellwood, 2010; Tagliabue et al., 2014, 2012b). These conditions are more likely to enhance primary production that translates into a faster rate of change of surface DIC (Fig. 4.8), which becomes the major driver of FCO_2 variability. In contrast, shorter periods of shallow MLD and lower iron inputs in the Pacific Basin (Tagliabue et al., 2012), probably account for a lower chlorophyll biomass and hence the weaker DIC control evidenced in this analysis ($M_{T\text{-}DIC} \approx 0$ in Fig. 4.8). In the Indian Basin, the winter mixed layer is deeper than in the Atlantic and deepens earlier in the season (Fig. 4.10, c). These conditions probably limit chlorophyll concentration (Fig. 4.9a) and possibly contribute to the slower rates of surface temperature change because of the enhanced mixing (cf Fig. 4.6 a-c). The resulting net driver in the Indian and Pacific Basins is a weaker DIC control, because both biological DIC and solubility changes are relatively weaker, and they oppose each other. Because of this, when the magnitudes of the rate of change of SST peak during cooling and warming (autumn and spring respectively), DIC control is weakest ($M_{T\text{-}DIC} \approx 0$), Fig. 4.8.

CMIP5 models do not capture these basin-specific features as demonstrated by the correlation analysis in Fig. 4.5, with the exception of three group-SST models (i.e. CESM1, GFDL and CMCC). These, in contrast, show generally comparable FCO_2 phasing in the three basins. The seasonal cycle of FCO_2 in the Southern Ocean is both zonally and meridionally uniform for most CMIP5 models, in contrast to the observational data product (Fig. 4.2-3). This indicates that CMIP5 models show equal sensitivity to basin scale FCO_2 drivers, suggesting that pCO_2 and FCO_2 driving mechanisms are less local than observations. Thus, the understanding of fine-scale (mesoscale and sub-mesoscale) processes responsible for basin-scale FCO_2 variability may be an important contribution to the next generation of ESM. Studies based on new available data from higher resolution autonomous platforms may provide useful constraints to these dynamics in ESMs (Briggs et al., 2015; Monteiro et al., 2015; Rosso et al., 2017; Williams et al., 2017a).

The major feature of group-SST models in the Sub-Antarctic Zone is the CO_2 out-gassing during summer and in-gassing from mid-autumn to winter (Fig. 4.3a-c), which the diagnostics in Fig. 4.6 attribute to temperature (solubility) control. The summer period coincides with the fastest warming rates (dSST/dt) in Fig 4.6 a-c, and is thus the related reduced surface CO_2 solubility. Similarly, exaggerated cooling rates at the onset of autumn (Fig. 4.5 a-c) enhance CO_2 solubility, causing a change in the direction of FCO_2 from outgassing into strengthening CO_2 in-gassing (Fig 4.3 a-c). Hence whilst group-SST models have a seasonal amplitude of FCO_2 comparable to observations, they are out of phase (Fig. 4.3), as was the case in a forced ocean model in Chapter 3.

In addition to increasing CO_2 solubility, the rapid cooling at the onset of autumn also deepens the MLD (March-June, Fig. 4.7), which induces entrainment of DIC, increasing surface CO_2 concentration and weakening the ocean-atmosphere gradient, and in some instances reversing the air-sea flux to out-gassing (a. Lenton et al., 2013; Mahadevan et al., 2011; Metzl et al., 2006b). While these processes (cooling and DIC entrainment) are likely to co-occur in the Southern Ocean, in CMIP5 models they are characterized by their extremes: temperature influence on solubility exceeds the rate of entrainment on group-SST models (Fig. 4.6 & 4.10). Hence because of the dominance of the solubility effect in group-SST models, the influence of DIC entrainment on surface pCO_2 changes (weakening of CO_2 in-gassing / out-gassing) only happens in mid-late winter (June-July to August) when entrainment fluxes peak (Fig. 4.12) and the SST rate of change approaches zero (Fig. 4.6).

In the spring-summer transition, primary production is expected to enhance net CO_2 uptake (Le Quéré and Saltzman, 2013; Thomalla et al., 2011). However, elevated surface warming rates during spring reduce CO_2 solubility in group-SST models and overwhelms the role of primary production in the seasonal cycle of pCO_2 and FCO_2 (atmospheric CO_2 uptake). As a consequence, group-SST models

generally show constant or weakening net CO_2 uptake flux during spring in the Pacific and Atlantic Basins even though primary production occurs and is relatively elevated (Figs 4.3 & 4.10). Though some models show chlorophyll concentrations comparable to observations (e.g. GFDL, CNRM, CanESM2), and in some instances even greater than (e.g. MRI), the effect of temperature-driven solubility still dominates due to the phasing of the rates of the two drivers (Fig. 4.2 a-c). The Indian Basin however shows the only exception to this phenomenon. Here, the amplitude of seasonal surface warming is relatively smaller (~ 0.5 $^{o}C^{-1}$ $month^{-1}$ lower than the Pacific and Atlantic Basins), and biologically-driven CO_2 uptake becomes notable and shows net strengthening of the sink of CO_2 during spring (Fig. 4.3 c).

Though almost all analyzed CMIP5 models (with the exception of NorESM1) exaggerate the warming and cooling rates in autumn and spring, group-DIC models do not manifest the expected temperature-driven solubility influence on pCO_2 and FCO_2 (Fig. 4.2). Instead, the seasonal cycle of pCO_2 and FCO_2 are controlled by DIC changes, which are driven by overestimated seasonal primary production and the associated export carbon (Fig. 4.11). It is striking how in these models, the seasonal cycles of chlorophyll and FCO_2 are in phase (Figs 4.3 a-c, 4.10 a-c, with linear correlation coefficients always larger than 0.9, not shown) but, as discussed below, this is not because the rates of temperature change are correctly scaled but because the rates of biogeochemical processes are exaggerated (Fig. 10).

Because of the particularly overestimated biological production in group-DIC models, the CO_2 sink is stronger (Fig. 4.10) with respect to observation estimates during spring. This is visible in the reduction of surface DIC during the spring-summer seasons (negative dDIC/dt in Fig. 4.9a, a, g-i) which can only be explained by drawdown due to the formation and export of organic matter (Le Quéré and Saltzman, 2013). However, note that in the same way, after the December production peak, both CMIP5 models and observations show an increase of surface DIC concentrations (positive dDIC/dt) until March (Fig. 4.9b, g-i). These DIC growth rates are particularly enhanced in group-DIC models compared to some group-SST and observations (Fig. 4.11). The onset of these DIC increases also coincides with the depletion of surface oxygen (Fig. 4.11), which we assume is due to the remineralization of organic matter to DIC through respiration. This is also because the start of increasing surface CO_2 concentrations that ultimately leads to outgassing in March for group-DIC models, begins in mid-summer after the production peak and prior to MLD deepening. Unfortunately, only a few models have stored the respiration rates, therefore the full reason for this DIC rebound remains to be examined at a later stage. One would however tend to exclude other processes, because the onset of CO_2 out-gassing seen in March in group-DIC models occurs prior to significant MLD deepening (Fig. 4.10) and entrainment fluxes, therefore remineralization is likely be a key process here (Fig. 4.9).

Note that while CMIP5 models show similarities in mechanisms of CO_2 uptake within group-DIC and group-SST models as discussed above, this grouping is not apparent on the mean annual fluxes (Table 4.2). In some instances, comparable annual mean CO_2 uptake are shown by group-DIC models, NorESM2 (-0.67 Pg C yr^{-1}), HadGEM2 (-0.49 Pg C yr^{-1}), and MPI (-0.87 Pg C yr^{-1}) and group-SST models, CMCC (-0.82 Pg C yr^{-1}) and CESM1 (-0.53 Pg C yr^{-1}), (Table 4.2). However, the mechanisms that explained these are different within group-SST and group-DIC models. For example, the CO_2 uptake in CMCC is mostly explained by the solubility driven CO_2 uptake during autumn and part of winter, while in group-DIC models the CO_2 uptake is mostly biological driven.

4.4.2 Antarctic Zone

The seasonal cycle framework summarized in Fig. 4.7-8 shows that the variability of FCO_2 and pCO_2 in the Landschützer et al. (2014) product is characterized by a stronger DIC control (annual mean $M_{T\text{-}DIC} < -2$) relative to the Sub-Antarctic ($M_{T\text{-}DIC} \approx -1$), except in the spring season ($M_{T\text{-}DIC} > -1$). This DIC control is spatially uniform in the Antarctic Zone across all three basins (Fig. 4.5). The available datasets indicate that the combination of weaker SST rates of change due to reduced solar heating fluxes (Fig. 4.6), and stronger, shallower vertical DIC maxima (Fig. 4.11) favor stronger DIC control through larger surface DIC rates of change. The spatial uniformity in the seasonality of FCO_2 is also evident in the satellite chlorophyll and calculated dDIC/dt from GLODAP2 in Fig. 4.9. Contrary to the Sub-Antarctic, this might suggest that FCO_2 mechanisms here are less local. It could be hypothesized that the seasonal extent of sea-ice, deeper mixing and heat balance differences affect this region more uniformly than the Sub-Antarctic Zone, hence the mechanisms of FCO_2 are spatially homogeneous. However, one should not forget that sparseness of observations in this region is a key limitation of data products (Bakker et al., 2014; Gregor et al., 2017a; Monteiro et al., 2010; Rödenbeck et al., 2013) that might hamper the emergence of basin-specific features. This highlights the importance and need to prioritize independent observations in the Southern Ocean south of the polar front and in the Marginal Ice Zone. Improved observational constraints should also include a variety of high resolution observational platforms (Monteiro et al., 2015) and biogeochemical floats (Johnson et al., 2017) to complement ongoing ship-based measurements.

In general terms, CMIP5 models are in overall agreement (with an exception of MRI) with the observational product on the dominant role of DIC in regulating the seasonal cycle of FCO_2 (Fig. 6 d-f), though not all models agree in the phase of the seasonal cycle of FCO_2 (e.g. CanESM2, Fig. 4.2). Though CMIP5 models still generally show the biases in the SST rates of change in autumn and

spring with respect to observed estimates, the stronger and near-surface vertical DIC maxima (Fig. 11) probably favor DIC as the dominant driver of FCO_2 changes. Differences between group-SST and group-DIC models are only evident in mid-summer when SST change rates increase and primary production peaks (Figs 4.3 & 4.9). Probably because of sea ice presence, the onset of SST warming is a month late (November) in comparison to the Sub-Antarctic (October). This allows the onset of primary production before the surface warming, which then permits the biological CO_2 uptake to be evident in group-SST models. Therefore, the two model groups (SST and DIC) here agree in the phasing of FCO_2 in-gassing during spring (Fig. 4.3e-f). Group-SST models being the closest to the observational product. The MRI is the only model showing anomalous solubility dominance during autumn and spring as in the Sub-Antarctic Zone.

This coherence of CMIP5 models and observations in the Antarctic Zone may suggest that CMIP5 models compare better to observations in this region (Fig. 4.4). However, because CMIP5 models also show spatial homogeneity in the Sub-Antarctic Zone (contrary to observational estimates), it is not clear whether this indicates CMIP5 models have improved skill concerning the mechanisms of FCO_2 in this region, or both CMIP5 models and observational product lack spatial sensitivity to the drivers of FCO_2. The sparseness of observations in the Antarctic Zone points to the latter.

5. Summary

The findings highlight two major biases with respect to the seasonality of pCO_2 and FCO_2 in 10 CMIP5 models relative to observed estimates in the Southern Ocean.

Firstly, the general exaggeration of the seasonal rates of change of SST was examined with respect to available observations in autumn and spring seasons during peak cooling and warming, respectively. These elevated rates of SST change tip control of the seasonal cycle of pCO_2 and FCO_2 towards SST from DIC and result in a divergence between the observed and modelled seasonal cycles, particularly in the Sub-Antarctic Zone. While almost all analyzed models (9 of 10) show these SST-driven biases, 3 of the 10 (namely NorESM1, HadGEM2 and MPI) do not show such solubility biases because of their exaggerated primary production (and remineralization) rates such that biologically-driven DIC changes mainly regulate the seasonal cycle of FCO_2. These models reproduce the observed phasing of FCO_2 as a result of incorrect scaling of the biogeochemical fluxes. In the Antarctic Zone, CMIP5 models compare better with observations than in the Sub-Antarctic Zone. This is mostly because both CMIP5 models and observational product estimates show spatial and temporal uniformity in the

characteristics of FCO_2 in the Antarctic Zone. However, it is not certain if this is because model process dynamics perform better in this high latitude zone or that the observational product variability is itself limited by the lack of in situ data. This remains an open question that needs to be explored further and highlights the need for increased scale-sensitive and independent observations south of the Polar Front and into the sea-ice zone.

The second major bias is that contrary to observational product estimates, CMIP5 models generally show equal sensitivity to basin scale FCO_2 drivers (except for CMCC, GFDL and CESM1) and hence the seasonal cycle of FCO_2 has similar phasing in all three basins of the Sub-Antarctic Zone. This is in contrast to observational and remote sensing products that highlight strong seasonal and interannually varying basin differences in both pCO_2 and phytoplankton biomass. It is not clear if this is due to inadequate carbon process parameterization or improper representation of the dynamics of the physics. This should be investigated further with CMIP6 models and this analysis framework is proposed as a useful tool for diagnosing the dominant drivers. Contrary to observed estimates, CMIP5 models simulate FCO_2 seasonal dynamics that are zonally homogeneous, and it is suggested that any investigation of local (basin-scale) mechanisms, dynamics and long-term trends of FCO_2 using CMIP5 models should remain tentative and treated with caution. This highlights a key area of development for the next generation of CMIP.

The cause of differences in the seasonal rates of SST change in group-SST models remains a subject of ongoing research. The Southern Ocean is part of the global ocean (upwelling) where earth systems models have a persistent warming SST bias (Hirahara et al., 2014). Several studies previously highlighted potential explanations, but the main reasons remain uncertain. For example, CMIP5 models show differences in the magnitude and meridional location of the peak of wind speeds in the Southern Ocean (Bracegirdle et al., 2013), and MLD differences (Meijers, 2014; Sallée et al., 2013) may be such that the net effect of change on surface turbulence and mixing leads to these amplified rates of change in SST. Other known CMIP5 model biases which may contribute includes: heat fluxes and storage (Frölicher et al., 2015) and sea-ice dynamics (Turner et al., 2013). Notwithstanding these, investigation of the reasons for the sources of these dSST/dt biases is beyond the scope of this study. The aim here was to show that understanding biases in the drivers of pCO_2 (DIC and SST) at the seasonal scale is necessary to understand differences in the seasonal cycle of FCO_2 between models and observational products. I hope that this process-based understanding of the FCO_2 biases in CMIP5 models in the Southern Ocean can be helpful in focusing on key areas of modelling development for the next generation of CMIP.

The above analysis demonstrates that cooling and warming biases form the leading drivers in CMIP5 FCO_2 biases, shown by 9 out of the 10 analyzed models. Efforts to improving the realistic

representation of these rates would ameliorate carbonate system dynamics in the next generation of CMIP. This will not only reduce the exaggerated temperature-driven solubility but will also most likely aid the emergence of the observed biological CO_2 uptake during spring in group-SST models. Because two of the three group-DIC models (MPI-ESM-MR and HadGEM2-ES) also show this bias, correcting the NPP biases will only switch the main bias from primary production to temperature-driven solubility in these models. Thus, prioritizing the biases linked to rates of change of temperature (SST) will be a crucial improvement for oceanic carbon cycle in the Southern Ocean.

Chapter 5

Long-term Changes in the Seasonality and Drivers of CO_2 in CMIP5 ESMs in the Southern Ocean

5.1 Introduction

The long-term role of the Southern Ocean as a sink of CO_2 has contrasting views in the literature; some studies suggest that the CO_2 sink is likely to weaken on century time scales (Le Quéré et al., 2007; Roy et al., 2011; Segschneider and Bendtsen, 2013), while other recent studies propose the opposite (Hauck and Völker, 2015; Takahashi et al., 2012; Zickfeld et al., 2008). Thus, earth system models are important tools for investigating oceanic mechanisms of CO_2 uptake, and simulation of long-term climate changes. Nonetheless as shown in Chapter 4, the latest generation of CMIP models (CMIP5) have limited skill in simulating both the seasonality and spatial variability of FCO_2 in the Southern Ocean compared to observed estimates (Anav et al., 2013; Kessler and Tjiputra, 2016; Lenton et al., 2013). Because of these differences, predicting long-term changes in the mechanisms of CO_2 dynamics and in the CO_2 sink in the Southern Ocean may be problematic in the CMIP5 models (a. Lenton et al., 2013). It is not clear whether CMIP5 models will converge under anthropogenic forcing, so that the drivers of CO_2 uptake are similar within CMIP5 models by the end of the century, or whether the mechanisms of CO_2 uptake will vary as they do at present? The latter may suggest that CMIP5 models lack sufficient sensitivity to appropriately simulate the long-term CO_2 characteristics in the Southern Ocean. It also worth mention that the modelled ocean CO_2 sink still has large uncertainties(~ 30%) mostly attributed to internal variability and as well emission scenarios that further hinder determination of the future scenarios (Khatiwala et al., 2013; Lovenduski et al., 2016; McKinley et al., 2016; Randerson et al., 2015). A recent study based on the MPI-ESM shows that the largest internal variability is in the Southern Ocean and North Atlantic (Li and Ilyina, 2018).

Expected changes in the mechanisms that regulate CO_2 uptake in the Southern Ocean have been broadly explored based on modelling and observational studies (Bopp et al., 2013, 2005; Fu et al., 2016; Hauck and Völker, 2015; Kessler and Tjiputra, 2016; Kwiatkowski and Orr, 2018; McNeil and Sasse, 2016). Modelling-based studies by Hauck and Völker, (2015) and McNeil and Sasse, (2016) demonstrate that the Revelle factor is likely to increase by the end of the century, associated with

increased atmospheric CO_2 which in turn is expected to reinforce CO_2 uptake in the Southern Ocean. Because smaller DIC changes will have larger pCO_2 variation under lower CO_2 bufferinf capacity, biological driven DIC changes are projected to result in a relatively larger CO_2 uptake . An increased Revelle factor is also projected to amplify the seasonal pCO_2 amplitude (winter-summer) since small changes in DIC will result in larger pCO_2 changes under a lower ocean CO_2 buffering capacity, (Hauck, 2018; Hauck and Völker, 2015). A recent observation-based study by Landschützer et al. (2018) demonstrates that these changes (increased Revelle factor and amplified seasonal pCO_2 amplitude) are already apparent from historical observational datasets (1982 – 2015) in the Southern Ocean. In addition to weakened CO_2 buffering capacity, anthropogenic changes are likely to cause a warmer and more stratified surface ocean by the end of the century (Bopp et al., 2013; Caldeira, 2000, 2005; Cao and Zhang, 2017; Fu et al., 2016). The warmer surface ocean may weaken CO_2 solubility, but will also probably alter the role of the biological pump in the oceanic carbon cycle (Steinacher et al., 2010; Bopp et al., 2013; Cao and Zhang, 2016). The intensification of westerly winds associated with the projected increasing positive anomaly of the SAM index is also expected to enhance the upwelling of natural carbon and thus likely to weaken the Southern Ocean CO_2 sink (Archer and Caldeira, 2008; Thompson and Solomon, 2002; Thompson and Wallace, 2000; Wang et al., 2011).

An analysis by Kessler and Tjiputra (2016) based on 9 CMIP5 models shows that the annual mean biases of every single model in FCO_2 against the ensemble mean in the present-day climate persist to the end of the century in the Southern Ocean. Thus models which tend to show a CO_2 in-gassing bias (out-gassing bias) relative to the ensemble mean in the present-day climate show stronger CO_2 uptake (weaker CO_2 uptake) than the ensemble mean by the end of the century. This indicates that the contemporary FCO_2 biases in CMIP5 models are preserved to the end of the century. Chapter 4 established the two main biases that play a leading role in the limited skill of CMIP5 models to simulating the seasonal cycle of FCO_2 in the present-day climate. These biases are the exaggerated role of surface CO_2 solubility changes during peak warming and cooling seasons (i.e. autumn and summer) in some models, and primary production in other models. Here I now examine the implications of these present-day biases in FCO_2 for the simulated of CO_2 uptake at the end of the century. I use five models from the RCP8.5 scenario, representative of the two model groups (group-SST and group-DIC) shown in Chapter 4 to investigate how the role of CO_2 solubility, biological CO_2 activity and vertical mixing in FCO_2 respond to long-term anthropogenic forcing (RCP8.5) within these two model groups.

5.2. Methods

The Southern Ocean is here defined as shown in Fig. 2.4, however for this Chapter, basin-scale analyses are ignored, given the zonal homogeneity highlighted in Chapter 4. This analysis focuses on the zonal mean of the Sub-Antarctic and Antarctic Zones.

5.2.1 Datasets

Five models from the Coupled Model Intercomparison Project version 5 (CMIP5) Earth System Models (ESM) were used, focusing on the Representative Concentration Pathway (RCP) 8.5 scenario shown in Table 5.1. The selection criterion for the models was based on the availability of essential variables for the analysis on the public servers (https://esgf-data.dkrz.de/search/cmip5-dkrz/) at the time of writing: i.e. monthly FCO_2, partial pressure of CO_2 (pCO_2), surface Dissolved Inorganic Carbon (DIC), vertical annual DIC, Sea Surface Temperature (SST) and vertical temperature fields. Note that for the rest of the Chapter CMCC-CESM, IPSL-CM5A-MR and MPI-ESM-MR are abbreviated as CMCC, IPSL and MPI respectively for convenience.

Table 5.1: A description of the 5 CMIP5 ESMs used in this analysis, showing the ocean resolution, atmospheric resolution, and available nutrients for the biogeochemical component, sea-ice model, vertical levels and the marine biogeochemical component for each ESM. For ease of reading, some model names have been replaced by abbreviated acronyms below.

Full name and Source	Model Name	Ocean Resolution	Atmospheric Resolution	Nutrients	Sea ice model	Veridical Levels	Ocean Biology	Reference
Canadian Centre for Climate Modelling and Analysis, Canada	CanESM2	CanOM4 0.9º x1.4º	2.8125º x 2.8125º	N (accounts for Fe limitation)	CanSIM1	40 levels	NPZD	Zahariev et al., 2008
Centro Euro-Mediterraneo Sui Cambiamenti Climatici, Italy	CMCC-CESM = CMCC	OPA8.2 0.5-2ºx2º	3.8º x 3.7º	P, N, Fe, Si	CICE4	21 levels	PELAGOS	Vichi et al., 2007
Institut Pierre-Simon Laplace, France	IPSL-CM5A-MR = IPSL	NEMO2.3 0.5-2º x 2º	2.58º x 1.25º	P, N, Fe, Si	LIM2	31 levels	PISCES	Séférian et al., 2013
Max Plank Institute for Meteorology, Germany	MPI-ESM-MR = MPI	MPIOM 1.41º×0.89º	1.875º x 1.875º	P, N, Fe, Si	MPIOM	40 levels	HAMOCC5.2	Ilyina et al., 2013
Hadley Global Environment Model 2 – Earth System, UK	HadGEM2-ES	0.3º x 1º	2.5◦ x 2.0◦	N,Fe,S		40 levels	Diat-HadOCC	Palmer and Totterdell, 2001

5.2.2 Sea-Air CO_2 Flux Drivers: The Seasonal Cycle Diagnostic Framework (Part B)

This Section provides a description of the diagnostic framework used to examine the seasonal variability between models and observations of the main drivers of surface pCO_2 (SST and DIC).

Note that for this chapter the diagnostic indicator ($M_{T\text{-}DIC}$) is here computed in pCO_2 units (µatm $month^{-1}$) instead of DIC (µmol kg^{-1} $month^{-1}$) as done in Chapters 3 and 4. This change was necessary considering large uncertainties in the Revelle factor values at the end of the century for some models (e.g. HagGEM2-ES, std(γ_{DIC}) ≈ 5) which introduced large uncertainties in the computed diagnostic indicator $M_{T\text{-}DIC}$, (Fig. 5.1). Consequently, the main difference between the methodology used in Chapters 3 and 4 and this Chapter, is that the step that converts the temperature driven pCO_2 changes into DIC units (Eq. 2.4,) is here omitted (details below). Instead, here surface pCO_2 variability is decomposed into its four components (i.e. DIC, SST, Total Alkalinity and salinity), and the DIC component is estimated by subtraction from the other three components. A detailed explanation is provided below with an example showing that these two methods yield comparable results.

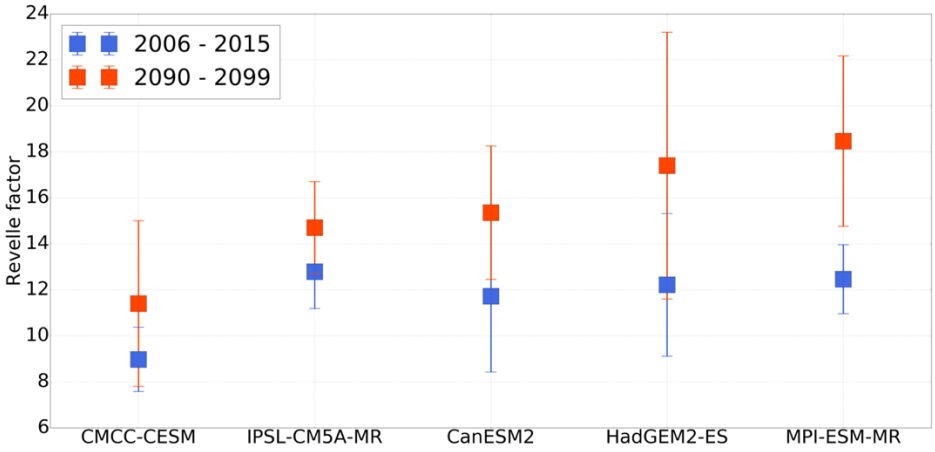

Figure. 5.1 The Revelle factor for the mean Southern Ocean domain (south of the tropical front) for 2006 – 2015 (blue) and 2090 – 2100 (orange). The uncertainty intervals present the decadal standard deviation.

The total derivative of pCO_2 with respect to time in the surface layer consists of the contributions of SST, surface salinity (Sal), total alkalinity (TAlk) and DIC changes (Landschützer et al., 2018; Jorge Louis Sarmiento and Gruber, 2006; Takahashi et al., 1993), (Eq. 5.1).

$$\left(\frac{dpCO_2}{dt}\right)_{Tot} = \left(\frac{\partial pCO_2}{\partial t}\right)_{DIC} + \left(\frac{\partial pCO_2}{\partial t}\right)_{TAlk} + \left(\frac{\partial pCO_2}{\partial t}\right)_{Sal} + \left(\frac{\partial pCO_2}{\partial t}\right)_{SST} \quad (5.1)$$

$$\left(\frac{dpCO_2}{dt}\right)_{Tot} \approx \left(\frac{\partial pCO_2}{\partial t}\right)_{DIC} + \left(\frac{\partial pCO_2}{\partial t}\right)_{SST} \quad (5.2)$$

$$\left(\frac{dpCO_2}{dt}\right)_{DIC} \approx \left(\frac{\partial pCO_2}{\partial t}\right)_{Tot} - \left(\frac{\partial pCO_2}{\partial t}\right)_{SST} \quad (5.3)$$

$$M_{T-DIC} \approx \left|\left(\frac{\partial pCO_2}{\partial t}\right)_{SST}\right| - \left|\left(\frac{\partial pCO_2}{\partial t}\right)_{DIC}\right| \quad (5.4)$$

The SST component of pCO_2 is estimated according to the Takahashi et al., (1993) expression, as presented in Section 2.3.1. The contribution of TAlk and salinity are here ignored as secondary drivers of pCO_2 as explained in Section 2.3.1. Consequently, the DIC component of pCO_2 can be estimated by subtracting the temperature component from the total rate of change of pCO_2 (Eq. 5.3). Once again, to determine the dominant instantaneous driver of pCO_2 change, the SST and DIC components of surface pCO_2 are compared by subtracting their absolute values (Eq. 5.4). The computed $M_{T\text{-}DIC}$ is used as a diagnostic indicator as in Chapters 3 and 4, but now given in pCO_2 units ($\mu atm\ month^{-1}$). Thus $M_{T\text{-}DIC} > 0$ indicates periods when temperature driven (solubility, K_0) processes dominate instantaneous changes in surface pCO_2, whereas when $M_{T\text{-}DIC} < 0$, pCO_2 changes are mainly controlled by DIC processes. Fig. 5.2 compares $M_{T\text{-}DIC}$ computed in this chapter (Part B, $\mu atm\ month^{-1}$) and using the standard methodology of Chapters 3 and 4 (Part A, $\mu mol\ kg^{-1}\ month^{-1}$) for HadGEM2 in the Sub-Antarctic Zone. It indeed illustrates that these two methods yield comparable results.

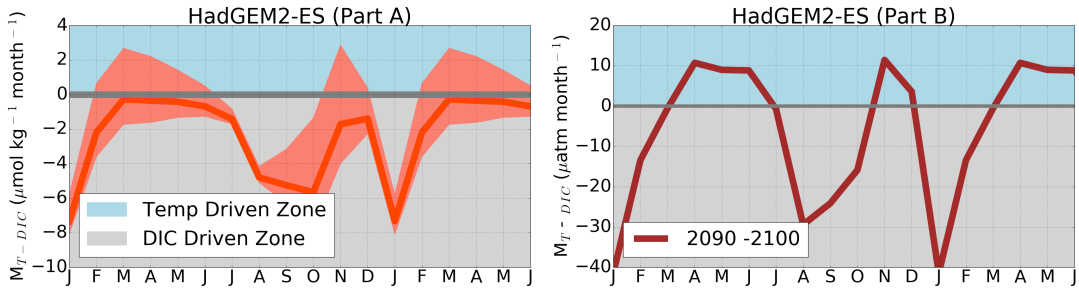

Figure. 5.2 The diagnostic indicator ($M_{T\text{-}DIC}$) for HadGEM2 in the Sub-Antarctic zone. It compares $M_{T\text{-}DIC}$ computed using of the methodology in Chapter 2 (Part A) applied in Chapters 3-4 and this Chapter (Part B) for a decadal mean at the end of the century (2090 -2100). The shaded area in part A represents the uncertainty, here defined as the standard deviation of the Revelle factor between 2090 -2100 as shown in Fig 5.1.

5.2.2.2 Revelle factor

For the purposes of examining changes in the surface water buffering capacity of CO_2 at the end of the century (2090 – 2100), the Revelle factor (γ_{DIC}) is estimated using Eq. 5.5.

$$\gamma_{DIC} = \left(\frac{\Delta pCO_2}{pCO_2}\right)_{DIC} / \frac{\Delta DIC}{DIC} \quad (5.5)$$

Note that this calculation is based on monthly means data of the DIC component of pCO_2 (Eq. 1.4) and surface DIC for each model. We here use the DIC component of pCO_2 instead of the total pCO_2 changes to avoid uncertainties associated with pCO_2 variability due to temperature changes, which are not accounted for by the Revelle factor. For analysis, the Revelle factor magnitudes are computed only for the whole Southern Ocean domain (south of the subtropical front). This is regional Revelle factor (Sub-Antarctic and Antarctic) were neglected due to large variability in computed magnitudes within the analyzed models.

5.3 Results

This Section is partitioned into five subsections; Section 5.3.1 evaluates changes in the phasing and magnitude of the mean decadal climatology of the seasonal cycle of FCO_2 from 2006 - 2015 and 2090 - 2100 in the Sub-Antarctic and Antarctic zone. Section 5.3.2 uses the diagnostic framework described in Section 5.2.3 to examine how changes in the seasonal variability of the drivers of surface pCO_2 (SST and DIC) explain the differences in the seasonal cycle of FCO_2. Section 5.3.4 evaluates the role of surface temperature and DIC long-term changes (2006 - 2015 vs 2090 - 2100) to the seasonal cycle of FCO_2 changes. Section 5.3.4 explores the role of long-term changes in the ocean vertical DIC concentrations and MLDs. Finally, Section 5.3.5 examines the role of CO_2 buffering capacity on long-term changes in surface pCO_2 and DIC, and this Section concludes by examination of the mean long-term changes in the temperature and DIC components of surface pCO_2.

5.3.1 Century-scale Seasonal Cycle of FCO_2 Changes

The decadal climatologies of the seasonal cycles of the selected mean monthly FCO_2 for 2006 - 2015 (blue) and 2090 - 2100 (brown) are shown in Fig. 5.3 for the five CMIP5 models. The shaded area represents the decadal standard deviation in each model for the Sub-Antarctic and Antarctic Zones. The seasonal cycle of FCO_2 phasing changes between the current scenario and end of the century is examined through the correlation coefficient (r^2), Table 5.1. The analyzed models portray a general similarity based on the phasing characteristics of the two major groups, viz. (CMCC, CanESM2 & IPSL), and (MPI & HadGEM2) described in Chapter 4, as group-SST and group-DIC, respectively.

Models in each cluster were found to show similarities in the seasonal variability of the primary drivers (SST and DIC) of FCO_2, and they showed similar biases against observational estimates in the present climate (1995 - 2005).

In the Sub-Antarctic Zone, CMCC, CanESM2 & IPSL generally maintain comparable seasonal cycle phasing at the end of the century relative to the contemporary ($r^2 > 0.75$, Table. 5.1). Although they all show increased CO_2 uptake, particularly during Autumn (Fig. 5.3 a,c,e). The most notable difference in phasing occurs during winter in IPSL (from mid-winter) and CMCC (Fig. 5.3 c, e), they both show a change in the direction of FCO_2 from a weakened uptake to strengthened sink of CO_2 (Fig. 5.3a, d). CanESM2 shows the least change of all five models for both phasing and magnitude of the seasonal cycle. Nevertheless, as anticipated all five models show larger annual uptake by the end of the century (Fig. 5.4 and Table 5.2), including CanESM2, i.e. -0.33±0.07 Pg Cyr^{-1} for 2006 - 2015 vs -0.46±0.04 Pg Cyr^{-1} for 2090 - 2100. The CMCC anomalous net CO_2 source in the Sub-Antarctic zone becomes a sink by the end of the century (Section 4.3.1), and thus it shows the largest net sink change for group-SST models (Fig. 5.4). Interestingly, note that the largest net sink CO_2 increase for group-DIC models (HadGEM2 and MPI) is in the Sub-Antarctic Zone by end of the century, however, group-SST shows the opposite, showing a larger CO_2 sink increases in the Antarctic Zone with respect to Sub-Antarctic.

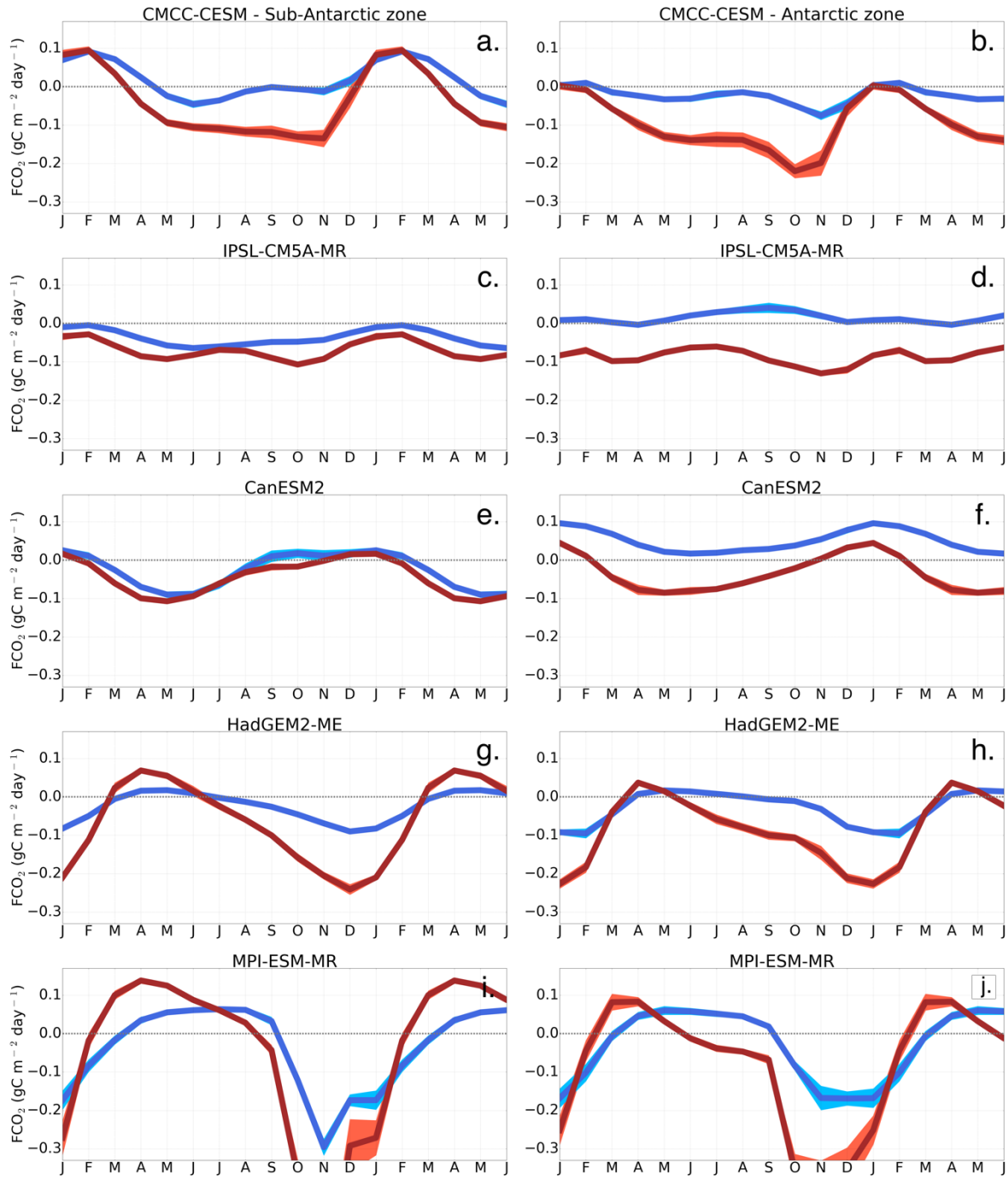

Figure. 5.3 The seasonal cycle of FCO_2 in CMIP5 ESMs in g C m^{-2} day^{-1}, decadal mean climatology seasonal cycle over the periods 2006 - 2015 (blue) and 2090 - 2100 (brown) in the Sub-Antarctic Zone (first column) and Antarctic Zone (second column). The shaded areas represent the decadal standard deviation for each model.

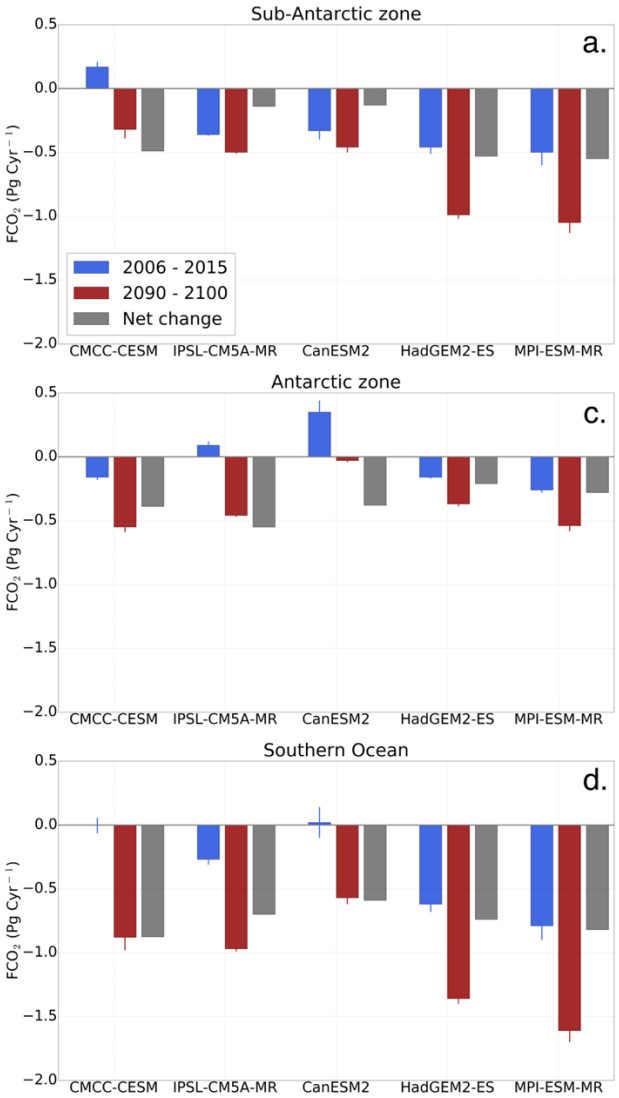

Figure. 5.4 The decadal mean climatology of CO_2 annual mean over 2006 – 2015 (blue) and 2090 – 2100 (red) in Pg C yr^{-1} in the Sub-Antarctic Zone (first column) and Antarctic Zone (second column), the grey bars represent the net change between the present (2006 – 2015) and future (2090 – 2100) scenarios. The vertical bars represent the uncertainty due to the decadal standard deviation.

\

Table 5.2: Sea-Air CO_2 fluxes (Pg C yr^{-1}) annual mean uptake in the Southern Ocean (first column), here defined as south of the Sub-tropical front, Sub-Antarctic Zone (second column), mean of the Southern Ocean (fourth column). The seventh column shows the Correlation Coefficient (R) for the contemporary (2006 - 2015) vs century (2090 - 2100) decadal mean climatological seasonal cycle of monthly mean seasonal cycle of FCO_2.

	Sub-Antarctic zone	Net change	Antarctic zone	Net change	Southern Ocean	Net change
IPSL	2006 - 2015 (-0.36±0.01) 2090 - 2100 (-0.50±0.01)	-0.14	2006 - 2015 (0.09±0.03) 2090 - 2100 (-0.46±0.01)	-0.55	2006 - 2015 (-0.27±0.04) 2090 - 2100 (-0.97±0.02)	-0.70
CMCC	2006 - 2015 (0.17±0.04) 2090 -2100 (-0.32±0.07)	-0.49	2006 - 2015 (-0.16±0.02) 2090 - 2100 (-0.55±0.04)	-0.39	2006 - 2015 (-0.004±0.06) 2090 - 2100 (-0.88±0.10)	-0.88
CanESM2	2006 - 2015 (-0.33±0.07) 2090 - 2100 (-0.46±0.04)	-0.13	2006 - 2015 (0.35±0.09) 2090 - 2100 (-0.03±0.01)	-0.38	2006 - 2015 (0.02±0.12) 2090 - 2100 (-0.57±0.05)	-0.59
MPI	2006 - 2015 (-0.50±0.10) 2090 - 2100 (-1.05±0.08)	-0.55	2006 - 2015 (-0.26±0.02) 2090 - 2100 (-0.54±0.04)	-0.28	2006 - 2015 (-0.79±0.11) 2090 - 2100 (-1.61±0.09)	-0.77
HadESM2	2006 - 2015 (-0.46±0.05) 2090 - 2100 (-0.99±0.03)	-0.53	2006 - 2015 (-0.16±0.01) 2090 - 2100 (-0.37±0.02)	-0.21	2006 - 2015 (-0.62±0.06) 2090 - 2100 (-1.36±0.04)	-0.74
Seasonal cycle Correlations coefficient (r^2) 2006 - 2015 vs. 2090 - 2100	r^2 (CMCC) = 0.92 r^2 (CanESM2) = 0.96 r^2 (IPSL) = 0.79 r^2 (MPI-) = 0.92 r^2 (HadGEM2) = 0.98		r^2 (CMCC) = 0.73 r^2 (Can) = 0.87 r^2 (IPSL) = 0.13 r^2 (MPI) = 0.83 r^2 (HadGEM2) = 0.85		r^2 (CMCC) = 0.86 r^2 (CanESM2) = 0.74 r^2 (IPSL) = 0.38 r^2 (MPI) = 0.89 r^2 (HadGEM2) = 0.93	

MPI and HadGEM2 (group-DIC) show comparable changes in the seasonal cycle of FCO_2 phasing at the end of the century relative to 2006 – 2015, as anticipated. Both models show an increased amplitude of FCO_2 characterized by: enhanced CO_2 outgassing flux in autumn, weakened winter CO_2 outgassing (even strengthened CO_2 uptake in HadGEM2) and more substantial CO_2 uptake during the spring-summer seasons. The spring-summer CO_2 uptake was previously associated with biologically driven CO_2 uptake in the previous chapter and in Kessler and Tjiputra, (2016). Note that the CO_2 outgassing peak (August) occurs four months earlier (April) and much enhanced at the end of the century relative to the present in MPI (> 0.05 gC m^{-2} day^{-1} vs. ≈ 0.15 gC m^{-2} day^{-1}). Whilst the CO_2 outgassing flux has increased during autumn, the spring-summer CO_2 uptake increase is stronger (Fig. 5.3 g, i) in MPI and HadGEM2. Hence the net change is an enlarged CO_2 sink at the end of the century (Fig. 5.3 & 5.4). For example, the modelled threefold increase in the amplitude of the FCO_2 seasonal cycle in HadGEM2, only results in the doubling of the annual CO_2 sink at the end of the century, i.e. -0.46±0.05 Pg C yr^{-1} (2006 - 2015) vs -0.99±0.03 Pg C yr^{-1} (2090 - 2100).

In the Antarctic Zone, CMCC and CanESM2 generally maintain the same phasing at the end of the century as found in the present climate but show stronger CO_2 uptake at the end of the century (Fig. 5.3-4 a-f). For IPSL and CanESM2, the Antarctic Zone CO_2 net fluxes switches from being a net CO_2 source at present (e.g. IPSL 0.09±0.03 Pg Cyr^{-1}) into a CO_2 sink (e.g. IPSL -0.46±0.01 Pg C yr^{-1}) at the end of the century. Of the five models in the Antarctic Zone, IPSL shows the largest difference in the phasing of FCO_2 between the periods 2006 - 2015 and 2090 - 2100 (R= 0.13, Table. 5.1). This is mainly because of the weakening CO_2 uptake peak which occurs three months earlier (July) at the end of the century than the contemporary (September). HadGEM2 and MPI show similar seasonal cycle phasing changes with respect to the Sub-Antarctic, however, the net CO_2 annual uptake is halved with respect to the Sub-Antarctic at the end of the century (Fig. 5.3, Table 1). Similarly, HadGEM2 and MPI show increased amplitude of FCO_2, but they here show more extensive winter CO_2 uptake at the end of the century (Fig. 5.1 g-k).

5.3.2 Changes in the Seasonal variability of the drivers of CO_2

This section uses the diagnostic framework described in Sec. 5.2.2 to examine the seasonal variability of the main drivers of FCO_2 between the periods 2006 - 2015 (present scenario) and 2090 - 2100 (future scenario) in the Sub-Antarctic and Antarctic Zones.

5.3.2.1 Sub-Antarctic zone

In the Sub-Antarctic Zone, CMCC, CanESM2 and IPSL show no major changes in the seasonal variability of the drivers of CO_2 at the end of the century (Fig. 5.5 a, d, e). Although CMCC show increased FCO_2 seasonal amplitude by the end of the century, the seasonal cycle phasing shows little change. This is with the exception of the winter season; this exception is explained by the early (July vs June for 2006 – 2015) switch of surface pCO_2 (hence FCO_2) from temperature control to DIC control. This switch in the drivers was linked to increased surface rates of change of DIC associated with vertical mixing induced by deepening of the MLD in the previous chapter (Section 4.3.4). Otherwise, consistent with the present-day climate, surface pCO_2 variability in group-SST models maintains the dominance of temperature ($M_{T\text{-}DIC} > 0$) as the leading mode during autumn (March – May) and spring to mid-summer (Sept – Jan). They also show DIC control ($M_{T\text{-}DIC} < 0$) the first of half winter as found in the present climate (Fig. 5.5 a, c, e). Note that temperature control strengthens in group-SST models during the spring-summer seasons (September – January) at the end of the century, with the exception of CanESM2. As a consequence, the biologically driven CO_2 uptake expected during spring shown by observations in present climate (Section 4.3.4) is still off-set by

surface warming (weakened CO_2 uptake) at the end of the century in group-SST models. This feature was shown to be contrary to observed estimates for the present-day climate in Chapter 4. The CanESM2 model shows minimal changes in the $M_{T\text{-}DIC}$ in the Sub-Antarctic Zone at the end of the century consistent small changes in the seasonal cycle of FCO_2 (Fig. 5.4e).

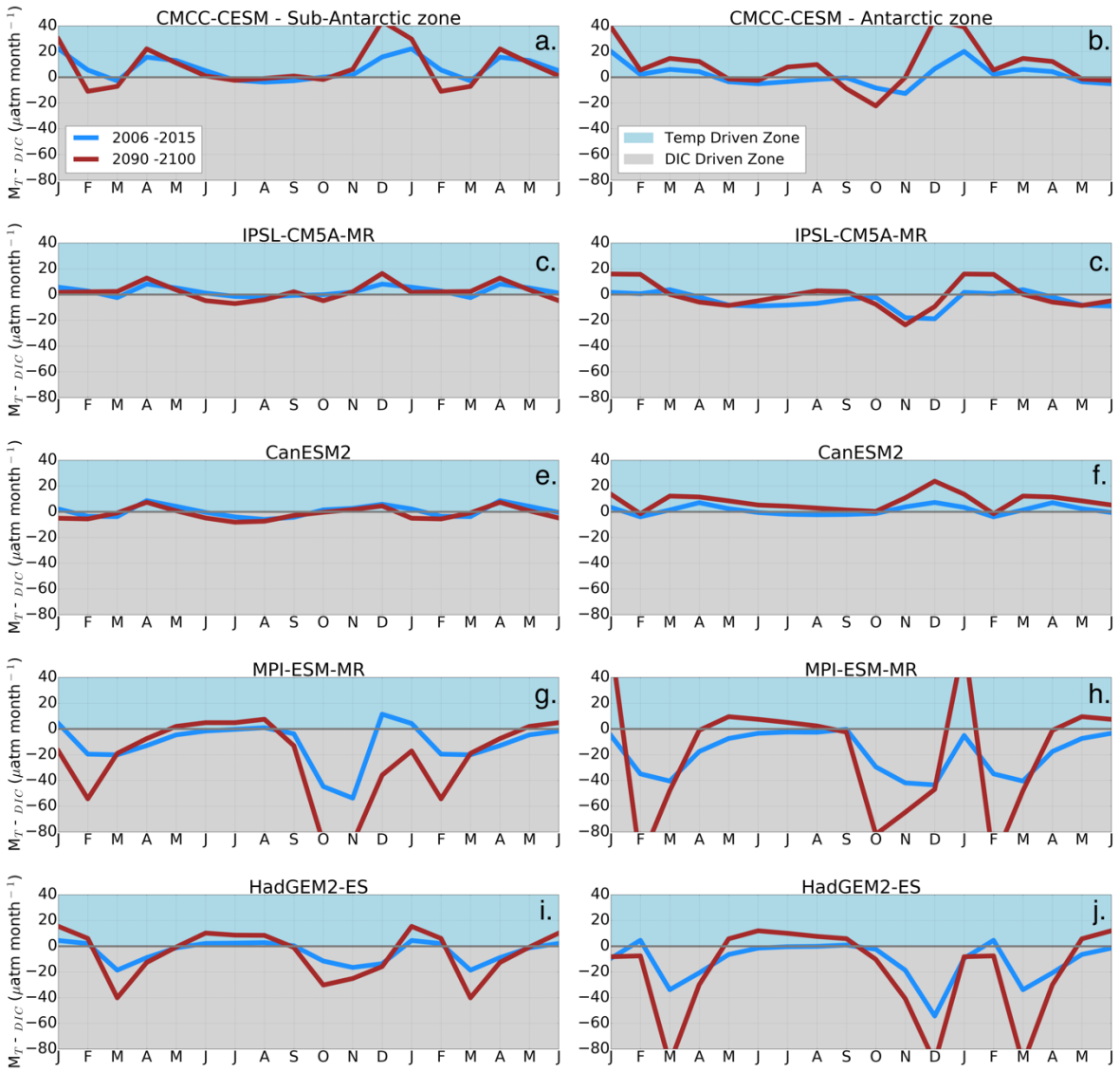

Figure. 5.5 The DIC-temperature diagnostic indicator ($M_{T\text{-}DIC}$) given in µatm month^{-1} for the decadal mean climatology over 2006 - 2015 (present scenario, blue) and 2090 - 2100 (future scenario, red). Increase in the positive direction (blue zone) indicates strength of the temperature driver and the negative direction (grey zone) shows the strength of the DIC driver. The first column shows the Sub-Antarctic Zone and the second column the Antarctic Zone.

Group-DIC models (HadGEM2 and MPI) show two important changes in the seasonal variability of drivers ($M_{T\text{-}DIC}$) of pCO_2 and FCO_2 (Fig. 5.5). They show a switch of the leading driver of surface pCO_2 and FCO_2 between autumn and winter (April/May – August) from DIC-control ($M_{T\text{-}DIC} < 0$) to

temperature-control ($M_{T\text{-}DIC} > 10$ μatm month^{-1}). These changes suggest that by the end of the century the role of DIC as a leading driver of surface pCO_2 and FCO_2 during autumn-winter is overturned by the temperature control which instead strengthens CO_2 uptake through surface solubility (Fig. 5.5 g,i). This explains the weakened CO_2 uptake during winter shown by MPI and HadGEM2 (Fig. 5.3 g, i). HadGEM2 even shows heightened CO_2 uptake during winter. In addition to these changes, HadGEM2 and MPI feature a stronger DIC control between spring and summer (Sept – Dec) at the end of the century. For example, the HadGEM2 $M_{T\text{-}DIC}$ maxima in spring is -15 μatm month^{-1} in the present and -20 μatm month^{-1} at the end of the century. This is with the exception of a brief period between December – February where the HadGEM2 demonstrates an enhanced solubility driver at the end of the century. Importantly, note that whilst surface pCO_2 and FCO_2 in MPI and HadGEM2 feature a switch from DIC control to temperature control in winter (June – August), CMCC and IPSL show the opposite, DIC control is instead strengthened at the end of the century compared to the present scenario.

5.3.2.2 Antarctic zone

In the Antarctic zone, by the end of the century, CMCC and CanESM2 show a general strengthening of temperature control in surface pCO_2 and FCO_2 variability ($M_{T\text{-}DIC}$ increase) during most of the year except for spring (Fig. 5.5 b, d). Consequently, surface pCO_2 and FCO_2 variability in CanESM2 switched from being partially temperature- and DIC-driven (March - August) to almost completely temperature controlled by the end of the century. Of the three group-SST models, IPSL is the only model preserving the most DIC control in FCO_2 changes, it only features temperature control during summer at the end of the century (Fig. 5.5 c).

MPI and HadGEM2 show a similar Sub-Antarctic/Antarctic Zone behavior at the end of the century for the drivers of pCO_2 and FCO_2, viz. a switch from DIC to a temperature control between autumn and winter, and stronger DIC control during the spring and summer seasons (Fig. 5.5h, k). However, the Antarctic Zone has a larger difference in the diagnostic indicator ($M_{T\text{-}DIC} > 10$ μatm month^{-1}) during winter. Thus, the switch from DIC to temperature control is stronger in this region. This larger change in $M_{T\text{-}DIC}$ properly explains the larger change in FCO_2 in this region (compared to the Sub-Antarctic), both MPI and HadGEM2 switched from outgassing to a strong CO_2 sink during the winter by the end of the century (Fig. 5.3 & 5.5 h, i).

5.3.3 Century-scale surface temperature and DIC changes

5.3.3.1 Surface temperature changes

Anthropogenic warming is expected to raise surface ocean temperatures in some areas of the ocean by the end of the century, and this is likely to be reflected in the RCP8.5 model outputs (Bopp et al., 2013; Fu et al., 2016). However, in the Sub-Antarctic Zone, Fig. 5.6 shows that this is only partially true in the models analyzed; only two of the five models (IPSL and HadGEM2) show a net warming (>1.5ºC increase) at the end of the century. However, one is aware that there might be a decadal cycle associated with the SAM/ENSO that might oscillate over longer timescales and hence it is possible that increased SST might be a local change (McKinley et al., 2016). For example, CMCC and MPI show net (> 0.5ºC) surface cooling in the Sub-Antarctic Zone in the future scenario (Fig. 5.6 a, g). Although mean SST changes have important implications for the mean state of CO_2 solubility and surface stratification in the ocean, the seasonal cycle of pCO_2 is more directly regulated by the rate of change of SST through Eq. 2.6.

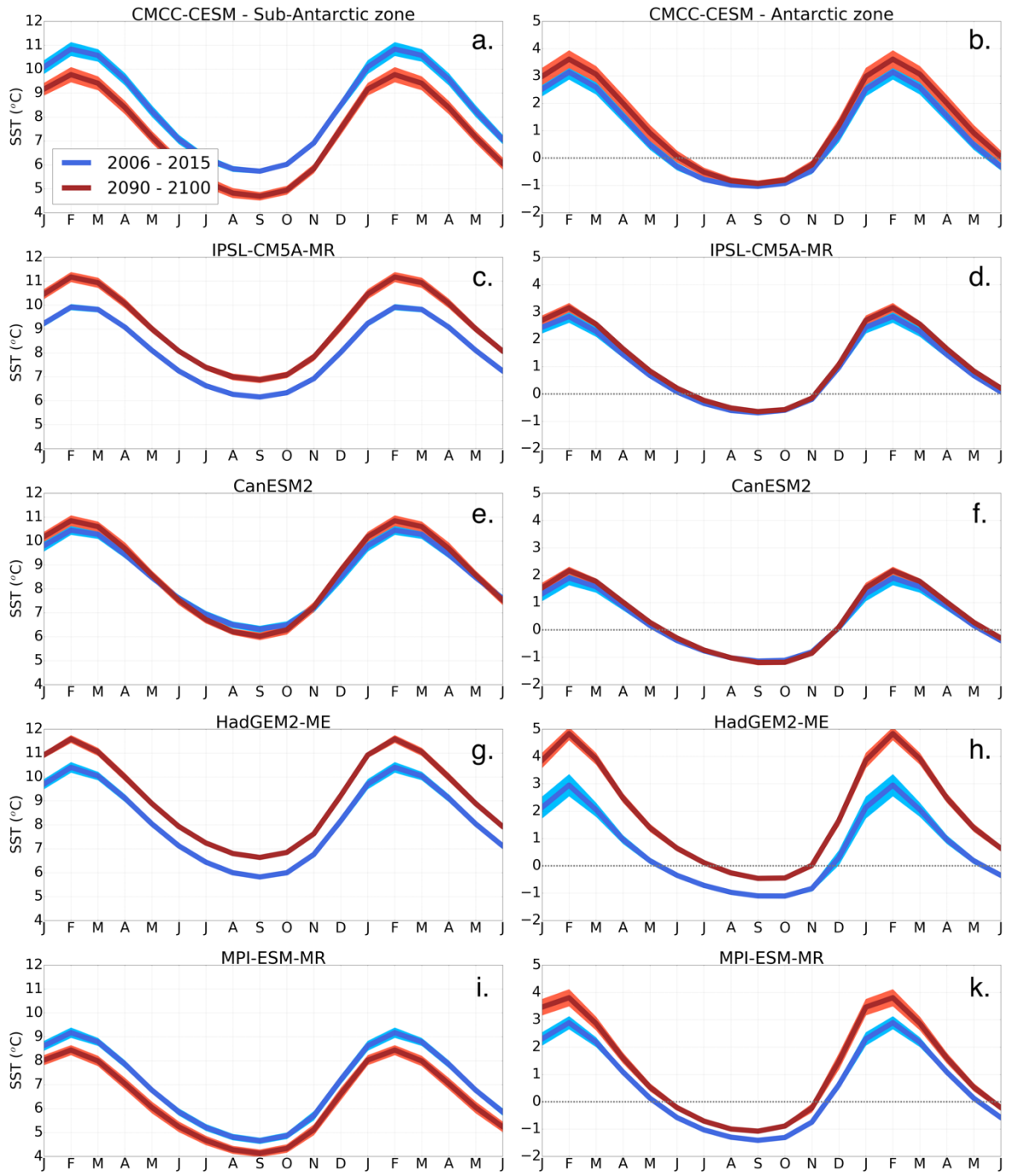

Figure 5.6. The decadal mean climatology of Sea Surface Temperature (SST) over 2006 - 2015 (present scenario, blue) and 2090 - 2100 (future scenario, red) ºC in the Sub-Antarctic Zone (first column) and Antarctic Zone (second column). The shaded areas represent the decadal standard deviation.

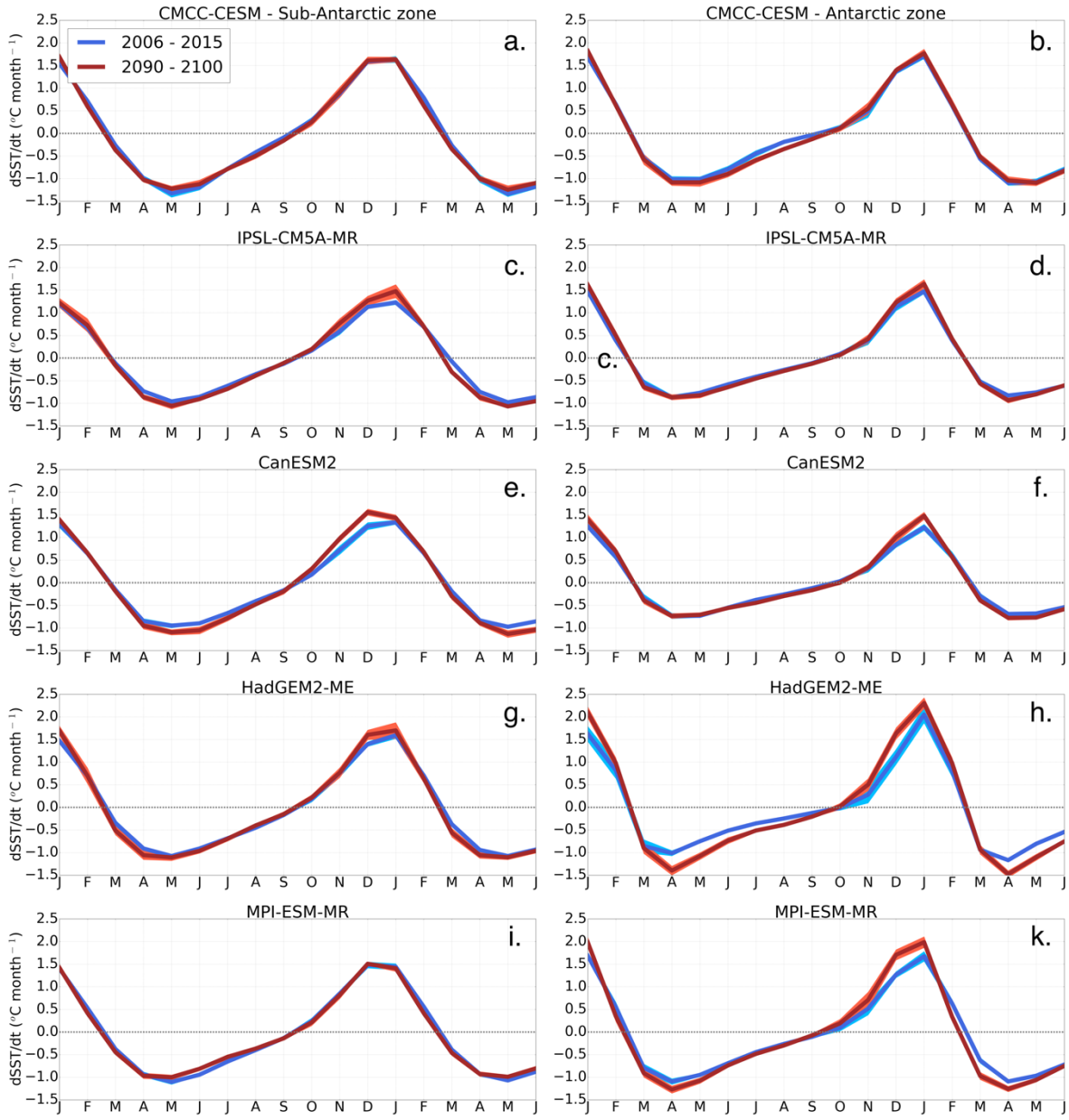

Figure. 5.7 The decadal mean climatology of the rate of change of SST (dSST/dt) over 2006 – 2015 (present scenario, blue) and 2090 – 2100 (future scenario, red) given ^{o}C $month^{-1}$ in the Sub-Antarctic Zone (first column) and Antarctic Zone (second column). The shaded area represents the decadal standard deviation.

The seasonal cycle of dSST/dt is shown in Fig. 5.7. It demonstrates that except for MPI and HadGEM2 in the Antarctic Zone, the models examined show no significant differences in dSST/dt for both phasing and magnitudes between the present and future scenarios. All other models feature small changes of < 0.5 ^{o}C $month^{-1}$ increase in amplitude at end of the century. The exceptions are HadGEM2 and MPI which have about 0.5^{o}C $month^{-1}$ increase in the amplitude of dSST/dt. This is clear during peak cooling and warming seasons i.e. mid-autumn and mid-spring in the Antarctic Zone (Fig. 5.7 h, j) and these higher SST rates are anticipated to strengthen the temperature control on pCO_2 this region. However, whilst the increased seasonal amplitude of dSST/dt probably explains the

stronger role of temperature in HadGE and MPI models in the Antarctic Zone by the end of the century, the same is not true of the Sub-Antarctic or the other models. Nonetheless, all five models do show a general strengthening role of temperature in driving the seasonal cycle of FCO_2, particularly in the Antarctic Zone and some parts of the Sub-Antarctic (Fig. 5.5). In the next section, the possible role of changes in surface DIC is explored.

5.3.3.2 Surface DIC changes

Changes in the amplitude of the seasonal cycle of DIC are illustrated in Fig. 5.8, demonstrating that the seasonal amplitude of DIC predicted is decreased from the present by the end of the century in all models but CanESM2. Note that while this decrease occurs in both the Sub-Antarctic and Antarctic Zones for all five models analyzed, they are particularly pronounced in the Antarctic Zone, especially in HadGEM2 and MPI (Fig. 5.8). For example, HadGEM2 shows about 5 µmol kg^{-1} DIC seasonal amplitude decrease in the Sub-Antarctic and about 18 µmol kg^{-1} in the Antarctic Zone. This is with the exception of CanESM2. The decreased DIC amplitudes are also reflected in the corresponding seasonal cycles of dDIC/dt in Fig. 5.9.

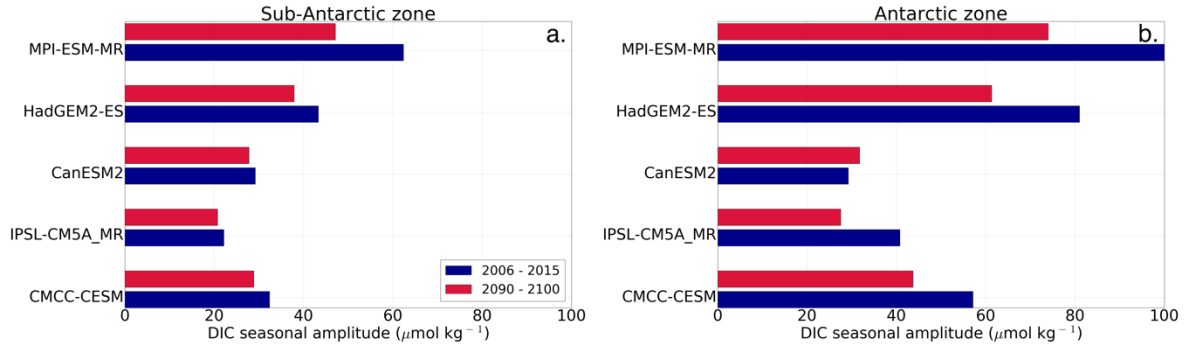

Figure. 5.8 The seasonal cycle of DIC amplitude between 2006 - 2015 (present scenario, blue) and 2090 - 2100 (future scenario, red) given µmol kg^{-1} in the Sub-Antarctic Zone (first column) and Antarctic Zone (second column).

In the Antarctic Zone, with exception of CanESM2, all models had a decrease in the seasonal cycle of the rate of change of DIC in the future scenario (Fig. 5.8). Consistent with the smallest changes in the amplitude of the seasonal cycle of DIC, the Sub-Antarctic Zone generally shows minimal changes in the amplitude of dDIC/dt. For example, CMCC shows about 5 µmol kg^{-1} $month^{-1}$ in the Antarctic vs. ~ 1 µmol kg^{-1} $month^{-1}$ Sub-Antarctic. Once again, the fairly pronounced changes in amplitude of the DIC seasonal cycle in HadGEM2 and MPI models are also reflected in dDIC/dt in the Antarctic Zone (=>10 µmol kg^{-1} $month^{-1}$). These two models show a larger decrease in dDIC/dt during the spring and

summer. The reason for these DIC amplitude dDIC/dt reductions might be linked to decreased primary production and/or vertical mixing in the models by the end of the century.

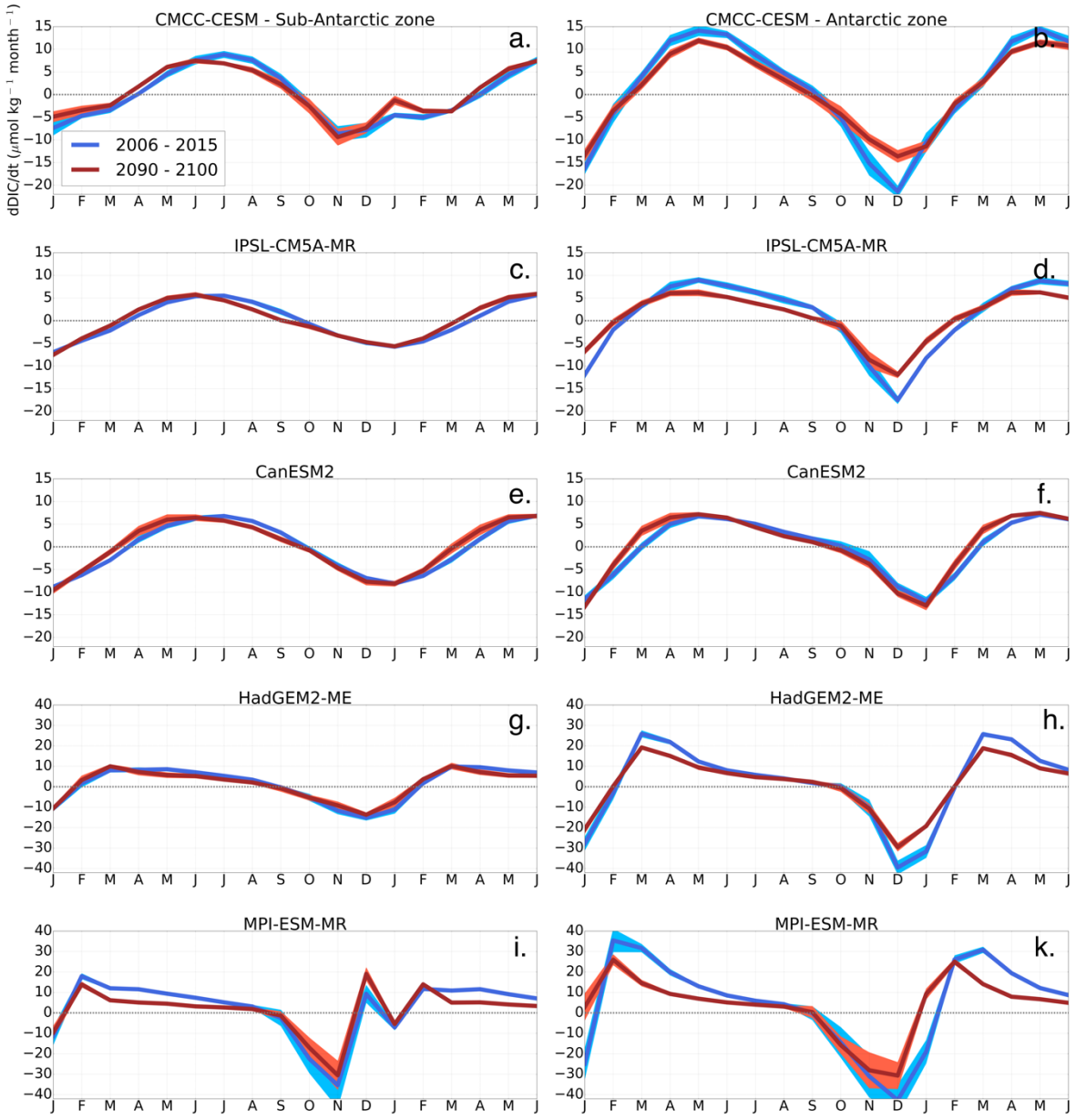

Figure. 5.9 The decadal mean climatology of the rate of change of Dissolved Inorganic Carbon (DIC), (dDIC/dt) over 2006 – 2015 (present scenario, blue) and 2090 – 2100 (future scenario, red) in μmol kg^{-1} $month^{-1}$ in the Sub-Antarctic Zone (first column) and Antarctic Zone (second column). The shaded area represents the decadal standard deviation.

To explore the role of biological activity in the seasonal amplitudes of modelled DIC at the century-scale, possible changes in the Net Primary Production (NPP) are examined in Fig. 5.10. The seasonal cycle of NPP only shows minor changes in phasing or magnitude between present and future scenarios (Fig. 5.10); MPI and HadGEM2 even have a small (≈ +0.2 mmol Chl) increase in NPP,

particularly in the Antarctic Zone by the end of the century. The increase in NPP contrasts with the apparent decrease of seasonal amplitudes of DIC and dDIC/dt in Figs 5.8 - 5.9. Overall NPP does not have major changes at the end of the century; as with the present scenario, larger NPP magnitudes are shown in the Sub-Antarctic Zone (e.g. the HadGEM2 spring maximum is 1.2 mmol Chl) compared to the Antarctic Zone (HadGEM2 spring maximum 1.0 mmol Chl). Nonetheless, there are essential seasonal characteristics of NPP apparent in both the present and future periods that are important for understanding the change in the seasonality of dDIC/dt in the future scenario and thus FCO_2 in the models. For example, the seasonal cycles of NPP do not peak at the same time in the models as shown by Hague and Vichi, (2018) and these are preserved over the century timescale. In the Sub-Antarctic Zone, for example, NPP peaks in November for IPSL and HadGEM2, and December for CanESM2 (Hague and Vichi, 2018). Contrary to other models, the seasonal cycle of NPP peaks twice in MPI; first in November and then December for MPI. In the Antarctic Zone, the seasonal cycle of NPP peaks in December for IPSL, HadGEM2 and MPI, November for CMCC and January for CanESM2. Note that for example, the NPP double peak displayed by MPI in the Sub-Antarctic Zone is also reflected in dDIC/dt (Fig. 5.8-9). Because these features in the peak of NPP are also found in the seasonal cycle of dDIC/dt (Fig. 5.8), they may have a common mechanistic cause that will be explored in the next sections.

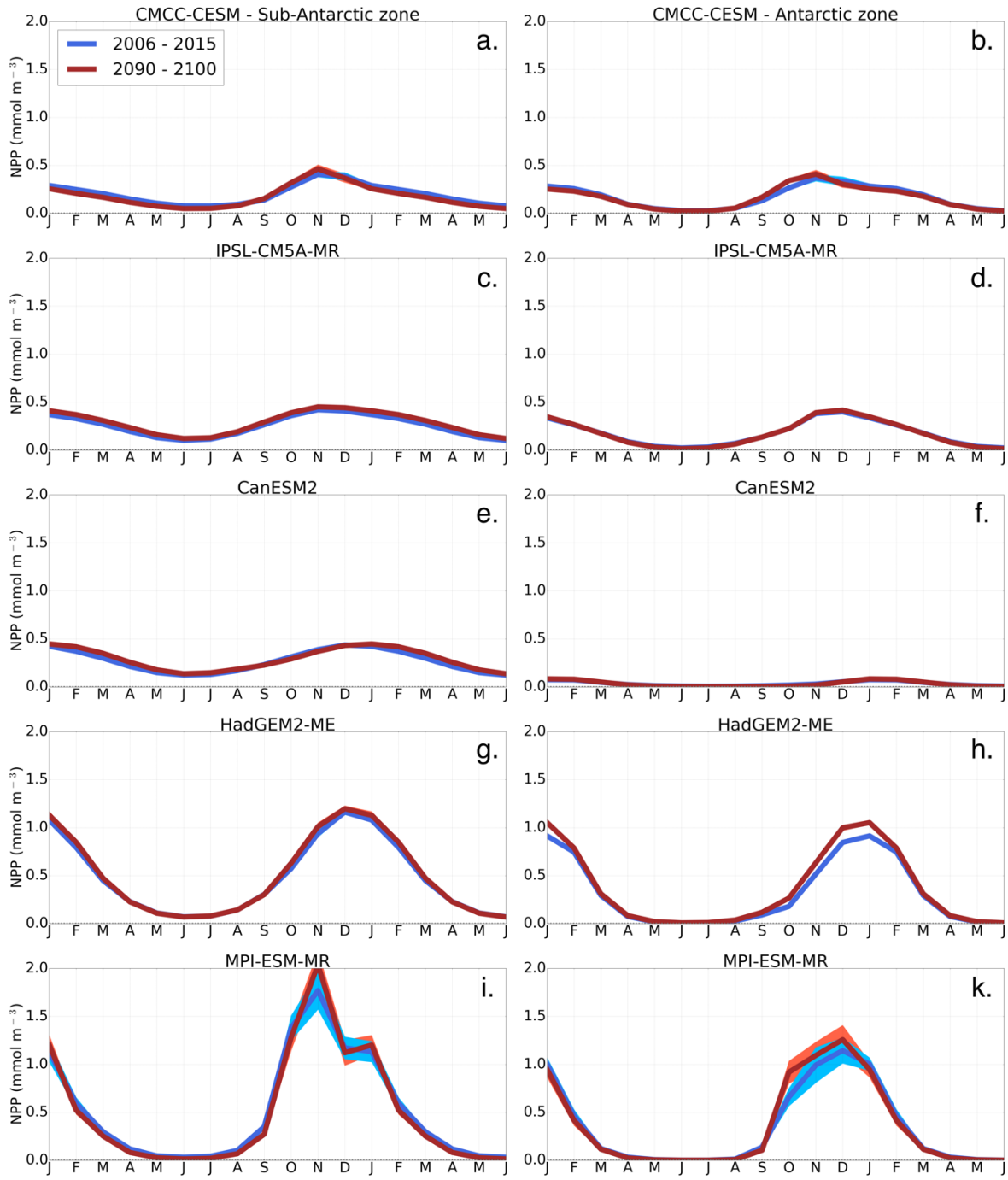

Figure 5.10. The decadal mean climatology of Net Primary Production (NPP) over 2006 – 2015 (present scenario, blue) and 2090 – 2100 (future scenario, red) in mmol m^{-3} in the Sub-Antarctic (first column) and Antarctic Zones (second column). The shaded area represents the decadal standard deviation.

The next Section examines possible changes in the vertical profiles of DIC concentration and mixing that might explain this feature.

5.3.4 Vertical DIC and mixing changes

Anthropogenically driven surface warming is expected to shoal and stratify the mixed layer in the Southern Ocean by the end of the century (Bopp et al., 2001, 2013; Fu et al., 2016; Kessler and Tjiputra, 2016). The seasonal cycles of MLD for the three models (IPSL, CanESM2 and MPI) whose data are still available at the servers are illustrated in Fig. 5.11. They show that indeed the MLD has shoaled by the end of the century in all three models. Note that the MLD is shallower in the MPI model despite the prediction that net surface temperature will have cooled by the end of the century. The modelled decrease in the depth of the mixed layer is might weaken mixing of the surface ocean with subsurface waters.

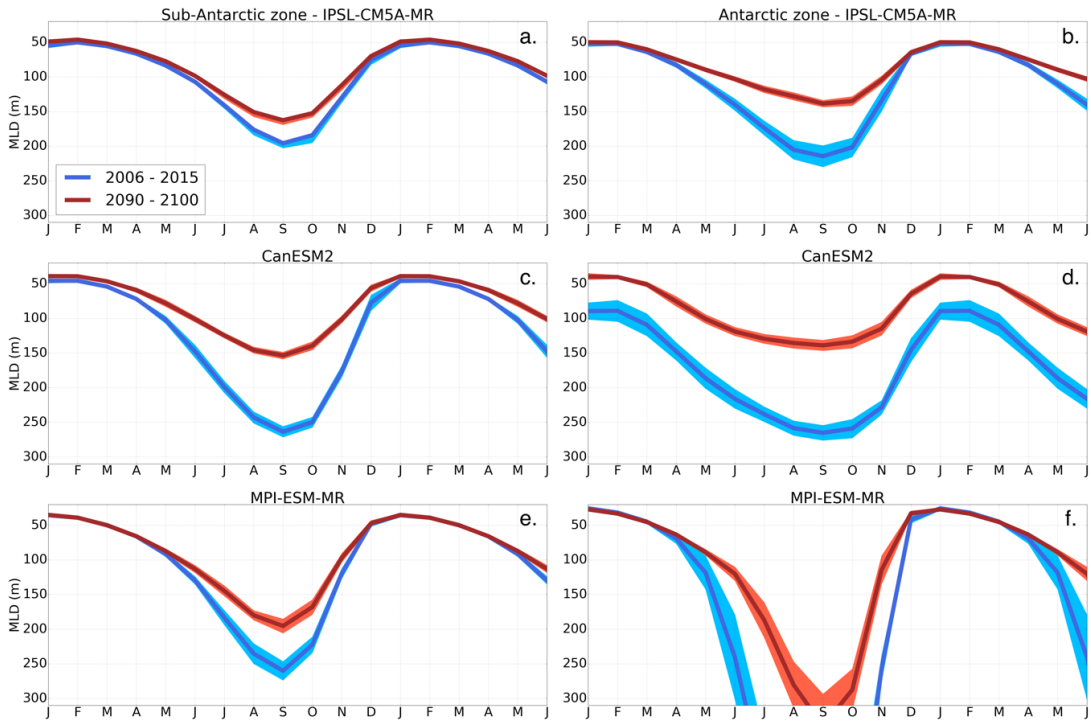

Figure 5.11. The decadal mean climatology of the Mixed Layer Depth (MLD) over 2006 – 2015 (present scenario, blue) and 2090 – 2100 (future scenario, red) in meters depth in the Sub-Antarctic Zone (first column) and Antarctic Zone (second column). The shaded area represents the decadal standard deviation. The depth limits are here set to show the differences, full range figure is shown in the appendix.

To examine possible century-scale vertical DIC concentration changes, Fig. 5.12 shows these with the subsequent vertical DIC gradients in the Sub-Antarctic and Antarctic Zones. It demonstrates that surface DIC concentration increases by about 100 µmol kg^{-1} between present and future scenarios for all five models in both Sub-Antarctic and Antarctic Zones. This accumulation of DIC in the upper ocean by the end of the century shows that the biological pump is slower than the rate at which DIC

accumulates due to increased air-sea CO_2 exchange. Thus, produced organic matter is not transported downwards fast enough to maintain a strong DIC surface/sub-surface gradient. This is indeed indicated by the decrease in the vertical DIC gradient (dDIC/dz) in Fig. 5.12 j-p. The combined effect of shoaled MLDs and weakened DIC vertical gradients diminish the entrainment of DIC in the upper layer and hence the modelled decrease in the seasonal amplitude of DIC and dDIC/dt demonstrated in Figs 5.8- 5.9.

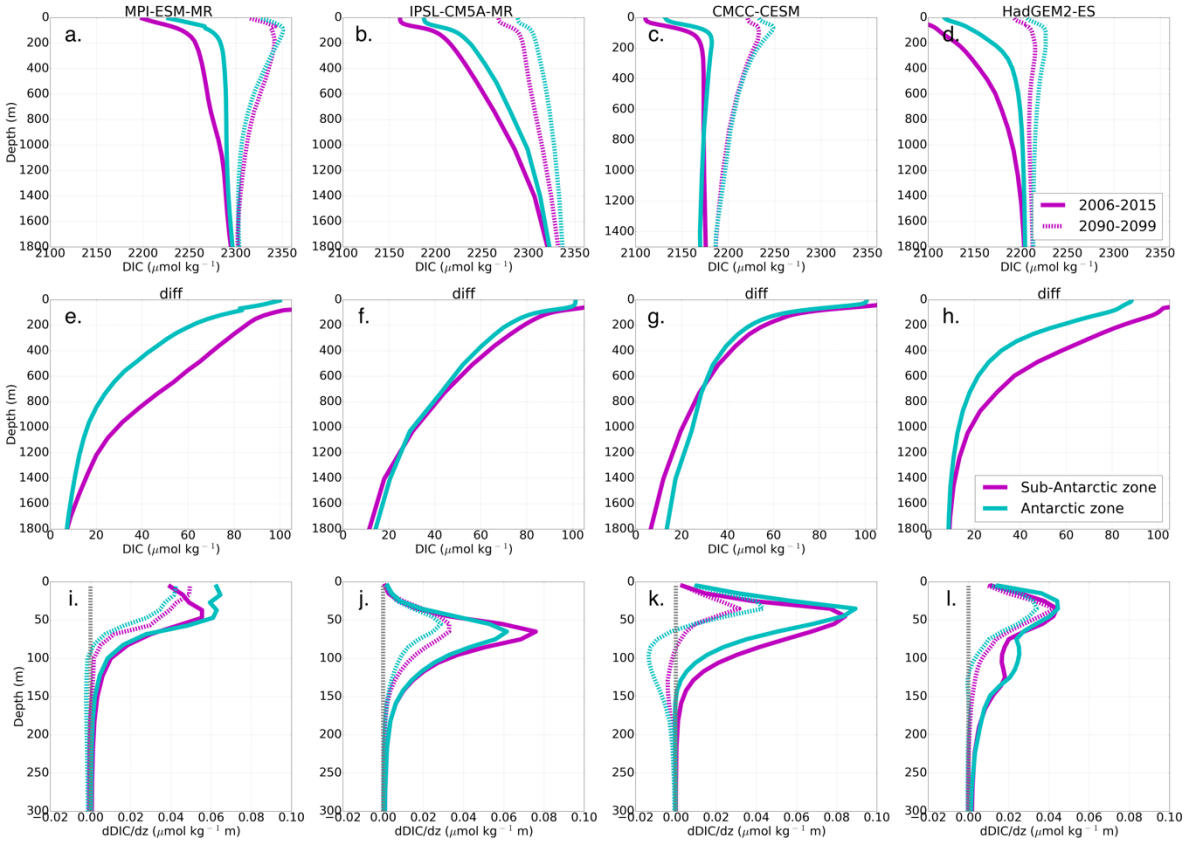

Figure 5.12. The decadal mean climatology of the vertical profile of DIC (a-d) in µmol kg^{-1} over 2006 – 2015 (present scenario, solid line) and 2090 – 2100 (future scenario, dotted line), DIC concentration difference (e-h) between 2006 – 2015 and 2090 – 2100) in µmol kg^{-1}, and vertical DIC gradients (dDIC/dz, depth(i+1 – depth(i) where I is vertical levels increasing with depth (i-l). The Sub-Antarctic Zone shown in magenta and Antarctic Zone in blue.

5.3.5 Buffering capacity and pCO_2 components changes

The dissolution of atmospheric CO_2 into the surface ocean is buffered such that only about 1 of 20 molecules increases the surface CO_2 concentration, the rest of the dissolved CO_2 (aq) either react with a carbonate ion (CO_3^{2-}) to form two bicarbonate (HCO^{2-}) ions or dissociate into a bicarbonate ion (secton 1.2.3). This buffering is quantified by the Revelle factor defined by Eq. 5.5; the ratio of the change in pCO_2 ($dpCO_2/pCO_2$) for a change in DIC (dDIC/DIC). The Revelle factor is projected to increase as the ocean takes up more CO_2 which leads to weakening the buffering capacity of the surface ocean (Hauck, 2018; Hauck and Völker, 2015). Hence, smaller DIC changes are expected to result in larger pCO_2 changes at the end of the century (Hauck, 2018; Hauck and Völker, 2015). To examine this phenomenon and its impact on the seasonal cycle of pCO_2 and FCO_2, the mean Revelle factor magnitudes between present and future scenarios were shown in Fig. 5.1 for the Southern Ocean (south of STF). Fig. 5.1 indicates that the Revelle factor has increased in all five models at the end of the century models, consistent with previous studies (e.g. Hauck and Völker, 2015; McNeil and Sasse, 2016). Note that while all five models have an increased Revelle factor by the end of the century, the uncertainty (decadal standard deviation) is larger in the future scenario. Group-DIC models (MPI and HadGEM2) show a larger increase in the Revelle factor over century timescales than group-SST models (Fig. 5.1)

The effect of CO_2 buffering changes on surface pCO_2 over century timescales is evaluated in Fig. 5. 14. The seasonal cycle amplitudes of pCO_2 and DIC are here illustrated together for convenience though the seasonal cycle amplitudes changes in DIC was already shown in Fig. 5.8. It demonstrates that the seasonal amplitude of pCO_2 is indeed generally increased, although the seasonal amplitude of DIC has decreased for all five models.

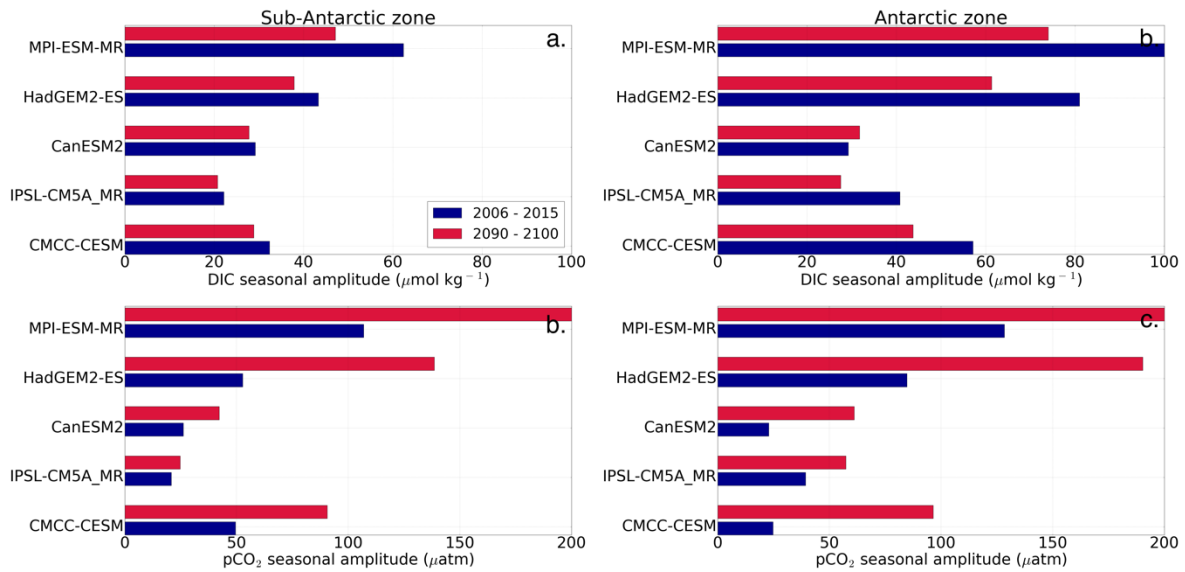

Figure. 5.13 The seasonal cycle of DIC and pCO_2 amplitude between 2006 – 2015 (blue) and 2090 – 2100 (red) given µmol kg^{-1} and µatm respectively in the Sub-Antarctic zone (first column) and Antarctic zone (second column).

Having analyzed changes in temperature, biological activity and vertical DIC structure between the present climate and end of the century, the following examines their net effect on the seasonality of pCO_2 (and hence FCO_2). This is done by evaluating the net change in the temperature ($\Delta(dpCO_2/dt)_{SST}$) and DIC components ($\Delta(dpCO_2/dt)_{DIC}$) of surface pCO_2 between the present climate and end of the century. Note that $(dpCO_2/dt)_{SST}$ and $(dpCO_2/dt)_{DIC}$ are the terms used to compute the $M_{T\text{-}DIC}$ in Eq. 5.4. Thus, as outlined in Section 5.2.2, variations in $(dpCO_2/dt)_{SST}$ are governed by Eq. 2.5 and $(dpCO_2/dt)_{DIC}$ by Eq. 2.4.

The seasonal cycles of $\Delta(dpCO_2/dt)_{SST}$ and $\Delta(dpCO_2/dt)_{DIC}$ are given in Fig. 5.14. The analyzed models show similarity in the seasonal cycle of $\Delta(dpCO_2/dt)_{SST}$ in both phasing and magnitude in the Sub-Antarctic Zone but have differences in magnitudes in the Antarctic Zone. Note that the CMIP5 models' agreement in $\Delta(dpCO_2/dt)_{SST}$ seasonal phasing is consistent with models generally agreement in the long-term changes in the seasonal cycle of dSST/dt (Fig. 5.7). Hence larger changes shown by MPI and HadGEM2 in the Antarctic Zone are consistent with their relatively larger changes in the seasonal amplitude of dSST/dt between the present climate and end of the century (Fig. 5.7 h, i).

On the other hand, the seasonal cycles of $\Delta(dpCO_2/dt)_{DIC}$ show major differences between group-SST and group-DIC models (Fig. 5.14 b, d). In group-SST models, $\Delta(dpCO_2/dt)_{DIC}$ peak in between May-June and have a minimum in mid-summer (January) in the Sub-Antarctic Zone. In the Antarctic Zone, group-SST models generally show smaller $\Delta(dpCO_2/dt)_{DIC}$ magnitudes with respect to the Sub-

Antarctic and peaks two-three months earlier (Fig. 5.14d). In group-DIC models, $\Delta(dpCO_2/dt)_{DIC}$ demonstrate more seasonal variability (with respect to group-SST) and larger magnitudes during the spring-summer seasons in both Sub-Antarctic and Antarctic Zone with respect to group-SST models. This is with an exception of HadGEM2 in the Sub-Antarctic zone, which has comparable magnitudes with group-SST models (Fig. 5.14b). In the Antarctic Zone, group-DIC models generally show a similar phasing with the Sub-Antarctic Zone excepts that magnitudes are larger (Fig. 5.14d).

The seasonal variability and magnitudes of $\Delta(dpCO_2/dt)_{DIC}$ is governed by long-term changes in the surface DIC rates of changes (dDIC/dt (Fig. 5.9), and these are linked to changes in the vertical mixing and biological terms of DIC according to Eq. 2.4. The horizonal component is here neglected as explained in Section 5.2.2. Subsequently, long-term changes in the $\Delta(dpCO_2/dt)_{DIC}$ associated with vertical mixing changes are expected during the autumn-winter periods when entrainment fluxes peak (Fig. 4.11). Similarly, biologically linked changes in $\Delta(dpCO_2/dt)_{DIC}$ are anticipated during the spring-summer seasons when biological activity heightens (NPP, Fig. 5.10). Although, entrainment fluxes are not directly calculated for this chapter, estimates for the present climate are shown in the previous chapter (Fig. 4.11). Thus, the long-term changes in the vertical mixing and biological component in $\Delta(dpCO_2/dt)_{DIC}$ can be roughly inferred by examining dDIC/dt differences between present climate and future accordingly.

Consequently, as anticipated the seasonal cycle of $\Delta(dpCO_2/dt)_{DIC}$ in group-SST models features a peak during the autumn-winter seasons coinciding with the timing of enhanced vertical mixing and minimum in late-summer coinciding with NPP (Fig. 5.10). Therefore, these $\Delta(dpCO_2/dt)_{DIC}$ changes can be roughly ascribed to long-term vertical mixing and biological activity related to changes. However, addition to these, group-DIC models show a $\Delta(dpCO_2/dt)_{DIC}$ peak three-four months earlier (February – March), thus vertical mixing changes are unlikely to be the driver. The associated DIC changes here may be related the return of organic matter to DIC through respiration.

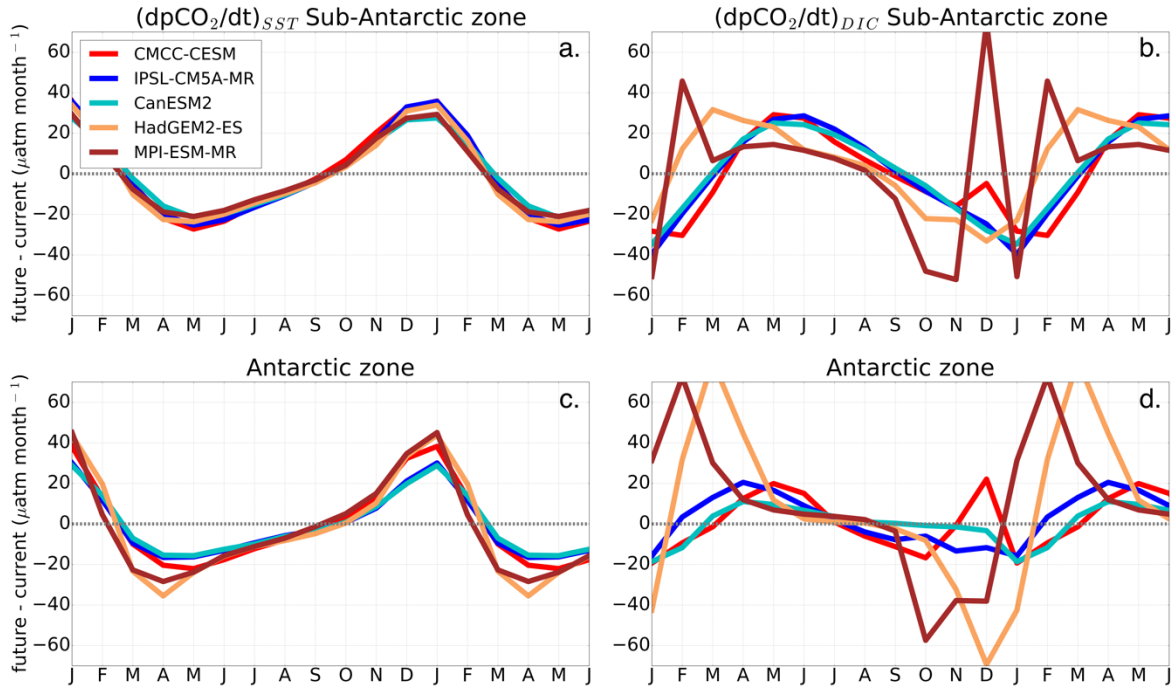

Figure. 5.14 Five models: The seasonal cycle of the difference between (future [2090-2100] – present [2006-2015] scenarios in the SST (i.e. $\{(dpCO_2/dt)_{SST\ future}\} - \{dpCO_2/dt)_{SST\ present}\}$ and DIC components of pCO_2 in μatm $month^{-1}$ in the Sub-Antarctic Zone (top row) and Antarctic Zone (lower row).

5.4 Discussion

A recent study by Kessler and Tjiputra (2016) showed that both the mean annual uptake and seasonal cycle of FCO_2 biases in CMIP5 models in the present climate persist to the end of the century with respect to the ensemble mean. This indicates that present-day FCO_2 biases are preserved to the end of the century in CMIP5 models. Chapter 4 established the two primary sources of bias responsible for the limited skill in the seasonal cycle of FCO_2 in the Southern Ocean: overestimated warming and cooling rates (group-SST models), and exaggerated biological activity (group-DIC). Here the implications of these FCO_2 biases to long-term modelled mechanisms of CO_2 uptake are examined.

It was found that modelled seasonal cycle of FCO_2 characteristics at the end of the century show similarities within group-SST and group-DIC models such that a similar grouping can be applied (Fig. 5.3). More importantly, while all five models showed increased CO_2 uptake at the end of the century consistent with previous studies (e.g. Hauck and Völker, 2015; Wang et al., 2016), the mechanisms driving the increased uptake differs. These could be categorized into group-SST and group-DIC at the

end of the century, consistent with the present-climate grouping based on a phasing criteria presented in Chapter 4. The subsequent sections explore the mechanisms of CO_2 uptake within group-SST and group-DIC at the end of the century with respect to the present climate.

5.4.1 Response to a warming scenario in temperature biased models

Group-SST models overall show minimal changes in the drivers of surface pCO_2 (and hence FCO_2) in the Sub-Antarctic Zone by the end of the century (Fig. 5.5). Temperature generally remains a dominating driver of surface pCO_2 and FCO_2 variability during autumn and spring - summer as found in the present-day climate. This is with the exception of a brief period in mid-summer when CanESM2 and CMCC switch from temperature control ($M_{T\text{-}DIC} > 0$) to DIC control ($M_{T\text{-}DIC} < 0$) , (Fig. 5. 5). Because of the predicted increased atmospheric CO_2 at the end of the century under the RCP8.5 scenario, the air-sea CO_2 gradient is enhanced and thus also CO_2 uptake. CO_2 uptake for group-SST models is stronger during autumn and part of winter at the end of the century due to increased surface solubility linked to cooled surface waters (Figs 5.3 and 5.5 a, c, e). Although the first half of winter surface pCO_2 changes are dominantly DIC controlled in group-SST models, this only weakens the rates of CO_2 uptake, but the net CO_2 sink is increased during winter at the end of the century in the Sub-Antarctic zone (Fig. 5.5 a ,c, e). This is also because DIC control is only dominant the first half of winter (Fig. 5.5), temperature control overturn DIC control by late winter (August) and spring. During spring, group-SST models generally show strengthened temperature control by the end of the century, with the exception of CanESM2. Consequently, the biological CO_2 uptake expected in spring is still offset by surface warming at the end of the century as found in the present climate in the Sub-Antarctic zone. In the Antarctic Zone, SST-models show a general strengthening of temperature control. Thus the seasonal cycle of pCO_2 and FCO_2 in CMCC and CanESM2 switch from being partly temperature- and partly DIC- controlled, to being mostly temperature controlled with an exception for spring at the end of the century (Fig. 5.5 b, d, I). IPSL is the only model in the group-SST models that preserve DIC control most of the year by the end of the century (Fig. 5).

The two main factors that influence the modelled long-term changes in the seasonal drivers and sink of CO_2 in group-SST models are the increased Revelle factor and increased atmospheric CO_2 (Fig. 5.12). In the Sub-Antarctic Zone for example, although the rate of change of SST and DIC demonstrate limited change (Fig. 5.7 & 5.9), the temperature ($\Delta(dpCO_2/dt)_{SST}$) and DIC components ($\Delta(dpCO_2/dt)_{DIC}$) of surface pCO_2 increase by comparable amounts at the end of the century (Fig. 5.14). For $\Delta(dpCO_2/dt)_{SST}$, these changes are mainly driven by increased surface pCO_2 which is caused by raised atmospheric CO_2 under RCP8.5. Secondly, seasonal scale variations in pCO_2 are larger at end of the century due to reduced surface CO_2 buffering capacity (Fig.5.1). Similarly, the

increase in the DIC component $\Delta(dpCO_2/dt)_{DIC}$) is mostly influenced by reduced surface buffering capacity since the amplitude of seasonal DIC variation is decreased at the end of the century (Fig. 5.13). The seasonal amplitude of pCO_2 change under a weaker buffering capacity feature a net increase although the seasonal amplitude of DIC had decreased by the end of the century related to weakened vertical mixing (Fig. 12-13). However, contributions to the pCO_2 seasonality from the SST and DIC components increase similarly in the Sub-Antarctic Zone for group-SST models at the end of the century (Fig. 5.14). But because the FCO_2 in group-SST models is biased by the overestimated rates of change of SST in the present climate, the resulting net driver between autumn and summer remains temperature. This outcome emphasises the importance of present-day biases in the seasonal cycle of FCO_2 as a determinant of future changes in the sink and variability of CO_2.

In the Antarctic Zone, surface rates of change of DIC (dDIC/dt, Fig. 4.9) decrease more than the Sub-Antarctic consistent with the decrease in the DIC seasonal amplitude (Fig. 5.13), hence although the Revelle factor has increased, net changes in $\Delta(dpCO_2/dt)_{DIC}$) are smaller. The reason for these differences in the seasonal amplitudes of DIC between the Sub-Antarctic and Antarctic Zones remains unknown. However, I speculate that these are probably due to weaker vertical mixing in the Antarctic region than in the Sub-Antarctic at the end of the century. This speculation is partly supported by differences in the mean MLD changes between the present climate and end of the century. MLD shoals more in the Antarctic by the end of the century than in the Sub-Antarctic Zone; for example, IPSL and HadGEM2 shoals by about 50 m and 110 m, respectively, in the Sub-Antarctic Zone, but up to 90 m and 130 m in the Antarctic Zone (Fig. 5.12). Thus, shallower MLDs probably lead to weaker vertical mixing and hence weaker surface DIC seasonal variations. Because NPP does not show major changes in this region (except for the MPI and HadGEM2 models) it is likely that the vertical component of DIC (entrainment) is responsible for these differences. As a consequence of the weaker increase in $\Delta(dpCO_2/dt)_{DIC}$ by the end of the century with respect $\Delta(dpCO_2/dt)_{SST}$ in the Antarctic Zone (Fig. 5.14), temperature control strengthens as a driver of pCO_2 and FCO_2 with respect the present climate. Thus surface pCO_2 and FCO_2 variability is mostly temperature controlled in CanESM2 and CMCC. This weakening of DIC control also applies to IPSL, but IPSL starts with a net stronger DIC control in the present climate, thus the net change remains under DIC control (Fig. 5.5d).

Models that show DIC control in surface pCO_2 during spring in the present climate in the Antarctic Zone (CMCC and IPSL), showed a strengthened DIC control by the end of the century (Fig. 5.5b,d). This spring DIC control was linked to biological uptake in the previous chapter. Thus this preservation of DIC control during spring suggests that the biologically driven CO_2 uptake is preserved to the end of the century in CMCC and IPSL (Fig. 5.3, 14b,d). Once more, although NPP does not show a significant increase by the century end in these models in CMCC and IPSL, because

of the decreased ocean buffering capacity at the end of the century, CO_2 uptake is larger for smaller DIC changes (Figs 5.1, 5.10 & 5.13).

5.4.2 Response to a warming scenario in DIC biased models

Group-DIC models (MPI and HadGEM2) show two similar important changes in the drivers of surface pCO_2 and FCO_2 at the end of the century in the Sub-Antarctic and Antarctic Zones. These are: i) a switch from DIC controlled surface pCO_2 and FCO_2 variability to temperature controlled between late autumn and winter, and ii) Strengthening of the DIC control in surface pCO_2 and FCO_2 between mid-spring to mid-summer.

The leading factor that distinguishes how group-DIC models respond to long-term changes in the drivers of surface pCO_2 and FCO_2 in comparison with group-SST models is linked to NPP and the subsequent DIC rates of change in the present climate (Figs 5.8 – 5.9). In Chapter 4, it was demonstrated that the seasonal cycle of FCO_2 is mainly driven by biological activity in group-DIC models in the present climate and exaggerates NPP with respect to observed estimates. One of the features emerging from overestimated NPP which is also speculated about in Chapter 4, is the role of respiration in surface DIC and pCO_2 changes. In particular, the return of organic of DIC in the surface ocean after maximum production (NPP peak). This is shown by the rapid increase of surface DIC concentration immediately after the NPP peak and co-occurs with surface O_2 depletion (Figs 5.8, 5.9 and 5.15). This feature is more visible in MPI and HadGEM2 models but also illustrated by CMCC to a lesser extent (Figs 5.8, 5.9 and 5.15) and it becomes an important determinant of how long-term changes in the drivers of surface pCO_2 occur in group-DIC models as outlined below.

The net long-term change in the DIC component of surface pCO_2 ($\Delta(dpCO_2/dt)_{DIC}$) in Fig. 5.14 is regulated by surface DIC terms in Eq. 2.4: vertical mixing (entrainment), biological (Production + Respiration) and lateral mixing. For this analysis it is assumed that lateral mixing can be ignored given the mid-low resolution models used, however, this assumption is pending further investigation when the necessary variables are available (monthly 3D DIC), but currently they are not. The seasonal variability of the vertical mixing term is modulated by the solar cycle-driven buoyancy fluctuations over seasonal timescales (Dong et al., 2008) and can be roughly examined through seasonal MLD changes (Chapter 4, Fig. 4.11). Consequently, changes in $\Delta(dpCO_2/dt)_{DIC}$) resulting from vertical mixing are anticipated between autumn-winter when vertical mixing is most actively induced by weakened buoyance flux (deepening of the MLD). Consequently, the role of long-term changes in vertical mixing in $\Delta(dpCO_2/dt)_{DIC}$) is clearer in group-SST models in the Sub-Antarctic Zone. It is

shown by the $\Delta(dpCO_2/dt)_{DIC}$) peak in early winter coinciding with the timing of entrainment fluxes shown in Chapter 4 (Fig. 4.11), (Fig. 5. 11, 14b). Once more, note that although dDIC/dt shows a net decrease at the end of the century during winter, decreased CO_2 buffering capacity enhances pCO_2 changes such the net change in $\Delta(dpCO_2/dt)_{DIC}$) increases by the end of the century. In the Antarctic Zone, this peak occurs two months earlier (April) and with smaller magnitude, this is consistent with the relatively reduced seasonal DIC amplitudes and rates of changes (with respect to the Sub-Antarctic) (Figs 5.9 & 5.13). These features are also shown by group-DIC models but magnitudes are smaller although the net change in NPP, DIC and dDIC/dt are larger relative to group-SST models at the end of the century (Figs 5.9-11). The following shows why this is the case.

The second term in Eq. 2.4 is DIC variation by biological processes, consumption of surface DIC to form organic matter by primary production occurring when the ocean stratifies and light is available. It starts in spring in the Southern Ocean and peaks in early to mid-summer. Once more, long-term changes associated with this term are expected during the spring-summer seasons when surface biological production is most active (Fig. 5.10). Hence the $\Delta(dpCO_2/dt)_{DIC}$) seasonal minimum in mid-summer in Fig. 5.14 is ascribed to primary production which also coincides with the NPP peak (Fig. 5.10). From Fig. 5.14 it is evident that both group-SST and group-DIC show this feature, however, exemplified most in MPI and HadGEM2 due to larger long-term changes in NPP (Fig. 5.10). Subsequently, the increased DIC control (group-DIC models) can be linked to $\Delta(dpCO_2/dt)_{DIC}$) changes in spring and thus CO_2 uptake increase at the end of the century in Fig. 5.14. Once again, the large increase in the DIC control ($M_{T\text{-}DIC}$) and CO_2 uptake at the end of the century shown by group-DIC models although smaller changes are seen in NPP and dDIC/dt, is most probably linked the weakened buffering capacity at the end of the century. Note that the Revelle factor increase at the end of the century is particularly large in group-DIC models.

After the spring minimum, $\Delta(dpCO_2/dt)_{DIC}$) shows a rapid increase and peaks in mid-summer in group-DIC models (Fig. 5.14); this feature is also visible in the surface DIC rates of change (Fig. 5.9). As explained above, these changes are speculated to be due to the return of organic matter to DIC through respiration. By the end century, the change in this early summer $\Delta(dpCO_2/dt)_{DIC}$) peak is larger than the early winter $\Delta(dpCO_2/dt)_{DIC}$) peak associated with vertical mixing (Fig. 5.14). Both the Sub-Antarctic and Antarctic Zones show this behaviour in group-DIC models, but this is more pronounced in the Antarctic Zone. Because the long-term changes in the influence of vertical mixing (Apr/May) are smaller than the temperature component ($\Delta(dpCO_2/dt)_{SST}$) during winter, temperature replaces DIC as a dominant driver of surface pCO_2 and FCO_2 by the end of the century in group-DIC models between autumn and winter. As a result, surface pCO_2 and FCO_2 variability become mainly regulated by solubility changes between autumn and winter. This strengthens CO_2 uptake through solubility (cooled surface ocean) as opposed the vertical mixing driven CO_2 outgassing found in the

present-day climate. Note that the double peak in NPP shown by MPI is also shown the corresponding double peak in ($\Delta(dpCO_2/dt)_{DIC}$ in late summer (Fig. 5.14).

5.5 Conclusion

This chapter sets out to investigate the implications of the two main seasonal cycles of FCO_2 biases shown in Chapter 4 to long-term (present climate vs end of the century) modelled FCO_2 characteristics. The overestimated rates of surface warming and cooling during peak seasons (autumn and spring) in group-SST models, and exaggeration of primary production in group-DIC models. The outcome showed that although long-term CO_2 uptake is increased by the end of the century in both model groups, the mechanisms are different in these two model groups.

Group-SST models show minor long-term changes in the drivers of surface pCO_2 and FCO_2 at the end of the century, and temperature remains a dominant driver during autumn and spring to mid-summer in the Sub-Antarctic Zone. Thus, biologically driven uptake remains offset by surface warming in group-SST models. In the Antarctic Zone, surface pCO_2 and FCO_2 in group-SST models mostly transition from being partly temperature and partly DIC-controlled to being mostly temperature controlled except the spring season. This is with the exception of the IPSL model which still preserves DIC control for most of the year at the end of the century. During the spring, group-SST models that featured DIC control in the present climate, show enhanced DIC control at the end of the century during spring.

On the other hand, group-DIC models show two important changes in the drivers of pCO_2 and FCO_2 at the end of the century: first, during winter DIC control in surface pCO_2 and FCO_2 associated with vertical mixing is overtaken by temperature control. This change enhances CO_2 uptake during winter in group-DIC models through solubility, as opposed to decreased CO_2 uptake driven by vertical mixing as found in the present climate. Second, the DIC control of pCO_2 associated with primary production is enhanced by the end of the century driven by an increased Revelle factor. This leads to an increased CO_2 uptake during spring is increased although primary production does not show significant changes at the end of the century, consistent with Hauck and Völker (2015) and McNeil and Sasse, (2016).

This outcome has important implications for long-term Earth System Modelling of CO_2 in the Southern Ocean. It suggests that modelled CO_2 characteristics are model-specific in CMIP5 models,

depending on which models are used the mechanisms that explain the CO_2 sink are different. This emphasises that a single models or supervised model selection for ensemble approaches to long-term prediction should be approached with consideration of the mechanistic skill of the model. Needless to say, the paucity of observations in the Southern Ocean is well recognized and important phenomena (e.g. Fay et al., 2018; Ritter et al., 2018). Thus the contribution that these unceratainties have to the biases remain poorly understood. However, in addition to considering biases that may arise from these, considering limitations that relate to model skill as it relative representing the mechanisms might also be a key aspect. For example, the approach taken by Wang et al. (2016) to select models based on performance against observations is a novel idea that does reduce model spread. However, a consequence of this approach is that it tends to select models that underestimate biological activity in the Southern Ocean (group-SST models). Although model uncertainty is reduced, the selected models inadequatly represents the role of biological activity. In contrast, Hauck and Völker (2015) suggest that biological activity plays a strengthening role in century-scale CO_2 uptake in the Southern Ocean; this outcome is here only supported by models that overestimate primary production (group-DIC models). Although the model analysed in Hauck and Völker (2015) was not analysed here, it probably falls into group-DIC of this dissertation as they show the seasonal characteristics. Once again, the increase in the seasonal amplitude of CO_2 shown by McNeil and Sasse (2016) at the end of the century, and by Landschützer et al. (2018) based on observations estimates (due to the increased Revelle factor), is only supported by group-DIC models. This feature is likely to be real because it is also shown by historical observations (Landschützer et al., 2018). The fact that it is only shown by models that overestimate primary production (group-DIC) in relation to observed estimates in the present climate, quantifying its extent is rather difficult given the NPP bias in these models. This outcome once more highlights that biases in the seasonal cycle of FCO_2 in the present climate may be a key limitation to appropriately simulating long-term changes in the Southern Ocean CO_2 sink and related climate sensitivities, as suggested by Lenton et al. (2013).

In undertaking this analysis there are some important limitations worth highlighting. First, because this chapter uses five models in contrast to 10 used in the previous chapter (selection was limited by availability of data of essential variables), the conclusion drawn here may not be representative all CMIP5 models. Second, I am mindful that the premise of this study is that CMIP5 models show biases in relation to the observations of Landschützer et al. (2014) and
Takahashi et al., (2009) which at the time of writing provide the most widely accepted representation of available datasets in the Southern Ocean. However, in situ observations in the Southern Ocean are still limited, and these datasets are still subject to uncertainties (e.g. Ritter et al., 2018). Thus, it is possible that Landschützer et al. (2014) is not fully representative of the seasonal cycle of FCO_2 in the Southern Ocean, and thus biases of the models analysed may not be exactly as found here. In this regard, the recent endeavours with fine-scale measurement based on higher resolution autonomous

platforms (as shown by Monteiro et al., (2015), Williams et al., (2017). Briggs et al., (2018) and Rosso et al., (2017)) may be an important step forward in constraining these dynamics in Earth System Models, in addition to ship-based measurements.

Chapter 6

Synthesis

The seasonal cycle is a dominant mode of variability for CO_2 in the Southern Ocean (Lenton et al., 2012); hence the limited skill of CMIP5 models in simulating the seasonality of FCO_2 may be a significant challenge to long-term projection (Lenton et al., 2013; Anav et al., 2013). This limitation suggests that CMIP5 models may lack appropriate sensitivity to essential drivers of CO_2 that are crucial for appropriately modelling long-term changes in the Southern Ocean CO_2 sink. Although mean seasonal properties of CO_2 in the Southern Ocean have been well explored through observation-based studies, CMIP5 models generally show limited skill in simulating these. Hence the need for a process-based understanding of the sources of bias in the modelled seasonal cycle of FCO_2 and the implications for the long-term simulated CO_2 sink. Analytical tools available for model analysis are mostly statistically based, which is helpful for quantifying model biases and approximating mean long-term behavior, but they do not help in understanding the mechanisms causing the biases.

Consequently, this study set out with three main objectives; firstly, to develop a process-based diagnostic analytical tool (diagnostic framework) to analyze and examine major biases in the model-seasonal cycle of FCO_2. Secondly, to use the method developed to examine sources of bias responsible for the limited skill of 10 CMIP5 ESMs in simulating the seasonal cycle of FCO_2 with respect to observed estimates in the Southern Ocean. Thirdly, to investigate how the present-day biases in the seasonality and drivers of FCO_2 in CMIP5 ESMs affect modelled long-term changes in the mechanisms that drive CO_2 uptake in the Southern Ocean. The main outcomes are summarized below.

For objective 1: The seasonal cycle as a rigorous test for models

Chapter 3 establishes a diagnostic framework to analyze model-observation biases for the seasonal scale of FCO_2. Briefly, the diagnostic framework can be summarized as follows: since the difference between atmospheric and oceanic CO_2 ($dpCO_2$) is the main driver of FCO_2, but atmospheric CO_2 is relatively uniform in the Southern Ocean (Fujita et al., 2003), $dpCO_2$ changes are primarily regulated by surface pCO_2 variability (Sarmiento and Gruber, 2006). It is also known that dissolved inorganic

carbon (DIC) and sea surface temperature (SST) are the main drivers of surface pCO_2 (e.g. Takahashi et al., 1993). This analysis therefore examine the relative contributions of DIC and SST to temporal surface pCO_2 changes and link them to related processes (CO_2 solubility, biological processes and mixing) in observation estimates vs model output. In this way modelled FCO_2 biases can be linked to related processes. Applying this approach to NEMO PISCES ORCA2LP for example, it is shown that the limited model skill in simulating the seasonal cycle of FCO_2 with respect to observed estimates in the Sub-Antarctic zone is linked to weaker surface DIC seasonal variations (dDIC/dt) relative to observed estimates. These weaker than observed surface DIC rates of change in the model were found to be linked to a short-lived primary production season (lack of sustained production) and weaker DIC vertical gradients. Consequently, the surface temperature variability (dSST/dt) was larger than DIC variability. Thus, contrary to observed estimates, temperature variations (through solubility) dominantly modulate the seasonal cycle of pCO_2 and FCO_2 in ORCA2LP. The strength of this approach lies in its ability to link modelled FCO_2 biases to related processes at the seasonal scale which can be useful in highlighting areas of poor skill in the modelled FCO_2 compared to observed estimates.

For Objective 2: Sources of bias in the modelled seasonal cycle of CO_2

Using the diagnostic framework developed, I was able to isolate key biases that limit the ability of CMIP5 models to simulate the observed seasonal cycle of FCO_2 in the Southern Ocean. In particular, these biases are an exaggeration of the rates of change of SST during peak seasons (i.e. autumn and summer) (7 group-SST models), and exaggerated primary production for the other three models (group-DIC). It is shown that although 9 of the 10 models analysed overestimated warming and cooling rates, only 7 of the 10 models show an exaggerated role of surface solubility of CO_2 in the seasonality of FCO_2. The other three models overestimated primary production, which instead was found to be the predominant driver and main bias in the seasonality and sink of CO_2 in the group-DIC models. It was also found that contrary to observational estimates, CMIP5 models show zonal homogeneity in the seasonal cycle of FCO_2 in the Southern Ocean (with the exception of CMCC, GFDL and CESM1). CMIP5 models were found to show a similar seasonal cycle of FCO_2 phasing in the three basins of the Southern Ocean, particularly in the Sub-Antarctic Zone. In the Antarctic Zone, CMIP5 models generally compare better with observations than in the Sub-Antarctic Zone. It was unfortunately not possible as yet to assess why CMIP5 models perform more effectively in the Antarctic Zone, or whether basin-specific features are inhibited by limited in situ data in the observational products.

For objective 3: How well do CMIP5 models predict long-term evolution of CO_2 fluxes and sink in the Southern Ocean?

Using five CMIP5 models under the business as usual scenario (RCP8.5), the final section (Chapter 5) of the dissertation demonstrates that the present-day biases in seasonality and drivers of FCO_2 within CMIP5 ESMs play a role in the way models simulate CO_2 fluxes in a future Southern Ocean. It is shown that although all five models analysed are consistent with previous studies in showing increased annual mean CO_2 uptake by the end of the century (e.g. Hauck and Völker, 2015; Wang et al., 2016), they demonstrate essential differences in the mechanisms explaining the increased CO_2 uptake. Models that show a strong temperature bias in the seasonal cycle of FCO_2 (group-SST) in the present climate maintain this feature at the end of the century. Thus, the long-term increased CO_2 uptake in these models is mainly driven by temperature-driven solubility which is amplified due to increased anthropogenic atmospheric CO_2 under the RCP8.5 scenario and decreased surface CO_2 buffering capacity. But they show a weak to a null role of biological activity in the CO_2 variability and sink at the seasonal scale in the Sub-Antarctic Zone at the end of the century as in the present scenario. In group-SST models in the Antarctic Zone, surface pCO_2 and FCO_2 mostly transition from being partly temperature and partly DIC-controlled to being mostly temperature-controlled, except for spring. During spring, group-SST models are mostly DIC controlled in the present climate linked to primary production, at the end of the century this DIC control is strengthened and thus the associated biological CO_2 uptake is increased.

On the other hand, group-DIC models show two important changes in the drivers of pCO_2 and FCO_2 at the end of the century for both Sub-Antarctic and Antarctic Zones. Firstly, DIC control during winter in surface pCO_2 and FCO_2, which is associated with vertical mixing in the present climate, is overtaken by temperature control. Secondly, DIC control associated with primary production between spring-summer is enhanced at the end of the century mostly due to the increased Revelle factor. These changes enhance CO_2 uptake during winter (solubility driven) and spring (primary production driven), and increase CO_2 outgassing (possibly respiration driven) in autumn in group-DIC models. It was found that although primary production does not show significant changes at the end of the century, weakened surface CO_2 buffering capacity (increased Revelle factor) enhances pCO_2 and FCO_2 seasonal variation although surface DIC variations are even smaller at end of the century. Thus the biologically driven CO_2 uptake (spring) is increased in group-DIC models at the end of the century consistent with the findings of Hauck and Völker (2015). However, note that although the Revelle factor increases in all five models analysed, the amplification of the seasonal cycle of pCO_2 and FCO_2 amplitude is not shown in group-SST models. This is because the spring biological CO_2 uptake is still offset by surface warming at end of the century, as in the present scenario.

Implications of these findings

Given that the long-term biases seem to be set by the contemporary characteristics of the seasonal cycle of surface pCO_2 and FCO_2 in the Southern Ocean, these present-day biases are even more problematic. This outcome emphasizes that the long-term ability of CMIP5 models to simulate the sink and mechanisms of CO_2 dynamics of in the Southern Ocean is model specific. Consequently, the findings of Hauck and Volker (2015), which showed that increased biologically-driven CO_2 uptake at the end of the century linked to an increased Revelle factor and atmospheric CO_2 can only be reproduced in group-DIC models. Similarly, the predicted increasing amplitude of CO_2 and related pH changes that might strain ocean organisms at the end of the century, shown by McNeil and Sasse, (2016) and Kwiatkowski and Orr (2018) can here only be found in group-DIC models. The same conclusions cannot be drawn using group-SST models. This makes the long-term projection of CO_2 uptake by CMIP5 models in the Southern Ocean problematic. In particular, overestimated rates of temperature change make studying the long-term role of the biological pump and solubility challenging to interpret. While the overestimated warming and cooling rates result in an exaggerated role of solubility in the seasonal variability of FCO_2, perhaps even more concerning is their tendency to downplay the role of the biological pump. As a result, these biases keep the drivers of the carbonate system seasonally static on century timescales, such that present drivers of the FCO_2 seasonal variability are preserved to the end of the century. Note that these models are the majority of the models analysed (7 out 10) and all the models of Southern Ocean CO_2 sink simulation used by Wang et al. (2016). Consequently, these models give the impression that increasing atmospheric CO_2 drives the Southern Ocean CO_2 sink almost linearly through surface solubility.

Nevertheless, it important to note that it may be that this is because these present-day model biases unrealistically keep the system at a steady state away from tipping points of DIC vs SST dominance and thus the mechanisms of CO_2 uptake are mostly solubility driven. This may cause potential difficulties in examining the impact of anthropogenic temperature changes in the carbonate system over timescales longer than the end of the century. In particular, given that CMIP5 models start (present-day scenario) with overestimated temperature control, it may be hard to disentangle the anthropogenic impact. Nonetheless, observed present-day estimates of FCO_2, show that the ocean maintains a combined influence of both the temperature and DIC (physical and biological) drivers. Thus, it may be that these biases prevent realistic long-term evolution in CMIP5 models which might be different from either group-SST and group-DIC models.

Some studies have used model ensembles to cope with individual model biases (e.g. Anav et al., 2013; Frölicher et al., 2015), some have used weighted model ensembles (e.g. Gohar et al., 2017) and

yet others have used historical performance against observations to select models for an ensemble (Wang et al., 2016; Wang and Overland, 2012). This approach has proven useful in narrowing the model spread and thus reducing the uncertainty of long-term predictions. However, it is hard to distinguish whether the decreased uncertainty (or increased precision) also improves the accuracy of the simulation. Given the limited skill of CMIP5 models at modelling the drivers of FCO_2 at the seasonal scale, it is likely to be the former (precision). Models are may becoming more precise, that is more similar, but less accurate. For example, when considering the case of model selection by historical performance against observations (e.g. Wang et al., 2016): because this selection is based on partial comparison with observations upon passing an established threshold, it is important to be mindful of the mechanistic implications of this partial comparison (and limitation of the observations). The models selected by Wang et al. (2016) are all group-SST models of this study (Chapters 4-5). As a consequence, although the chosen models compare well with observed estimates in relative terms, they generally underestimate the role of the biological pump (Chapters 4-5). However, it also worth mentioning that the simulation of the biological pump is also uncertain in CMIP5 models as shown by Hague and Vichi (2018).

Therefore, although using only group-SST models will inherently reduce model spread, the predicted long-term CO_2 sink is likely to exclude or limit the role of biological activity. Although a carefully weighted model ensemble or selected models may reproduce the observed seasonal cycle of FCO_2 well, it is not certain whether or not individual model biases will have similar sensitivity to the chosen weighting over century timescales so that the long-term simulation is trustworthy. This is not to say that statistical methods are misleading, but that complementing these with mechanistic interpretations of the underlying assumptions will be more robust. Thus, the approach taken in this dissertation could be a useful as an complementary method of analyzing the representation of the drivers of FCO_2 dynamics.

In addition to model biases, it worth mention that data estimates still have significant biases in the Southern Ocean. All three main data estimates(products) used in this study for FCO2 (i.e. Takahashi et al., 2009; Landschützer et al. 2014 and Gregor et a., 2017) are still subject to important biases, particularly in the Southern Ocean. The primary bias in the Southern Ocean emerge from limited in situ measurements, during winter there are only a few measures mostly from the Atlantic basin (Fay et al., 2018). This is a significant limitation, it is, therefore, possible that winter estimates are not well representative of the observed dynamics in most of the Southern Ocean. For example, a recent study based on float measurements by Gray et al. (2018) suggest a controversial significantly larger winter CO2 outgassing fluxes than previous measurements indicated in the Southern Ocean. This recent addition of autonomous instruments including floats, wave and sea gliders measurement is an essential addition to the already ongoing ship-based measurements (e.g. Fay et al., 2018; Johnson et

al., 2017; Monteiro et al., 2015). Thus, a coordinated effort toward improving CO_2 measurements in the Southern Ocean will be useful for both improved understandings of CO_2 dynamics and modelling the oceanic carbon cycle.

Future Model Improvement

It is evident that model improvement in representing rates of SST and DIC change and their processes will be necessary to reduce the uncertainty in the simulated Southern Ocean CO_2 sink. Overall this analysis points to two main areas where model improvement may be crucial:

a) Improving spatial (basin-scale) characteristics of the seasonality and drivers of FCO_2
b) Reducing warming and cooling rate biases.

Model improvement in these two areas is likely to greatly improve the representation of modelled biogeochemical properties in the Southern Ocean, a few anticipated changes are as follows:
Firstly, enhanced representation of local (basin-scale) processes will probably strengthen the knowledge of important localized CO_2 outgassing and in-gassing hotspots, and their related processes. For example, a recent study based on an eddy-resolving model shows that the Sub-Antarctic Zone has upwelling hotspots along the ACC path that coincide with topographical features (Tamsitt et al., 2017). These are likely to be critical areas of CO_2 outgassing and/or drivers of local productivity.

Secondly, improved representation of the spatial variability of the seasonal cycle of FCO_2 will possibly improve understanding of the basin-specific contribution of present and long-term Southern Ocean CO_2 sink. For example, how the higher productivity in the Atlantic Ocean sector will cope with anthropogenic changes can be better investigated, or whether it will continue to drive CO_2 uptake reinforced by decreased surface CO_2 buffering capacity? Alternatively, the predicted reduced rate of entrainment (decreased nutrient supply) because of shallower MLDs and more stratified surface ocean may tip the system into being mainly temperature driven. Similarly, improved estimates of the rates of change of temperature will help adjust the modelled role of solubility in the seasonal cycle of FCO_2 closer to observed estimates. This will allow the role of biological CO_2 uptake to emerge (spring-summer) in group-SST models. It will also help elucidate whether the modelled century-scale switch from DIC-driven (entrainment CO_2 outgassing) to temperature-driven (solubility CO_2 in-gassing) in mid-winter (as shown by some models) is realistic in group-DIC models (Chapter 5, Fig. 5.3).

Whilst some models overestimate primary production, this is a model specific problem and is likely to be improved in the next generation of CMIP models. Overall the reasons for these biases remain uncertain; however, two possible sources of these biases are speculated on below.

First, it is important to note the parameterization of the Southern Ocean biological pump including Redfield ratios (Redfield, 1934), were based on average datasets over large oceanic regions (Bopp and Le Quéré, 2009; Sarmiento and Gruber, 2006); however it is not certain that these properties remain uniform at the basin-scale. Also, the fact that the three basins of the Southern Ocean show differences in both land-based and continental iron supply for primary production (Tagliabue et al., 2012) is likely to be a key factor in the zonal variability of FCO_2 properties. For example, high productivity in the Atlantic Basin has previously been linked to larger iron supplies from continental shelves and land (Boyd and Ellwood, 2010; Tagliabue et al., 2012; 2014); whereas reduced iron inputs in the Pacific Basin explained lower productivity (Tagliabue et al., 2012). Thus, the lack of zonal differences in the seasonality and drivers of FCO_2 may partly be due to the zonal uniformity of biogeochemical properties of the Southern Ocean in CMIP5 models. (This feature is confirmed by the zonal homogeneity in the seasonal cycle of chlorophyll and NPP in Chapter 4 (Fig. 4.10)). Nevertheless, most CMIP5 ESMs do show basin scale differences in the seasonal cycle of MLD although differences in magnitude are still prevalent (Fig. 4.9). This may suggest that the physics do partly resolve zonal differences that are consistent with observations. This hypothesis highlights the need for high-resolution year-round observations of CO_2, nutrients and phytoplankton in the Southern Ocean to help constrain the biogeochemical properties in ESMs. Thus, the recent fine-scale measurements based on higher resolution autonomous instruments including biogeochemical ARGO floats, sea and wave gliders (Monteiro et al., 2015; Williams et al., 2017; Briggs et al., 2018; Rosso et al., 2017) may be useful in providing this kind of data in the long-term. This may be an important step forward in constraining the Southern Ocean carbon dynamics in ESMs.

Another key factor which is likely to play a role is model resolution. Thus lack of zonal differences may be limited by the inability of models to resolve fine scale dynamics driving variability at the local scale. Hence, increased resolution in the next generation of CMIP models may improve representation of mesoscale features and related biogeochemical properties (Lévy et al., 2012; Mahadevan, 2016; McGillicuddy, 2016; Nicholson et al., 2016; Swart et al., 2014) and CO_2 mixing and transport (Gnanadesikan et al., 2015; Ito et al., 2010).

Second, CMIP5 models also show biases in MLD properties and the times of the Southern Hemisphere wind peaks, which is likely to affect surface SST biases through surface turbulence and mixing (Meijers, 2014; Sallée et al., 2013). However, another more likely source of the SST bias is related to biases in atmospheric models (Bodas-Salcedo et al., 2016; Grise and Polvani, 2014; Hawcroft et al., 2017; Kay et al., 2016). The Southern Ocean SST biases have also been linked to biases in shortwave radiation associated with the vertical structure of clouds; in particular, supercooled clouds are overestimated in the Southern Hemisphere in CMIP5 models (Bodas-Salcedo et al., 2016; Kay et al., 2016). Because of these biases, the shortwave radiation absorbed is limited at

high latitudes, creating a high-low latitude heat gradient, leading to enhanced southward transport of heat from the tropics (Bodas-Salcedo et al., 2016; Kay et al., 2016). Grise and Lorenzo (2014) also found that CMIP5 model differences in cloud fraction were linked to shortwave radiative differences; they found that models with reduced cloud fraction showed enhanced shortwave radiative anomalies in the mid-latitudes of the Southern Hemisphere. Some studies show that the optical depth of low-lying clouds is likely responsible for these biases (Kay et al., 2016; Mauritsen, 2016). Whilst advances in the understanding of this problem are been made (Bodas-Salcedo et al., 2014, 2012; Grise and Polvani, 2014; Hawcroft et al., 2017; Kay et al., 2016; Williams et al., 2013), a full understanding and correction of these biases is still a subject of ongoing research and provides a real academic challenge.

Finally, it is important to note that although CMIP5 models still show some limitations with respect to processes driving CO_2 and related climate sensitivities, they remain the most important and objective tool for investigating earth system processes. Working with and improving ESMs is a complex process, thus there is a need for constant evaluation and isolating key areas of model development as attempted in this thesis. I hope that this analysis and the diagnostic framework provided will be useful for model development and assessment of Earth System Models in general.

References

Abernathey, R., Ferreira, D., 2015. Southern Ocean isopycnal mixing and ventilation changes driven by winds. Geophys. Res. Lett. 42, 10357–10365. https://doi.org/10.1002/2015GL066238

Adachi, Y., Yukimoto, S., Deushi, M., Obata, A., Nakano, H., Tanaka, T.Y., Hosaka, M., Sakami, T., Yoshimura, H., Hirabara, M., Shindo, E., Tsujino, H., Mizuta, R., Yabu, S., Koshiro, T., Ose, T., Kitoh, A., 2013. Basic performance of a new earth system model of the Meteorological Research Institute. Pap. Meteorol. Geophys. 64, 1–19. https://doi.org/10.2467/mripapers.64.1

Anav, A., Friedlingstein, P., Kidston, M., Bopp, L., Ciais, P., Cox, P., Jones, C., Jung, M., Myneni, R., Zhu, Z., 2013a. Evaluating the land and ocean components of the global carbon cycle in the CMIP5 earth system models. J. Clim. 26, 6801–6843. https://doi.org/10.1175/JCLI-D-12-00417.1

Anav, A., Friedlingstein, P., Kidston, M., Bopp, L., Ciais, P., Cox, P., Jones, C., Jung, M., Myneni, R., Zhu, Z., 2013b. Evaluating the Land and Ocean Components of the Global Carbon Cycle in the CMIP5 Earth System Models. J. Clim. 26, 6801–6843. https://doi.org/10.1175/JCLI-D-12-00417.1

Anderson, R.F., Ali, S., Bradtmiller, L.I., Nielsen, S.H.H., Fleisher, M.Q., Anderson, B.E., Burckle, L.H., 2009. Wind-driven upwelling in the Southern Ocean and the deglacial rise in atmospheric CO2. Science 323, 1443–1448. https://doi.org/10.1126/science.1167441

Anderson, T.R., Hawkins, E., Jones, P.D., 2016. CO2, the greenhouse effect and global warming: from the pioneering work of Arrhenius and Callendar to today's Earth System Models. Endeavour 40, 178–187. https://doi.org/10.1016/j.endeavour.2016.07.002

Archer, C.L., Caldeira, K., 2008. Historical trends in the jet streams. Geophys. Res. Lett. 35, 1–6. https://doi.org/10.1029/2008GL033614

Aumont, O., Bopp, L., 2006. Globalizing results from ocean in situ iron fertilization studies. Global Biogeochem. Cycles 20. https://doi.org/10.1029/2005GB002591

Bakker, D.C.E., Hoppema, M., Schröder, M., Geibert, W., de Baar, H.J.W., 2008. A rapid transition from ice covered CO_2-rich waters to a biologically mediated CO_2 sink in the eastern Weddell Gyre. Biogeosciences Discuss. 5, 1205–1235. https://doi.org/10.5194/bgd-5-1205-2008

Bakker, D.C.E., Pfeil, B., Smith, K., Hankin, S., Olsen, a., Alin, S.R., Cosca, C., Harasawa, S., Kozyr, a., Nojiri, Y., O'Brien, K.M., Schuster, U., Telszewski, M., Tilbrook, B., Wada, C., Akl, J., Barbero, L., Bates, N.R., Boutin, J., Bozec, Y., Cai, W.J., Castle, R.D., Chavez, F.P., Chen, L., Chierici, M., Currie, K., De Baar, H.J.W., Evans, W., Feely, R. a., Fransson, a., Gao, Z., Hales, B., Hardman-Mountford, N.J., Hoppema, M., Huang, W.J., Hunt, C.W., Huss, B., Ichikawa, T., Johannessen, T., Jones, E.M., Jones, S.D., Jutterström, S., Kitidis, V., Körtzinger, a., Landschützer, P., Lauvset, S.K., Lefèvre, N., Manke, a. B., Mathis, J.T., Merlivat, L., Metzl, N., Murata, a., Newberger, T., Omar, a. M., Ono, T., Park, G.H., Paterson, K., Pierrot, D., Ríos, a. F., Sabine, C.L., Saito, S., Salisbury, J., S. Sarma, V.V.S., Schlitzer, R., Sieger, R., Skjelvan, I., Steinhoff, T., Sullivan, K.F., Sun, H., Sutton, a. J., Suzuki, T., Sweeney, C., Takahashi, T., Tjiputra, J., Tsurushima, N., C. Van Heuven, S.M. a, Vandemark, D., Vlahos, P., Wallace, D.W.R., Wanninkhof, R., Watson, a. J., 2014. An update to the surface ocean CO2 atlas (SOCAT version 2). Earth Syst. Sci. Data 6, 69–90. https://doi.org/10.5194/essd-6-69-2014

Barbero, L., Boutin, J., Merlivat, L., Martin, N., Takahashi, T., Sutherland, S.C., Wanninkhof, R., 2011. Importance of water mass formation regions for the air-sea CO2 flux estimate in the southern ocean. Global Biogeochem. Cycles 25, 1–16. https://doi.org/10.1029/2010GB003818

Bodas-Salcedo, A., Hill, P.G., Furtado, K., Williams, K.D., Field, P.R., Manners, J.C., Hyder, P., Kato, S., 2016. Large contribution of supercooled liquid clouds to the solar radiation budget of the Southern Ocean. J. Clim. https://doi.org/10.1175/JCLI-D-15-0564.1

Bodas-Salcedo, A., Williams, K.D., Field, P.R., Lock, A.P., 2012. The surface downwelling

solar radiation surplus over the southern ocean in the met office model: The role of midlatitude cyclone clouds. J. Clim. https://doi.org/10.1175/JCLI-D-11-00702.1

Bodas-Salcedo, A., Williams, K.D., Ringer, M.A., Beau, I., Cole, J.N.S., Dufresne, J.L., Koshiro, T., Stevens, B., Wang, Z., Yokohata, T., 2014. Origins of the solar radiation biases over the Southern Ocean in CFMIP2 models. J. Clim. https://doi.org/10.1175/JCLI-D-13-00169.1

Boé, J., Hall, A., Qu, X., 2009. September sea-ice cover in the Arctic Ocean projected to vanish by 2100. Nat. Geosci. 2, 341–343. https://doi.org/10.1038/ngeo467

Bopp, L., Aumont, O., Cadule, P., Alvain, S., Gehlen, M., 2005. Response of diatoms distribution to global warming and potential implications: A global model study. Geophys. Res. Lett. 32, 1–4. https://doi.org/10.1029/2005GL023653

Bopp, L., Le Quéré, C., 2009. Ocean Carbon Cycle, in: Surface Ocean–Lower Atmosphere Processes. https://doi.org/10.1029/2008GM000780

Bopp, L., Resplandy, L., Orr, J.C., Doney, S.C., Dunne, J.P., Gehlen, M., Halloran, P., Heinze, C., Ilyina, T., Séférian, R., Tjiputra, J., Vichi, M., 2013. Multiple stressors of ocean ecosystems in the 21st century: Projections with CMIP5 models. Biogeosciences 10, 6225–6245. https://doi.org/10.5194/bg-10-6225-2013

Boutin, J., Merlivat, L., Hénocq, C., Martin, N., Sallée, J.B., 2008. Air-sea CO2 flux variability in frontal regions of the Southern Ocean from CARbon Interface OCean Atmosphere drifters. Limnol. Oceanogr. 53, 2062–2079. https://doi.org/10.4319/lo.2008.53.5_part_2.2062

Boyd, P.W., Ellwood, M.J., 2010. The biogeochemical cycle of iron in the ocean. Nat. Geosci. 3, 675–682. https://doi.org/10.1038/ngeo964

Bracegirdle, T.J., Shuckburgh, E., Sallee, J.B., Wang, Z., Meijers, A.J.S., Bruneau, N., Phillips, T., Wilcox, L.J., 2013. Assessment of surface winds over the atlantic, indian, and pacific ocean sectors of the southern ocean in cmip5 models: Historical bias, forcing

response, and state dependence. J. Geophys. Res. Atmos. 118, 547–562. https://doi.org/10.1002/jgrd.50153

Briggs, N.T., Omand, M.M., Asaro, E.A.D., Lee, C.M., Perry, M.J., Briggs, N., Cetini, I., 2015. Eddy-driven subduction exports particulate organic carbon from the spring bloom Eddy-driven subduction exports particulate organic carbon from the spring bloom 348. https://doi.org/10.1126/science.1260062

Caldeira, K., 2005. Ocean model predictions of chemistry changes from carbon dioxide emissions to the atmosphere and ocean. J. Geophys. Res. 110, 1–12. https://doi.org/10.1029/2004JC002671

Caldeira, K., 2000. The Role of the Southern Ocean in Uptake and Storage of Anthropogenic Carbon Dioxide. Science (80-.). 287, 620–622. https://doi.org/10.1126/science.287.5453.620

Cao, L., Zhang, H., 2017. The role of biological rates in the simulated warming effect on oceanic CO2 uptake. J. Geophys. Res. Biogeosciences 122, 1098–1106. https://doi.org/10.1002/2016JG003756

Collins, M., 2009. Insight despite imperfection.

Conkright, M.E., Antonov, J.I., Baranova, O.K., Boyer, T.P., Garcia, H.E., Gelfeld, R., Johnson, D., Locarnini, R.A., Murphy, P.P., O'Brien, T.D., Smolyar, I. V., Stephens, C., 2002. World Ocean Database 2001, NOAA Atlas NESDIS 42.

Cox, P.M., Huntingford, C., Williamson, M.S., 2018. Emergent constraint on equilibrium climate sensitivity from global temperature variability. Nature 553, 319–322. https://doi.org/10.1038/nature25450

de Boyer Montégut, C., 2004. Mixed layer depth over the global ocean: An examination of profile data and a profile-based climatology. J. Geophys. Res. 109, C12003. https://doi.org/10.1029/2004JC002378

Dickson, A.G., Millero, F.J., 1987. A comparison of the equilibrium constants for the

dissociation of carbonic acid in seawater media. Deep Sea Res. Part A, Oceanogr. Res. Pap. 34, 1733–1743. https://doi.org/10.1016/0198-0149(87)90021-5

Dong, S., Sprintall, J., Gille, S.T., Talley, L., 2008. Southern ocean mixed-layer depth from Argo float profiles. J. Geophys. Res. Ocean. 113, 1–12. https://doi.org/10.1029/2006JC004051

Dufour, C.O., Griffies, S.M., de Souza, G.F., Frenger, I., Morrison, A.K., Palter, J.B., Sarmiento, J.L., Galbraith, E.D., Dunne, J.P., Anderson, W.G., Slater, R.D., 2015. Role of Mesoscale Eddies in Cross-Frontal Transport of Heat and Biogeochemical Tracers in the Southern Ocean. J. Phys. Oceanogr. 45, 3057–3081. https://doi.org/10.1175/JPO-D-14-0240.1

Dufour, C.O., Sommer, J. Le, Gehlen, M., Orr, J.C., Molines, J.M., Simeon, J., Barnier, B., 2013. Eddy compensation and controls of the enhanced sea-to-air CO2 flux during positive phases of the Southern Annular Mode. Global Biogeochem. Cycles 27, 950–961. https://doi.org/10.1002/gbc.20090

du Plessis, M., Swart, S., Ansorge, I.J., Mahadevan, A., 2017. Submesoscale processes promote seasonal restratification in the Subantarctic Ocean. J. Geophys. Res. Ocean. 122, 2960–2975. https://doi.org/10.1002/2016JC012494

Dunne, J.P., John, J.G., Shevliakova, S., Stouffer, R.J., Krasting, J.P., Malyshev, S.L., Milly, P.C.D., Sentman, L.T., Adcroft, A.J., Cooke, W., Dunne, K.A., Griffies, S.M., Hallberg, R.W., Harrison, M.J., Levy, H., Wittenberg, A.T., Phillips, P.J., Zadeh, N., 2013. GFDL's ESM2 global coupled climate-carbon earth system models. Part II: Carbon system formulation and baseline simulation characteristics. J. Clim. 26, 2247–2267. https://doi.org/10.1175/JCLI-D-12-00150.1

Egleston, E.S., Sabine, C.L., Morel, F.M.M., 2010. Revelle revisited: Buffer factors that quantify the response of ocean chemistry to changes in DIC and alkalinity. Global Biogeochem. Cycles 24, 1–9. https://doi.org/10.1029/2008GB003407

Fay, A.R., Lovenduski, N.S., McKinley, G.A., Munro, D.R., Sweeney, C., Gray, A.R.,

Landschützer, P., Stephens, B.B., Takahashi, T., Williams, N., 2018. Utilizing the Drake Passage Time-series to understand variability and change in subpolar Southern Ocean pCO2. Biogeosciences. https://doi.org/10.5194/bg-15-3841-2018

Falkowski, P.G., Barber, R.T., Smetacek, V., 1998. Biogeochemical Controls and Feedbacks on Ocean Primary Biogeochemical Controls and Feedbacks on Ocean Primary Production 200, 200–207. https://doi.org/10.1126/science.281.5374.200

Feely, R.A., Wanninkhof, R., McGillis, W., Carr M. E, Cosca, C., 2004. Effects of wind speed and gas exchange parameterizations on the air-sea CO 2 fluxes in the equatorial Pacific Ocean. J. Geophys. Res. 109, C08S03. https://doi.org/10.1029/2003JC001896

Friedlingstein, B.P., Dufresne, J., Cox, P.M., Rayner, P., 2003. How positive is the feedback between climate change and the carbon cycle ? Tellus 55B, 692–700. https://doi.org/10.1034/j.1600-0889.2003.01461.x

Friedlingstein, P., Cox, P., Betts, R., Bopp, L., von Bloh, W., Brovkin, V., Cadule, P., Doney, S., Eby, M., Fung, I., Bala, G., John, J., Jones, C., Joos, F., Kato, T., Kawamiya, M., Knorr, W., Lindsay, K., Matthews, H.D., Raddatz, T., Rayner, P., Reick, C., Roeckner, E., Schnitzler, K.-G., Schnur, R., Strassmann, K., Weaver, A.J., Yoshikawa, C., Zeng, N., 2006. Climate–Carbon Cycle Feedback Analysis: Results from the C 4 MIP Model Intercomparison. J. Clim. https://doi.org/10.1175/JCLI3800.1

Frölicher, T.L., Sarmiento, J.L., Paynter, D.J., Dunne, J.P., Krasting, J.P., Winton, M., 2015. Dominance of the Southern Ocean in Anthropogenic Carbon and Heat Uptake in CMIP5 Models. J. Clim. 28, 862–886. https://doi.org/10.1175/JCLI-D-14-00117.1

Fu, W., Randerson, J.T., Keith Moore, J., 2016. Climate change impacts on net primary production (NPP) and export production (EP) regulated by increasing stratification and phytoplankton community structure in the CMIP5 models. Biogeosciences. https://doi.org/10.5194/bg-13-5151-2016

Fujita, D., Ishizawa, M., Maksyutov, S., Thornton, P.E., Saeki, T., Nakazawa, T., 2003. Inter-annual variability of the atmospheric carbon dioxide concentrations as simulated with

global terrestrial biosphere models and an atmospheric transport model. Tellus Ser. B-Chemical Phys. Meteorol. 55, 530–546. https://doi.org/10.1034/j.1600-0889.2003.00044.x

Fung, I.Y., Doney, S.C., Lindsay, K., John, J., 2005. Evolution of carbon sinks in a changing climate. Proc. Natl. Acad. Sci. U. S. A. 102, 11201–11206. https://doi.org/10.1073/pnas.0504949102

Gent, P.R., Mcwilliams, J.C., 1990. Isopycnal Mixing in Ocean Circulation Models. J. Phys. Oceanogr. https://doi.org/10.1175/1520-0485(1990)020<0150:IMIOCM>2.0.CO;2

Gnanadesikan, A., Pradal, M.A., Abernathey, R., 2015. Isopycnal mixing by mesoscale eddies significantly impacts oceanic anthropogenic carbon uptake. Geophys. Res. Lett. 42, 4249–4255. https://doi.org/10.1002/2015GL064100

Gohar, L.K., Lowe, J.A., Bernie, D., 2017. The Impact of Bias Correction and Model Selection on Passing Temperature Thresholds. J. Geophys. Res. Atmos. 122, 12,045-12,061. https://doi.org/10.1002/2017JD026797

Graham, R.M., Boer, A.M. De, Sebille, E. Van, Kohfeld, K.E., Schlosser, C., 2015. Deep-Sea Research I Inferring source regions and supply mechanisms of iron in the Southern Ocean from satellite chlorophyll data. Deep. Res. Part I 104, 9–25. https://doi.org/10.1016/j.dsr.2015.05.007

Graham, R.M., De Boer, A.M., 2013. The dynamical subtropical front. J. Geophys. Res. Ocean. 118, 5676–5685. https://doi.org/10.1002/jgrc.20408

Gray, A.R., Johnson, K.S., Bushinsky, S.M., Riser, S.C., Russell, J.L., Talley, L.D., Wanninkhof, R., Williams, N.L., Sarmiento, J.L., 2018. Autonomous Biogeochemical Floats Detect Significant Carbon Dioxide Outgassing in the High-Latitude Southern Ocean. Geophys. Res. Lett. https://doi.org/10.1029/2018GL078013

Gregor, L., Kok, S., Monteiro, P.M.S., 2017a. Empirical methods for the estimation of Southern Ocean CO₂: Support Vector and

Random Forest Regression. Biogeosciences Discuss. 1–18. https://doi.org/10.5194/bg-2017-215

Gregor, L., Kok, S., Monteiro, P.M.S., 2018. Interannual drivers of the seasonal cycle of CO2 in the Southern Ocean. Biogeosciences 15, 2361–2378. https://doi.org/10.5194/bg-15-2361-2018

Grise, K.M., Polvani, L.M., 2014. Southern hemisphere cloud-dynamics biases in CMIP5 models and their implications for climate projections. J. Clim. 27, 6074–6092. https://doi.org/10.1175/JCLI-D-14-00113.1

Gruber, N., Gloor, M., Mikaloff Fletcher, S.E., Doney, S.C., Dutkiewicz, S., Follows, M.J., Gerber, M., Jacobson, A.R., Joos, F., Lindsay, K., Menemenlis, D., Mouchet, A., Müller, S. a., Sarmiento, J.L., Takahashi, T., 2009. Oceanic sources, sinks, and transport of atmospheric CO2. Global Biogeochem. Cycles 23, 1–21. https://doi.org/10.1029/2008GB003349

Hague, M., Vichi, M., 2018. A Link Between CMIP5 Phytoplankton Phenology and Sea Ice in the Atlantic Southern Ocean. Geophys. Res. Lett. 45, 6566–6575. https://doi.org/10.1029/2018GL078061

Hauck, J., 2018. Unsteady seasons in the sea. Nat. Clim. Chang. 8, 97–98. https://doi.org/10.1038/s41558-018-0069-1

Hauck, J., Völker, C., 2015. Rising atmospheric CO2 leads to large impact of biology on Southern Ocean CO 2 uptake via changes of the Revelle factor. https://doi.org/10.1002/2015GL063070.1.

Hauck, J., Völker, C., Wolf-Gladrow, D. a., Laufkötter, C., Vogt, M., Aumont, O., Bopp, L., Buitenhuis, E.T., Doney, S.C., Dunne, J., Gruber, N., John, J., Le Quéré, C., Lima, I.D., Nakano, H., Totterdell, I., 2015. On the Southern Ocean CO2 uptake and the role of the biological carbon pump in the 21st century. Global Biogeochem. Cycles 29, 1451–1470. https://doi.org/doi:10.1002/2015GB005140

Hawcroft, M., Haywood, J.M., Collins, M., Jones, A., Jones, A.C., Stephens, G., 2017. Southern Ocean albedo, inter-hemispheric energy transports and the double ITCZ: global impacts of biases in a coupled model. Clim. Dyn. https://doi.org/10.1007/s00382-016-3205-5

Hirahara, S., Ishii, M., Fukuda, Y., 2014. Centennial-scale sea surface temperature analysis and its uncertainty. J. Clim. https://doi.org/10.1175/JCLI-D-12-00837.1

Ilyina, T., Six, K.D., Segschneider, J., Maier-Reimer, E., Li, H., Núñez-Riboni, I., 2013. Global ocean biogeochemistry model HAMOCC: Model architecture and performance as component of the MPI-Earth system model in different CMIP5 experimental realizations. J. Adv. Model. Earth Syst. 5, 287–315. https://doi.org/10.1029/2012MS000178

IPCC, 2014. Climate Change 2014: Synthesis Report. Contrib. Work. Groups I, II III to Fifth Assess. Rep. Intergov. Panel Clim. Chang. Core Writ. Team, Pachauri RK, Meyer LA IPCC, Geneva, Switzerland, 151 p. 1–112. https://doi.org/10.1017/CBO9781107415324

Ito, T., Woloszyn, M., Mazloff, M., 2010. Anthropogenic carbon dioxide transport in the Southern Ocean driven by Ekman flow. Nature 463, 80–83. https://doi.org/10.1038/nature08687

Iudicone, D., Madec, G., McDougall, T.J., 2008. Water-mass transformations in a neutral density framework and the key role of light penetration 1357–1376. https://doi.org/10.1175/2007JPO3464.1

Iudicone, D., Rodgers, K.B., Stendardo, I., Aumont, O., Madec, G., Bopp, L., Mangoni, O., Ribera D'Alcala', M., 2011. Water masses as a unifying framework for understanding the Southern Ocean Carbon Cycle. Biogeosciences 8, 1031–1052. https://doi.org/10.5194/bg-8-1031-2011

Jähne, B., Münnich, K.O., Bösinger, R., Dutzi, A., Huber, W., Libner, P., 1987. On the parameters influencing air-water gas exchange. J. Geophys. Res. Ocean. 92, 1937–1949. https://doi.org/10.1029/JC092iC02p01937

Johnson, K.S., Plant, J.N., Coletti, L.J., Jannasch, H.W., Sakamoto, C.M., Riser, S.C., Swift, D.D., Williams, N.L., Boss, E., Haëntjens, N., Talley, L.D., Sarmiento, J.L., 2017. Biogeochemical sensor performance in the SOCCOM profiling float array. J. Geophys. Res. Ocean. 122, 6416–6436. https://doi.org/10.1002/2017JC012838

Johnson, R., Strutton, P.G., Wright, S.W., Mcminn, A., Meiners, K.M., 2013. Three improved satellite chlorophyll algorithms for the Southern Ocean 118, 3694–3703. https://doi.org/10.1002/jgrc.20270

Joos, F., Spahni, R., 2007. Rates of change in natural and anthropogenic radiative forcing over the past 20 , 000 years. Proc. Natl. Acad. Sci. U. S. A. 105, 1425–1430. https://doi.org/10.1073/pnas.0707386105

Kay, J.E., Wall, C., Yettella, V., Medeiros, B., Hannay, C., Caldwell, P., Bitz, C., 2016. No access global climate impacts of fixing the Southern Ocean shortwave radiation bias in the Community Earth System Model (CESM). J. Clim. 29, 4617–4636. https://doi.org/10.1175/JCLI-D-15-0358.1

Keeling, C.D., Bacastow, R.B., Bainbridge, A.E., Ekdahl Jr., C.A., Guenther, P.R., Waterman, L.S., Chin, J.F.S., 1976. Atmospheric carbon dioxide variations at Mauna Loa Observatory, Hawaii. Tellus. https://doi.org/10.3402/tellusa.v28i6.11322

Kessler, A., Tjiputra, J., 2016a. The Southern Ocean as a constraint to reduce uncertainty in future ocean carbon sinks. Earth Syst. Dyn. 7, 295–312. https://doi.org/10.5194/esd-7-295-2016

Key, R.M., Kozyr, A., Sabine, C.L., Lee, K., Wanninkhof, R., Bullister, J.L., Feely, R.A., Millero, F.J., Mordy, C., Peng, T.H., 2004. A global ocean carbon climatology: Results from Global Data Analysis Project (GLODAP). Global Biogeochem. Cycles 18, 1–23. https://doi.org/10.1029/2004GB002247

Khatiwala, S., Primeau, F., Hall, T., 2009. Reconstruction of the history of anthropogenic CO2 concentrations in the ocean. Nature. https://doi.org/10.1038/nature08526

Khatiwala, S., Tanhua, T., Mikaloff Fletcher, S., Gerber, M., Doney, S.C., Graven, H.D., Gruber, N., McKinley, G.A., Murata, A., Ríos, A.F., Sabine, C.L., 2013. Global ocean storage of anthropogenic carbon. Biogeosciences 10. https://doi.org/10.5194/bg-10-2169-2013

Kwiatkowski, L., Orr, J.C., 2018. Diverging seasonal extremes for ocean acidification during the twenty-first centuryr. Nat. Clim. Chang. https://doi.org/10.1038/s41558-017-0054-0

Landschützer, P., Gruber, N., Bakker, D.C.E., Schuster, U., Nakaoka, S., Payne, M.R., Sasse, T.P., Zeng, J., 2013. A neural network-based estimate of the seasonal to inter-annual variability of the Atlantic Ocean carbon sink. Biogeosciences 10, 7793–7815. https://doi.org/10.5194/bg-10-7793-2013

Landschützer, P., Gruber, N., Bakker, D.C.E., Schuster, U., 2014. Recent variability of the global ocean carbon sink. Global Biogeochem. Cycles 28, 927–949. https://doi.org/10.1002/2014GB004853

Landschützer, P., Gruber, N., Haumann, F.A., Rödenbeck, C., Bakker, D.C.E., Van Heuven, S., Hoppema, M., Metzl, N., Sweeney, C., Takahashi, T., Tilbrook, B., Wanninkhof, R., 2015. The reinvigoration of the Southern Ocean carbon sink. Science (80-.). https://doi.org/10.1126/science.aab2620

Landschützer, P., Gruber, N., Bakker, D.C.E., Stemmler, I., Six, K.D., 2018. Strengthening seasonal marine CO2 variations due to increasing atmospheric CO2. Nat. Clim. Chang. https://doi.org/10.1038/s41558-017-0057-x

Large, W.G., Yeager, S.G., 2004. Diurnal to decadal global forcing for ocean and sea--ice models: {The} data sets and flux climatologies. NCAR Tech. Note TN--460+ST, 105pp. https://doi.org/10.5065/D6KK98Q6

Latif, M., Martin, T., Reintges, A., Park, W., 2017. Southern Ocean Decadal Variability and Predictability. Curr. Clim. Chang. Reports 3, 163–173. https://doi.org/10.1007/s40641-017-0068-8

Lauvset, S.K., Key, R.M., Olsen, A., Van Heuven, S., Velo, A., Lin, X., Schirnick, C., Kozyr, A., Tanhua, T., Hoppema, M., Jutterström, S., Steinfeldt, R., Jeansson, E., Ishii, M., Perez, F.F., Suzuki, T., Watelet, S., 2016. A new global interior ocean mapped climatology: The 1° × 1° GLODAP version 2. Earth Syst. Sci. Data 8, 325–340. https://doi.org/10.5194/essd-8-325-2016

Le Quéré, C., Andrew, R.M., Canadell, J.G., Sitch, S., Ivar Korsbakken, J., Peters, G.P., Manning, A.C., Boden, T.A., Tans, P.P., Houghton, R.A., Keeling, R.F., Alin, S., Andrews, O.D., Anthoni, P., Barbero, L., Bopp, L., Chevallier, F., Chini, L.P., Ciais, P., Currie, K., Delire, C., Doney, S.C., Friedlingstein, P., Gkritzalis, T., Harris, I., Hauck, J., Haverd, V., Hoppema, M., Klein Goldewijk, K., Jain, A.K., Kato, E., Kortzinger, A., Landschutzer, P., Lefevre, N., Lenton, A., Lienert, S., Lombardozzi, D., Melton, J.R., Metzl, N., Millero, F., Monteiro, P.M.S., Munro, D.R., Nabel, J.E.M.S., Nakaoka, S.I., O'Brien, K., Olsen, A., Omar, A.M., Ono, T., Pierrot, D., Poulter, B., Rodenbeck, C., Salisbury, J., Schuster, U., Schwinger, J., Seferian, R., Skjelvan, I., Stocker, B.D., Sutton, A.J., Takahashi, T., Tian, H., Tilbrook, B., Van Der Laan-Luijkx, I.T., Van Der Werf, G.R., Viovy, N., Walker, A.P., Wiltshire, A.J., Zaehle, S., 2016. Global Carbon Budget 2016. Earth Syst. Sci. Data 8, 605–649. https://doi.org/10.5194/essd-8-605-2016

Le Quéré, C., Andrew, R.M., Friedlingstein, P., Sitch, S., Pongratz, J., Manning, A.C., Korsbakken, J.I., Peters, G.P., Canadell, J.G., Jackson, R.B., Boden, T.A., Tans, P.P., Andrews, O.D., Arora, V.K., Bakker, D.C.E., Van Der Laan-Luijkx, I.T., Van Der Werf, G.R., Van Heuven, S., Viovy, N., Vuichard, N., Walker, A.P., Watson, A.J., Wiltshire, A.J., Zaehle, S., Zhu, D., 2018. Global Carbon Budget 2017. Earth Syst. Sci. Data Etsushi Kato Markus Kautz Ralph F. Keeling Kees Klein Goldewijk Nathalie Lefèvre Andrew Lent. Danica Lomb. Nicolas Metzl Yukihiro Nojiri Antonio Padin Janet Reimer 1010333739, 405–448. https://doi.org/10.5194/essd-10-405-2018

Le Quéré, C., Saltzman, E.S., 2013. Surface Ocean-Lower Atmosphere Processes, Surface Ocean-Lower Atmosphere Processes. https://doi.org/10.1029/GM187

Le Quéré, C., Takahashi, T., Buitenhuis, E.T., Rödenbeck, C., Sutherland, S.C., 2010. Impact of climate change and variability on the global oceanic sink of CO2. Global

Biogeochem. Cycles 24, 1–10. https://doi.org/10.1029/2009GB003599

Le Quéré, C., Rödenbeck, C., Buitenhuis, E.T., Conway, T.J., Langenfelds, R., Gomez, A., Labuschagne, C., Ramonet, M., Nakazawa, T., Metzl, N., Gillett, N., Heimann, M., 2007. Saturation of the southern ocean CO2 sink due to recent climate change. Science 316, 1735–8. https://doi.org/10.1126/science.1136188

Le Quéré, C., Saltzman, E.S., 2013. Surface Ocean-Lower Atmosphere Processes, Surface Ocean-Lower Atmosphere Processes. https://doi.org/10.1029/GM187

Le Quéré, C., Takahashi, T., Buitenhuis, E.T., Rödenbeck, C., Sutherland, S.C., 2010. Impact of climate change and variability on the global oceanic sink of CO2. Global Biogeochem. Cycles 24, 1–10. https://doi.org/10.1029/2009GB003599

Lee, K., Tong, L.T., Millero, F.J., Sabine, C.L., Dickson, A.G., Goyet, C., Park, G.H., Wanninkhof, R., Feely, R. a., Key, R.M., 2006. Global relationships of total alkalinity with salinity and temperature in surface waters of the world's oceans. Geophys. Res. Lett. 33, 1–5. https://doi.org/10.1029/2006GL027207

Lenton, a., Tilbrook, B., Law, R.M., Bakker, D., Doney, S.C., Gruber, N., Ishii, M., Hoppema, M., Lovenduski, N.S., Matear, R.J., McNeil, B.I., Metzl, N., Fletcher, S.E.M., Monteiro, P.M.S., Rödenbeck, C., Sweeney, C., Takahashi, T., 2013. Sea-air CO2 fluxes in the Southern Ocean for the period 1990-2009. Biogeosciences 10, 4037–4054. https://doi.org/10.5194/bg-10-4037-2013

Lenton, A., Metzl, N., Takahashi, T., Kuchinke, M., Matear, R.J., Roy, T., Sutherland, S.C., Sweeney, C., Tilbrook, B., 2012. The observed evolution of oceanic pCO2 and its drivers over the last two decades. Global Biogeochem. Cycles 26, 1–14. https://doi.org/10.1029/2011GB004095

Lenton, A., Matear, R.J., 2007. Role of the Southern Annular Mode (SAM) in Southern Ocean CO2 uptake. Global Biogeochem. Cycles 21, 1–17. https://doi.org/10.1029/2006GB002714

Lévy, M., Ferrari, R., Franks, P.J.S., Martin, A.P., Rivière, P., 2012. Bringing physics to life at the submesoscale. Geophys. Res. Lett. 39, 1–13. https://doi.org/10.1029/2012GL052756

Lee, K., Tong, L.T., Millero, F.J., Sabine, C.L., Dickson, A.G., Goyet, C., Park, G.H., Wanninkhof, R., Feely, R. a., Key, R.M., 2006. Global relationships of total alkalinity with salinity and temperature in surface waters of the world's oceans. Geophys. Res. Lett. 33, 1–5. https://doi.org/10.1029/2006GL027207

Leung, S., Cabré, A., Marinov, I., 2015. A latitudinally banded phytoplankton response to 21st century climate change in the Southern Ocean across the CMIP5 model suite. Biogeosciences 12, 5715–5734. https://doi.org/10.5194/bg-12-5715-2015

Li, H., Ilyina, T., 2018. Current and Future Decadal Trends in the Oceanic Carbon Uptake Are Dominated by Internal Variability. Geophys. Res. Lett. https://doi.org/10.1002/2017GL075370

Li, Q.P., Franks, P.J.S., Landry, M.R., Goericke, R., Taylor, A.G., 2010. Modeling phytoplankton growth rates and chlorophyll to carbon ratios in California coastal and pelagic ecosystems. J. Geophys. Res. Biogeosciences 115, 1–12. https://doi.org/10.1029/2009JG001111

Locarnini, R.A., Mishonov, A. V., Antonov, J.I., Boyer, T.P., Garcia, H.E., Baranova, O.K., Zweng, M.M., Paver, C.R., Reagan, J.R., Johnson, D.R., Hamilton, M., Seidov, D., 2013. World Ocean Atlas 2013. Vol. 1: Temperature., S. Levitus, Ed.; A. Mishonov, Technical Ed.; NOAA Atlas NESDIS. https://doi.org/10.1182/blood-2011-06-357442

Lovenduski, N.S., Gruber, N., 2005. Impact of the Southern Annular Mode on Southern Ocean circulation and biology. Geophys. Res. Lett. 32, 1–4. https://doi.org/10.1029/2005GL022727

Lovenduski, N.S., Gruber, N., Doney, S.C., Lima, I.D., 2007. Enhanced CO2 outgassing in the Southern Ocean from a positive phase of the Southern Annular Mode. Global Biogeochem. Cycles. https://doi.org/10.1029/2006GB002900

Lovenduski, N.S., Gruber, N., Doney, S.C., 2008. Toward a mechanistic understanding of the decadal trends in the Southern Ocean carbon sink. Global Biogeochem. Cycles 22, 1–9. https://doi.org/10.1029/2007GB003139

Lovenduski, N.S., McKinley, G.A., Fay, A.R., Lindsay, K., Long, M.C., 2016. Partitioning uncertainty in ocean carbon uptake projections: Internal variability, emission scenario, and model structure. Global Biogeochem. Cycles 30, 1276–1287. https://doi.org/10.1002/2016GB005426

Madec, G., 2015. NEMO ocean engine.

Madec, G., Imbard, M., 1996. A global ocean mesh to overcome the North Pole singularity. Clim. Dyn. 12, 381–388. https://doi.org/10.1007/BF00211684

Mahadevan, A., 2016. The Impact of Submesoscale Physics on Primary Productivity of Plankton. Ann. Rev. Mar. Sci. 8, 161–184. https://doi.org/10.1146/annurev-marine-010814-015912

Mahadevan, A., D'Asaro, E., Lee, C., Perry, M.J., 2012. Eddy-driven stratification initiates North Atlantic spring phytoplankton blooms. Science (80-.). 336, 54–58. https://doi.org/10.1126/science.1218740

Mahadevan, A., Tagliabue, A., Bopp, L., Lenton, A., Mémery, L., Lévy, M., 2011. Impact of episodic vertical fluxes on sea surface pCO2. Philos. Trans. R. Soc. London A Math. Phys. Eng. Sci. 369, 2009–2025. https://doi.org/10.1098/rsta.2010.0340

Majkut, J.D., Carter, B.R., Frölicher, T.L., Dufour, C.O., Rodgers, K.B., Sarmiento, J.L., 2014. An observing system simulation for Southern Ocean carbon dioxide uptake. Philos. Trans. A. Math. Phys. Eng. Sci. 372, 20130046-. https://doi.org/10.1098/rsta.2013.0046

Marinov, I., Gnanadesikan, a, Toggweiler, J.R., Sarmiento, J.L., 2006. The Southern Ocean biogeochemical divide. Nature 441, 964–967. https://doi.org/10.1038/nature04883

Marinov, I., Gnanadesikan, a., 2011. Changes in ocean circulation and carbon storage are decoupled from air-sea CO2 fluxes. Biogeosciences 8, 505–513. https://doi.org/10.5194/bg-8-505-2011

Marshall, G.J., 2003. Trends in the Southern Annular Mode from observations and reanalyses. J. Clim. https://doi.org/10.1175/1520-0442(2003)016<4134:TITSAM>2.0.CO;2

Marshall, J., Speer, K., 2012. Closure of the meridional overturning circulation through Southern Ocean upwelling. Nat. Geosci. 5, 171–180. https://doi.org/10.1038/ngeo1391

Matear, R.J., Lenton, a., 2008. Impact of Historical Climate Change on the Southern Ocean Carbon Cycle. J. Clim. 21, 5820–5834. https://doi.org/10.1175/2008JCLI2194.1

Mauritsen, T., 2016. Global warming: Clouds cooled the Earth. Nat. Geosci. 9, 865–867. https://doi.org/10.1038/ngeo2838

McGillicuddy, D.J., 2016. Mechanisms of Physical-Biological-Biogeochemical Interaction at the Oceanic Mesoscale, Annual Review of Marine Science. https://doi.org/10.1146/annurev-marine-010814-015606

McKinley, G.A., Fay, A.R., Lovenduski, N.S., Pilcher, D.J., 2016a. Natural Variability and Anthropogenic Trends in the Ocean Carbon Sink. Ann. Rev. Mar. Sci. 9, 125–150. https://doi.org/10.1146/annurev-marine-010816-060529

McKinley, G.A., Pilcher, D.J., Fay, A.R., Lindsay, K., Long, M.C., Lovenduski, N.S., 2016b. Timescales for detection of trends in the ocean carbon sink. Nature 530, 469–472. https://doi.org/10.1038/nature16958

McNeil, B.I., Metzl, N., Key, R.M., Matear, R.J., Corbiere, A., 2007. An empirical estimate of the Southern Ocean air-sea CO2 flux. Global Biogeochem. Cycles 21, 1–16. https://doi.org/10.1029/2007GB002991

McNeil, B.I., Matear, R.J., 2013. The non-steady state oceanic CO 2 signal : its importance , magnitude and a novel way to detect it 2219–2228. https://doi.org/10.5194/bg-10-2219-2013

McNeil, B.I., Sasse, T.P., 2016. Future ocean hypercapnia driven by anthropogenic amplification of the natural CO2cycle. Nature. https://doi.org/10.1038/nature16156

Mehrbach, C., Culberson, C.H., Hawley, J.E., Pytkowitz, R.M., 1973. Measurement of the aparent dissociation constants of carbonic acid in seawater at atmospheric pressure. Limnol. Oceanogr. 18, 897–907. https://doi.org/10.4319/lo.1973.18.6.0897

Meijers, 2014. The Southern Ocean in the Coupled Model Intercomparison Project phase 5 The Southern Ocean in the Coupled Model Intercomparison Project phase 5.

Metzl, N., 2009. Decadal increase of oceanic carbon dioxide in Southern Indian Ocean surface waters (1991-2007). Deep. Res. Part II Top. Stud. Oceanogr. 56, 607–619. https://doi.org/10.1016/j.dsr2.2008.12.007

Metzl, N., Brunet, C., Jabaud-Jan, a., Poisson, a., Schauer, B., 2006. Summer and winter air-sea CO2 fluxes in the Southern Ocean. Deep. Res. Part I Oceanogr. Res. Pap. 53, 1548–1563. https://doi.org/10.1016/j.dsr.2006.07.006

Mignone, B.K., Gnanadesikan, A., Sarmiento, J.L., Slater, R.D., 2006. Central role of Southern Hemisphere winds and eddies in modulating the oceanic uptake of anthropogenic carbon. Geophys. Res. Lett. https://doi.org/10.1029/2005GL024464

Mikaloff Fletcher, S.E., Gruber, N., Jacobson, A.R., Doney, S.C., Dutkiewicz, S., Gerber, M., Follows, M., Joos, F., Lindsay, K., Menemenlis, D., Mouchet, A., Müller, S. a., Sarmiento, J.L., 2006. Inverse estimates of anthropogenic CO2 uptake, transport, and storage by the ocean. Global Biogeochem. Cycles 20, 1–16. https://doi.org/10.1029/2005GB002530

Mikaloff Fletcher, S.E., Gruber, N., Jacobson, A.R., Gloor, M., Doney, S.C., Dutkiewicz, S., Gerber, M., Follows, M., Joos, F., Lindsay, K., Menemenlis, D., Mouchet, a., Müller, S.

a., Sarmiento, J.L., 2007. Inverse estimates of the oceanic sources and sinks of natural CO2 and the implied oceanic carbon transport. Global Biogeochem. Cycles 21, 1–19. https://doi.org/10.1029/2006GB002751

Mongwe, N.P., Chang, N., Monteiro, P.M.S., 2016. The seasonal cycle as a mode to diagnose biases in modelled CO2 fluxes in the Southern Ocean. Ocean Model. 106, 90–103. https://doi.org/10.1016/j.ocemod.2016.09.006

Mongwe, N, P., Vichi, M., Monteiro, P.M.S., 2018. The seasonal cycle of pCO2 and CO2 fluxes in the Southern Ocean: diagnosing anomalies in CMIP5 Earth system models. Biogeosciences 155194, 2851–2872. https://doi.org/10.5194/bg-15-2851-2018

Monteiro, P.M.S., Gregor, L., Lévy, M., Maenner, S., Sabine, C.L., Swart, S., 2015. Intra-seasonal variability linked to sampling alias in air – sea CO_2 fluxes in the Southern Ocean. Geophys. Res. Lett. 1–8. https://doi.org/10.1002/2015GL066009

Monteiro, P.M.S., Schuster, U., Hood, M., Lenton, A., Metzl, N., Olsen, A., Rodgers, K.B., Sabine, C.L., Takahashi, T., Tilbrook, B., Yoder, J., Wanninkhof, R., Watson, A., 2010. A GLOBAL SEA SURFACE CARBON OBSERVING SYSTEM : ASSESSMENT OF CHANGING SEA SURFACE CO2 AND AIR-SEA CO2 FLUXES. ESA Publ. WPP-306.

Moore, J.K., Doney, S.C., Lindsay, K., 2004. Upper ocean ecosystem dynamics and iron cycling in a global three-dimensional model. Global Biogeochem. Cycles. https://doi.org/10.1029/2004GB002220

Nicholson, S.A., Levy, M., Llort, J., Swart, S., Monteiro, P.M.S., 2016. Investigation into the impact of storms on sustaining summer primary productivity in the Sub-Antarctic Ocean. Geophys. Res. Lett. 43, 9192–9199. https://doi.org/10.1002/2016GL069973

Orsi, A.H., Whitworth, T., Nowlin, W.D., 1995. On the meridional extent and fronts of the Antarctic Circumpolar Current. Deep. Res. Part I 42, 641–673. https://doi.org/10.1016/0967-0637(95)00021-W

Palmer, J.R., Totterdell, I.J., 2001. Production and export in a global ocean ecosystem model. Deep. Res. Part I Oceanogr. Res. Pap. 48, 1169–1198. https://doi.org/10.1016/S0967-0637(00)00080-7

Pasquer, B., Metzl, N., Goosse, H., Lancelot, C., 2015. What drives the seasonality of air–sea CO2 fluxes in the ice-free zone of the Southern Ocean: A 1D coupled physical–biogeochemical model approach. Mar. Chem. 177, 554–565. https://doi.org/10.1016/j.marchem.2015.08.008

Pierrehumbert, R.T., 2004. Warming the world - economic models of global warming, Nature. https://doi.org/10.1038/432677a

Pierrot, D.E. Lewis, Wallace, D.W.R., 2006. MS Excel Program Developed for CO2 System Calculations. ORNL/CDIAC-105a. Carbon Dioxide Information Analysis Center, Oak Ridge National Laboratory. U.S. Department of Energy, Oak Ridge, Tennessee.

Randerson, J.T., Lindsay, K., Munoz, E., Fu, W., Moore, J.K., Hoffman, F.M., Mahowald, N.M., Doney, S.C., 2015. Multicentury changes in ocean and land contributions to the climate-carbon feedback. Global Biogeochem. Cycles. https://doi.org/10.1002/2014GB005079

Revelle, R., Suess, H.E., 1957. Carbon Dioxide Exchange Between Atmosphere and Ocean and the Question of an Increase of Atmospheric CO2 during the Past Decades. Tellus. https://doi.org/10.3402/tellusa.v9i1.9075

Rintoul, R., Trull, W., 2001. Water mass properties along a north-south hydrographic 106.

Ritter, R., Landschützer, P., Gruber, N., Fay, A.R., Iida, Y., Jones, S., Nakaoka, S., Park, G.H., Peylin, P., Rödenbeck, C., Rodgers, K.B., Shutler, J.D., Zeng, J., 2017. Observation-Based Trends of the Southern Ocean Carbon Sink. Geophys. Res. Lett. https://doi.org/10.1002/2017GL074837

Rödenbeck, C., Bakker, D.C.E., Gruber, N., Iida, Y., Jacobson, A.R., Jones, S.,

Landschützer, P., Metzl, N., Nakaoka, S., Olsen, A., Park, G.H., Peylin, P., Rodgers, K.B., Sasse, T.P., Schuster, U., Shutler, J.D., Valsala, V., Wanninkhof, R., Zeng, J., 2015. Data-based estimates of the ocean carbon sink variability - First results of the Surface Ocean pCO2Mapping intercomparison (SOCOM). Biogeosciences Discuss. https://doi.org/10.5194/bgd-12-14049-2015

Rödenbeck, C., Keeling, R.F., Bakker, D.C.E., Metzl, N., Olsen, a., Sabine, C., Heimann, M., 2013. Global surface-ocean p^{CO}_2 and sea–air CO_2 flux variability from an observation-driven ocean mixed-layer scheme. Ocean Sci. 9, 193–216. https://doi.org/10.5194/os-9-193-2013

Rodgers, K.B., Aumont, O., Mikaloff Fletcher, S.E., Plancherel, Y., Bopp, L., De Boyer Montégut, C., Iudicone, D., Keeling, R.F., Madec, G., Wanninkhof, R., 2014. Strong sensitivity of Southern Ocean carbon uptake and nutrient cycling to wind stirring. Biogeosciences 11, 4077–4098. https://doi.org/10.5194/bg-11-4077-2014

Roobaert, A., Laruelle, G.G., Landschützer, P., Regnier, P., 2018. Uncertainty of the global oceanic CO₂ uptake induced by wind forcing: quantification and spatial analysis. Biogeosciences Discuss. 1–32. https://doi.org/10.5194/bg-2017-391

Rosso, I., Mazloff, M.R., Verdy, A., Talley, L.D., 2017. Space and time variability of the Southern Ocean carbon budget. J. Geophys. Res. Ocean. 122, 7407–7432. https://doi.org/10.1002/2016JC012646

Roy, T., Bopp, L., Gehlen, M., Schneider, B., Cadule, P., Frölicher, T.L., Segschneider, J., Tjiputra, J., Heinze, C., Joos, F., 2011. Regional impacts of climate change and atmospheric CO2 on future ocean carbon uptake: A multimodel linear feedback analysis. J. Clim. 24, 2300–2318. https://doi.org/10.1175/2010JCLI3787.1

Sabine, C.L., Feely, R. a, Gruber, N., Key, R.M., Lee, K., Bullister, J.L., Wanninkhof, R., Wong, C.S., Wallace, D.W.R., Tilbrook, B., Millero, F.J., Peng, T.-H., Kozyr, A., Ono, T., Rios, A.F., 2004. The oceanic sink for anthropogenic CO2. Science 305, 367–371. https://doi.org/10.1126/science.1097403

Sallée, J.B., Wienders, N., Speer, K., Morrow, R., 2006. Formation of subantarctic mode water in the southeastern Indian Ocean. Ocean Dyn. 56, 525–542. https://doi.org/10.1007/s10236-005-0054-x

Sallée, J.-B., Speer, K., Rintoul, S., Wijffels, S., 2010. Southern Ocean Thermocline Ventilation. J. Phys. Oceanogr. 40, 509–529. https://doi.org/10.1175/2009JPO4291.1

Sallée, J.B., Shuckburgh, E., Bruneau, N., Meijers, a. J.S., Bracegirdle, T.J., Wang, Z., 2013. Assessment of Southern Ocean mixed-layer depths in CMIP5 models: Historical bias and forcing response. J. Geophys. Res. Ocean. 118, 1845–1862. https://doi.org/10.1002/jgrc.20157

Sarmiento, J.L., Gruber, N., 2006. Ocean Biogeochemical Dynamics. Carbon N. Y. 67. https://doi.org/10.1063/1.2754608

Sarmiento, J.L., Gruber, N., Brzezinski, M. a, Dunne, J.P., 2004. High-latitude controls of thermocline nutrients and low latitude biological productivity. Nature 427, 56–60. https://doi.org/10.1038/nature10605

Sarmiento, J.L., Hughes, T.M.C., Stouffer, R.J., Manabe, S., 1998. Simulated response of the ocean carbon cycle to anthropogenic climate warming. Nature. https://doi.org/10.1038/30455

Séférian, R., Iudicone, D., Bopp, L., Roy, T., Madec, G., 2012. Water Mass Analysis of Effect of Climate Change on Air–Sea CO2 Fluxes: The Southern Ocean. J. Clim. 25, 3894–3908. https://doi.org/10.1175/JCLI-D-11-00291.1

Segschneider, J., Bendtsen, J., 2013. Temperature-dependent remineralization in a warming ocean increases surface pCO2 through changes in marine ecosystem composition. Global Biogeochem. Cycles 27, 1214–1225. https://doi.org/10.1002/2013GB004684

Sokolov, S., 2008. Chlorophyll blooms in the Antarctic Zone south of Australia and New Zealand in reference to the Antarctic Circumpolar Current fronts and sea ice forcing. J.

Geophys. Res. Ocean. 113. https://doi.org/10.1029/2007JC004329

Sokolov, S., Rintoul, S.R., 2009. Circumpolar structure and distribution of the antarctic circumpolar current fronts: 1. Mean98 circumpolar paths. J. Geophys. Res. Ocean. 114, 1–19. https://doi.org/10.1029/2008JC005108

Son, S., Gerber, E., 2010. Impact of stratospheric ozone on Southern Hemisphere circulation change: A multimodel assessment. J, 115, D00M07. https://doi.org/10.1029/2010JD014271

Swart, N.C., Fyfe, J.C., Saenko, O.A., Eby, M., 2014.a Wind-driven changes in the ocean carbon sink. Biogeosciences 11, 6107–6117. https://doi.org/10.5194/bg-11-6107-2014

Swart, S., Thomalla, S.J., Monteiro, P.M.S., 2014b. The seasonal cycle of mixed layer dynamics and phytoplankton biomass in the Sub-Antarctic Zone: A high-resolution glider experiment. J. Mar. Syst. https://doi.org/10.1016/j.jmarsys.2014.06.002

Szulejko, J.E., Kumar, P., Deep, A., Kim, K.H., 2017. Global warming projections to 2100 using simple CO2greenhouse gas modeling and comments on CO2climate sensitivity factor. Atmos. Pollut. Res. 8, 136–140. https://doi.org/10.1016/j.apr.2016.08.002

Tagliabue, A., Mtshali, T., Aumont, O., Bowie, A.R., Klunder, M.B., Roychoudhury, A.N., Swart, S., 2012. A global compilation of dissolved iron measurements: Focus on distributions and processes in the Southern Ocean. Biogeosciences 9, 2333–2349. https://doi.org/10.5194/bg-9-2333-2012

Tagliabue, A., Sallée, J.-B., Bowie, A.R., Lévy, M., Swart, S., Boyd, P.W., 2014. Surface-water iron supplies in the Southern Ocean sustained by deep winter mixing. Nat. Geosci. 7, 314–320. https://doi.org/10.1038/NGEO2101

Tagliabue, A., Aumont, O., Death, R., Dunne, J.P., Dutkiewicz, S., Galbraith, E., Misumi, K., Moore, J.K., Ridgwell, A., Sherman, E., Stock, C., Vichi, M., Völker, C., Yool, A., 2016. How well do global ocean biogeochemistry models simulate dissolved iron distributions? Global Biogeochem. Cycles. https://doi.org/10.1002/2015GB005289

Takahashi, T., Olafsson, J., Goddard, J.G., Chipman, D.W., Sutherland, S.C., 1993. Seasonal variation of CO2and nutrients in the high-latitude surface oceans: A comparative study. Global Biogeochem. Cycles 7, 843–878. https://doi.org/10.1029/93GB02263

Takahashi, T., Sutherland, S.C., Wanninkhof, R., Sweeney, C., Feely, R. a., Chipman, D.W., Hales, B., Friederich, G., Chavez, F., Sabine, C., Watson, A., Bakker, D.C.E., Schuster, U., Metzl, N., Yoshikawa-Inoue, H., Ishii, M., Midorikawa, T., Nojiri, Y., Körtzinger, A., Steinhoff, T., Hoppema, M., Olafsson, J., Arnarson, T.S., Tilbrook, B., Johannessen, T., Olsen, A., Bellerby, R., Wong, C.S., Delille, B., Bates, N.R., de Baar, H.J.W., 2009. Climatological mean and decadal change in surface ocean pCO2, and net sea-air CO2 flux over the global oceans. Deep. Res. Part II Top. Stud. Oceanogr. 56, 554–577. https://doi.org/10.1016/j.dsr2.2008.12.009

Takahashi, T., Sutherland, S.C., Sweeney, C., Poisson, A., Metzl, N., Tilbrook, B., Bates, N., Wanninkhof, R., Feely, R. a., Sabine, C., Olafsson, J., Nojiri, Y., 2002. Global sea-air CO2 flux based on climatological surface ocean pCO2, and seasonal biological and temperature effects. Deep. Res. Part II Top. Stud. Oceanogr. 49, 1601–1622. https://doi.org/10.1016/S0967-0645(02)00003-6

Takahashi, T., Sweeney, C., Hales, B., Chipman, D., Newberger, T., Goddard, J., Iannuzzi, R., Sutherland, S., 2012. The Changing Carbon Cycle in the Southern Ocean. Oceanography 25, 26–37. https://doi.org/10.5670/oceanog.2012.71

Talley, L.D., Pickard, G.L., Emery, W.J., Swift, J.H., 2011. Descriptive Physical Oceanography, Descriptive Physical Oceanography. https://doi.org/10.1016/B978-0-7506-4552-2.10002-2

Tamsitt, V., Drake, H.F., Morrison, A.K., Talley, L.D., Dufour, C.O., Gray, A.R., Griffies, S.M., Mazloff, M.R., Sarmiento, J.L., Wang, J., Weijer, W., 2017. Spiraling pathways of global deep waters to the surface of the Southern Ocean. Nat. Commun. 8, 1–10. https://doi.org/10.1038/s41467-017-00197-0

Taylor, K.E., 2001. Summarizing multiple aspects of model performance in a single diagram.

J. Geophys. Res. Atmos. https://doi.org/10.1029/2000JD900719

Taylor, K.E., Stouffer, R.J., Meehl, G.A., 2012. An overview of CMIP5 and the experiment design. Bull. Am. Meteorol. Soc. 93, 485–498. https://doi.org/10.1175/BAMS-D-11-00094.1

Thomalla, S.J., Fauchereau, N., Swart, S., Monteiro, P.M.S., 2011. Regional scale characteristics of the seasonal cycle of chlorophyll in the Southern Ocean. Biogeosciences 8, 2849–2866. https://doi.org/10.5194/bg-8-2849-2011

Thomalla, S.J., Racault, M.F., Swart, S., Monteiro, P.M.S., 2015. High-resolution view of the spring bloom initiation and net community production in the Subantarctic Southern Ocean using glider data. ICES J. Mar. Sci. 72, 1999–2020. https://doi.org/10.1093/icesjms/fsv105

Thompson, D.W.J., Solomon, S., 2002. Interpretation of recent Southern Hemisphere climate change. Science 296, 895–899. https://doi.org/10.1126/science.1069270

Thompson, D.W.J., Solomon, S., Kushner, P.J., England, M.H., Grise, K.M., Karoly, D.J., 2011. Signatures of the Antarctic ozone hole in Southern Hemisphere surface climate change. Nat. Geosci. https://doi.org/10.1038/ngeo1296

Thompson, D.W.J., Wallace, J.M., 2000. Annular modes in the extratropical circulation. Part II: Trends. J. Clim. https://doi.org/10.1175/1520-0442(2000)013<1018:AMITEC>2.0.CO;2

Tjiputra, J.F., Roelandt, C., Bentsen, M., Lawrence, D.M., Lorentzen, T., Schwinger, J., Seland, Ø., Heinze, C., 2013. Evaluation of the carbon cycle components in the Norwegian Earth System Model (NorESM). Geosci. Model Dev. Discuss. 6, 301–325. https://doi.org/10.5194/gmd-6-301-2013

Turner, J., Bracegirdle, T.J., Phillips, T., Marshall, G.J., Scott Hosking, J., 2013. An initial assessment of antarctic sea ice extent in the CMIP5 models. J. Clim. https://doi.org/10.1175/JCLI-D-12-00068.1

Tyndall, J., 1861. The Bakerian Lecture: On the Absorption and Radiation of Heat by Gases and Vapours, and on the Physical Connexion of Radiation, Absorption, and Conduction. Philos. Trans. R. Soc. London. https://doi.org/10.1098/rstl.1861.0001

Vichi, M., Pinardi, N., Masina, S., 2007. A generalized model of pelagic biogeochemistry.for the global ocean ecosystem. Part I: Theory. J. Mar. Syst. 64, 89–109. https://doi.org/DOI 10.1016/j.jmarsys.2006.03.006

Visinelli, L., Masina, S., Vichi, M., Storto, A., Lovato, T., 2016. Impacts of data assimilation on the global ocean carbonate system. J. Mar. Syst. 158, 106–119. https://doi.org/10.1016/j.jmarsys.2016.02.011

Visbeck, M., 2009. A station-based southern annular mode index from 1884 to 2005. J. Clim. https://doi.org/10.1175/2008JCLI2260.1

Volk, T., Hoffert, M.I., 1985. Ocean carbon pumps: Analysis of relative strength and efficiencies in ocean-driven atmospheric CO_2 changes. Geophys. Monogr. Ser. https://doi.org/10.1029/GM032p0099

Wang, L., Huang, J., Luo, Y., Zhao, Z., 2016. Narrowing the spread in CMIP5 model projections of air-sea CO2 fluxes. Sci. Rep. 6, 1–13. https://doi.org/10.1038/srep37548

Wang, M., Overland, J.E., 2012. A sea ice free summer Arctic within 30 years: An update from CMIP5 models. Geophys. Res. Lett. 39, 2–6. https://doi.org/10.1029/2012GL052868

Wang, Z., Kuhlbrodt, T., Meredith, M.P., 2011. On the response of the Antarctic Circumpolar Current transport to climate change in coupled climate models. J. Geophys. Res. 116. https://doi.org/10.1029/2010JC006757

Wanninkhof, R., Asher, W.E., Ho, D.T., Sweeney, C., McGillis, W.R., 2009. Advances in quantifying air-sea gas exchange and environmental forcing. Ann. Rev. Mar. Sci. 1, 213–244. https://doi.org/10.1146/annurev.marine.010908.163742

Wanninkhof, R., Park, G.H., Takahashi, T., Sweeney, C., Feely, R., Nojiri, Y., Gruber, N., Doney, S.C., McKinley, G. a., Lenton, a., Le Quere, C., Heinze, C., Schwinger, J., Graven, H., Khatiwala, S., 2013. Global ocean carbon uptake: Magnitude, variability and trends. Biogeosciences 10, 1983–2000. https://doi.org/10.5194/bg-10-1983-2013

Williams, K.D., Bodas-Salcedo, A., Déqué, M., Fermepin, S., Medeiros, B., Watanabe, M., Jakob, C., Klein, S.A., Senior, C.A., Williamson, D.L., 2013. The transpose-AMIP II experiment and its application to the understanding of southern ocean cloud biases in climate models. J. Clim. https://doi.org/10.1175/JCLI-D-12-00429.1

Williams, R.G., Roussenov, V., Frölicher, T.L., Goodwin, P., 2017a. Drivers of Continued Surface Warming After Cessation of Carbon Emissions. Geophys. Res. Lett. 44, 10,633-10,642. https://doi.org/10.1002/2017GL075080

Williams, R.G., Roussenov, V., Goodwin, P., Resplandy, L., Bopp, L., 2017b. Sensitivity of global warming to carbon emissions: Effects of heat and carbon uptake in a suite of earth system models. J. Clim. 30, 9343–9363. https://doi.org/10.1175/JCLI-D-16-0468.1

Wolf-Gladrow, D. a., Zeebe, R.E., Klaas, C., Körtzinger, A., Dickson, A.G., 2007. Total alkalinity: The explicit conservative expression and its application to biogeochemical processes. Mar. Chem. 106, 287–300. https://doi.org/10.1016/j.marchem.2007.01.006

Weiss, R.F., 1974. Carbon dioxide in water and seawater: The solubility of a non-ideal gas. Mar. Chem. 2, 203–215

Williams, R.G., Follows, M.J., 2011. Ocean Dynamics and the Carbon Cycle. Cam- bridge University Press, Cambridge ISBN 9780521843690.

Young, I.R., 1999. Seasonal variability of the global ocean wind and wave climate. Int. J. Climatol. https://doi.org/10.1002/(SICI)1097-0088(199907)19:9<931::AID-JOC412>3.0.CO;2-O

Zahariev, K., Christian, J.R., Denman, K.L., 2008. Preindustrial, historical, and fertilization

simulations using a global ocean carbon model with new parameterizations of iron limitation, calcification, and N2 fixation. Prog. Oceanogr. 77, 56–82. https://doi.org/10.1016/j.pocean.2008.01.007

Zeebe, R.., Wolf-Gladrow, D., 2001. Stable Isotope Fractionation. CO2 Seawater Equilibrium, Kinet. Isot. Equilibrium, Kinet. Isot.

Zickfeld, K., Fyfe, J.C., Eby, M., Weaver, A.J., 2008. Comment on "Saturation of the southern ocean CO2 sink due to recent climate change". Science 319, 570; author reply 570. https://doi.org/10.1126/science.1149077